Università degli Studi di Catania

Dottorato di Ricerca Internazionale in Ingegneria dei Sistemi

XXVI Ciclo

Gaetano L'Episcopo

Nonlinear Methodologies in Transduction Mechanisms for Energy Harvesting and Sensors

Ph.D. Thesis

Coordinator: Prof. Ing. Luigi Fortuna

Tutor: Prof. Ing. Salvatore Baglio

2013

To those who believed in me

Abstract

The constant need of improving performance of transducers has pushed scientists to searching novel solutions in transduction mechanisms. The development of theories about Stochastic Resonance and the interplay between nonlinearity and noise represents one of the proposed strategies to improve performance of actual transducers in certain operating conditions.

Among nonlinear systems, bistable mechanisms have been investigated in this work. Several results of their application in the field of energy harvesting from mechanical vibrations and in the sensing of AC currents are presented with a special focus on the benefits due to their adoption in specific applica-

tions where traditional approaches based on linear transduction mechanisms exhibit issues in efficiency.

A special attention is also paid to the technological solutions to implement prototypes of integrated bistable devices and several rapid prototyping strategies are investigated and proposed.

Contents

Introduction

Stay foolish. Stay hungry.

Steve Jobs

The constant need to improve performance and the always widening range of applications for electronic-based devices push scientific research toward the endless exploration for novel solutions that can advance the state of the art overcoming traditional approaches.

Among electronics devices, a special attention is reserved to transducers (i.e. systems able to convert signals in one form of energy to another form) for their wide range of applications in sensing, actuating and energy harvesting.

Very often, transducers are considered to exploit linear mechanisms thus, the output signal or power is almost linearly proportional to the input in this case. However, although to consider a linear working principle helps to reduces the complexity of system handling and implementation, some issues in performance have been revealed when linear strategies are adopted in applications involving nonlinearities and noise. As shown in this work, for example, sensitivity in sensors is strongly affected by noise and linear energy harvesters from mechanical vibrations exhibit poor performance when wideband noisy vibrations are addressed as source energy to be scavenged. Therefore linear approaches, even if generally simpler, are not alway optimal and often the efforts descending from taking into account a more complex model rewards with better overall perfomances.

Some solutions exploiting nonlinear transducers and the interplay between noise and nonlinear dynamics have been proposed in literature, especially after the development of the theories about Stochastic Resonance, and have been shown to represent an effective way to overcome traditional limitations

of linear transducers and therefore to improve their performances.

In this work, nonlinear transduction mechanisms will be presented with a special focus on bistable strategies with several applications in the sensors field and in the energy harvesting from mechanical vibrations. Efforts will be paid to show the technical feasibility of the proposed solutions and to prove the performance improvement descending from nonlinearities.

In the first chapter, motivations of the adoption of nonlinear strategies in transduction mechanisms will be discussed by supporting them with theory and comparisons with linear transducers. Among nonlinear mechanisms, the attention will be focused on bistable strategies and the state of the art of their application in the field of sensors and of energy harvesting will be presented.

In the second chapter, several technology solutions to implement bistable devices will be treated. First of all, suitable standard technology processes to develop microscale devices in the field of microelectromechanical systems (MEMS) will be presented; secondly, some useful strategies and some re-

sults for rapid prototyping in Nanotechnology will be presented and, finally, an approach for rapid prototyping of low cost devices of centimeter size exploiting direct printing technology will be proposed.

In the third chapter, after covering the state of the art in the energy harvesting from mechanical vibrations, some solutions exploiting mechanically bistable oscillators will be proposed both in the field of MEMS and in direct printing technology. Models simulations along with experimental results will be presented to prove the feasibility of the proposed devices.

In the fourth chapter, attention will be focused on bistable AC current sensors and, after discussing the state of the art in this field, a bistable sensor for AC currents capable of scavenging energy from its own operative environment will be proposed along with its behavioral model and an experimental device prototype for testing.

1

Linear and nonlinear strategies in transduction mechanisms

Science shines forth in all its value as a good capable of motivating our existence, as a great experience of freedom for truth, as a fundamental work of service. Through research each scientist grows as a human being and helps others to do likewise.

John Paul II

1.1 Linear and nonlinear transduction strategies

There are many aspects of the environment that people need and/or want to monitor or modify for a wide range of purposes. Some examples of physical and chemical quantities

of interest are given by temperature, light intensity, mechanical vibrations, air pressure, humidity, chemicals present in water, chemical pollutants in air and so on. In order to handle such quantities, devices able to convert and relate with different physical and chemical fields are requested. Transducers represent this sort of specially made devices to respond to a chosen energy source and transform it into a different form of energy through a defined transduction mechanism. Transducers can be divided into sensors and actuators; sensors are used to detect a parameter in one form and report it in another form of energy, often an electrical signal, while actuators accepts energy as input and produces an action (e.g., movement) [249].

The traditional approach in implementing transduction mechanisms has been based on linear strategies. In these cases, the device transduction function is represented by a linear mathematical function (i.e. a straight line in a graph) expressing a linear proportional relationship between the input and the output quantities. As an example, this means that to a given variation of the sensed quantity corresponds a pro-

portional variation in the output signal of sensors. Deviations from such linear behaviour have been characterized in the specifications of transducers in terms of nonlinearity errors (e.g., the deviation of the device from its nominal linear operation) because nonlinearity has been traditionally considered as a negative point in transducers [70].

Since the beginnings of modern engineering sciences, the use of linear systems has been preferred by engineers and physicists to nonlinear systems because linear transducers satisfy mathematical properties like proportionality, superposition and homogeneity, which can greatly simplify their modeling, design and control in terms of analytical efforts and computational and development costs. In addition, linear time-invariant systems with zero initial conditions and zero-point equilibrium (i.e. a subset of linear systems) take advantage of transfer functions as useful mathematical representations of the input-output relationship, in terms of spatial or temporal frequency [84].

Although linear strategies are simpler to handle, nature is intrinsically highly nonlinear. Due to the complex interaction

among physical and chemical fields, the nonlinear behaviour can be certainly recognized as the ordinary feature of the vast majority of physical and chemical systems [227]. Sometimes, in engineering sciences, linear features of systems come from approximations of nonlinear behaviours. In the case of sensors, as an example, the linear behaviour is often exhibited only in a small interval of values of their operative range or under specific restricted conditions, thus limiting the sensor application range [177].

Recent studies about transducers have revealed some benefits of nonlinear transduction strategies over linear approaches, under certain conditions in some applications such as sensors and energy harvesting [92].

It is known that noise (intended both as any spurious disturb that superimposes and/or distorts the original signal produced by the transducer and as fluctuations affecting the relevant parameters of the transducer) is one of hardest unpleasant aspect in any linear transducer design. In fact, noise can significantly affect linear transducers performance by limiting their sensitivity and their dynamic range and increasing

signal distortion and leading them to exhibit an unwanted "nonlinear" behaviour [105].

On the contrary, many scientists have recently started to take a novel approach in transducers studies where noise and nonlinearity play a key role in the operation of some physical and chemical nonlinear systems. The most famous example of the work developed in this direction is probably due to the discovery of the stochastic resonance phenomenon [40, 91] where a proper quantity of noise can make a periodically driven bistable dynamic system to switch in synchrony with its driving input. As an example of the exploitation of stochastic resonance, a signal that is normally too weak to be detected by a sensor can be boosted by adding white noise to the signal, which contains a wide spectrum of frequencies; the frequencies in the white noise corresponding to the original frequencies of the signal will resonate with each other, amplifying the original signal while not amplifying the rest of the white noise (thereby increasing the signal-to-noise ratio which makes the original signal more prominent). Furthermore, the added white noise can be enough to be detectable by the sensor,

which can then filter it out to effectively detect the original, previously-undetectable signal [89].

Initially proposed as a possible explanation of the periodic recurrence of Earth ice ages [29], stochastic resonance has become a general paradigm for periodically driven noisy nonlinear dynamical systems [2]. Following the pioneering works on stochastic resonance, other studies have been developed in order to exploit the potential benefits of the interplay between noise and nonlinearities [104]. In the above mentioned field of sensors, a novel class of "noise activated nonlinear devices" has been introduced. In these devices noise and nonlinear response can be exploited in the framework of a different measurement strategy that allows for improving devices sensitivity and simplifying readout schemes [88]. This new approach is based on the monitoring of the mean residence time difference. The residence time is the time spent by the system output in each of its stable equilibrium states. The switches among these stable equilibrium states are affected both by the unknown target signal and the noise present during measurements [67]. A careful consideration of the statistics in the

residence time can lead to extract useful information about the hidden target signal [42]. This nonlinear transduction approach has been effectively exploited in the development of residence-times fluxgate magnetometers [14, 41] and electric field sensors based on ferroelectric materials [12, 13].

Another example of the benefits of nonlinear transducers in noisy environments is represented by the exploitation of the properties of non-resonant oscillators, characterized by a nonlinear dynamic response, in the harvesting of energy from mechanical vibrations [60, 92]. In fact, it has been demonstrated that, in presence of mechanical vibrations having wide spectrum at low frequencies (e.g., below 500 Hz), thus resembling a band-limited white noise, the application of nonlinear transducers can allow for scavenging a larger amount of energy than linear transducers thanks to their wider bandwidth [83, 235].

1.2 Nonlinear transduction methodologies: bistable strategies

Among nonlinear systems, since last decades bistable systems have been playing a prominent role in the field of nonlinear transducers exploiting benefits from stochastic resonance and noise [90, 167].

In its mathematical formulation, a system is defined "bistable" when it exhibits two stable equilibrium states, according to Lyapunov's theory [148], and one unstable equilibrium state between the two aforesaid stable equilibrium states. This formulation means that, if a bistable system lies in one of its stable equilibrium states, even if it is subjected to a "small perturbation" from an external forcing, the system will continue to keep its stable equilibrium state and/or, at least, it will continue to oscillate around it as long as the perturbation is smaller than a "certain limit value". When the applied energy of the incoming perturbation is large enough to overcome a defined barrier (i.e. the unstable equilibrium state) between the two stable equilibrium states, the system will switch to the other stable equilibrium state. At this point, that stable

equilibrium state will tend to be maintained until another external forcing, larger than a defined level, will lead the system to the previous stable equilibrium state. The behaviour of a bistable system can be further understood through the "ball-on-a-hill" analogy [116] in fig. 1.1.

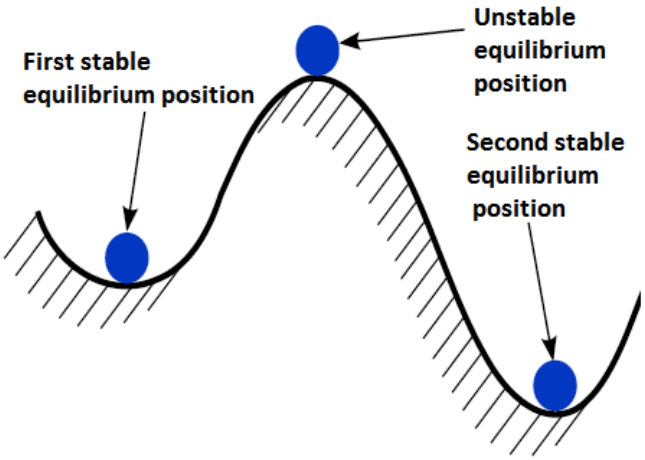

Fig. 1.1 – Ball on a hill equilibrium analogy.

The elevation profile of the hill in the "ball-on-a-hill" analogy in fig. 1.1 is a representation of the energy profile in the system. In fact, the two stable equilibrium states are the configurations of local minimum in the energy profile, while the unstable equilibrium state is the configuration of local maxi-

mum. Since dynamical systems attempt to remain in the lowest energy state possible, according to the Lagrange-Dirichlet theorem [38], no external energy is needed to maintain the system in its stable equilibrium states. However, due to different energetic levels between each of the two stable equilibrium states and the unstable equilibrium state (which defines the "energy barrier" of the system), external energy must be supplied to allow for commutations between the two stable equilibrium states in order to firstly come up the adverse energy slope, secondly to overtake the unstable equilibrium state and lastly to reach to the other stable equilibrium state by taking advantage of the favourable energy slope after passing the unstable equilibrium state (see fig. 1.1). The amount of external energy required to snap from the first stable equilibrium state to the second one could be different from the quantity of energy needed to switch in the opposite direction because of the eventual asymmetry in the energy level of the stable equilibrium states. In the case of asymmetry, there is a higher probability that the system will spend more time in its stable equilibrium state having the lower energy level [171].

Mechanics is one of the fields where the theory of bistability has been successfully applied to develop mechanically bistable devices [173]. In the specific case of mechanical systems, the energy profile with respect to a mechanical variable (e.g., a displacement) is determined by both the mechanical potential energy related to the gravitational forces and to the elastic energy stored in compliant mechanisms such as springs or flexible beams. As an example, a proper design of the geometry of the springs of a mechanism can result in a device exhibiting a bistable behaviour. [116]

Neglecting the effects of gravitational forces, the elastic potential energy U_m of a mechanical system can be written as a general function of its mechanical variables, such as linear displacements x and angular displacements θ, as in (1.1) [212].

$$U_m = f(x, \theta) \tag{1.1}$$

The plot of the elastic potential energy U_m with respect to one of its mechanical variables represents the energy profile of the system; an example of a bistable energy function is shown in fig. 1.2 [107].

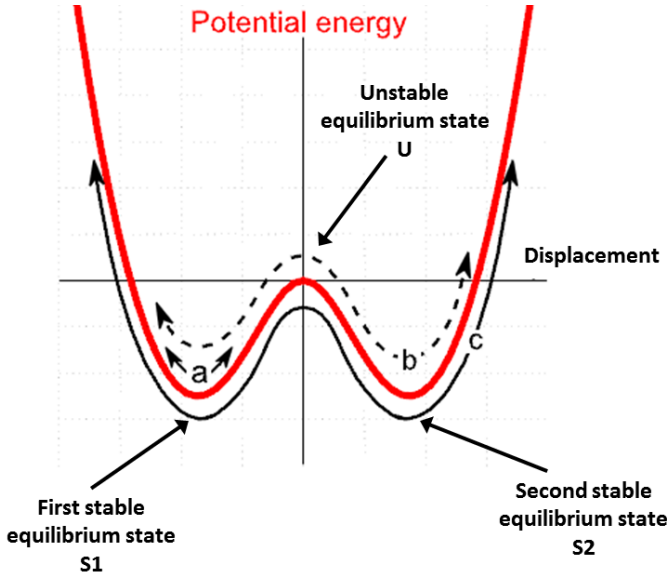

Fig. 1.2 – Energy potential of a generic bistable oscillator showing example trajectories for (a) intrawell oscillations, (b) chaotic interwell vibrations and (c) interwell oscillations [107]. The two stable equilibrium states, respectively $S1$ and $S2$, and the unstable equilibrium position U are marked.

The first derivative of the elastic potential U_m with respect to a linear displacement x gives a mechanical force F as in (1.2) [212], while the first derivative with respect to an angular displacement θ results in a torque T, as in (1.3) [212].

$$F = \frac{dU_m}{dx} \tag{1.2}$$

$$T = \frac{dU_m}{d\theta} \tag{1.3}$$

In the equilibrium states, the first derivative of the potential energy U_m is equal to zero. This means that no force/torque is required to maintain the system in the equilibrium state. The evaluation of the second derivative of the potential energy U_m in the equilibrium states leads to distinguish stable equilibrium states (when the second derivative is negative) from unstable equilibrium states (when the second derivative is positive) [116]. The static force/torque required to switch from the first stable equilibrium state to second one is named "critical force", F_{12}. Analogously, F_{21} is the critical force required to pass from the second equilibrium state to the first one. Lower critical forces result in higher probabilities of commutations between stable equilibrium states. An example of the restoring force and critical forces in a generic bistable system is illustrated in fig. 1.3.

Static switching can be achieved by applying a static force larger than the critical force. However, dynamical switching (i.e. when the force is applied at a certain frequency), can

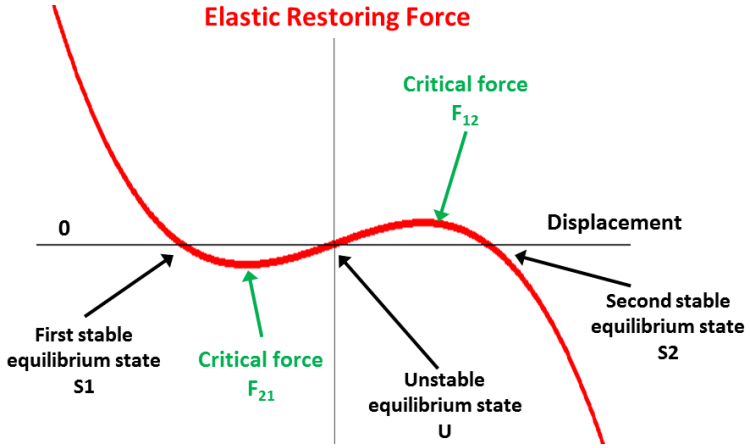

Fig. 1.3 – Restoring force for a generic bistable system. The two stable equilibrium states, respectively $S1$ and $S2$, and the unstable equilibrium position U are marked. Critical force required to switch from the first to second equilibrium state, F_{12} , and from the second to the first, F_{21}, are marked.

be achieved at a lower force than the critical force. It has been shown that harmonic excitation of bistable mechanical systems can reduce the input energy requirement to achieve commutations [46, 132].

On the dynamical point of view, the typical double-well potential of a bistable system (shown in fig. 1.2) provides for three distinct dynamic operating regimes depending on the input amplitude, as illustrated in fig. 1.2 and in fig. 1.4 [107]. Bistable systems may exhibit low-energy intrawell oscillations

as in figure 1(a). In this case, the system oscillates around one of the two stable equilibrium states with a small stroke per forcing period as in fig. 1.4(a) and phase portrait with an overlay Poincaré map as in fig. 1.4(d). Alternatively, the bistable oscillator may be excited to a degree so as to exhibit aperiodic or chaotic vibrations between stable equilibrium states such as in fig. 1.4(b) and fig. 1.4(e). As the excitation amplitude is increased still further, the device may exhibit periodic interwell oscillations (also known as high energy orbits or snap-through behaviour) as in fig. 1.4(c) and fig. 1.4(f). In some cases, the dynamic regimes may theoretically coexist although only one is physically realizable at a time [107].

Examples of bistable dynamical systems can be found in subsection 1.3.1

Several examples of bistable mechanical systems can be found in the field of compliant micromechanisms in MEMS technology, such as switches [195], relays [98], shutters [147], crash sensors [220], latchup testing [117] and micro-positioning devices [236].

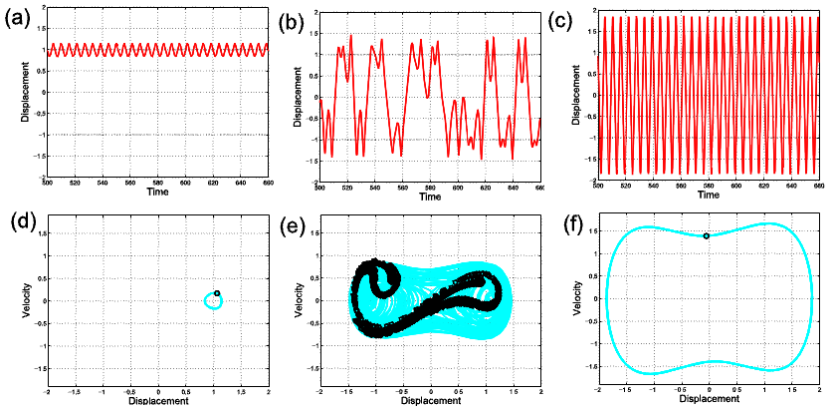

Fig. 1.4 – Example of displacement–time responses (top row) and phase plots with an overlap Poincaré map as black circles (bottom row) for three dynamic regimes of bistable oscillators, as reported in fig. 1.2: (a) and (d) intrawell oscillations, (b) and (e) chaotic interwell vibrations, (c) and (f) interwell oscillations [107].

More details about the applications of bistable systems in sensing and energy harvesting will be exposed in section 1.3.

1.3 Applications of bistable strategies: energy harvesting and sensors

The characteristics of the bistable mechanisms have been exploited in the field of sensors and energy harvesting to develop innovative solutions and to overcome some limits of traditional devices, under certain operating conditions [40, 107].

In the following subsections, some of the proposed bistable strategies in sensors (subsection 1.3.1) and in vibration energy harvesters (subsection 1.3.2) will be presented along with some background knowledge on mathematics and physics to motivate the adoption of these strategies.

Since a bistable AC current sensor is proposed in this work, a discussion about the state of the art in AC current sensors and about the benefits of bistability in this field will be addressed in section 4.1.

More general details about energy harvesting from mechanical vibrations and a discussion about the state of the art in vibrations microgenerators will be exposed in section 3.1.

1.3.1 Applications of bistable mechanisms in sensors

Since the development of the theories on stochastic resonance and on the benefits of the interplay between noise and nonlinearity, nonlinear dynamics sensors, especially bistable sensors, have been viewed with interest by scientific community [40].

In fact, in some applications where the Signal-to-Noise Ratio (SNR) is too small, signal detection could be quite challenging, especially for "weak" signals. However, there are cases where noise, instead of degrading the signal detection, can enhance the SNR, if principles of stochastic resonance are applied. This allows the information to be captured by the sensor, even when the noise floor is high. It has been demonstrated that the properties of overdamped bistable dynamic systems can be exploited to develop a novel class of sensors that properly operate in environments with a significant amount of noise, differently from many devices based on linear strategies. In addition, the environmental noise can activate their sensor operation and/or enhance their performance by interplaying with the nonlinearities in these devices. For this

reason this kind of detectors has been named "Noise Activated Nonlinear Dynamic Sensors" [88].

Noise Activated Nonlinear Dynamic Sensors

The operating principle of noise activated sensors can be understood by considering a bistable dynamic system, whose generic form is given by (1.4) [40].

$$\dot{x} = -\nabla U(x) \tag{1.4}$$

where x is the state variable and $U(x)$ is a generic bistable potential (a plot example is shown in fig. 1.2), which underpins the behaviour of numerous systems in the physical world such as electronic circuits (e.g., Schmitt trigger) [210], mechanical systems [116], systems with hysteresis (e.g., ferromagnetic and ferroelectric materials) [39] and decision-making processes in cell cycle progression, cellular differentiation, and apoptosis [254].

The most studied example is the overdamped Duffing system whose potential $U(x)$ is depicted by (1.5) [73].

$$U(x) = -ax^2 + bx^4 \tag{1.5}$$

The two parameters a and b determine the shape of the potential. When $a > 0$, the potential is bistable with the stable equilibrium states centered at $x = \pm\sqrt{a/(2b)}$, the unstable equilibrium state at $x = 0$ and a potential barrier $U_0 = a^2/(4b)$; while for $a \leq 0$ the system becomes monostable [73].

Another example of nonlinear bistable system is represented by the Analog Hopfield Neuron potential in (1.6) [114]:

$$U(x) = ax^2 - b\ln\big[\cosh(x)\big] \tag{1.6}$$

where x denotes a cell membrane voltage and a and b are parameters conditioning the shape of the potential.

A different example of bistable potential is given by the RF SQUID loop in (1.7) [43]:

$$U(x) = ax^2 b\cos(2\pi x) \tag{1.7}$$

in which x denotes the magnetic flux in the loop and a and b are parameters that shape the potential.

The simplest version of a nonlinear dynamic bistable system exhibiting stochastic resonance can be obtained by adding a time-periodic "deterministic" sinusoidal signal of amplitude A and frequency f_s and a "stochastic" noise $F(t)$ (which is generally Gaussian and exponentially correlated) to the system in (1.4). This leads to the (1.8) [40].

$$\dot{x} = -\nabla U(x) + F(t) + A\sin\big(2\pi f_s x\big) \tag{1.8}$$

In absence of any external forcing ($A = 0$ and $F = 0$), the system in (1.8) will settle near the bottom of one of the two potential wells.

A more complex behaviour is observed when the external time-periodic forcing of period T_s (i.e. $T_s = 1/f_S$) and the "stochastic" noise are applied to the system ($A \neq 0$ and $F(t) \neq 0$) in (1.8). The time-periodic forcing term causes a periodic rocking, back and forth, of the potential barriers in the bistable potential with the same period T_s of the periodic forcing. In a single period of the forcing signal, the potential is cycled through fig. 1.5(a)–fig. 1.5(d), antisymmetrically raising and lowering the left and right potential wells. The

maxima and minima of the time-periodic signal correspond to when the potential barrier is at its lowest at each side well, as in fig. 1.5(b) and in fig. 1.5(d) [106].

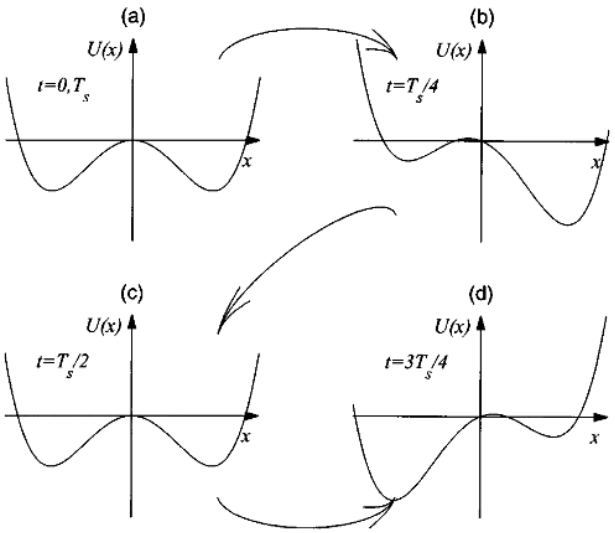

Fig. 1.5 – Periodic driving signal causes the bistable potential to be tilted back and forth, antisymmetrically raising and lowering the left and right potential wells during a period of the driving signal.

If the deterministic rocking is too weak to cause the system to climb over the potential barrier in absence of noise, the system exhibits a "subthreshold" behaviour with intrawell oscillations [40].

The addition of even small amounts of noise, however, can give a finite switching probability to the system response and, so, some potential barrier crossings could occur. For moderate noise, the switchings will acquire a degree of coherence with the underlying time-periodic signal because the switching probability is maximized whenever the absolute value of the time-periodic signal is at its maximum, as shown in fig. 1.5(b) and in fig. 1.5(d).

The barrier crossing rate, thus, depends critically on the noise intensity. If the noise intensity is very low, the probability of any switching occurring is quite tiny. On the other hand, intense noise can induce switchings even in an "unfavourable" interval (i.e. when the absolute value time periodic signal is at its minimum); in this case, the output signal is swamped. In between, there is a wide range of noise intensities introducing switching events in near-synchronicity with the applied time-periodic signal. This cooperation between the deterministic signal and stochastic noise introduces a certain "coherence" in the system.

This "coherence" in the system can be recognized by observing the SNR of the system as a function of the magnitude of the input stochastic noise. A peak in the SNR can be found at a given level of noise: this is the critical point of maximum coherence in the system. Past this critical noise strength, the switchings lose coherence with the time-periodic signal frequency and the dynamics become noise-dominated, thus decreasing the SNR. The earliest definition of stochastic resonance is given by the maximum of the signal amplitude as a function of the noise level [40]. In this case, the noise enhances the SNR and, thus, improve system performance. It is worth noted that this phenomenon has been observed also in monostable [226], multistable and coupled bistable [128] systems.

This theory coupled with proper readout mechanisms can be applied to sense quantities in applications where noise and device sensitivity could be critical.

Readout schemes for noise activated nonlinear dynamic sensors

In many cases, the detection of a small target signal (DC or low frequency) through a bistable system is based on a spectral technique [34], where a known periodic bias signal is applied to the sensor to saturate it and drive it very rapidly between its two (locally) stable attractors (corresponding to the minima of the bistable potential energy function, when the attractors are fixed points). Often, the amplitude of the bias signal is taken to be quite large in order to render the response largely independent from the noise. The effect of a target DC signal is, then, to skew the potential, resulting in the appearance of features at even harmonics of the bias frequency f_s in the system response [25]. The spectral amplitude at $2f_s$ is, then, proportional to the bias frequency and the square of the target signal amplitude; hence, the spectral amplitude can be used to yield the target signal. In practice, a feedback mechanism is frequently utilized for reading out the asymmetry-producing target signal via a nulling technique [34]. An example of this readout mechanism via bistable

dynamics mechanisms is the second harmonic fluxgate exploiting the bistability descending from saturation in hysteretic ferromagnetic cores [99].

The above readout scheme has some drawbacks. First of all, a large onboard power is needed to provide a high-amplitude and high-frequency bias signal. Furthermore, feedback electronics can be cumbersome and introduce their own noise floor into the measurement system. Finally, a high-amplitude and high-frequency bias signal often increases the noise floor in the system [88].

A different readout scheme is based on the residence time statistics in a bistable system. This approach consists in measuring the mean time spent by the system in each of its stable equilibrium states to both quantify the stochastic resonance phenomenon [40] and gain information on the presence of small-unknown target signals in sensors field [88].

Given a bistable dynamic system as that formulated in (1.8), in absence of noise ($F(t) = 0$) and in presence of the time-periodic signal ($A \neq 0$), when the bistable in intrinsically symmetric (e.g., the Duffing potential in (1.5)), the two residence

times will be, on average, identical and, thus their difference will be zero. The presence of even a small amount of noise leads to a residence times distribution (RTD) about a mean value, due to uncertainties in the switching time. The presence of an external target signal (i.e. the noise $F(t)$ in (1.8)) usually make the potential asymmetric with a concomitant difference in the mean residence times. This difference is proportional to the asymmetry-producing target signal itself.

This procedure has shown some advantages compared to the aforesaid procedure based on a spectral readout. It has been implemented experimentally without complicated feedback electronics and works with or without the bias signals. In fact, the difference in residence times is quantifiable even in the absence of the time-periodic bias signal, when the sensor is driven between its stable equilibrium states by only the noise, although some practical considerations (e.g., observation times depending on the relative magnitude of the noise standard deviation and on the barrier height), may limit the applicability of this strategy in some practical cases. It has been demonstrated also that residence-times based technique

works fine without the knowledge of the computationally demanding power spectral amplitude of the system output (in most cases a simple averaging procedure on the system output has worked just fine) and, finally, it has performed well even in presence of large levels of noise [88].

Applications of these readout scheme are given by RTD fluxgate magnetometers [14] and electric field sensors based on ferroelectric materials [13].

An autonomous bistable sensor exploiting the benefit from nonlinearity and noise for measurement of AC currents and energy harvesting is proposed in this work and a discussion about the state of the art of AC current sensors will be discussed in section 4.1

Threshold sensors

Apart from the applications of the theories on stochastic resonance, the bistable principle in the field of sensors has been exploited for detecting when the magnitude of certain physical quantities under observation exceeds a predefined threshold (i.e. threshold sensors). In these applications, when the threshold is passed, the bistable sensor snaps from one

of its stable equilibrium state to the other one, returning as output a status change handled by circuitry.

One of these applications is given by inertial switches [65]. This kind of devices has been thought to detect accelerations that are larger than the threshold imposed by the critical forces in bistable structures [267]. Their latching operation and the possibility to properly designing their switching threshold meet the requirements of some applications, especially in safety systems, where impulsive accelerations with large magnitudes descending from crashes and severe impacts must be handled. In these cases, when overthreshold applications are detected by snapping from one stable equilibrium position to the other one, these sensors trigger safety mechanisms (e.g., airbags in cars) to prevent major damages, as an example, caused by a sudden impact [154]. Other applications have been found in fuse systems and drop detection systems. The development of inertial switches in MEMS technologies has improved their operative range and their response time, thanks to the downscaling of their geometric dimensions [211].

Other examples of threshold sensors are represented by magnetic [240], flow [169] and thermo-optical sensors [165].

1.3.2 Application of bistable mechanisms in energy harvesting from vibrations

In the field of energy harvesting from mechanical vibrations, the adoption of bistable devices has been proposed to improve performance of power generators, at both millimetric and micrometric scale, when wideband vibrational sources must be addressed.

It is known that ambient mechanical vibrations come in a large variety of forms such as induced oscillations, seismic noise, vehicle motion, acoustic noise, multitone vibrating systems, and, more generally, noisy environments. Sometimes, the vibrational energy to be collected may be confined in a very specific region of the frequency spectrum, as in the case of rotating machines, but very often, energy is distributed over a wide spectrum of frequencies. In particular, several scenarios exist where a significant fraction of energy is generally distributed in the lower part of the frequency spectrum, very often below 500 Hz [200]. This requires energy harvesters hav-

ing a wideband frequency response at low frequencies in order to scavenge a larger amount of energy.

Bistable energy harvesters are one of the proposed solutions in literature to broaden the bandwidth at low frequencies of traditional linear resonant oscillating generators, which offer a good efficiency only when they work around their resonant frequency and, consequently, poor performance in out of resonance operations [161]. For this reason, in their design, resonant generators require the matching of their frequency of mechanical resonance with the main frequency of the vibrations coming out from the vibrating source.

Differently from resonant devices, bistable mechanical oscillators do not require the frequency matching with the source of mechanical vibrations. This aspect is very important because the achievement of very low resonance frequencies (e.g., in the order of a few hundreds of hertz or lower) with a significantly large quality factor is a challenging issue at microscale and limits the adoption of linear resonant microgenerators in MEMS technologies [9].

The operating regime of periodic interwell oscillations (also known as high energy orbits or snap-through behaviour) in bistable systems has been recognized as a means by which to dramatically improve energy harvesting performance. As the bistable mechanical system commutates between its stable equilibrium states, the shuttle (i.e. the inertial mass in the case of energy harvesters) has to displace a greater distance from one stable equilibrium state to the other one and its requisite velocity is much greater than that for intrawell or chaotic interwell oscillations. Since the electrical output of an energy harvester is often dependent on the device velocity (especially in the case of piezoelectric mechanical-to-electrical transducers), high-energy orbits substantially increase power per forcing cycle (as compared to intrawell and chaotic interwell oscillations) and are more regular in waveform (as compared with chaotic oscillations), which is preferable for external power storage circuits. The output voltage waveform coming from bistable harvester has been also exploited for diode-less and zero-threshold solutions for its rectification [95, 150].

Additionally, snap-through behaviour may be triggered regardless of the form or frequency of exciting vibrations, alleviating concerns about harvesting performance in many realistic vibratory environments dominated by effectively low-pass filtered excitation [107]. Moreover, the frequency of the inter-well commutations helps to enlarge the frequency response of the harvesters, especially at low frequencies (typically below 500 Hz) [17].

One of key limitations of bistable devices in energy harvesting is represented by the necessity of large amounts of input energy to maintain snap-through behaviour, as it is found in some of actual devices [107]. Some strategies to decrease the energy threshold required to switch between stable states have been developed; one of them consists in a time-periodic forced excitation mixed with external ambient noisy vibrations [156, 235]. In this particular case, noise effects on device performances are considered in the opposite way with respect to already introduced principle of "noise activated devices" [88]. Noise is no more used to allow the information to be captured by the sensor but energy harvesting device is aimed to capture

the largest amount of energy available in the environment by lowering the energy threshold barrier for snap-through operation [235].

Finally, the widespread diffusion of bistable solutions in integrated devices for energy harvesting is still restrained by the current difficulties in the implementation of bistable principles with microsystem technologies and in the lack of a well accepted design methodology.

Opposing magnetic forces is one of the strategies very often used to implement bistable mechanisms. In literature, there are several solutions based on the magnetic levitation obtained through permanent magnets having direct [87] or opposing [9] magnetization, owing to the possibility to "shape" the potential energy function of the system by altering the distance between magnets and, therefore, to "tune" its nonlinear behaviour. Magnetic strategies are therefore very common in the area of bistable energy harvesters, however, the presence of magnets and, in particular, of "moving" magnets is sometimes not desirable whenever the energy harvester is placed close to other electronic devices or magnetic sensors that may be

affected by the fluctuations in the magnetic field. For this reason, some solutions exploiting fully compliant bistable mechanisms have been addressed, at the price of complicating the design of the device [17, 170].

Energy harvesting from mechanical vibrations and the state of the art in vibrations microgenerators will be discussed with more details in section 3.1.

2

Technologies to fabricate integrated bistable devices

It is a great profession. There is the satisfaction of watching a figment of the imagination emerge through the aid of science to a plan on paper. Then it moves to realization in stone or metal or energy. Then it brings jobs and homes to men. Then it elevates the standards of living and adds to the comforts of life. That is the engineer's high privilege.

Herbert Hoover

In this chapter several technology solutions to fabricate bistable devices will be presented and discussed. First of all, consolidated microfabrication processes from MEMS industry will be introduced, then, rapid prototyping solutions for nanotechnology devices and centimeter size components in direct printing technologies will be proposed.

2.1 Microelectromechanical Systems (MEMS)

Microelectromechanical Systems, or MEMS, represent a technology field aimed to develop integrated miniaturized electro-mechanical elements (i.e. microstructures) that are made using the techniques of microfabrication. The critical physical dimensions of MEMS devices can vary from well below one micron on the lower end of the dimensional spectrum, all the way to several millimeters. Likewise, the types of MEMS devices can vary from relatively simple structures, having no moving elements, to extremely complex electromechanical systems with multiple moving elements under the control of integrated microelectronics. The one main criterion of MEMS is that there are at least some elements having some sort of mechanical functionality whether or not these elements can move [3].

While the functional elements of MEMS are miniaturized structures, sensors, actuators and microelectronics, the most notable (and perhaps most interesting) elements are microsensors and microactuators. Microsensors and microactu-

ators are appropriately categorized as "transducers", which are defined as devices that convert energy from one form to another. In the case of microsensors, the device typically converts a measured mechanical signal into an electrical signal [131]. Recently, MEMS devices have attracted growing interest in the field of energy harvesting from mechanical vibration for the opportunity of exploiting displacements and deformations in microstructures to generate electrical energy through mechanical-to-electrical transducers for powering low power devices [158].

Over the past several decades MEMS researchers and developers have demonstrated an extremely large number of microsensors for almost every possible sensing modality including temperature, pressure, inertial forces, chemical species, magnetic fields, radiation, etc. Remarkably, many of these micromachined sensors have demonstrated performances exceeding those of their macroscale counterparts. For example, the micromachined version of a pressure transducer, usually outperforms a pressure sensor made using the most precise macroscale level machining techniques. Another important

aspect of MEMS is represented by their method of production that exploits (with certain adaptations) the same batch fabrication techniques used in the integrated circuit industry, which can translate into low per device, as well as many other benefits. Consequently, it is possible to not only achieve stellar device performance, but to do so at a relatively low cost level. Not surprisingly, silicon based discrete microsensors were quickly commercially exploited and the markets for these devices continue to grow at a rapid rate [242].

The fabrication of MEMS evolved from the process technology in semiconductor device fabrication, i.e. the basic techniques are deposition of material layers, patterning by photolithography and etching to produce the required shapes. Various processes have been developed for the fabrication of MEMS devices. These processes can be separated into three main technologies: Bulk Micromachining, Surface Micromachining, and LIGA (Lithographie, Galvanoformung, Abformung) in terms of the strategy to implement released microstructures [3].

Each technology process has its advantages and limitations. Some of the metrics used to specify the capabilities of a process are defined as follows [3]:

- minimum linewidth, i.e. the smallest isolated line that can be reliably patterned;
- minimum spacing, i.e. the smallest patternable gap between features;
- sidewall profile, i.e. the degree to which an anisotropic etch deviates from an ideal (vertical) profile;
- layer thicknesses, i.e. the thickness of structural and sacrificial layers;
- aspect ratio, i.e. the ratio between layer thickness and minimum linewidth;
- number of mechanical and sacrificial layers.

One of the major goal of this work is to demonstrate the possibility of using microfabrication techniques to implement mechanical structures having nonlinear and bistable behaviours to be used in vibration energy harvesting and in nonlinear sensors.

Nonlinearity in MEMS can be caused through different strategies. One of them consists in fabricating flexible structures (e.g., beams, bridges, hinges and so on) having a specific designed shape to generate nonlinear restoring elastic forces, as in the case of compliant mechanisms [116]. Another approach involves the deposition of more "exotic" materials, such as permanent magnets, sometimes through unconventional techniques to implement nonlinearities [9]. Finally another strategy exploits strains, stresses and nonlinear material properties to develop nonlinear microstructures like in buckled beams [191].

Several MEMS technology processes adopted to design and develop the nonlinear devices proposed in this work will be presented in the following.

2.1.1 CNM BESOI process

The BESOI (Bulk and Etch Silicon-On-Insulator) process is a custom bulk micromachining MEMS technology process available through the Centro Nacional de Microelectrónica (CNM) of Barcelona (Spain).

This process starts from an SOI (Silicon-On-Insulator) substrate where the upper 15 µm thick n-doped single crystal silicon layer acts as primary structural material and also as electrical connection layer. A 2 µm thick silicon dioxide (SiO_2) layer separates as buried oxide the aforesaid upper single crystal silicon layer from the 450 µm thick n-doped silicon substrate (having <100> orientation).

The release of suspended mechanical structures is performed through both the photolithographic pattern of the upper silicon layer from the top and the Reactive Ion Etching (RIE) of the silicon substrate and of the buried oxide from the bottom of the wafer.

Depending on the specific application, several thin films of different materials can be deposited and patterned on the top of the SOI substrate. As an example, silicon dioxide (SiO_2) can act as electrically and thermally isolating material, aluminium and gold as thermal and electrical conductors, polycrystalline silicon (or polysilicon) for piezoresistors and so on. Recently, there is a study to integrate in the process thin films of piezoelectric materials like Lead Titanate Zirconate

(PZT), Aluminum Nitride (AlN) or Zinc Oxide (ZnO) to allow for self-generating mechanical-to-electrical transduction in autonomous sensors and/or energy harvesters.

A schematic of the cross section the BESOI process is reported in fig. 2.1 and a Scanning Electron Microscope (SEM) image of the SOI substrate used in the BESOI process is shown in fig. 2.2.

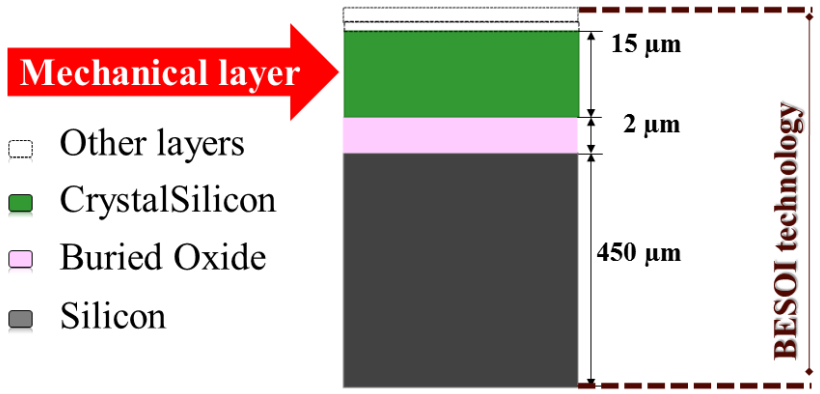

Fig. 2.1 – Schematic of the cross section of the BESOI technology from Centro Nacional de Microelectrónica (CNM) of Barcelona. Layers on the top of the mechanical structure layer are generically indicated as "other layers". The picture is not in scale.

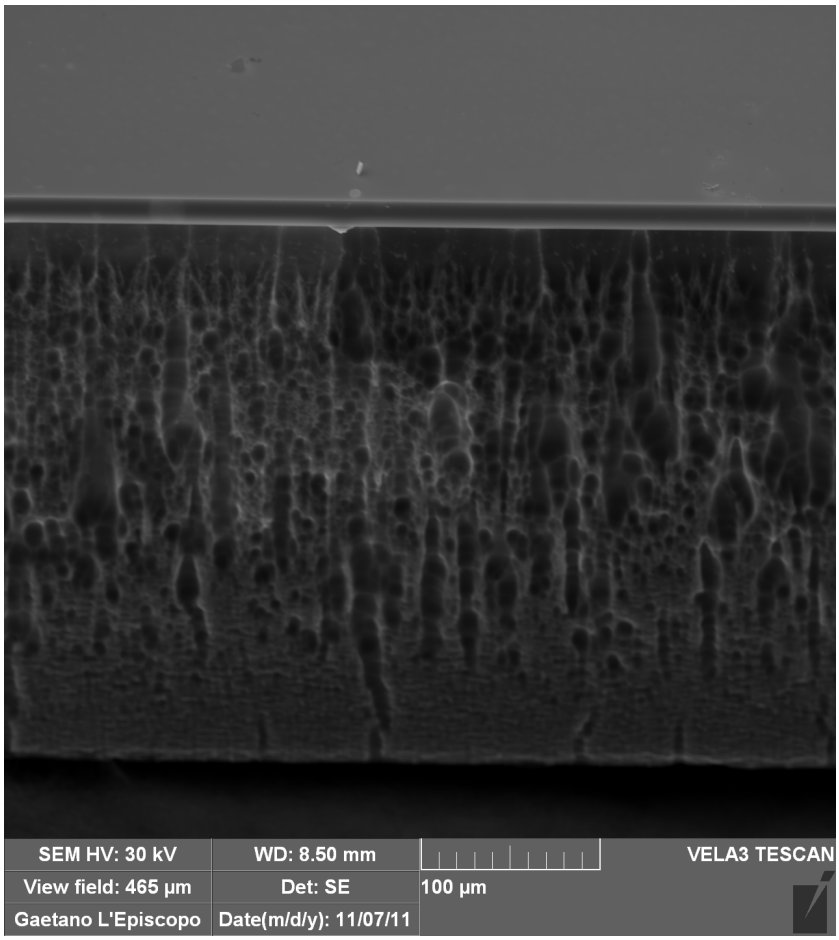

Fig. 2.2 – SEM image of the SOI substrate used in the BESOI process. Roughness in the etched sidewalls of the silicon substrate is due to the RIE.

This technology process promises interesting performance because of the possibility to design a large seismic masses with a tolerable definition of vertical shapes (thanks to the RIE) from the whole thickness of the wafer.

Examples of applications of this process are given by microresonators [5], seismometers [16], thermal sensors [10], lateral cantilevers [21] and bistable compliant mechanisms [17].

An example of nonlinear fully compliant structure released in the BESOI process and intended for research on bistable devices is shown in the SEM image in fig. 2.3.

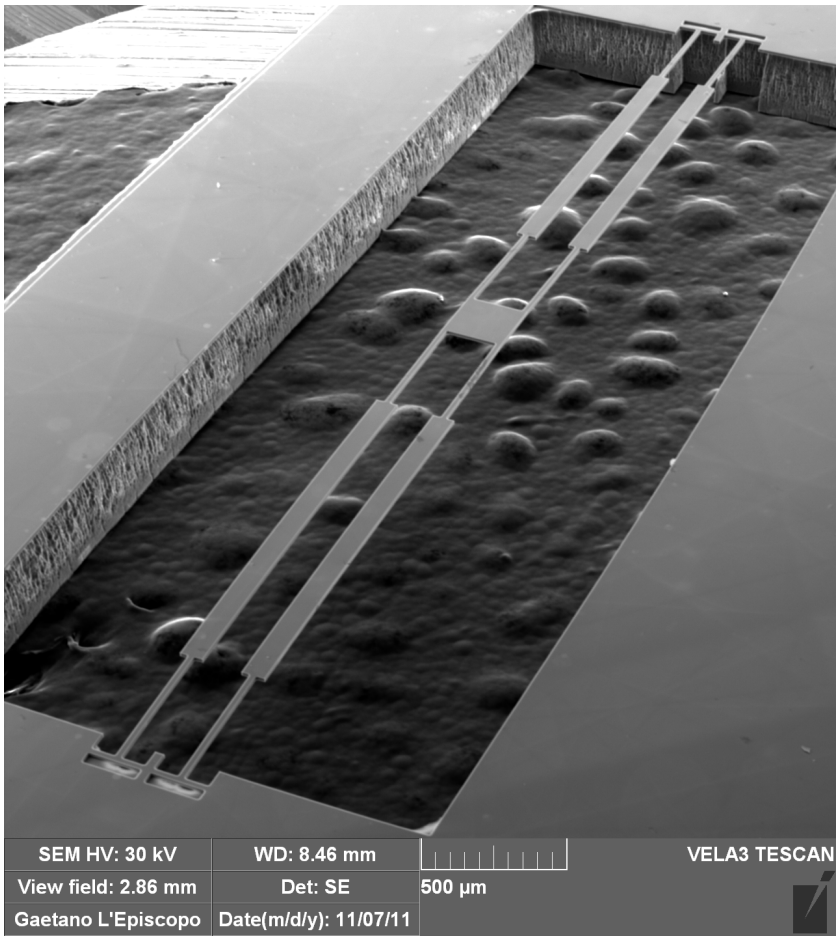

Fig. 2.3 – SEM image of a nonlinear fully compliant structure released in the BESOI process.

2.1.2 MEMSCAP™ MetalMUMPs® process

MetalMUMPs® is a standard commercial process provided by MEMSCAP™ for the program MUMPs (Multi-User MEMS Processes) in order to yield cost-effective multi-user and multi-purpose MEMS fabrication to industry, universities, and government worldwide.

MetalMUMPs® is an electroplated nickel hybrid micromachining process derived from work performed at MEMSCAP™ throughout the 1990s. This process flow was originally developed for the fabrication of MEMS micro-relay devices based on a thermal actuator technology [62], lately it has been applied to a very wide range of applications in the field of microsensors [18, 215] and microactuators [45, 94].

A schematic example of the cross section of a device in MetalMUMPs® process is shown in fig. 2.4.

This process has the following general features:

- 20.5 µm thick electroplated nickel is used as the primary structural material and electrical interconnect layer.

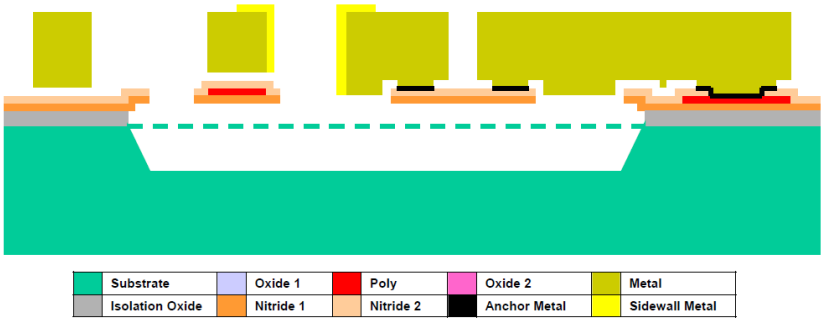

Fig. 2.4 – Schematic of the cross section of the MetalMUMPs® process provided by MEMSCAP™ [62]. The picture is not in scale.

- 0.7 µm thick doped polysilicon can be used for resistors, additional mechanical structures and/or cross-over electrical routing.
- Two 0.35 µm thick layers of silicon nitride (Si_3N_4) are used for electrical isolation.
- Two layers of phosphosilicate glass (PSG) are used as sacrificial layers.
- A trench layer in the silicon substrate can be incorporated for additional thermal and electrical isolation.
- Gold overplate can be used to coat the sidewalls of nickel structures with a low contact resistance material.

- Strategies descending from surface micromachining processes (i.e. the use of sacrificial layers) and bulk micromachining processes (i.e. the trench etch of silicon substrate) are adopted to release structures. Micromolding techniques are adopted to deposit and pattern the electroplated nickel layer.

A SEM picture of several devices (microsensors and microactuators) designed at the University of Catania (Italy) and realized in this process is reported in fig. 2.5.

Complete process flow and design rules are described in the documentation provided by MEMSCAP^{TM} [62].

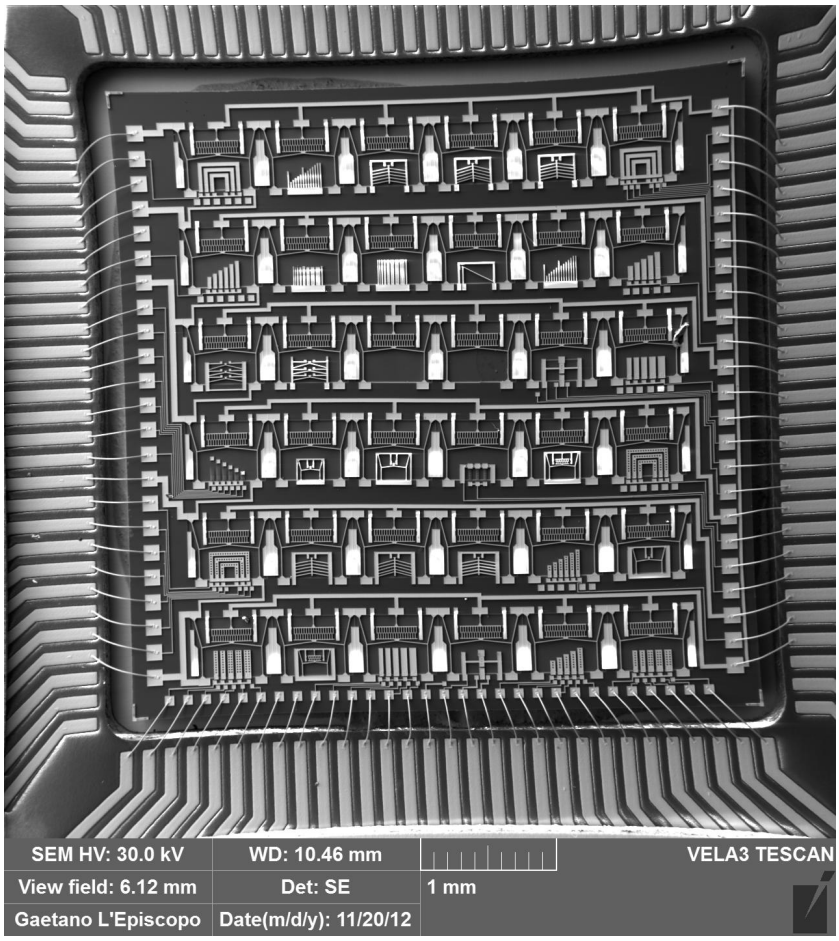

Fig. 2.5 – SEM image of some microdevices realized in the MetalMUMPs® process provided by MEMSCAP™.

2.1.3 MEMSCAP™ PiezoMUMPs® process

Similarly to MetalMUMPs®, PiezoMUMPs® is another multi-user process provided by MEMSCAP™ under the program MUMPs.

PiezoMUMPs® process has been introduced by MEMSCAP™ during the 2013 and is designed for general purpose micromachining of piezoelectric devices in a Silicon-On-Insulator (SOI) framework for sensors, actuators and energy harvesters [63].

The cross-section of this process is illustrated in the schematic in fig. 2.6.

A silicon-on-insulator wafer composed of a 10 µm thick silicon layer, 1 µm thick buried silicon dioxide and 400 µm thick handle wafer is used as the starting substrate.

The 10 µm thick silicon layer represents both the structural layer and an electrical connection layer as it is doped during the process flow.

Similarly to the BESOI process in the subsection 2.1.1, the SOI substrate of the PiezoMUMPs® process is patterned and etched from both its top (pattern of the silicon layer) and

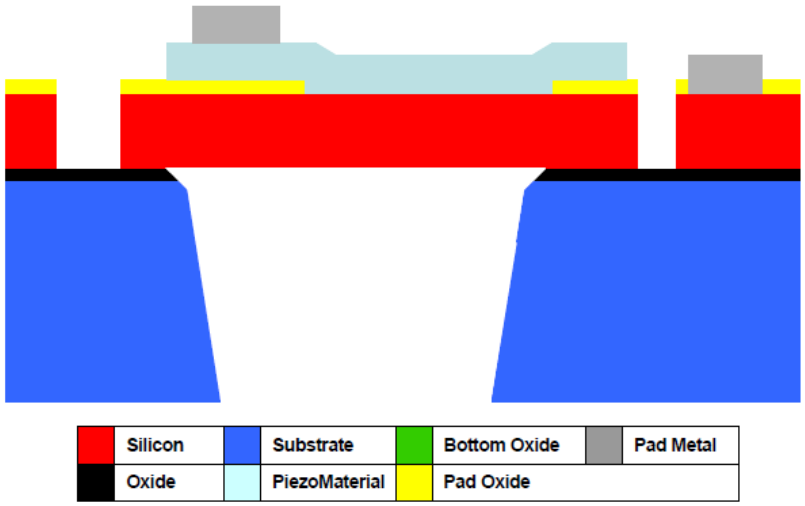

Fig. 2.6 – Schematic of the cross section of the PiezoMUMPs® process provided by MEMSCAP™ [63]. The picture is not in scale.

its bottom side (etch of the handle substrate): this allows for released structures.

A 0.5 µm thick piezoelectric layer of aluminum nitride (AlN) (i.e. the PiezoMaterial) is deposited and patterned on the silicon layer and allows for the development of piezoelectric sensors. A 1 µm thick aluminium layer deposited and patterned on the top of the aluminum nitride layer acts as top electrode of the piezoelectric layer (the bottom electrode is represented by the 10 µm thick silicon layer) and electrical

routing layer. A 0.2 µm thick silicon dioxide layer is used as electrical isolating layer.

Further details about process flow and design rules are described in the documentation provided by MEMSCAP™ [63].

A picture of a die with several devices such as cantilever beams and nonlinear test structures designed at the Nanotechlab of the University of Catania (Italy) and fabricated in the PiezoMUMPs® process at MEMSCAP™ is reported in fig. 2.7

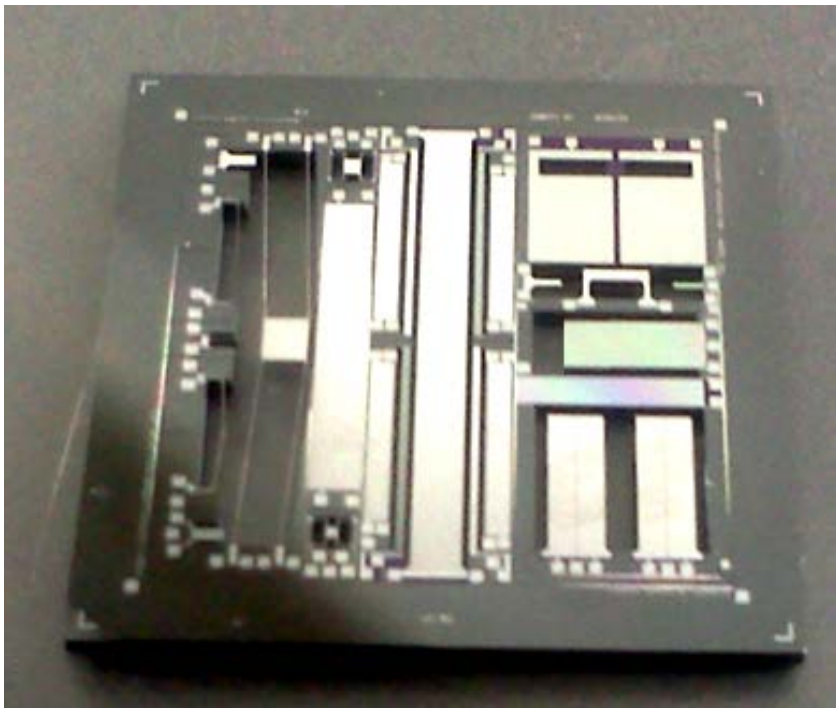

Fig. 2.7 – A die with several devices such as cantilever beams and nonlinear test structures designed at the Nanotechlab of the University of Catania (Italy) and fabricated in the PiezoMUMPs® process at MEMSCAP™.

2.1.4 STMicroelectronics ThELMA® process

ThELMA® is the acronym of "Thick Epitaxial Layer for Microactuators and Accelerometers" and is a standard process developed by STMicroelectronics for its sensors such as accelerometers and gyroscopes, which have occupied a large share of the market for mems sensors in recent years [56, 135].

The process involves the fabrication of 2 silicon wafers: one "Sensor" wafer which includes microelectromechanical components and one "Cap" wafer as sealing element at wafer level. The two wafers are "bonded" together in the final steps of the process through wafer-to-wafer bonding (glassfrit or anodic bonding). The cap wafer is needed to protect the microelectromechanical elements in the sensor wafer inside a sealed environment. It enables the use of standard microelectronics back-end technologies like testing, dicing and packaging and assures the reliability of the product overtime [183].

A schematic of the cross section of the ThELMA® process is illustrated in fig. 2.8.

Referring to the sensor wafer, ThELMA® is a surface micromachining process which adopts thick epitaxial doped

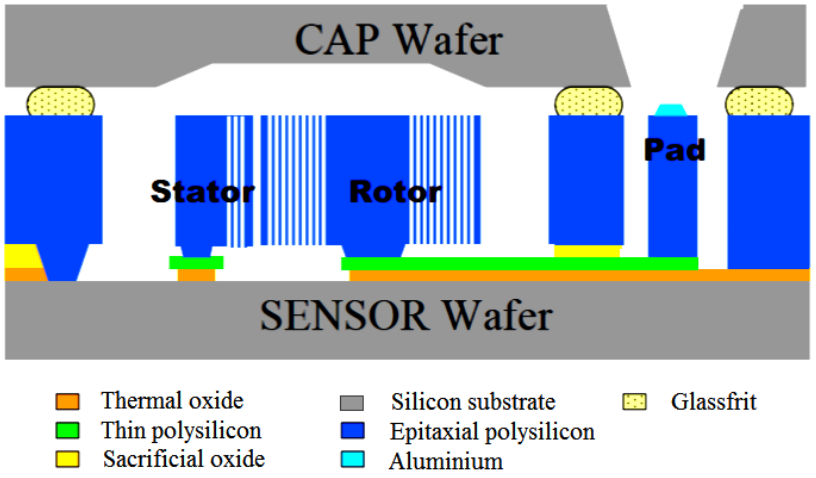

Fig. 2.8 – Schematic of the cross section of the ThELMA® process from STMicroelectronics (courtesy of the STMicroelectronics of Castelletto, Italy). The picture is not in scale.

polysilicon as a structural layer. Depending on the application, the epitaxial polysilicon layer can be designed to have different thicknesses (15 µm, 22 µm and 25 µm) and is also used as electrical conductive layer, especially in implementing plates of comb capacitances for electrostatic sensors and actuators in in-plane moving microstructures.

A 1.1 µm thick silicon dioxide layer is used as sacrificial layer to release epitaxial polysilicon structures according to surface micromachining techniques.

A 0.9 µm thin layer of heavily doped polysilicon is adopted as a conductive layer and for the electrical routing of microelectromechanical elements. The air-separation of 1.1 µm (due to the sacrificial silicon dioxide) between thick epitaxial polysilicon and thin polysilicon (two electrically conductive layers) generates a capacitance which changes its value when epitaxial polysilicon structures displace in the out-of-plane direction; for this reason this capacitance is exploited to sense electrostatically structural displacements in the out-of plane direction [234].

Pads are implemented through a 0.7 µm thick layer of aluminium and silicon substrate in the sensor wafer is protected through a 2.5 µm thick layer of thermal silicon dioxide.

Some SEM pictures of ThELMA® devices are reported in fig. 2.9 [135, 242].

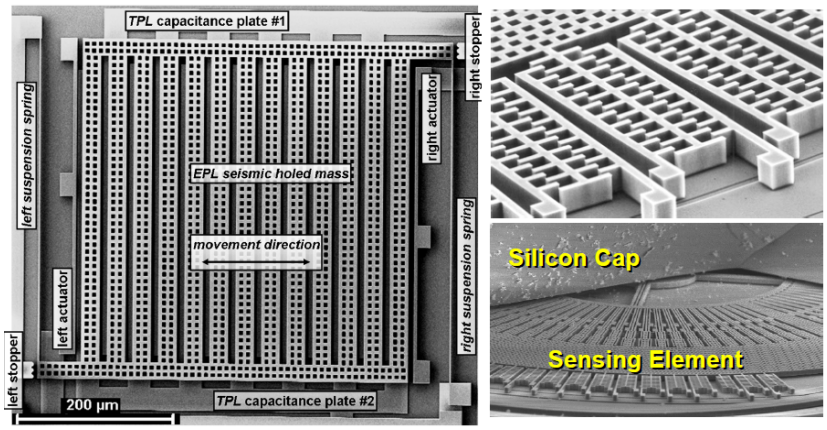

Fig. 2.9 – SEM pictures of some devices in the ThELMA® process from STMicroelectronics [135, 242].

2.1.5 Radiant pMEMs® process

Radiant is a company from Albuquerque (NM, USA) specialized in the fabrication of integrated ferroelectric devices. A specific fabrication process named "RTI 5μ®" has been developed by Radiant in order to implement a piezoelectric stack composed of a thin film of Lead Titanate Zirconate (PZT) and two platinum electrodes (one on the top and one on the bottom of the piezoelectric layer) for integrated ferroelectric capacitors (where top and bottom electrodes are the capacitor plates and the PZT is the dielectric) [12].

The nominal thickness of the PZT in about 250 nm; top and bottom platinum electrodes are about 150 nm thick.

The piezoelectric stack is patterned on a 500 nm thick silicon dioxide used to electrically and thermally isolate the piezoelectric stack from the underlying silicon substrate.

Several very thin (about 40 nm) buffer layers like titanium oxide are used among the aforesaid layers to favourite their adhesion, while several passivation layers are deposited on the top of the piezoelectric stack to protect the device.

Metal pads for electrical interconnections are implemented by an alloy of chromium and gold.

A schematic of the cross section of the RTI 5µ® process from Radiant is illustrated in fig. 2.10 and an SEM picture of the cross section resulting from the process is shown in fig. 2.11.

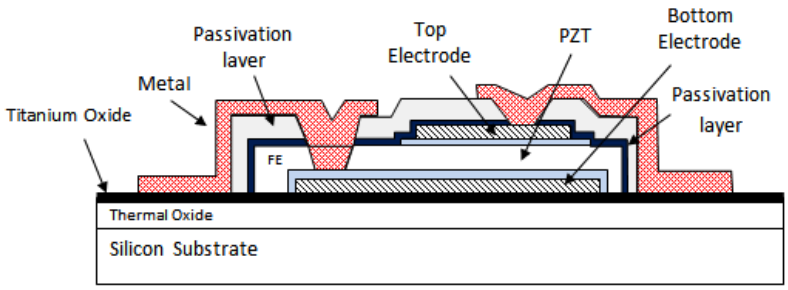

Fig. 2.10 – Schematic of the cross section of the RTI 5µ® process from Radiant (courtesy of Radiant inc.). The picture is not in scale.

The ferroelectric capacitors in RTI 5µ® have been previously used for electric field sensing applications [12, 13], and, in this work, they have been recycled for rapid prototyping of FIB machined piezoelectric nano-cantilever beams discussed in subsection 2.2.1. An example of one of these ferroelectric capacitors is shown in the optical microscope image in fig. 2.11.

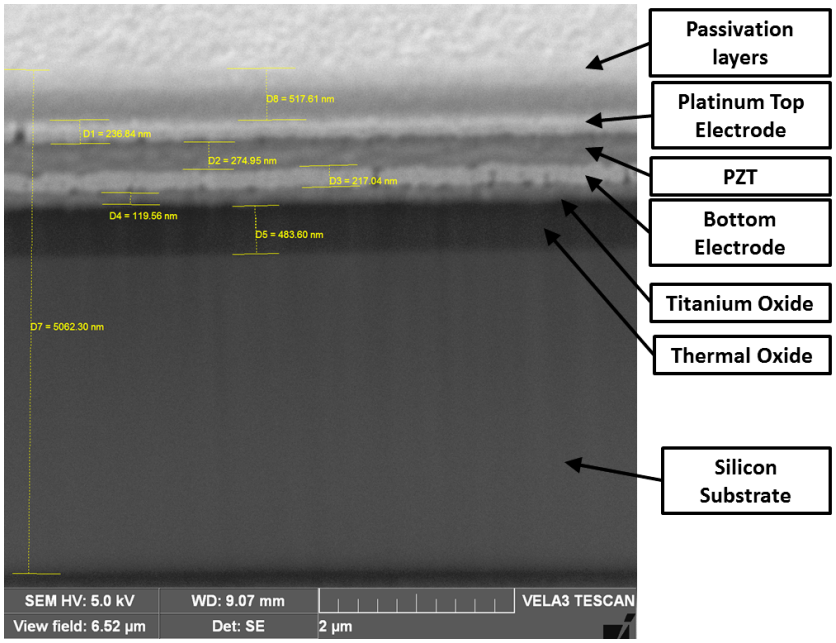

Fig. 2.11 – SEM picture of the resulting cross section from the RTI 5µ® process from Radiant.

An evolution of the RTI 5µ® process is actually under development at Radiant to set up a standard piezoelectric microfabrication process for MEMS devices, named "pMEMs®", based on the bulk micromachining of an SOI substrate (in the same way of BESOI process in subsection 2.1.1 and of the PiezoMUMPs process in subsection 2.1.3) and on the same piezoelectric stack as that used in the RTI 5µ® process.

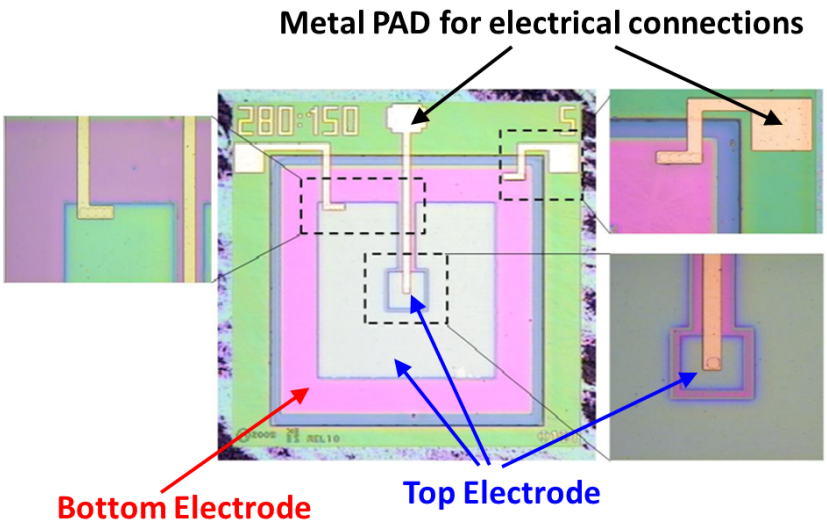

Fig. 2.12 – Optical microscope image of a ferroelectric capacitor in the RTI 5µ® process from Radiant. The same kind of capacitors will be recycled to build prototypes of piezoelectric nano-cantilever beams through FIB milling in subsection 2.2.1.

2.2 Rapid prototyping of devices in Nanotechnology

Nanotechnology is the ability to manipulate matter at the atomic or molecular level to make something useful at the nano-dimensional scale. It consists in the construction and in the usage of functional structures designed from atomic or molecular scale with at least one characteristic dimension measured in nanometers. Their size allows them to exhibit novel and significantly improved physical, chemical and biological properties because of their size. For example, when characteristic structural features are intermediate between isolated atoms and bulk materials in the range of about 1 nm to 100 nm, these objects often display physical attributes substantially different from those displayed by either atoms or bulk materials [184].

Phenomena at the nanometer scale are likely to be a completely new world. Properties of matter at nanoscale may not be as predictable as those observed at larger scales. Important changes in behaviour are caused not only by continuous modification of characteristics with diminishing size, but also by

the appearance of totally new phenomena such as quantum confinement (a typical example of which is that the color of light emitting from semiconductor nanoparticles depends on their sizes). Designed and controlled fabrication and integration of nanomaterials and nanodevices is likely to be revolutionary for science and technology [184].

In fact, Nanotechnology can provide unprecedented understanding about materials and devices and is likely to impact many fields. By using structure at nanoscale as a tunable physical variable, we can greatly expand the range of performance of existing chemicals and materials. Alignment of linear molecules in an ordered array on a substrate surface (self-assembled monolayers) can function as a new generation of chemical and biological sensors. Switching devices and functional units at nanoscale can improve computer storage and operation capacity by a huge factor. Entirely new biological sensors facilitate early diagnostics and disease prevention of cancers. Nanostructured ceramics and metals have greatly improved mechanical properties, both in ductility and strength [31].

Basically, there are two approaches in nanotechnology implementation: the top-down and the bottom-up. In the top-down approach, devices and structures are made using many of the same techniques as used in MEMS except they are made smaller in size, usually by employing more advanced photolithography (such as electron-beam lithography [180]) and etching methods. The bottom-up approach typically involves deposition, growing, or self-assembly technologies. The advantages of nano-dimensional devices over MEMS involve benefits mostly derived from the scaling laws, which can also present some challenges as well [253].

Nanotechnology is a promising way to put essentially every atom or molecule in the place and position desired (i.e. exact positional control for assembly), to make almost any structure or material consistent with the laws of physics that can be specified at the atomic or molecular levels and to have manufacturing costs not greatly exceeding the cost of the required raw materials and energy used in fabrication.

Although MEMS and Nanotechnology (also named NEMS, Nanoelectromechanical Systems) are sometimes cited as sep-

arate and distinct technologies, in reality the distinction between the two is not so clear-cut. In fact, these two technologies are highly dependent on one another. The well-known scanning tunneling-tip microscope (STM) which is used to detect individual atoms and molecules on the nanometer scale is a MEMS device. Similarly the atomic force microscope (AFM), which is used to manipulate the placement and position of individual atoms and molecules on the surface of a substrate, is a MEMS device as well. In fact, a variety of MEMS technologies are required in order to interface with the nano-scale domain [257].

An important aspect of nanotechnology in the research and development of novel devices is represented by the rapid prototyping techniques exploited to rapidly fabricate individual nanoscale devices for prototyping future electronic applications. Instead of being used in mass production, tools like Scanning Electron Microscope (SEM) and Focused Ion Beam (FIB) are adopted to rapidly fabricate in research laboratories prototypes of devices to be experimentally studied for future applications [133].

Prototypes can be built from scratch by taking advantage of adapted conventional MEMS processes in conjunction with novel nanomanufacturing processes (e.g., electron beam lithography [180], self-assembly [252], nanoimprint lithography [55], atomic layer epitaxy [229] and so on) or can be derived from existing MEMS or NEMS devices through modifications and size reduction (FIB milling and FIB gas-assisted deposition [224]).

Two techniques for rapid prototyping implemented at the Nanotechlab of the University of Catania (Italy) will be illustrated in the following subsections. In the subsection 2.2.1, the rapid prototyping of piezoelectric cantilever beams, starting from ferroelectric capacitors in the RTI 5µ® process from Radiant, through FIB milling [224] will be described, and in the subsection 2.2.2 a technique of deposition of thin films of Zinc Oxide through Pulsed Plasma Deposition (PPD) [100] will be discussed.

2.2.1 FIB milling of nano-cantilever beams

Dual-beam systems combining a Focused Ion Beam (FIB) with a Scanning Electron Microscope (SEM) in a single instru-

ment provide valuable rapid prototyping capability that can significantly shorten development times for nanoscale devices in a variety of applications. The strength of dual-beam systems in prototyping applications derives from their ability to simultaneously create and observe structures with nanoscale resolution. The FIB can remove and deposit material in complex patterns with dimensional control of a few nanometers. Simultaneous, high resolution SEM imaging of the milling and deposition processes offers unique control of the patterning process and provides immediate feedback to the operator. Successful nanoprototyping requires dedicated patterning and milling strategies that account for interactions between the FIB and the substrate in the milling and deposition processes. Although FIB prototype devices may have material characteristics that ultimately preclude their routine use in the intended application, they can provide a structural or electrical equivalent that permits proof of concept and refinement of design with much greater speed and lower cost than batch fabrication techniques [255].

A rapid prototyping application of dual-beam SEM-FIB systems has been developed at Nanotechlab of Catania (Italy) for releasing cantilever beams having a piezoelectric output through FIB milling from ferroelectric capacitors in the RTI 5µ® process from Radiant.

The structure of the ferroelectric capacitor (plates and ferroelectric dielectric) are used as piezoelectric stack. In fact, the 250 nm thick layer of PZT allows for mechanical-to-electrical conversion and the 150 nm thick top and bottom electrodes of the ferroelectric capacitors act as electrodes to collect charges from the PZT due to strains: in this configuration the cantilever beam works in d_{31} mode (see subsection 3.1.7).

An area of the die covered by the piezoelectric stack is selectively exposed to the to ion beam coming from the Tescan Vela3 SEM-FIB of the Nanotechlab of Catania (Italy) at several steps to have a maskless etching by sputtering in the area "bombarded" by the focused ions.

The intensity of the ion beam, the time of each exposition, the direction of the beam scanning and the angle between the the surface of the capacitor and the direction of the ion beam

are process parameters. They are changed at each step in order to finally get a cantilever beam having a triangular section. As example of how process parameters affect the maskless etching, high intensities of the ion beam current result in fast etching but lower resolutions due to the larger beam spot size and to the huger redeposition of the removed materials [224]. Electrical isolation provided by the outer passivation layers in the ferroelectric capacitors (see subsection 2.1.5) can cause problems in the resolution of the milling process due to charge collection.

The first step consists in performing a rough milling at high ion currents (around 4.7 nA and with large apertures in the case of cantilever beam having a length of a couple of hundred of micrometers) maintaining the ion beam perpendicular to the surface of the capacitor: this leads to an almost vertical etch (etched material redeposition causes non-vertical sidewalls) as those in fig. 2.13.

The second and third steps consist in changing the angle between the surface of the capacitor and the direction of the ion beam by tilting the capacitor in one direction in the second

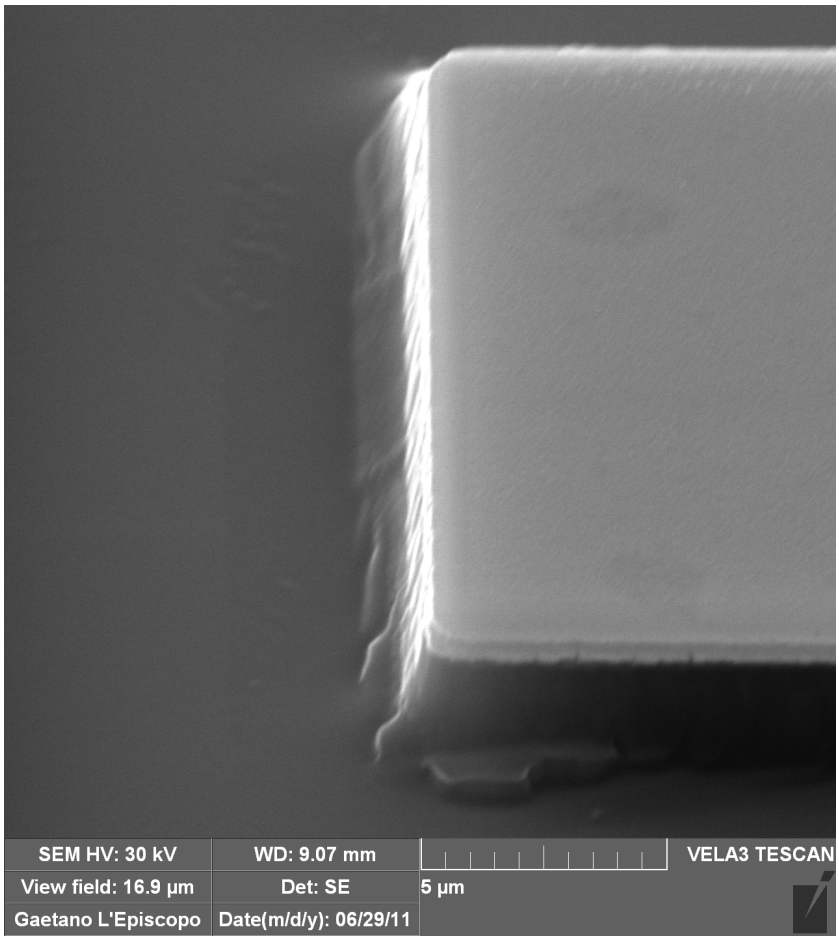

Fig. 2.13 – First step of process of releasing a cantilever beam through FIB milling (SEM picture).

step and in the opposed direction in the third step in order to have an angle below 90° and a sloped excavation to release the cantilever beam. Typical values of the angle between the ion beam and the surface of the capacitor are about 10° and 25°, depending on the wanted shape, and this value should be constant between second and third step in order to get a symmetric structure at the end of the process. These steps are performed at high currents (similarly to the first step) to speed up the prototype process.

The status of the tip of the cantilever beam before and after its release is shown respectively in the SEM pictures in fig. 2.14 and in fig. 2.15.

The final result of this process and the sizes of the beam are reported in figs. 2.16–2.17.

The position of the released cantilever beam inside the die previously used as ferroelectric capacitor can be observed in the SEM image in fig. 2.18, along with the three layers of the piezoelectric stack.

After the release of the beam at the third step, additional steps could be performed at lower ion currents (typically

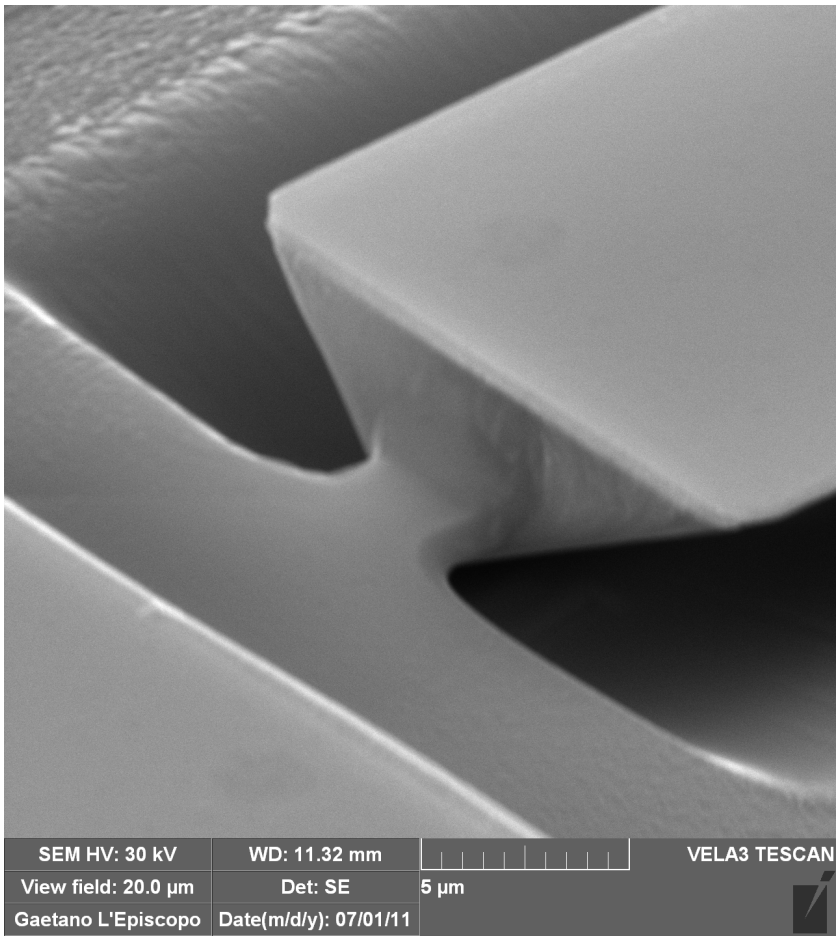

Fig. 2.14 – Tip of the cantilever beam just before its release (SEM picture).

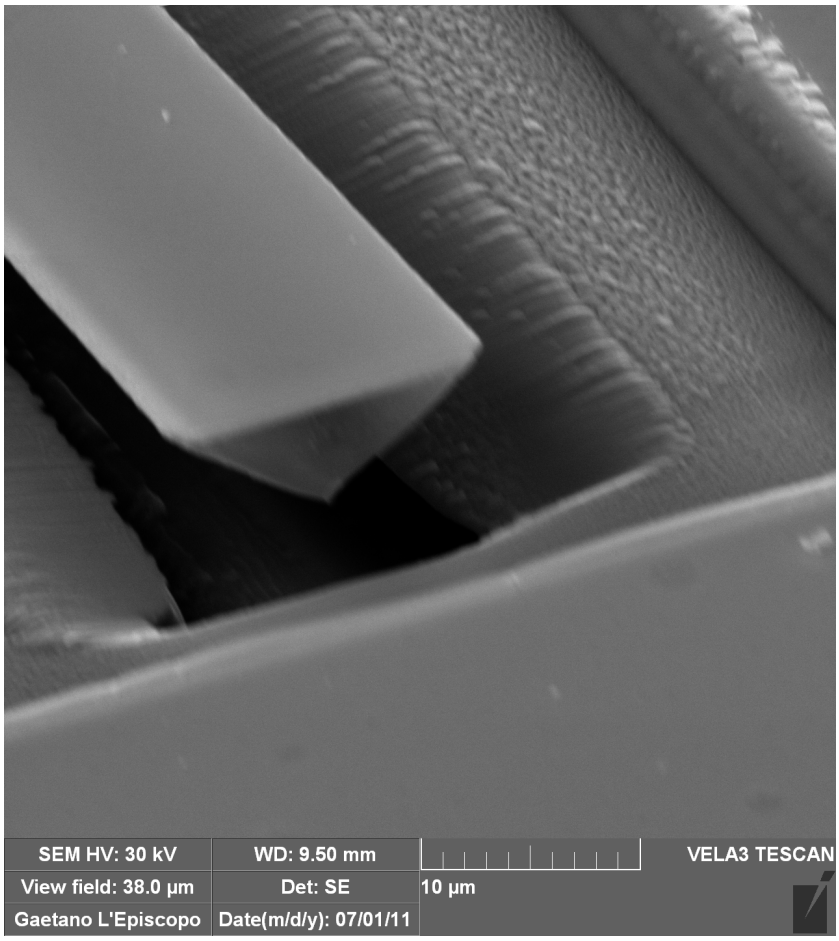

Fig. 2.15 – Tip of the cantilever beam after its release (SEM picture).

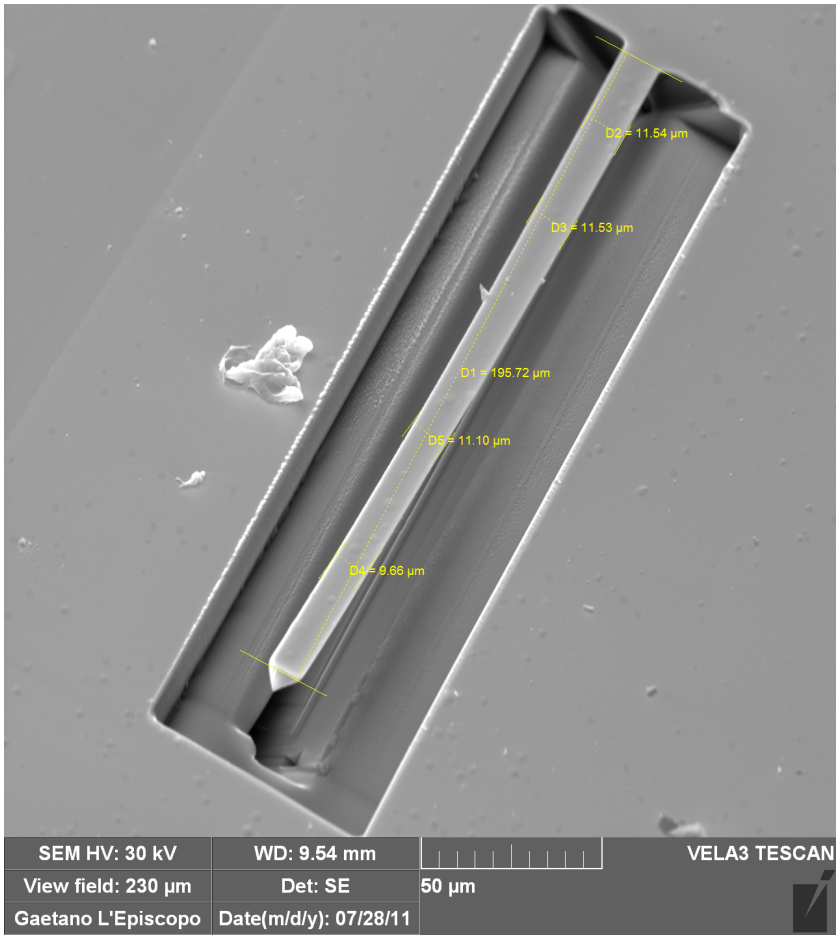

Fig. 2.16 – SEM picture of the finally released cantilever beam along with its sizes in length and width (tilt correction has been taken into account). A slight curvature in the out-of-plane direction is caused by the residual stress inside the structure due to the Radiant process.

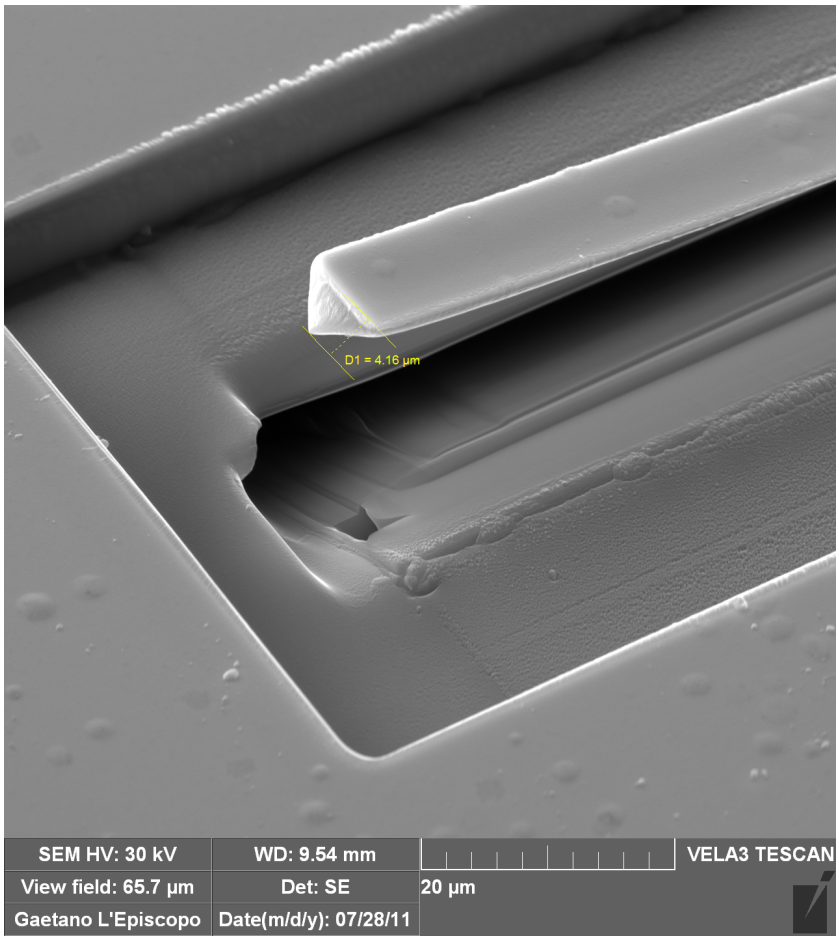

Fig. 2.17 – SEM picture of the finally released cantilever beam along with its sizes in thickness (tilt correction has been taken into account).

Fig. 2.18 – SEM picture illustrating the position of released cantilever beam inside the die previously used as ferroelectric capacitor. The areas occupied by the layers of the piezoelectric stack (top electrode, PZT and bottom electrode) are distinguished by the different shades of gray and indicated in the image for the sake of clearness.

around a a few hundreds of picoAmpère) to "polish" small imperfections and tolerances from the previous steps and/or to obtain wanted sizes (e.g., making thinner the cantilever beam or reducing its triangular shape) like achieving nanometric dimensions such as the cantilever beam shown in the SEM pictures in figs. 2.19–2.20.

This rapid prototyping technique allows the realization of piezoelectric cantilever beams having desired dimensions and shapes by precisely controlling the focused ion beam parameters. These devices can be used as nanotransducers for sensing applications (after the realization of a application-dependent functional area on the free end of the beam [217]) or for nanoactuators (a video of one of these cantilever beams, actuated by a sinusoidal voltage at 1 Hz is available on internet [142]).

The deposition of thin layers of permanent magnets [51, 155] on the free end of these cantilever beams and near the beam can allow for the realization of nonlinear devices through the magnetic levitation as in some macro and micrometric examples proposed in literature [6, 9].

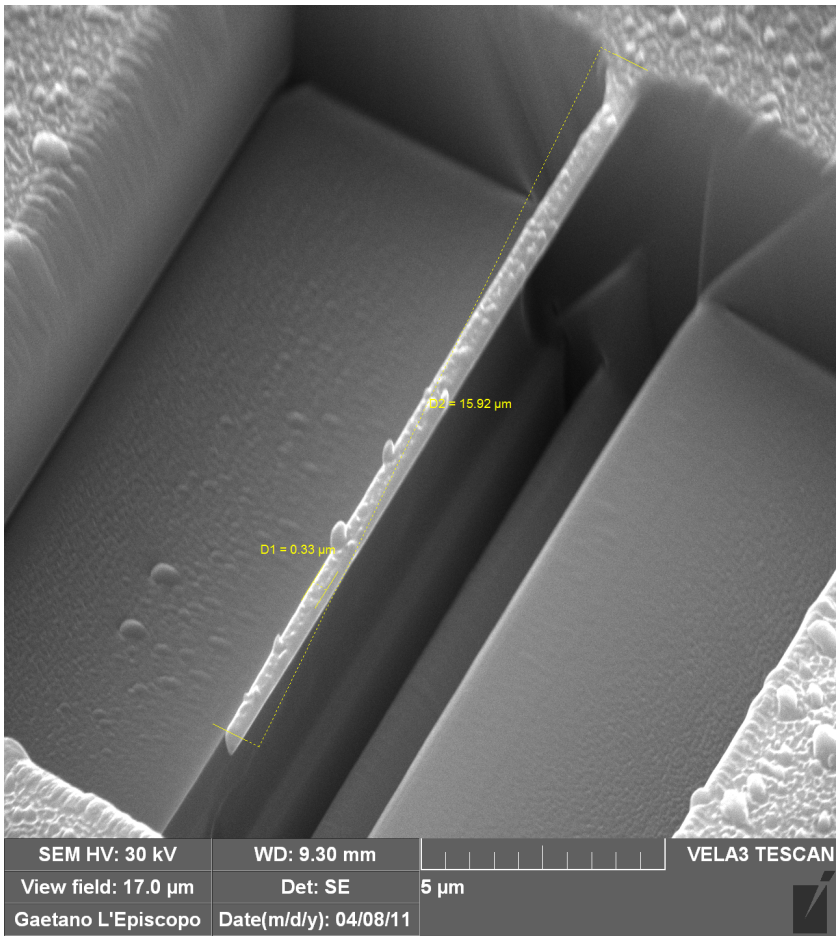

Fig. 2.19 – SEM picture of a polished cantilever beam along with its sizes in length and width (tilt correction has been taken into account).

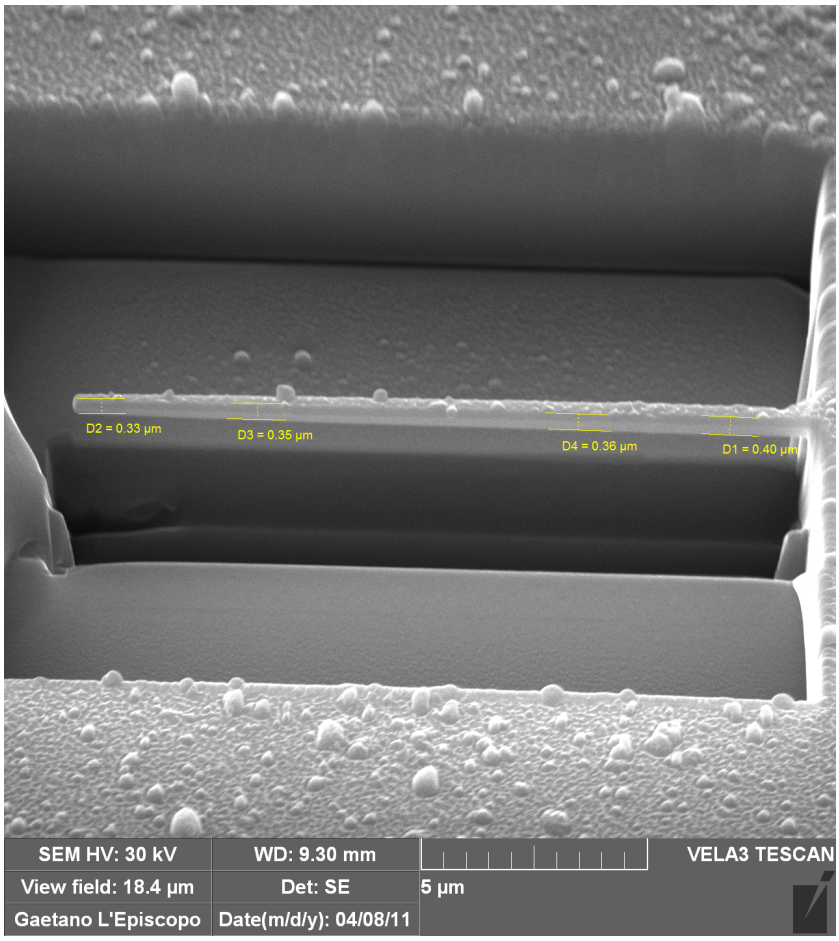

Fig. 2.20 – SEM picture of a polished cantilever beam along with its sizes in thickness (tilt correction has been taken into account).

2.2.2 Deposition of Zinc Oxide through Pulsed Plasma Deposition

Pulsed Plasma Deposition (PPD) is a Physical Vapor Deposition (PVD) technique to produce thin films (for some nanometers to several micrometers in thickness) of numerous materials such as oxides, nitrides, carbides and semiconductors [100].

The process exploits plasma generated through voltage pulses (around 40 kV with a few Hertz of frequency) from a source gas (e.g., oxygen). This plasma is accelerated through a voltage around 14 kV, oriented and directed, through a dielectric channel of glass or quartz, towards a grounded target (containing the target material to deposit) with enough energy density and power to cause a sub-surface explosion that projects, for sputtering, vaporized target material outward (ablation process or sublimation by explosion). The ablated material is ejected in the form of neutral or ionized atoms, molecules, radicals, cluster of atoms in amorphous or crystalline aggregates, whose spatial distribution can be seen as a cone with its axis perpendicular to the target surface. This

sort of feather of material named "plume" reaches the substrate which is fixed at an appropriate position (characterized by and distance and an angle from the target material), quite close in order to intercept the emission conoid and to allow the material deposition in a form of thin film on the target substrate.

All the phases of the process are carried out inside a closed chamber, named "PPD chamber", where pressure, temperature and gases concentration are controlled. The temperature of the substrate is controlled too. A system to prevent unwanted deposition on the target substrate by covering it, especially when the PPD machine is not in its steady state operation, has been installed.

Because ablation happens out of the thermodynamic equilibrium, stoichiometric composition of compounds is kept. The process of target material ablation is illustrated in the schematic in fig. 2.21 [100].

A picture of the components of the PPD inside the PPD chamber along with the pulsed plasma and the plume during a material deposition is reported in fig. 2.22.

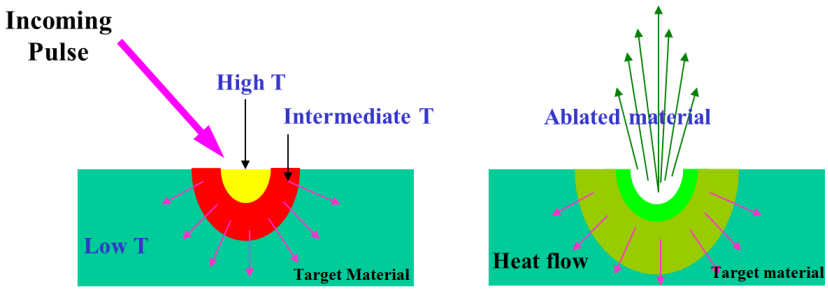

Fig. 2.21 – Schematic representing the process of ablation of the target material in the PPD.

Main deposition parameters are given by:

- amplitude and frequency of the pulses used for plasma extraction;
- number of pulses used for plasma extraction during deposition time;
- pulsed plasma accelerating voltage;
- distance and angle between dielectric channel and target material;
- distance and angle between target material and substrate;
- position of the substrate on its holding plate;
- pressure inside the PPD chamber;
- temperature of the substrate and of the PPD chamber.

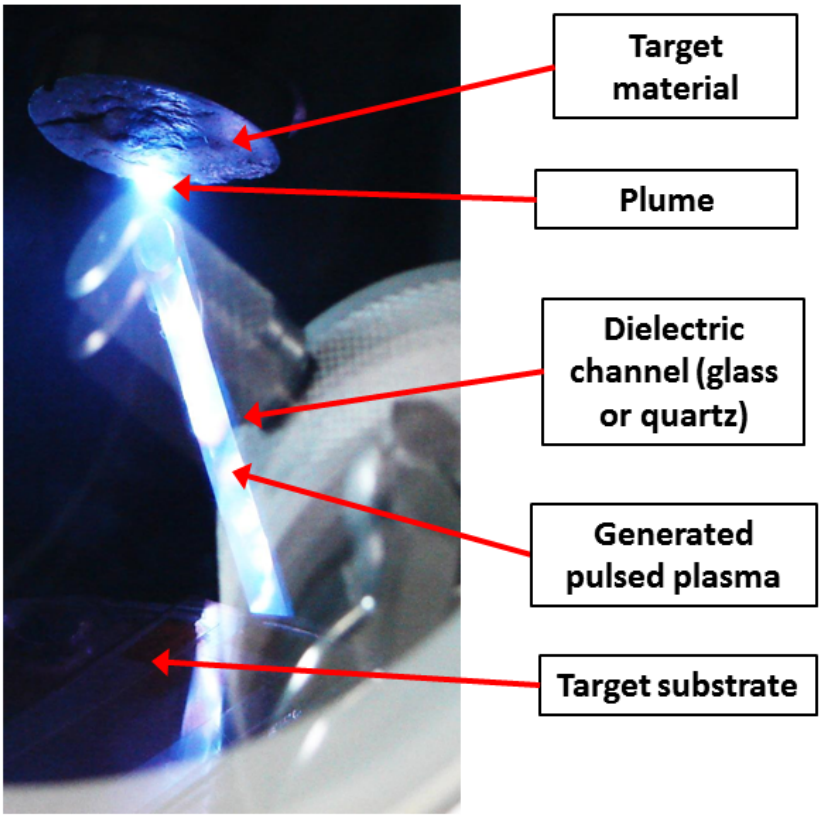

Fig. 2.22 – Picture of the components of the PPD along with the pulsed plasma and the plume during a material deposition.

Relations among all the aforesaid process parameters are complex and the complete description of all their relationships is outside the aim of this work. However, it is worth

noting only that the thickness of the deposited material layer is strongly affected by the number of plasma pulses used during the deposition process, by their accelerating voltage and by the pressure inside the PPD chamber. Substrate temperature plays an important role in the properties of the deposited material, as explained in the following.

A PPD machine is available at the Nanotechlab of the University of Catania (Italy) and has been exploited to deposit thin films of Zinc Oxide (ZnO) to be used as piezoelectric layers in a process step of rapid prototyping applications for micro e nano-devices.

The objective of the work presented in this subsection is the setup of the PPD machine to deposit ZnO layers having a controlled thickness and a uniform crystalline orientation to provide piezoelectric mechanical-to-electrical transduction. The patterning of the ZnO films, the realization of proper metal electrodes for readout and of the release of mechanical structures are currently under development in separated research projects at the Nanotechlab of the University of Catania (Italy). A studied and implemented rapid prototyp-

ing strategy to release suspended structures (e.g., cantilever beams having triangular section) based on FIB milling and compatible with this process has been presented in subsection 2.2.1.

Piezoelectricity in ZnO films is strictly related to their crystalline structure and in particular to its orientation, when ZnO exhibits wurtzite structure. Studies in literature have shown that deposition temperature strongly affects the orientation of wurtzite crystals in ZnO. Higher uniformity in crystalline orientation leads to improved quality in the piezoelectric properties of ZnO [265]. For this reason deposition of ZnO has been carried out adopting a system for substrate temperature control.

Quite all the process parameters except substrate temperature and the number of plasma pulses have been fixed at given values derived from previous experiences in the use of the PPD machine [100]. Among these parameters, the PPD chamber pressure has been fixed at 0.2 Pa, the pulsed plasma accelerating voltage at 14 kV, the frequency of the plasma pulses at 1 Hz and the plasma extraction voltage at 40 kV.

The number of plasma pulses in a single deposition has been adopted to control the thickness of the deposited film, when the PPD machine is in its steady state. Higher number of plasma pulses results in a larger thickness of the deposited film.

The temperature of the target substrate has been regulated to improve the crystalline orientation of the realized ZnO films.

ZnO has been deposited on silicon substrate having <100> orientation.

Two examples of the deposited ZnO films are shown in the SEM images in figs. 2.23–2.24: fig. 2.23 reports the morphology of the deposited films and the thickness of the film is shown in the cross-section in fig. 2.24.

The relation between the number of plasma pulses in a single deposition and the final thickness of the deposited ZnO film is shown in the plot in fig. 2.25, as resulting from the characterization of the deposition samples. Considering thicknesses below 100 nm, results are estimations given through models and observations from a Field Emission Gun SEM

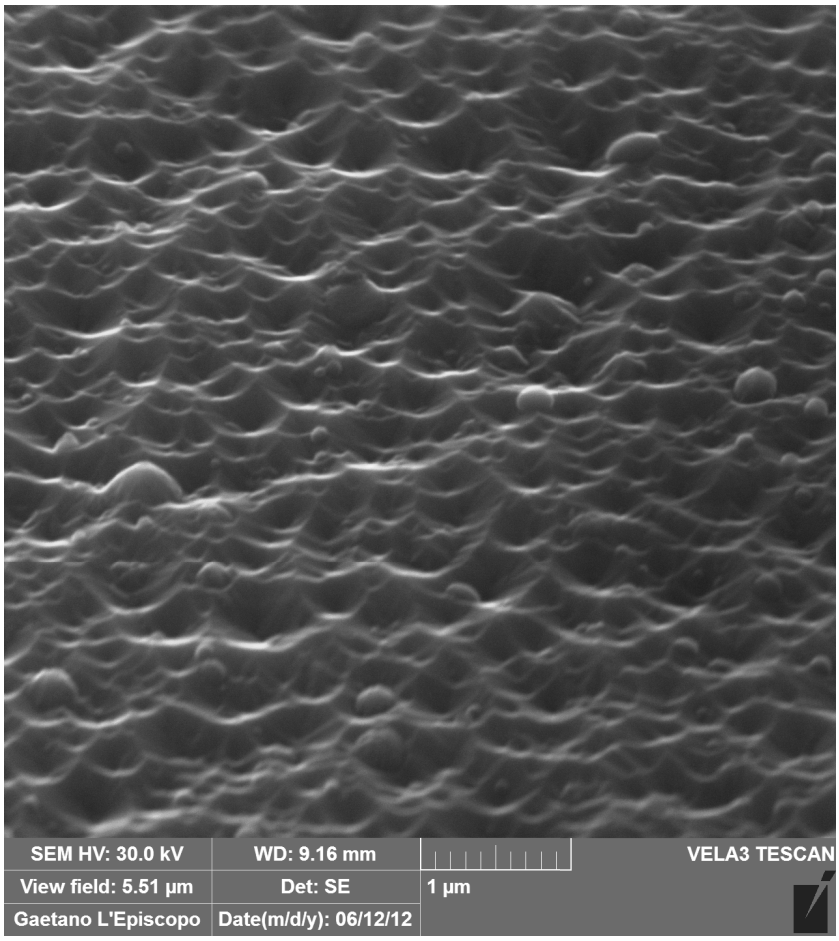

Fig. 2.23 – SEM picture showing the surface morphology of the deposited ZnO film.

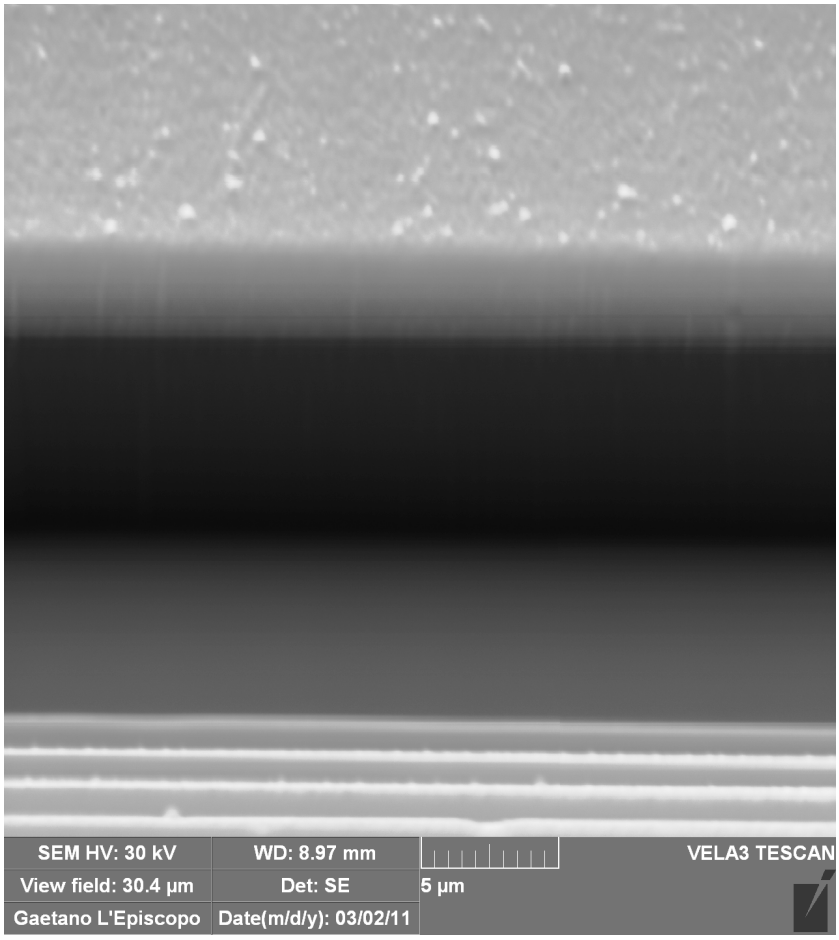

Fig. 2.24 – SEM picture showing a cross section of the deposited ZnO film. Top brighter layer is the deposited ZnO film and the bottom darker layer is the silicon substrate. This cross section has been realized through FIB milling.

(FEG-SEM) with Energy Dispersive X-Ray Spectroscopy (EDS) [97] of the Department of Chemistry of the University of Catania (Italy); measurements between 100 nm and 200 nm are obtained through Rutherford Backscattering Spectroscopy (RBS) [82] analyses held at at the Department of Physics of the University of Catania (Italy) and measurements above 200 nm are obtained through cross-sections observations by SEM (as the picture in fig. 2.24) carried out at the Nanotechlab of the University of Catania (Italy).

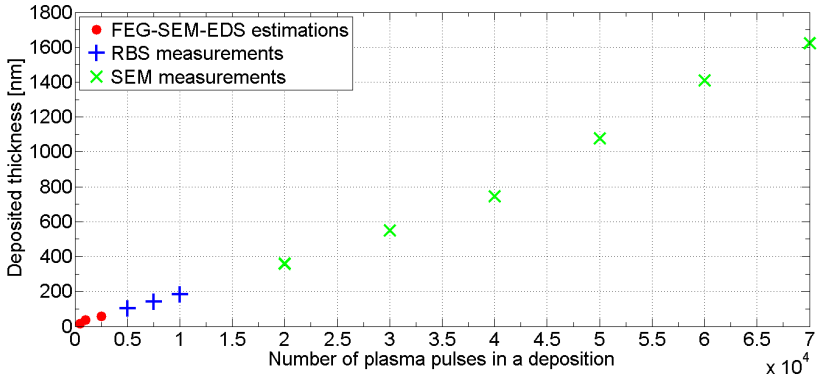

Fig. 2.25 – Relation between the number of plasma pulses in a single deposition and the final thickness of the deposited ZnO film, as resulting from the characterization of the depositions samples.

RBS analysis allows for also checking the chemical composition of the deposited ZnO layer. As resulting from these analyses from samples having a thickness between 100 nm and 200 nm, the zinc (Zn) is the 54% of the ZnO compound and oxygen (O) is the 46%. This confirms the optimum quality of the deposited compound because these data are not so far from the ideal 50%–50% stoichiometric ratio of ZnO. One example of the RBS spectra obtained from film characterization is reported in fig. 2.26.

The orientation and the uniformity of the crystalline orientation of the deposited ZnO films have been investigated through X-Ray Diffraction (XRD) [248] analyses carried out at the Department of Chemistry of the University of Catania (Italy). Three different kinds of samples having a thickness of 800 nm have been compared in detector scan XRD analyses [248]: the first group is represented by ZnO films deposited at a substrate temperature of 400℃, the second group at 600℃ and the third at room temperature. Characterization results of the comparison are reported in fig. 2.27.

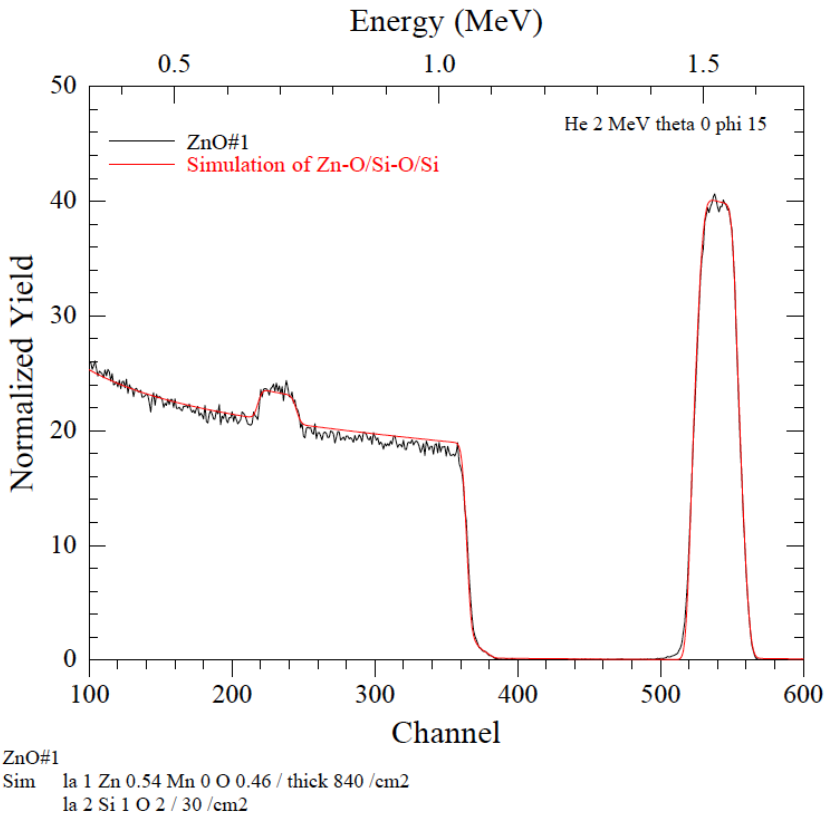

Fig. 2.26 – RBS spectrum obtained from ZnO film characterization. Peaks of the element zinc and of the element oxygen are detected and the stoichiometric ratio is derived from data elaborations.

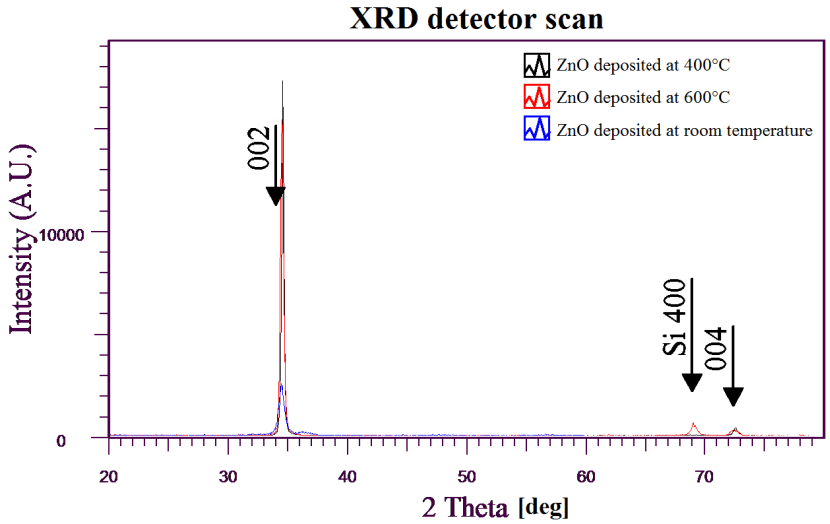

Fig. 2.27 – XRD detector scan spectra comparison of three ZnO samples deposited at different substrate temperatures. Crystalline orientations observed are indicated in the plot.

Results from fig. 2.27 indicates a preeminent crystallinity orientation in the direction <002> (i.e. the direction perpendicular to the substrate plane) in the films deposited at 400℃ and 600℃, as required from the application, while crystalline orientation in the sample obtained at room temperature is very poor and unsuitable for a layer having good piezoelectric properties. This confirms literature results about the

effects of the substrate temperature during depositions on the crystalline orientation of ZnO films [182].

The quality of the crystalline orientation of the analyzed ZnO samples deposited at 400℃ and 600℃ of substrate temperature has been investigated through their XRD rocking curves reported in fig. 2.28, as resulting from XRD analyses.

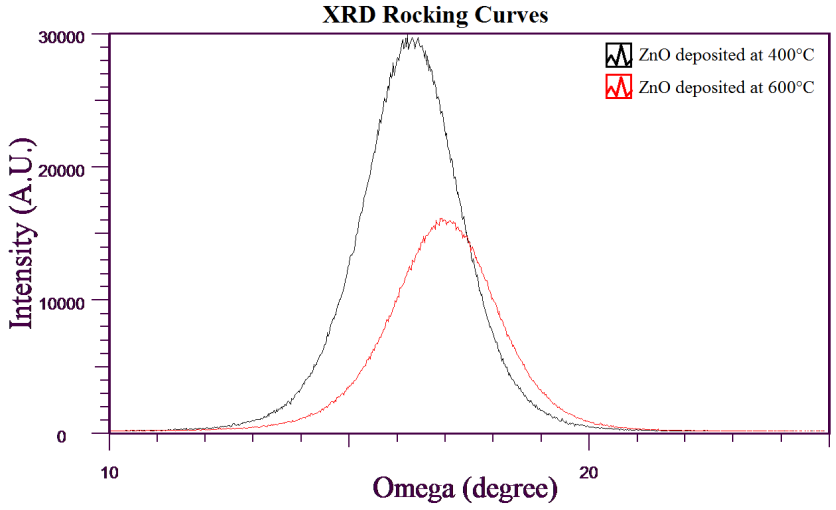

Fig. 2.28 – XRD rocking curves comparison of two ZnO samples deposited at substrate temperatures respectively of 400℃ and 600℃.

Rocking curves in fig. 2.28 indicate a slight better quality in crystalline orientation of the films deposited at 400℃ of

substrate temperature with respect to samples deposited at 600℃, confirming the suitability of these films for piezoelectric applications.

2.3 Devices in direct printing technology

In the past decades scientific community has shown a growing interest in the possibility to make very low-cost electronics and sensors exploiting technologies coming from the graphic industry and adopting innovative materials and flexible substrates. This interest is driven by needs for low cost mass-production processes (e.g., RFID tags, antennas, keyboards, display and sensors production) [11, 151].

The availability of novel technologies for the development of low cost and sometimes disposable sensors would move the market interest towards new applications, previously not much attractive because of the costs of traditional silicon electronics. Moreover, the rapid prototyping of cheap devices and sensors by printing technologies is also of great importance for the scientific community including research laboratories and academy.

Among several printing fabrication strategies, screen printing is a technique requiring the use of a mask acting as stencil. This stencil delimits the areas where ink is free to adhere to the substrate, following a mechanical pressure exerted typically through a roller. Examples of sensors realized by screen printing are: gas detectors exploiting conductive patterns realized by screen printing nanoparticles inks [64], humidity sensors for smart packaging applications [238], impedance sensors applied to biosensors [37] and resistive force sensors [134].

Given the spread of this technology at a global level, a good range of conductive, insulating and functional materials, compatible with screen printing, are now commercially available. Furthermore, screen printing allows to easily obtain thick layers of material which increases tracks conductivity.

In spite of processes based on photolithography and in general requiring masks such as screen printing, inkjet printing does not require any masks or micromachining. Inkjet printing of polymers and materials is a fairly new technique which could replace in specific contexts traditional techniques (e.g. sputtering, lithography, and post-processing). By this drop-

on-demand technique a layer of functional ink can be easily deposited on the substrate in well defined patterns without the need of patterning techniques and thus reducing time, costs and waste of materials. Small volumes of materials, in the range of 1–30 picoliters, may be filed with a high spatial resolution and good reproducibility. Moreover, inkjet printing is a contactless deposition technique which makes it applicable to many different substrates.

Specifically, inkjet-based sensors offer the possibility to combine performances of flexible substrates and functional inks with a cheap rapid prototyping technique. Traditional materials adopted to realize sensors by inkjet systems are electrical conducting polymers (such as PEDOT-PSS) and functionalized polymers (such as polianiline, PANI).

PEDOT-PSS is a conductive polymer (3,4-ethylen dioxythiophene) oxidized with polystyrene sulfonated acid. It is a p-doped material with a good ambient and thermal stability and a relatively high electrical conductivity. The use of PEDOT-PSS to realize conductive patterns requires several printing

cycles in order to reduce the electric resistivity of the pattern deposited.

Polyaniline (PANI) is a conducting polymer. Many applications of this material are related to gas sensors. Concerning its physical properties, it can be dissolved in organic solvents or in aqueous solutions which are suitable to be used by inkjet printing.

The implementation of resistors, pads and electrodes by PEDOT-PSS on PET [222], all-polymer RC filter [146], PANI based devices for the detection of ammonia [64] and complex MEMS structures with silver nanoparticles [86] are examples of devices realized through inkjet techniques.

For what concerns printing equipments, there are various solutions available on the market allowing for inkjet printing of functional materials [85, 159]. Usually, printer adopting drop-on-demand mode are used where the ink droplets are ejected by the use of a pulse generated by thermal or piezoelectric strategies.

Many printing systems for rapid prototyping are piezoelectric because of their intrinsic suitability when different sol-

vents are used. Systems based on piezoelectric heads provide resolutions in the order of the tens of micrometers. Usually, inkjet printers are expensive equipments due to the need for both printing heads compatibility with different kinds of inks and the implementation of repeated printing cycles. The latter is mandatory (e.g., for the realization of conductive patterns by PEDOT-PSS). It can be observed that the use of expensive inkjet printing systems allows for the realization of complex devices.

Actually, one of the main deals using low cost inkjet printing is the nature and the physical property of inks with particular regards to their viscosity and their electrical properties. As an example metal based inks (e.g., silver based solutions), which could play a strategic role for electrodes and sensing structures due to the extremely low resistivity and mechanic properties, are difficult to be used with cheap inkjet systems due to nozzle occlusions problems. Many efforts have been dedicated to make conductive inks compatible to specifications required by common inkjet apparatus.

Many examples in the literature adopt a mixed approach for the realization of low cost devices by direct printing technology. Conductive structures such as wires, coils, capacitor electrodes are usually implemented by screen printing technology. As an example, it must be recalled that the development of conductive layers by polymers such as PEDOT-PSS requires several printing cycles which are not implementable by low-cost inkjet printers. But, once electrodes have been realized, polymer layers (such as PEDOT-PSS) for piezoresistors, resistive devices and functional layers (such as PANI) for gas sensors are successively deposited by low cost inkjet printers. The possibility to use cheap printing systems for the realization of all inkjet devices (including both electrodes and other functional layers) would be highly profitable especially for research laboratories and academy.

In the research field of low-cost printed sensors, the Sensor Lab of the University of Catania (Italy) has developed a cheap solution for rapid prototyping of printed devices having sizes of several centimeters for sensors [15] and nonlinear energy harvesters [4] through an ordinary commercial piezo inkjet

printer from EPSON®, a conductive ink and a plastic flexible substrate.

The metal ink used in the realization of the conductive pattern in these devices is the silver nano-particles solution "Metalon® JS-B15P" by Novacentrix® [172]. An SEM image showing the surface morphology and the typical thickness of the metal ink after its deposition through the inkjet printer on the plastic flexible substrate is reported in fig. 2.29.

The substrate adopted in the printing is given by the "Novele™ IJ-220 coated PET" from Novacentrix®, a treated polymer film based on polyethylene terephthalate (PET) having electrical isolating properties and coated on one of its sides to allow for a proper and reliable adhesion of metal ink on the substrate during the printing process. The coating on one of the two sides of the substrate allows to print metal electrodes only on the coated side. The thickness of the substrate is about 165 µm. A SEM picture showing the cross section of this substrate is reported in fig. 2.30 and the coating is visible at the top side of the substrate.

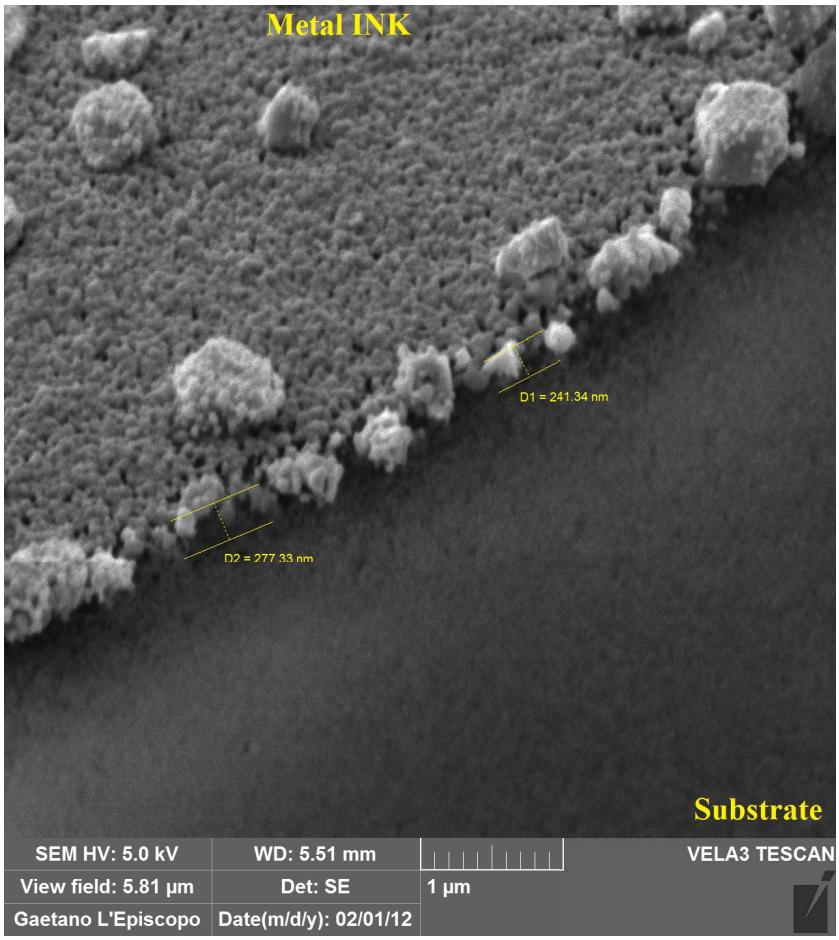

Fig. 2.29 – SEM picture showing the surface morphology and the typical thickness of the metal ink (left upper side of the picture) after its deposition through the inkjet printer on the plastic flexible substrate (right lower side of the picture).

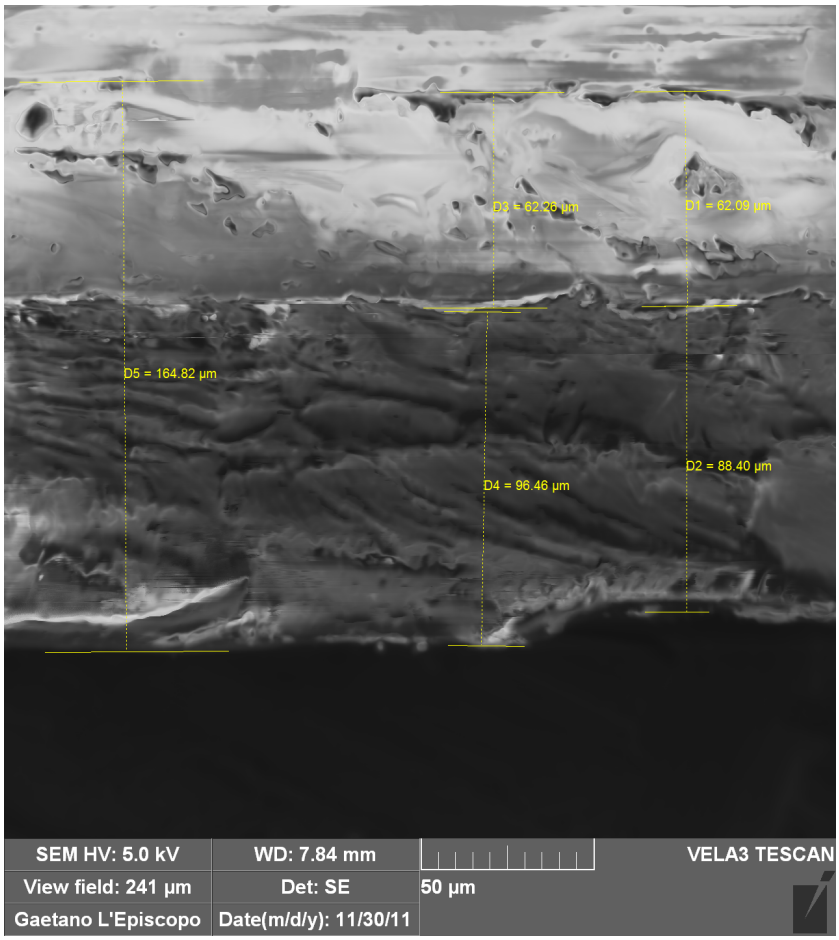

Fig. 2.30 – SEM picture showing the cross section of the "Novele^{TM} IJ-220 coated PET" from Novacentrix® used in the printed devices developed at the Sensor Lab of the University of Catania (Italy). Substrate coating to improve metal ink adhesion is clearly visible at the top side of the substrate (i.e. the side allowed for printing).

The fabrication of these devices simply consists in directly printing the metal tracks on the plastic substrate. The substrate is then trimmed according to the geometrical requirements of the applications. The observed resolution of these process is around 200 µm. Because the adopted ink exhibits piezoresistive properties, these device can be used as a strain sensor [15]. Other kind of devices can be created from this architecture by depositing a patterned functional layer on the printed conductive electrodes in order to satisfy a specific application (e.g., the sensing of a chemical quantity). In the case of the nonlinear energy harvester realized in printed technology at Sensor Lab of the University of Catania (Italy) [4], a layer of Lead Titanate Zirconate (PZT) has been deposited through screen printing on the metal electrodes.

Three samples of devices realized in printed technology at the Sensor Lab of the University of Catania (Italy) are shown in the photos in fig. 2.31.

Resolution, tolerances, dimensions and surface morphology of the tracks of the printed electrodes have been investigated using the SEM at the Nanotechlab of the University of Cata-

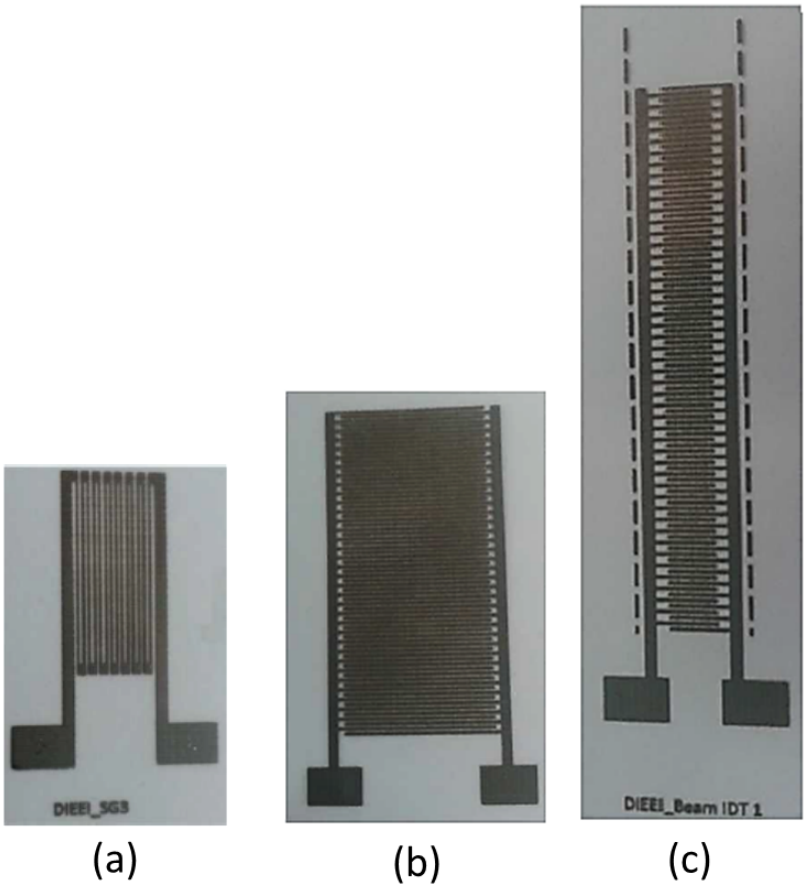

Fig. 2.31 – Photos of devices realized in printed technology at the Sensor Lab of the University of Catania (Italy): (a) strain-gage; (b) interdigitated electrodes; (c) interdigitated electrodes on a beam.

nia (Italy). An example of the SEM images used in this study is shown in fig. 2.32.

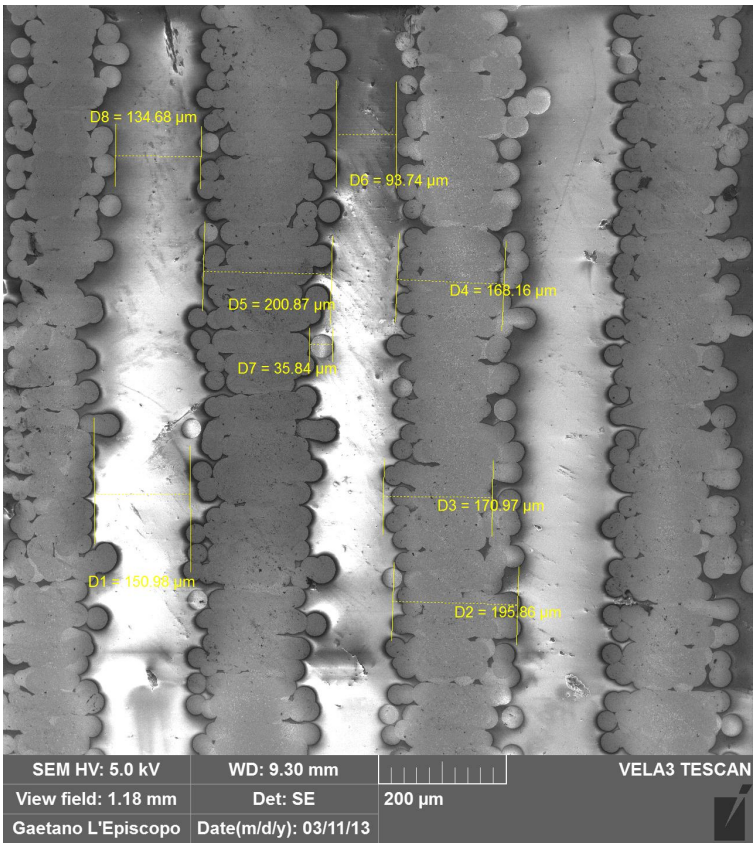

Fig. 2.32 – Example of the SEM images used for the inspection of the resolution, tolerances, dimensions and surface morphology of the tracks of the printed electrodes. Dimensions are shown in the image and effects of the ink bubbles coming from the printing process are clearly visible.

3

Bistable devices for vibration energy harvesting

Nothing is lost, nothing is created, everything is transformed.

Antoine Laurent de Lavoisier

In this chapter, after an overview about the state of the art in the field of energy harvesting from mechanical vibrations, several solutions based on bistable oscillators will be proposed to scavenge energy from vibrations in a more efficient way than traditional approaches exploiting linear resonators.

3.1 Energy harvesting from vibrations: state of the art

Energy Harvesting (also known as Power Harvesting or Energy Scavenging) is a scientific discipline that deals with the scavenging of energy (which would otherwise be lost) from one or more free ambient energy sources (such as sunlight, the mechanical vibrations, thermal gradients), its transduction into an electrical form and its accumulation for later uses.

Differently from photovoltaic and aeolic systems, which deliver high amounts of power (e.g., in the order of kilowatts and megawatts) on large scale for civil and industrial use, energy harvesting is dedicated to provide small amounts of power (e.g., in the order of milliwatts and microwatts) recovered from the operation environment of some low-power miniaturized devices such as wireless sensor nodes, MEMS and VLSI systems, wearable electronics, mobile devices, biomedical systems and so on, for their powering needs [189].

In last decades, the rapid and constant development of electronics silicon-based devices having smaller dimensions, lower power consumption and wireless operation is limited by the

traditional powering systems represented by power cables and electrochemical batteries. In fact, the use of power lines could be expensive (especially in their installation), cumbersome and too limitative for wireless operations. Similarly, traditional electrochemical batteries have a limited lifetime charge (this introduces costs for replacement operations), bulky size (with respect to actual microelectronics devices), issues in high temperature applications and polluting environmental impact caused by their disposal [256]. Furthermore, energy density of batteries has increased by only a factor of 3 over the past 15 years [244].

The harvesting of small amounts of the available energy in the operative environment of low-power electronics devices and its reuse to power these systems have been identified as a possible solution to power devices by making them autonomous. This is possible only if a source of energy is available in the operative environment of these devices and if these devices have low power consumption (e.g., in the range of milliwatt or microwatt).

Some data about power consumption of several target devices for energy harvesting applications are shown in the plot in fig. 3.1, as reported in literature [108].

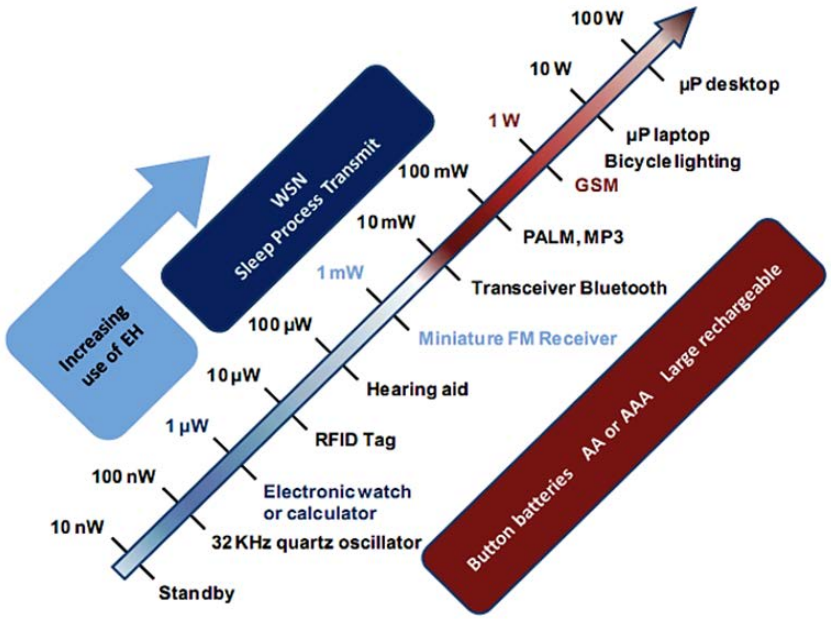

Fig. 3.1 – Plot of the power consumption of several target devices for energy harvesting applications compared with power available from batteries and power scavenged by energy harvesters in actual technologies [108].

A very recurrent example of application of energy harvesting in literature is given by wireless sensor networks, which

are commonly used in several monitoring and control applications like environmental and structural monitoring, smart cities, medical remote sensing, military and aerospace applications and so on [202]. Each node of the network is usually composed of one or more sensors, a microcontroller unit and a transceiver with antenna for wireless communication (which is the most power consuming component of the node, especially during transmission and receiving activities). The power consumption of a sensor node has been estimated between 1 μW and 2 μW by various authors in recent works [244]. Traditionally, the power of each node is provided by electrochemical batteries having often large size and a limited lifetime (typically between one and ten years). When the charge in these batteries is low, as already said, the need of substituting them introduces maintenance costs and issues if the number of nodes is high and harsh environments are involved. Sometimes lifetime of nodes ends when batteries must be replaced because of costs. If miniaturized energy harvesters are adopted, each sensor node become autonomous and its lifetime is indefinitely extended. Furthermore, the development

of fabrication technologies at microscale (e.g., MEMS) results in the possibility to reduce the size of nodes [256]. This also increase the range of potential applications, opening the possibility to create ubiquitous wireless sensor networks.

A brief survey of available sources of energy is presented in subsection 3.1.1.

3.1.1 Sources of energy

Several forms of energy sources have been considered for energy harvesting applications, along with their transduction mechanisms to proper generate an electrical output [244]. Optical energy usually consists in sunlight that exploits photovoltaic effects [181]. Kinetic energy is generally represented by mechanical vibrations [202], whose mechanical energy can be converted by means of piezoelectric [81], electrostatic [162], electromagnetic [47] and magnetostrictive [245] transducers. Thermal energy is given by thermal gradients transduced through thermoelectric effects such as Seebeck effects [144]. RF energy is captured through antennas and converted through electromagnetic transduction [118]. Chemical energy is used in energy harvesting applications through fuel cells [125].

Some data taken from literature about available energy sources are shown in table 3.1 [202]: both fixed energy sources (such as batteries) and power scavenging sources have been considered.

Table 3.1 – Comparison of power scavenging and energy sources. The top part of the table contains sources with a fixed level of power generation; the bottom part of the table displays sources with a fixed amount of energy storage [202].

	Power density (1 year lifetime) [$\mu W/cm^3$]	**Power density (10 year lifetime) [$\mu W/cm^3$]**
Solar (outdoors, direct sun)	15000	15000
Solar (outdoors, cloudy day)	150	150
Solar (indoors, office desk)	6	6
Vibrations (piezoelectric conversion)	250	250
Vibrations (electrostatic conversion)	50	50
Acoustic noise at 75 dB	0.003	0.003
Acoustic noise at 100 dB	0.96	0.96
Temperature 10°C gradient	15	15
Shoe inserts	330	330
Batteries (non-rechargeable lithium)	45	3.5
Batteries (rechargeable lithium)	7	0
Hydrocarbon fuel (micro heat engine)	333	33
Fuel cells (methanol)	280	28

The data show that batteries are a reasonable solution only for short lifetimes. However, another solution is requested for long lifetimes. Fuel cells represent a potentially large improvement over batteries as an energy reservoir but research to miniaturize fuel cells is currently underway, even if it is very promising [262]. Solar cells offer excellent power density only in direct sunlight. However, in dim office lighting, or areas with no light, they are inadequate. Power scavenged from thermal gradients is also substantial enough to be of interest if the necessary thermal gradients are available. It is, however, difficult to find thermal gradients greater than a 10℃ in a volume of 1 cm^3.

Among different power sources, mechanical vibrations represent one of the most ubiquitously and continuously available sources that can potentially deliver a significant amount of energy. For this reason, kinetic energy from vibrational sources has been watched with an increasing interest by scientific community in order to build generators able to efficiently scavenge energy to power low-power mobile electronic devices.

A more detailed overview about vibrational energy sources is reported in subsection 3.1.2 and some details about energy harvesters from mechanical vibrations are discussed in subsection 3.1.3.

3.1.2 Sources of mechanical vibrations

Vibration is a mechanical phenomenon whereby oscillations occur around an equilibrium point. They are two kinds of mechanical vibrations: free vibrations and forced vibrations. Free vibrations are generated by mechanical vibrating systems without any external forcing; ideally, if those systems are non subjected to any kind of friction, damping or energy loss, they would continue to vibrate for an infinite time; such systems vibrate because they are forced by their non-zero initial conditions; a simple example is the case of an inertial mass connected to a frame by means of a spring initially compressed. Forced vibrations occur when an external forcing is applied to the system, for example in a washing machine, whose drum, equipped with a shock absorber, is continuously subjected to a rotating force and to an inertial force generated by the asymmetrical arrangement of inside clothes [194].

Ambient mechanical vibrations (also known as ambient noisy vibrations) come in a large variety of forms such as induced oscillations, seismic noise, vehicle motion, acoustic noise, multitone vibrating systems, and, more generally, noisy environments. Suitable vibrations can be found in numerous applications including common household goods (fridges, washing machines, microwave ovens etc), industrial plant equipments, moving structures such as automobiles and aeroplanes and structures such as buildings and bridges [17].

Depending on the mechanism that generates vibrations, existing vibrational sources can be categorized into three major groups [189]. The first group is composed of rigid structures subjected to their own movement such as vehicles in general, containers, mobile devices, fans and motors, elevators and escalators in public places, home appliances, refrigerators, bridges, building structures and so on. The second group consists of elastic structures exhibiting an elastic deformation of their walls such as rotor blades, wings of airplanes, pumps, motors, pipelines, ventilation and air conditioning. Finally, the third group is given by compliant structures with

low modulus of elasticity and high deformation coefficients like textile materials, leather, rubber tubing, pipelines typically traveled by a moving fluid, etc.

Vibrations sources are typically considered as accelerations characterized in terms of acceleration magnitude and frequency spectrum with an associated kinetic energy [194].

On the basis of the acceleration magnitude, vibrations are generally classified into: low-magnitude vibrations (if amplitude is lower than 0.1 m/s^2), mid-magnitude vibrations (when amplitude is between 0.1 m/s^2 an 2 m/s^2) and high-magnitude vibrations (if amplitude is larger than 2 m/s^2) [194].

On the basis of the frequency spectrum of the source, vibrations can be categorized into: wideband vibrations (if a bandwidth larger than about 100 Hz is exhibited) and resonant or quite-resonant vibrations (if they are characterized by narrow energy spectra with a few peaked modes). In the case of resonant or quite-resonant vibrations, it is possible to distinguish low-frequency vibrations (if main harmonics are confined in a range below 10 Hz), mid-frequency vibrations (when main harmonics are contained in a range between 10 Hz and

150 Hz) and high-frequency vibrations (if main harmonics are within a range starting over 150 Hz) [189].

In terms of the level of the kinetic energy carried by vibrations, it is possible to split vibrations into two groups. First group is given by low-level vibrations that convey a low or a mid level of energy; this sort of source can be found in a very wide range of applications, especially in domestic and civil fields. Second group is represented by high-level vibrations, coming from industrial applications, having a potential smaller range of applications than low-level vibrations [27].

For example, human based sources are generally characterized by low frequency high amplitude accelerations, as shown in the time series of the acceleration of the footsteps of a walking and a running person reported respectively in fig. 3.2 and in fig. 3.3.

The kinetic energy carried by vibration sources is strongly committed with magnitude and spectrum of the associated accelerations. In fact, sometimes, the delivered energy is concentrated in a very tight region of the frequency spectrum, as in the case of rotating machines [263], especially when oscil-

Fig. 3.2 – Time series of the acceleration coming from the footsteps of a walking person, measured through an accelerometer placed near the heel.

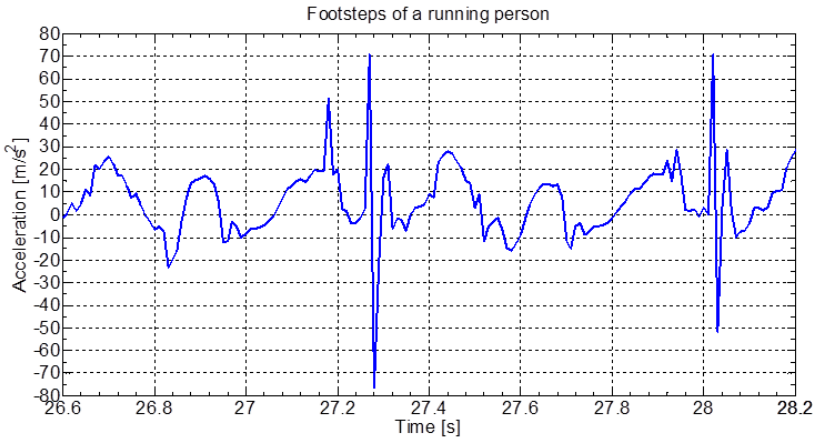

Fig. 3.3 – Time series of the acceleration coming from the footsteps of a running person, measured through an accelerometer placed near the heel.

lations from vibrations follow a periodic or defined dynamics. On the contrary, energy is very often distributed over a wide spectrum of frequencies in other applications; in particular, several scenarios exist where a significant fraction of energy is generally distributed in the lower part of the frequency spectrum, below 500 Hz [200]: this is the case of vibrations having random dynamics.

Some data on mechanical sources of low-level vibrations are listed in table 3.2, as reported from literature [202].

Two examples of vibration spectra (a small microwave oven and a large office windows next to a busy street), taken from literature [202], are illustrated in fig. 3.4.

In order to harvest energy from mechanical vibrations, the first step is to study and characterize the specifications of the vibrational target source and then trying to find a solution for the development of efficient energy harvesters. Several solutions matching with different sources exist. The strategies implemented in literature are presented in subsection 3.1.3, along with some details about the architectures for vibration

Table 3.2 – Acceleration magnitude and frequency of fundamental vibration mode for various sources [202].

Vibration source	**Peak acceleration [m/s^2]**	**Peak frequency [Hz]**
Car engine compartment	12	200
Base of 3-axis machine tool	10	70
Blender casing	6.4	121
Clothes dryer	3.5	121
Persons tapping their heel	3	1
Car instrument panel	3	13
Door frame just after door closes	3	125
Small microwave oven	2.5	121
HVAC vents in office building	0.2–1.5	60
Windows next to a busy road	0.7	100
CD on notebook computer	0.6	75
Second story floor of busy office	0.2	100

energy harvesters, with a special focus on solutions based on MEMS technologies.

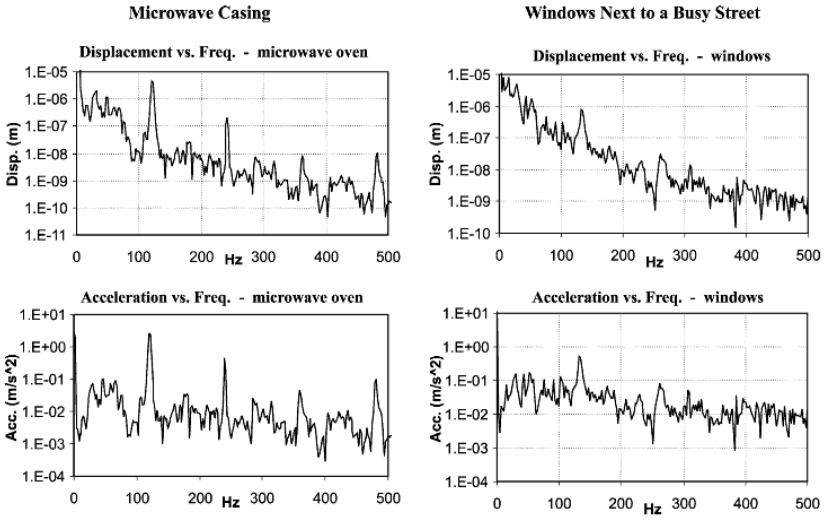

Fig. 3.4 – Vibration spectra for a microwave oven and office windows next to a busy street [202].

3.1.3 Architecture of vibration energy harvesters

Devices aimed to energy harvesting from mechanical vibrations have generally an overall architecture based on three base blocks [264].

The first block is represented by the coupling (or oscillating) mechanical structure. It has to directly interface to the input vibrational sources and to vibrate after being forced by the incoming vibrations. It generally consists of an inertial

mass and some flexures having different shapes. The task of the coupling structure is getting a fraction of the incoming kinetic energy from the source and delivering it to the second block in form of displacements, velocities, stresses and/or strains.

Then, the outputs from the coupling mechanical structure are converted into an electrical usable form (i.e. voltages or electrical currents) by the second block, that consists of one or more mechanical-to-electrical transducers based on piezoelectric [81], electrostatic [162], electromagnetic [47] or magnetostrictive [245] strategies.

Electrical energy coming from the mechanical-to-electrical transducer is finally used and/or properly adapted (in terms of waveform and level) to some specific applications through proper circuits (i.e. AC-DC and/or DC-DC power converters) in the third final block. Depending on the application and on the amount of scavenged energy, the electrical output energy from vibration energy generators can be used to direct power devices or to recharge backup batteries and/or supercapacitors used to support target devices powering.

The general architecture of energy harvesters from mechanical vibrations is summarized in fig. 3.5.

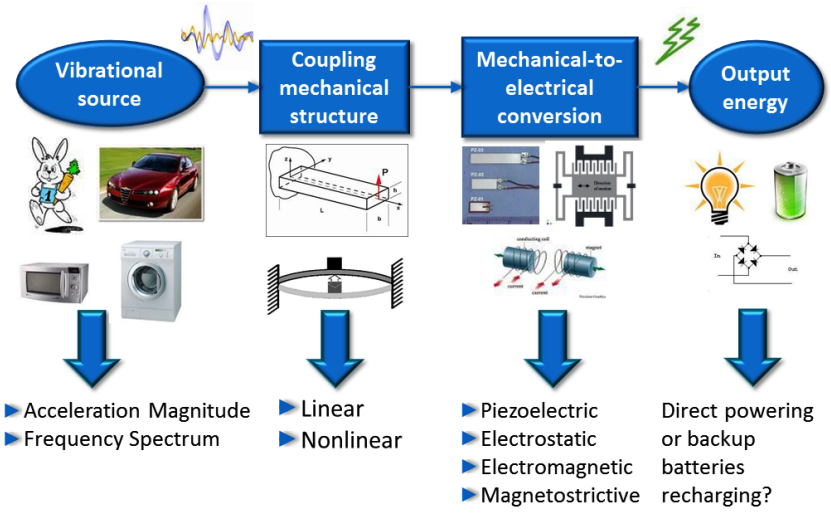

Fig. 3.5 – General architecture of devices for energy harvesting from mechanical vibrations.

The overall efficiency of the system is given by the efficiency of each block. For this reason, each block must be properly designed to adapt to the mechanical source and to selected application.

In fact, the mechanical coupling structure has a crucial role because the amount of energy collected strongly depends

on it and consequently it affects heavily the efficiency of the overall system. Its definition cannot be separated, upstream, by the characteristics of the source and, downstream, by the transducer specifications. Depending on the application, several types of structures have been proposed and studied in the literature and, because of the aim of this work, they will be illustrated in subsections 3.1.4, 3.1.5 and 3.1.6.

In the same way of coupling structures, mechanical-to-electrical transducers have a huge impact on the harvester efficiency, but, due to the topic of this work, they will be generally discussed in subsection 3.1.7.

3.1.4 Linear resonant coupling structures

Traditionally mechanical coupling structures have been based on linear resonant structures, which are characterized by a linear relationship between displacement and reaction forces.

An example of linear resonant structure is represented by a cantilever beam having a proof mass on its free end and experiencing linear elastic deformations. In this case, accelerations coming from the vibrational sources put in oscillation the can-

tilever beam (especially its free end) by means of the proof mass. Beam oscillations are then converted both in stresses and strains, near the fixed end of the beam (attached to a fixed inertial frame), and in displacements and velocities in the "moving" free end of the beam.

The dynamics of this kind of structures is typically modeled through the 1 degree-of-freedom second-order mass-damper-stiffness model in (3.1) [223].

$$m\ddot{z} + c_m\dot{z} + c_e(\dot{z}, z) + kz = -m\ddot{y} \tag{3.1}$$

where m is the proof mass, k is the stiffness coefficient of the beam, c_m is the coefficient of mechanical damping c_e is the damping of the mechanical-to-electrical transducer, $\ddot{y}$ is the absolute external acceleration applied to the inertial frame and z, $\dot{z}$ and $\ddot{z}$ are respectively the relative (with respect to the inertial frame) displacement, velocity and acceleration of the free end of the cantilever beam.

The modeling of the mass-damper-stiffness system is illustrated in fig 3.6, along with a schematization of a cantilever beam with proof mass.

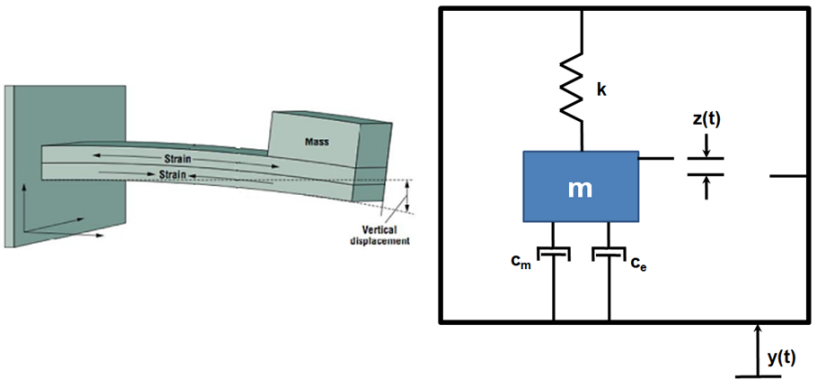

Fig. 3.6 – Schematization of a cantilever beam having a proof mass on its free end (left) and of the 1 degree-of-freedom second order mass-damper-stiffness model (right).

Considering $c_e = 0$, the damping ratio ζ of the system is given by (3.2) [3].

$$\zeta = \frac{c_m}{2\sqrt{km}} \tag{3.2}$$

Considering a sinusoidal excitation $\ddot{y} = A\sin(2\pi ft)$, where A is the amplitude, f is the frequency of the input acceleration and t is the time, for $\zeta < 1$ (underdamped system) the system exhibits its maximum output (i.e. displacement) with respect to the frequency, when the external excitation $\ddot{y}$ has a frequency $f = f_n$, equal to the resonant frequency f_n

of the system (see eq. (3.3) [3]), thus exhibiting a resonant behaviour.

$$f_n = \frac{1}{2\pi}\sqrt{\frac{k}{m}} \tag{3.3}$$

The quality factor Q of the system, defining the bandwidth of the resonator, is expressed in (3.4) [3].

$$Q = \frac{1}{2\zeta} \tag{3.4}$$

An estimation of the power harvested by a linear resonant system is plotted in fig. 3.7 for different frequencies and values of the damping ratio ζ, which defines both the quality factor and the bandwidth of the system [58].

As can be seen from fig. 3.7, the fraction of power extracted from the source is significant only around the resonant frequency of the system. The bandwidth of the linear resonant system can be enlarged only by increasing the value of the damping ratio ζ near to 1, but this is practically very difficult because typical values of the damping ratio ζ in microsystems applications can be found only below 0.2 [24, 241].

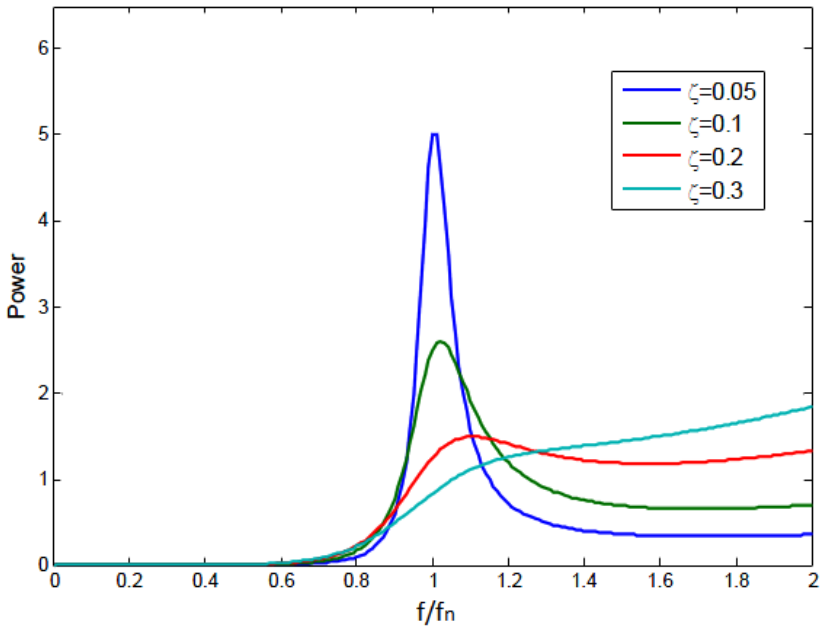

Fig. 3.7 – Example of the frequency spectrum of the power harvested by a linear resonant system for different values of the damping ratio ζ [58].

Due to their resonant behaviour, linear systems provide good performance in harvesting power only when their resonant frequency f_n matches, within their bandwidth, the main frequency mode of the sources. For this reason, each resonant harvester must be suitably designed for a specific application and, sometimes, a single vibrational source. However, these properties strongly adapt to vibrational sources having

a narrow spectrum and one peaked resonant mode but lead linear systems to poor performance outside their resonant frequencies and impose several constraints and limitations to the design and fabrication (especially in MEMS technologies) of these systems.

In fact, MEMS resonators can be very sensitive to small dimensional imperfections caused by microfabrication processes and this results in disadvantageous fluctuations in efficiency, because frequency matching is inaccurate. Moreover, the achievement of very low resonance frequencies (e.g., in the order of a few hundreds of hertz or lower) with a significantly large quality factor is a challenging issue at microscale, and therefore, resonant microsystems will generally work outside resonance and thus have a poor efficiency. A further reduction is experienced in the case of wideband vibrations since linear resonant devices collect energy mainly around their resonance peak [161].

For these reasons, the necessity of enlarging the bandwidth of energy harvesting devices, of overcoming the need of frequency matching with the source and of allowing for the down-

scaling of devices without loosing too much efficiency have pushed scientific research to find novel solutions for energy harvesters [232, 269].

Those solutions will be presented in subsection 3.1.5.

3.1.5 Coupling mechanical structures: from linear to nonlinear

Several solutions have been proposed to overcome the limits of linear resonant devices and to improve their performance, especially at microscale, where the power per volume unit scavenged by microgenerators is quite low. In particular, two different approaches have been followed by research. The first one deals with the development of systems having the ability to adjust or tune (autonomously or through a control strategy) their resonant frequency so that it can match the main mode of the vibrational sources at all time and situations. The second path is aimed to enlarge the operative bandwidth of harvesters by involving either linear or nonlinear strategies [269].

The adjustment of resonant frequencies in linear harvesters is performed by changing the mechanical characteristics of the

structure or the electrical load of the generator. Changing the mechanical characteristics of a generator has previously been called passive or active tuning depending on the approach.

Passive tuning is defined as a tuning mechanism that operates periodically. This approach consists in tuning the generator before its operation and afterwards in turning off the tuning system while the new resonance frequency is maintained during harvesting operation. This strategy only consumes power during the tuning operation and uses negligible energy once the generator is matched to the frequency of the ambient vibrations.

Active tuning is defined as a tuning mechanism that runs continuously for matching and eventually adjusting the resonant frequency of the mechanical oscillating structure with the ambient vibration frequency.

Since both of these approaches involve some form of active process, the tuning process is power consuming, so the first constraint is to scavenge a larger amount of power from the source than the power spent in adjusting the harvester characteristics [204].

One of the frequency adjusting approaches exploits a mechanical feature of clamped-clamped beams. It consists in applying a compressive or tensile axial preload (e.g., a force or a stress), below buckling, to a clamped-clamped beam, through mechanical or piezoelectric actuators. This induce in changing (lowering or increasing) the resonant frequency of the beam [138] (see fig. 3.8(a)–(b)).

Another tuning strategy consists in exploiting the electrostatic spring softening effect given by gap closing capacitors in MEMS devices [1] (see fig. 3.8(c)). In this case, an electric voltage, below pull-in voltage, is continuously used to control the stiffness of a coupling mechanical structure through the creation of an electrostatic force opposing the restoring force of the structure like a negative spring. This lowers the device mechanical stiffness constant and consequently its resonant frequency, according to (3.3).

Other frequency tuning strategies involve the application of forces coming from piezoelectric actuators [74], from magnetic levitation caused by permanent magnets [48] (see fig. 3.8(d)) or from thermal expansion due to applied thermal stress [231],

in order to affect the mechanical properties of the oscillating structure.

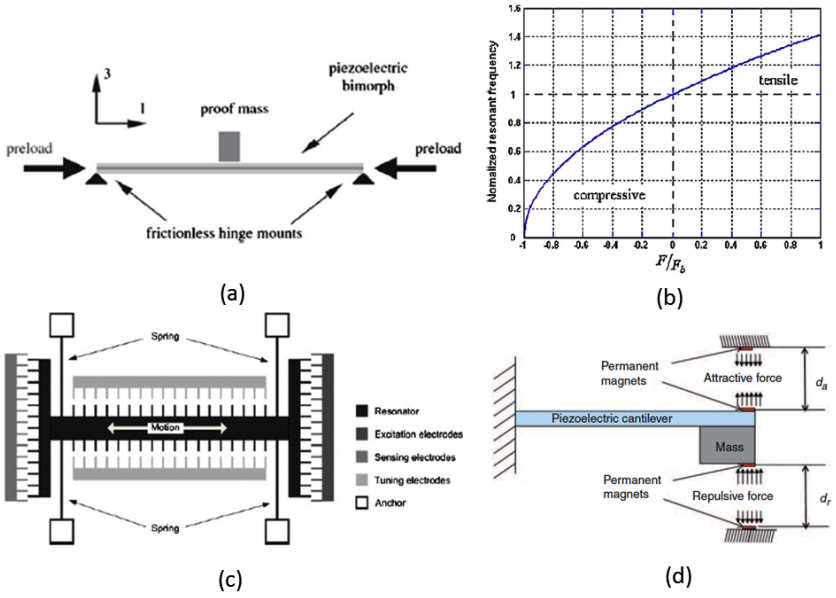

Fig. 3.8 – (a) Resonant frequency tuning of a clamped-clamped beam through axial preload [138]. (b) Resonant frequency shift after tensile and compressive axial preload of clamped-clamped beam [138]. (c) Example of structure exploiting electrostatic spring softening to tune resonant frequency [1]. (d) Resonant frequency tuning through magnetic levitation forces [48].

A different way in tuning the resonant frequency of devices is exploiting an electrical tuning to change the electri-

cal damping c_e in (3.1) by adjusting the load, which causes the power spectrum of the generator to shift. This strategy has been applied to energy harvesters having piezoelectric mechanical-to-electrical transducers. As resistive loads reduce the efficiency of power transfer and load inductances are difficult to be varied, it is most feasible to adjust capacitive loads to realize electrical tuning [258].

The second approach is to widen the bandwidth (i.e. the operative frequency range) of the generator in order to increase the device performance and make it compatible with several vibrational source, without tuning needs.

The first method consists in a generator composed of an array (named "mechanical band-pass filter") of small linear resonant generators (i.e. cantilever beams), each of which has different dimensions and mass and hence different resonant frequencies, as in fig. 3.9(a). Considering the superimposition of the frequency spectra of these devices (e.g., when these devices are connected in series), the operative bandwidth is widened, whilst the quality factor does not decrease and larger dimensions are required [214] (see fig. 3.9(b)).

Another strategy is given by multi-mass systems, where several proof masses having different dimensions are placed in appropriate positions on a clamped-clamped beam [201].

The adoption of amplitude limiters (e.g., mechanical stoppers) in order to limits the oscillation magnitude in microresonators (i.e. cantilever beams) has been proven as another strategy to improve microgenerators performance (see fig. 3.9(c)). In this case, some kinds of nonlinearities introduced by the impacts between the mechanical stopper and the oscillating structure (see fig. 3.9(d)) positively affect device dynamics and enlarge device bandwidth [145].

A novel identified approach to widen the bandwidth of microgenerators is to exploit the nonlinear dynamics descending from certain structures. In this case, nonlinearities arise from the adoption of structures having defined shapes or exploiting the interaction of components coming from different physics fields (like mechanical structures and permanent magnets) [60].

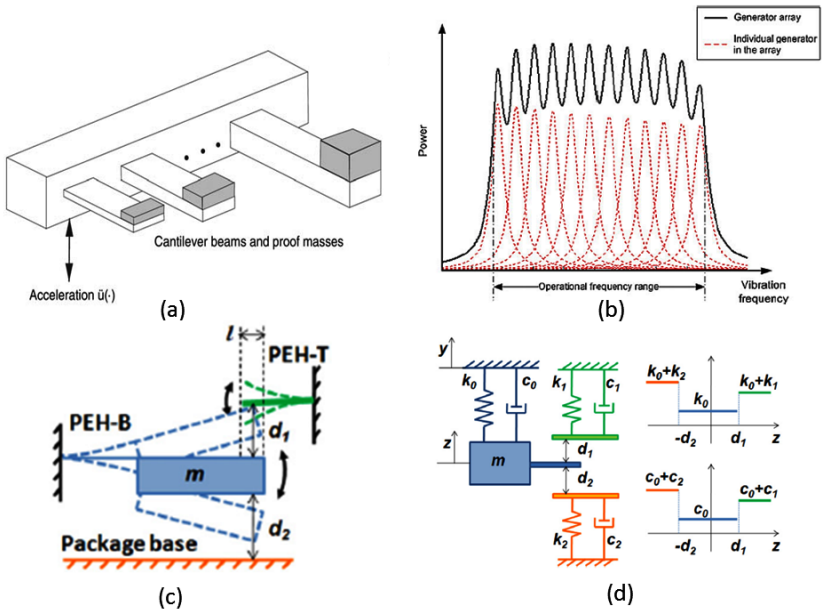

Fig. 3.9 – (a) Array of linear resonant structures [214]. (b) Frequency spectrum of the output from an array of linear resonant structures [214]. (c) Cantilever beam with amplitude limiter [145]. (d) Nonlinearities in spring stiffness and damping introduced by mechanical stoppers [145].

Nonlinear mechanical coupling structures and the benefits introduced by nonlinearities in energy harvesting will be discussed in subsection 3.1.6.

3.1.6 Nonlinear coupling structures

Nonlinear mechanical coupling structures have been proposed to overcome the limits of linear resonant structures and of tuning systems by increasing the complexity of the harvesting systems.

Several mechanisms have been explored to induce nonlinearity in a coupling mechanical structure. One strategy exploits the adoption of nonlinear elastic springs where nonlinearity is introduced by the geometrical parameters of the structure and/or by the properties of the materials used in the device [17]. Another strategy applies stresses/strains in mechanical structures to implement nonlinear behaviour, as an example in buckled beams [59]. Another approach couples mechanics with other fields (e.g., magnetics) to allow for nonlinearities [9].

In the case of mechanical nonlinearities, the second-order mass-damper-stiffness model in (3.1) modifies in (3.5) [60].

$$m\ddot{z} + c_m\dot{z} + c_e(\dot{z}, z) + k(z) = -m\ddot{y} \tag{3.5}$$

where $k(z)$ is a nonlinear function of the structure displacement z, differently from the linear case in (3.1). The term $k(z)$ represents the first derivative of a generic potential energy function $U(z)$ as in (3.6) [60], with reference to (1.4).

$$k(z) = \frac{dU(z)}{dz} \tag{3.6}$$

In the case of linear systems expressed in (3.1), the potential energy function $U(z)$ is given by the elastic potential of a linear spring $U(z) = (kz^2)/2$ [212], whose first derivative with respect the displacement z returns a linear function, while in the case of a nonlinear system it is represented by a nonlinear mathematical function whose first derivative is nonlinear. An example of nonlinear potential $U(z)$ that can be implemented in (3.6) and in (3.5), is represented by the Duffing potential in (1.5) [73], which has been widely used in the modeling of nonlinear oscillators exhibiting a nonlinear restoring force, such as the inverted pendulum [60].

Differently from linear systems that, under harmonic forcing, perform harmonic oscillations whose amplitude and phase depend on only the modes (e.g., the frequency) of the forcing

input, the behaviour of nonlinear systems is characterized, under harmonic forcing, by nonlinear nonharmonic oscillations, whose amplitude and phase depend on both the amplitude and the modes of the input forcing [101].

As an example, in the case of Duffing oscillator, the frequency response of the system in terms of amplitude A and phase ϕ can lead to different behaviours for increasing and decreasing values of the input forcing for different values of the parameter a from (1.5), as shown in fig. 3.10 [113].

In the case of nonlinear oscillating systems, resonant behaviours can be found and are known as nonlinear resonance because they are determined by both the amplitude and the frequency of the input forcing, differently from linear resonance.

The dependency of the eigenfrequency of a nonlinear oscillator on the amplitude and the nonharmoniticity of the oscillation lead to behaviours that are impossible in harmonic oscillators, namely, the foldover effect and superharmonic resonance, respectively [76].

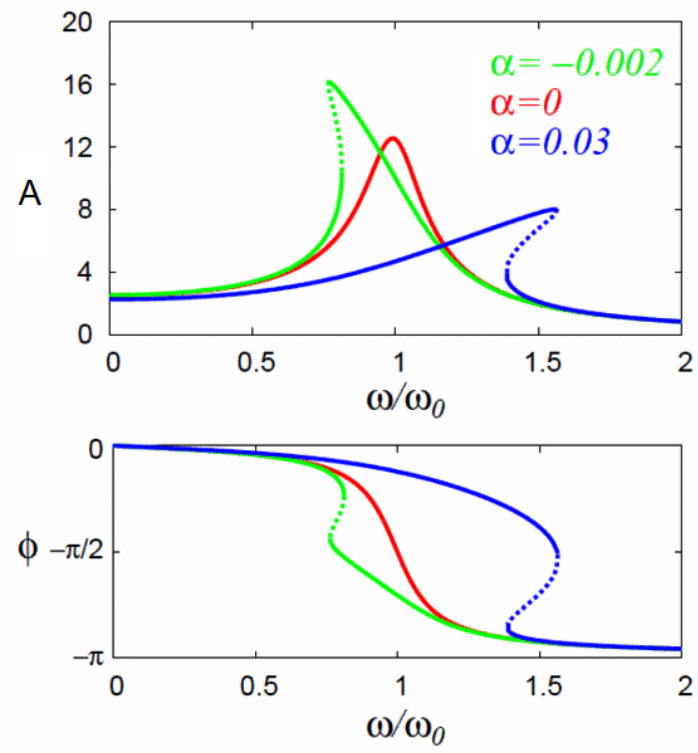

Fig. 3.10 – Example of the frequency response function for the Duffing oscillator in terms of amplitude A and phase ϕ. The solid and dotted lines correspond to the stable and unstable equilibria, respectively. When $a = 0$, the frequency response function shows a peak of the usual resonance at $\omega \approx \omega_0$, and, when $a \neq 0$, this peak is curved. For a hardening spring ($a < 0$), the peak curves to the right, and to the left for a softening spring ($a > 0$) [113].

The foldover effect gets its name from the bending of the resonance peak in a amplitude versus frequency plot. This bending is due to the frequency-amplitude relation which is typical for nonlinear oscillators. As an example, the frequency response of a sinusoidally driven inverted pendulum is shown in fig. 3.11. As long as the driving amplitude A is "small", the resonance line is very well approximated by the result for an underdamped harmonic oscillator. For a stronger driving, the resonance lines "folds", leading to bistability and hysteresis. That is, the nonlinear oscillator oscillates either with a large amplitude or a small amplitude. In the middle there is always an unstable periodic solution (shown as a dotted line). At the ends of the interval of bistability, this unstable limit cycle annihilates with one of its stable counterpart in a saddle-node bifurcation [77].

The foldover effect also occurs in superharmonic resonance.

Because nonlinear oscillators do not oscillate harmonically, their oscillation is a (infinite) sum of harmonic (i.e., sinusoidal) oscillations with frequencies which are integer multiples of the fundamental frequency (i.e the inverse of the pe-

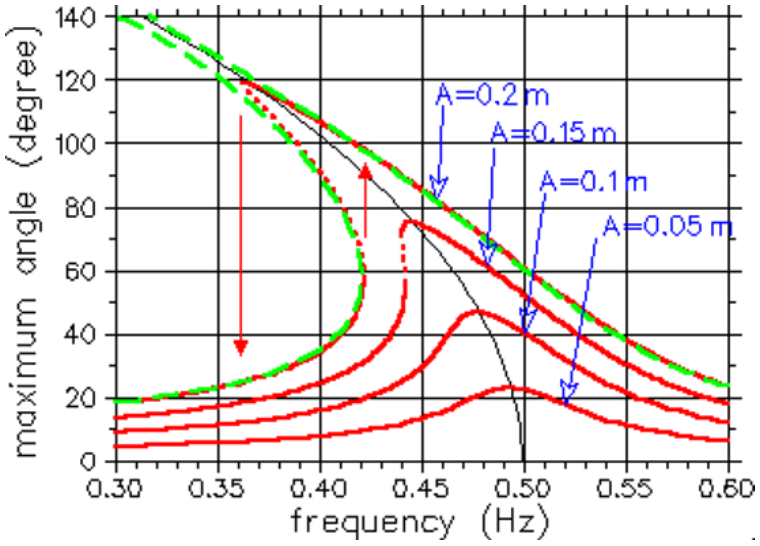

Fig. 3.11 – Example of foldover effect in the frequency response of an inverted pendulum [77].

riod of the nonlinear oscillation), according to the theorem of Fourier [36]. Superharmonic resonance is simply the resonance with one of this higher harmonics of a nonlinear oscillation. In a plot of oscillation amplitude versus driving frequency additional resonance peaks can be, therefore, expected. In general, they appear at driving frequencies which are integer fractions of the fundamental frequency. As an example, in the case of an inverted pendulum driven by a periodic force subjected

to relatively large driving amplitudes and low values of the damping constant, due to its symmetry, the nonlinear oscillation does not contain frequencies which are even multiples of the fundamental frequency and, thus, the first superharmonic resonance occurs near one third of the fundamental frequency along with the foldover effect, as shown in fig. 3.12 [228].

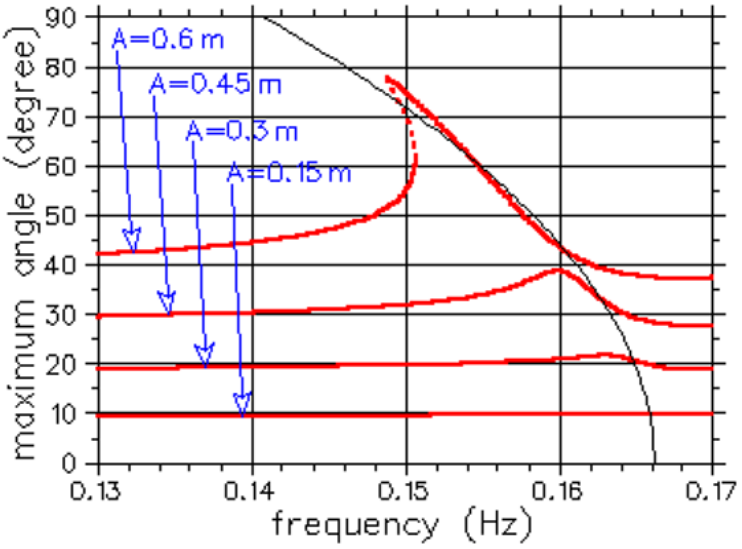

Fig. 3.12 – Example of superharmonic resonace in an inverted pendulum [228].

These effects are very important in the case of weak damping and can be exploited in the field of energy harvesting

from mechanical vibrations to enlarge the bandwidth of harvesters and improve their performance, especially when vibrations having random dynamics (e.g., environmental dynamical noise) and wide spectrum are considered as a target.

Several papers have shown the potential benefits descending from the application of a nonlinear stiffness to energy harvesters [193] through the theory of the nonlinear resonance. Different devices exploiting mechanical nonlinear springs [168, 237] have been proposed and results from their characterization exhibit a wider bandwidth (than linear resonant devices) thanks to the foldover effect and the superharmonic resonance. Examples of these devices are shown in fig. 3.13.

Bistable energy harvesters

Among nonlinear solutions for mechanical coupling structures, a special attention is deserved to strategies based on bistable oscillators (whose properties have been shown in section 1.2), which have attracted significant attention in recent years due to some of their unique features. Through snap-through actions, transitions from one stable equilibrium state to the other one in bistable systems can cause large amplitude

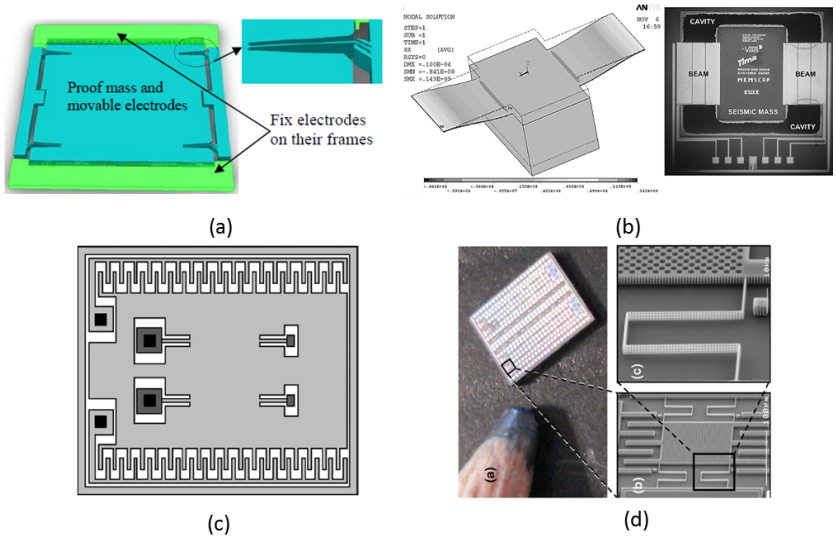

Fig. 3.13 – Example of devices adopting nonlinear springs in their mechanical coupling structure that have been proposed in literature: (a) [168], (b) [152], (c) [237] and (d) [166].

motion and dramatically increase power generation. Due to their nonlinear characteristics, such devices may be effective across a broad-frequency bandwidth. Motivations, impact, issues and benefits of the application of bistable mechanisms in energy harvesting have been discussed in section 1.3.2, a discussion about proposed bistable mechanical coupling structures in literature is presented in the following.

Bistable coupling mechanical structures proposed in the literature can be categorized into three groups in terms of the physical principle adopted to induce bistability.

The first group is composed of devices using magnetic attraction to allows for bistability in cantilevered ferromagnetic beams as shown in fig. 3.14(a). In one of these configurations, a centrally suspended magnet is attracted by two end-suspended magnets along the axis of a tube. As base excitation increases, the central magnet is attracted so as to magnetically attach to one of the end magnets; external excitation thereafter causes the release of the central magnet from one end, which allows the end magnet to ring down through the axis of a coil, thus inducing flow of current in a harvesting circuit [87].

The second group consists in devices exploiting magnetic repulsion to destabilize the linear equilibrium position. Numerous of these investigations have considered a cantilevered piezoelectric beam with magnetic tip mass, having opposed magnetization with respect to a facing fixed permanent magnet which may be moved a certain distance to the beam end

so as to tailor the strength of the bistability and "tune" the bistable potential, as illustrated in fig. 3.14(b). One feature of this configuration is that the repulsive magnets may be moved a great distance away so as to remove the nonlinearity and provide for the comparison against an equivalent linear harvester [83]. One of the drawbacks is due to the deposition of permanent magnets on the tip of the cantilever beams that is not so compatible with some MEMS technology batch processes. Because the fabrication on MEMS devices of ferromagnets placed very close one each other and having non-parallel magnetization is seriously challenging, solutions based on coupled parallel cantilevers having an equally oriented permanent magnet on each tip in order to provide repulsive forces that in turn induce antisymmetric bistable behaviours in the cantilevers have been proposed [6] and adapted to multidimensional applications [8].

The third group includes devices exploiting mechanical properties, mechanical design and/or mechanical loading to implement bistable coupling mechanical structures. Several solutions are based on compliant mechanisms exhibiting bi-

stable behaviour after a proper design of their geometrical parameters before fabrication [17, 170]. These strategies match almost perfectly MEMS batch fabrication processes but actually some issues have been investigated about their reliability. Some of these devices are biologically inspired [126]. Among mechanical solutions using mechanical loading (e.g., forces, stresses and so on), a special attention can be deserved to buckled beams where bucking is induced through the application of an axial tensile or compressive stress, as illustrated in fig. 3.14(c). Sometimes in this case mechanical-to-electrical transduction is achieved by means of piezoelectric material layers [59].

Several solutions adopting mechanical bistability to implement coupling mechanical structures will be proposed in this chapter along with their design and, where applicable, their validation.

3.1.7 Mechanical-to-electrical transduction strategies

Displacements and/or stresses and strains coming out from the mechanical coupling structures must be converted into an electrical usable form, such as voltages and currents, to power

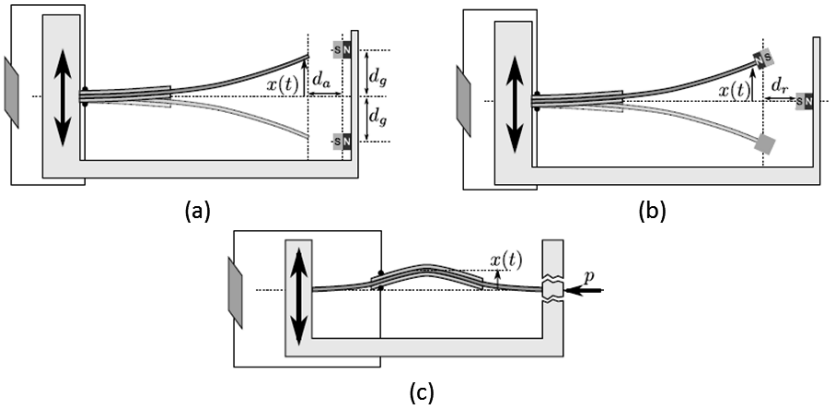

Fig. 3.14 – Strategies to implement bistability in energy harvesters [107]: (a) magnetic attraction, (b) magnetic repulsion and (c) mechanical bistability.

electronic devices through mechanical-to-electrical transducers. Transduction mechanisms based on piezoelectric, electrostatic, electromagnetic and magnetostrictive transducers are usually used in energy harvesting and will be briefly discussed in next subsections [223].

It is worth observing that several power electronic circuits are used downstream of the entire system to process and regulate the flow of energy coming from the previous steps in order to adapt it to the applications. Power converters (such as AC-DC converters with capacitive filters), voltage DC-DC regu-

lators are adopted to "shape" (e.g., rectify oscillating waveforms) the output waveforms from mechanical-to-electrical transduction mechanisms and to "adjust" the level of the electrical harvested power [163]. Their use is essential since output voltage waveforms of vibration harvesters are very similar to highly irregular AC signals or have incompatible magnitude levels, and therefore, not suitable for the power supply of electronic circuits and conventional sensors and/or the recharging of electrochemical batteries [176]. Moreover, due to the irregular and often intermittent nature of vibration sources, an energy storage recovering system (e.g. backup batteries to be recharged through energy harvesters) is often required as an energy reservoir to ensure a continuous power supplying of the downstream electronic circuits.

Piezoelectric transduction strategies

Piezoelectricity is the term used to describe the property of certain materials to generate electric charges, and therefore electric fields, after the application of a mechanical stress. This is a reversible phenomenon, therefore, piezoelectric materials undergo a deformation after the application of an electric field.

For this reason, direct and converse piezoelectric effect are defined as shown in fig. 3.15.

In the first case, the pressure applied to the piezoelectric material as a result of a mechanical deformation involves a dislocation of electrical charges of opposite sign on the opposite faces of the crystal, which, consequently behaves as a capacitor whose plates are subjected to a potential difference.

In the second case, the piezoelectric material undergoes a compression or expansion when it is subjected to a potential difference. It is worth noting that, in the direct piezoelectric effect an electrical current, called the piezoelectric current, can be pulled out when the faces of the piezoelectric crystal are properly connected to an electrical load [93].

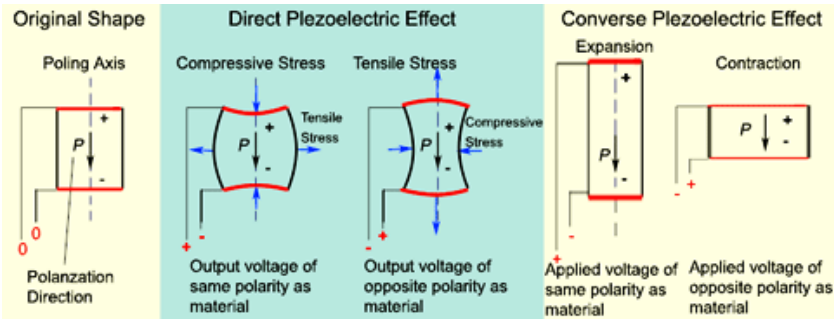

Fig. 3.15 – Direct and converse effect in piezoelectric materials.

Piezoelectric materials can have either crystalline form or amorphous form. In any case, it is essential that their structure is strongly electrically anisotropic, since, if they had a center of electrical symmetry, it would not be possible to induce any polarization from stress/strain. On the basis of the kind of polarization, it is possible to identify different subclasses of piezoelectric materials, as shown in fig. 3.16: all these classes belong to the macro-set of materials without central symmetry. A first group is given by materials whose polarization is induced by the application of a stress (such as quartz and tourmaline). Then, piezoelectric materials can be distinguished into pyroelectric, polar materials with spontaneous polarization (like Zinc Oxide and Aluminum Nitride) and that can have temporary polarization due to a change of a suitable temperature, and ferroelectric, whose polarization is reversible and is caused by the application of an electric field over a given temperature (named "Curie Temperature") in a process called "poling". Examples of ferroelectric materials are represented by Perovskites ceramics, such Lead Titanate Zirconate (PZT), Barium Titanate and Calcium Titanate [93].

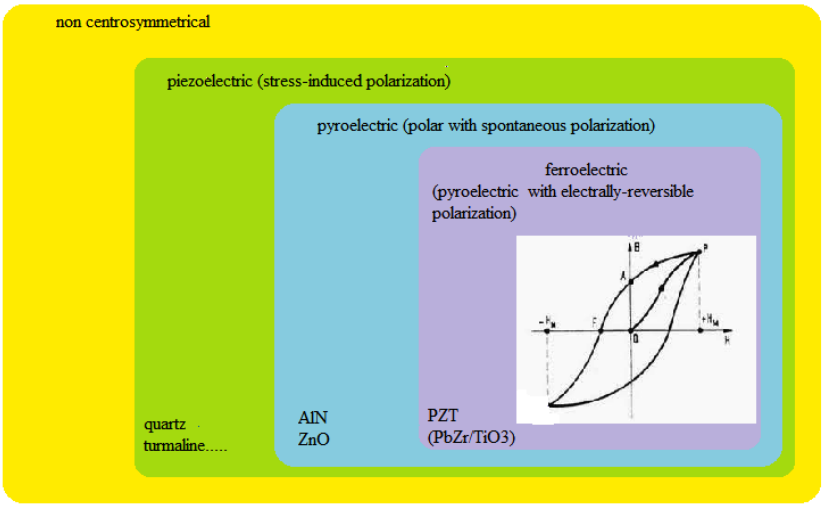

Fig. 3.16 – Classification of piezoelectric materials.

A very important aspect in the application of piezoelectric materials to energy harvesting is represented by their characteristic parameters. Among them, a special attention is deserved to the piezoelectric coupling coefficients in strain-charge form d_{ij}, measured in C/N and defined as the ratio between the charge density of short circuit in the direction i and the stress applied in the direction j (where the subscripts i and j can be equal to 1, 2 and 3, which are respectively the Cartesian axes x, y and z). Analogously piezoelectric coupling coefficients can be written also in stress-charge form e_{ij}:

in this case they are measured in C/m^2 and can be easily derived from piezoelectric coupling coefficients in strain-charge form through matrix manipulations [81]. Another important quantifying parameter in the mechanical-to-electrical conversion is the coupling factor k_{ij} representing the ratio between output electrical energy in the direction of the i and the input mechanical energy in the direction j [19].

On the basis of the piezoelectric coupling coefficients d_{ij}, two different operating modes are adopted in energy harvesters: the first one is represented by the d_{33} mode and the second one by the d_{31} mode, illustrated in fig. 3.17.

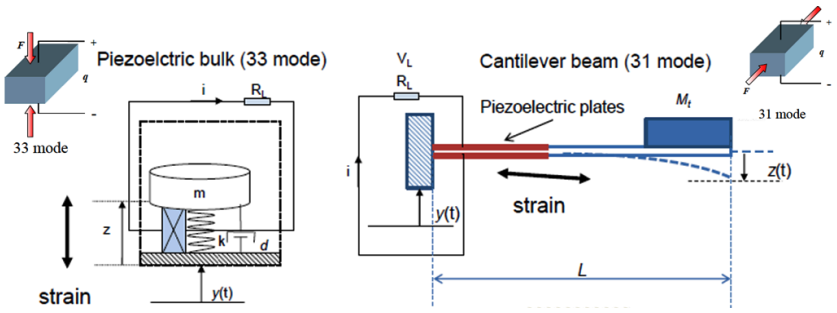

Fig. 3.17 – d_{33} mode and d_{31} mode in piezoelectric devices.

In d_{33} mode, a mechanical loading (e.g., a force or a stress) is applied in the same direction as the poling direction and a voltage/current is read in the same direction. An example of piezoelectric structure operating in the d_{33} mode is represented by a membrane, whose piezoelectric layer is poled in the direction orthogonal to the plane of the membrane; this membrane is subjected to an orthogonal (with respect to the plane of the membrane) mechanical loading and the electrical output is "acquired" through two electrodes, one on the top side of the piezoelectric layer and one on the bottom side.

In d_{31} mode, a mechanical loading (e.g., a force or a stress) is applied in the direction perpendicular to the poling axis and a voltage/current is read in the poling direction. An example of piezoelectric structure operating in the d_{31} mode is represented by a cantilever beam, whose piezoelectric layer is poled in the direction orthogonal to the plane of the beam; in this case, the beam is subjected to a loading on its free end in the orthogonal direction and the consequently axial stress, near the fixed end, generates an electrical output "acquired"

through two electrodes, one on the top side of the piezoelectric layer and one on the bottom side [203].

Because d_{31} mode typically yields a lower coupling coefficient than d_{33} mode (and so lead to a lower conversion efficiency), a geometry based on interdigitated electrodes has been developed in cantilever beams (i.e. one of the most used mechanical coupling structures in piezoelectric microgenerators), to make them work in d_{33} mode. The two electrodes configurations in cantilever beams to select the operating mode are shown in fig. 3.18 [266].

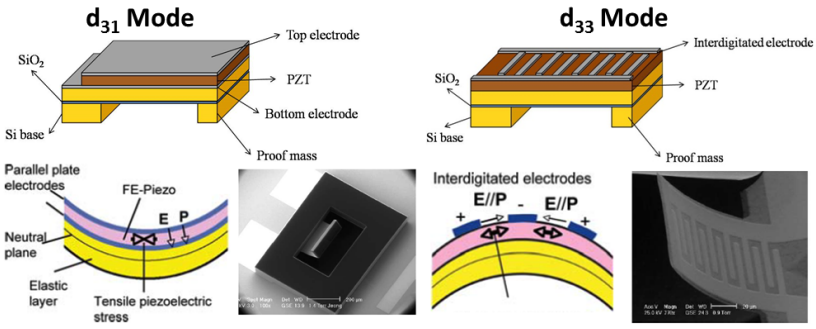

Fig. 3.18 – Electrodes configurations to exploit d_{33} mode and d_{31} mode in cantilever beams.

Many examples of piezoelectric energy harvesters based on MEMS cantilever beams operating in d_{33} mode [120, 268] and in d_{31} mode [54, 196] along some industrial microfabrication process developments for piezoelectric devices [79, 174] can be found in literature. Sometimes the sensitivity of the device to mechanical vibrations is increased by adding a proof mass to the free end of the beam [216]. Several attempts to improve the power output of piezo-MEMS cantilever beams have been studied, among them it has been proved that cantilever beams with a trapezoidal (or triangular) shape exhibit a larger axial mechanical stress (and consequently the voltage output) than beams having a rectangular shape [201]. Another improvement in the voltage output can be achieved from the implementation of bimorph piezoelectric cantilever beam at the cost of higher complexity [80].

An example of lumped parameter 1 DOF modeling of a simple piezoelectric cantilever beam operating in d_{31} mode is presented in (3.7) [81] and obtained by adding the mechanical-to-electrical piezoelectric transduction to the (3.1).

$$\begin{aligned} m\ddot{z} + c_m\dot{z} + kz - \theta V &= -m\ddot{y} \\ \dot{V} &= -\frac{\theta}{C_p}\dot{\bar{z}} - \frac{1}{R_L C_p}V \end{aligned} \tag{3.7}$$

where θ is the piezoelectric coupling term for the beam and it is defined as $\theta = -e_{31}w_p$ [81], in which w_p is the width of the piezoelectric layer in the cantilever beam. Other parameters in (3.7) are V, state variable defining the output voltage of the generator, $\dot{\bar{z}}$, the first derivative of the axial strain (i.e. the axial velocity of the strain) at the fixed end of the beam, R_L, the electrical load resistance attached to the generator and C_p, the piezoelectric capacitance, defined in (3.8) [81].

$$C_p = \frac{\epsilon_{33} w_e l_e}{t_p} \tag{3.8}$$

where ϵ_{33} is the electrical permittivity in the 33 direction of the piezoelectric material, t_p is the thickness of the piezoelectric layer and w_e and l_e are respectively width and length of the electrodes used in the piezo-stack to read the voltage difference V generated by the piezoelectric layer.

An important result from (3.7) is the dependence of the piezoelectric output voltage on the velocity in the axial strain $\dot{\bar{z}}$. This means that the power output from piezoelectric scav-

engers can be improved by both increasing strains in mechanical coupling structures and augmenting velocity in their movements. For this reason nonlinear coupling structures, especially bistable devices, leading to both larger strains and velocities than linear strictures, have been studied to be used in energy harvesters adopting piezoelectric mechanical-to-electrical transduction [107].

Other examples of piezoelectric microgenerators make use of other mechanical coupling structures such as clamped-clamped beams [102], plates [57], "cymbals" [127], "windmills" [188] and so on [205].

Piezoelectric transduction is also very promising for the implementation of nanogenerators exploiting nanostructures like arrays of nanowires and nanorods composed of piezoelectric materials (zinc oxide and lead titanate zirconate) [190, 246]. Due to the large nonlinear strains, the high density of nanostructures per volume unit and the exploitation of the benefits of other effects at nanoscale, nanogenerators can provide better performance than microgenerators in the future [260].

Advantages of the piezoelectric mechanical-to-electrical transduction in vibration energy harvesting are represented by [19]:

- high energy density;
- self-generating behaviour (i.e. they do no need an external energy source to work);
- direct conversion from mechanical input;
- possibility of microfabricating thin films of piezoelectric materials (e.g., Zinc Oxide, Lead Titanate Zirconate and Aluminum Nitride).

However, some disadvantages descend from [19]:

- poor coupling coefficient of some thin piezoelectric films;
- depolarization and ageing problems (reduced performance after long and heavy uses);
- charge leakage and high output impedance;
- operation in predefined single direction because of polarization;
- complexity and sometimes incompatibility with standard microfabrication process of piezoelectric thin film deposition techniques (requirement of high temperatures, high film stress, etc.).

Electrostatic transduction strategies

Electrostatic transducers use electrostatic forces F_{el} between charges stored on electrodes to couple energy from the mechanical domain into the electric domain. The charge separation Q on the electrodes depends on the electric potential difference V between them through the constitutive equation of a capacitance C_v in (3.9) [212].

$$Q = C_v V \tag{3.9}$$

The capacitance C_v is a function of the geometry of the electrodes and the characteristics of the materials surrounding them. For this reason, capacitance represents the coupling between mechanical and electric fields in the electrostatic transduction. As moving parts (e.g., the proof mass or shuttles) of mechanical coupling structures displace due to external vibrations, the capacitance C_v changes its value, sometimes oscillating between a maximum value C_{max} and a minimum value C_{min}. The electrical energy extracted from the mechanical motion then depends strongly on the capacitance C_v vari-

ation during time and on how the variable capacitance C_v is connected to the electronic circuitry [157].

The microfabrication of integrated variable capacitances has been standardized in the field of microsystems both through surface micromachining techniques and bulk micromachining processes [3, 131]. These capacitors has been widely used in the implementation of the capacitive readout in some sensors like accelerometers and gyroscopes and in the realization of comb drive electrostatic actuators (especially in gyroscopes) in MEMS industry [242]. Their development allows for the operation in the three cartesian axes in a single microdevice [164].

Integrated variable capacitors can be exploited in implementing energy harvesters based on electrostatic mechanical-to-electrical transduction by adding them to the mechanical oscillating structures. Depending on the direction of the motion and on the implementation of the capacitances, three kinds of integrated capacitance configurations have been identified in literature [27] and illustrated in fig. 3.19: in-plane

overlap variable capacitors, in-plane gap closing capacitors and out-of-plane gap closing capacitors.

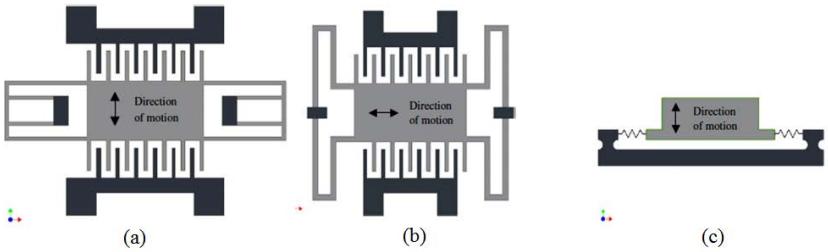

Fig. 3.19 – Configuration of integrated capacitors for electrostatic energy harvesters: (a) in-plane overlap variable capacitors, (b) in-plane gap closing capacitors and (c) out-of-plane gap closing capacitors.

An in-plane overlap variable capacitor consists in an interdigitated capacitor (i.e. comb electrodes structure) of N fingers in each electrode, whose capacitance changes by the variation of the overlap between two fingers facing each other of the structure after an in-plane displacement of the mechanical coupling structure, see fig. 3.19(a). The time variation of the capacitance $C_v(t)$ caused by a relative displacement $z(t)$ in the direction parallel to the length of the electrodes of the coupling mechanical structure is determined by (3.10) [27] .

$$C_v(t) = 2N\epsilon\frac{t[l_0 \pm z(t)]}{g} \tag{3.10}$$

where N is the number of fingers of each comb electrode, t is the thickness of the capacitance fingers, l_0 is the fabrication overlap (i.e. when $z(t) = 0$) between two fingers facing each other and g is the gap between the electrodes of the capacitance.

An in-plane gap closing capacitor consists in an interdigitated capacitor (i.e. comb electrodes structure) of N fingers in each electrode, whose capacitance changes by the variation of the gap of the electrodes of the capacitor after an in-plane displacement of the mechanical coupling structure, see fig. 3.19(b). The time variation of the capacitance $C_v(t)$ caused by a relative displacement $z(t)$ in the direction orthogonal to the length of the electrodes of the coupling mechanical structure is determined by (3.11) [27] .

$$C_v(t) = 2N\epsilon\frac{tl}{g_0 \pm z(t)} \tag{3.11}$$

Differently from (3.10), in (3.11) l is the length of the of the electrodes of the capacitance and g_0 is the fabrication gap (i.e. when $z(t) = 0$) between the electrodes of the capacitance.

It is worth noting that both in-plane configurations create two variable capacitors with the capacitances 180° out of phase.

An out-of-plane gap closing capacitor consists in a capacitor, whose capacitance changes by the variations of the the gap between the two plates of the capacitor after an out-of-plane displacement in the direction orthogonal to the plates plane, see fig. 3.19(b). The time variation of the capacitance $C_v(t)$ caused by a relative displacement $z(t)$ is determined by (3.12) [27].

$$C_v(t) = \epsilon \frac{wl}{g_0 \pm z(t)} \tag{3.12}$$

where w and l are respectively the width and the length of the electrodes.

The general 1 DOF lumped parameter model of an electrostatic harvester is derived from (3.1) and is illustrated in (3.13) [202].

$$m\ddot{z} + c_m\dot{z} + kz + d_e(z) = -m\ddot{y} \tag{3.13}$$

where $d_e(z)$ is modeled in (3.14) [202] and is the electrostatic damping representing the work done by the relative displacement z of the mechanical coupling structure against the electrostatic force due to the polarization of the variable capacitance C_v through the voltage V, see (3.9). Thus, $d_e(z)$ is the energy subtracted to the mechanical system and converted into electrical form (i.e. the output from the energy harvester) by the electrostatic mechanical-to-electrical transducer.

$$d_e(z) = \frac{\partial}{\partial z}\left[\frac{1}{2}C_v(z)V^2\right] = \frac{\partial}{\partial z}\left[\frac{1}{2}\frac{Q^2}{C_v(z)}\right] \tag{3.14}$$

The form and the value of $d_e(z)$ depends on the kind of variable capacitor C_v used and on the technique adopted in the operation of the transducer.

The most used technique in the electrostatic mechanical-to-electrical transducers for energy harvesting is represented by the "switching mode". In order to illustrate the switching mode operation, the circuit in fig. 3.20 [162], where $SW1$ and $SW2$ are two switches, C_v is the variable capacitor, C_{par} models the parasitic capacitances (neglected in this discus-

sion) and C_{stor} is the storage capacitor for the output energy, must be considered.

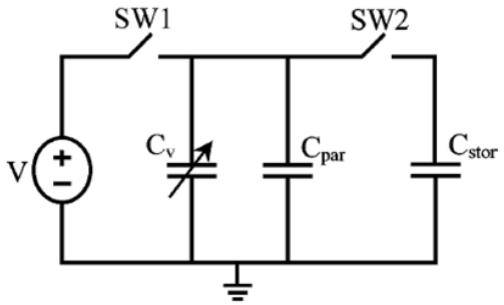

Fig. 3.20 – Circuit used in the switching mode operation of electrostatic transducer

Two different switching mode operations have been identified in literature [162]: constant voltage and constant charge, depending on the electrical quantity that is constrained in the transducer. These two operational modes consist in two different cycles, illustrated in fig. 3.21 and based on the circuit in fig. 3.20.

In constant voltage mode, the capacitor is pre-charged and then, whilst the capacitor is connected to a constant voltage V, a reduction in capacitance between the electrodes caused by relative displacement z would result in charge be-

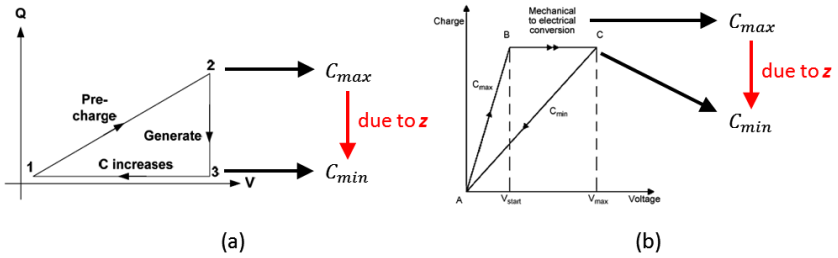

Fig. 3.21 – Switching operating modes cycles for electrostatic mechanical to electrical transducers: (a) constant voltage, (b) constant charge. In both graphs, the x-axis represents voltages and the y-axis charges.

ing removed from the capacitor and being pushed back into the voltage source, thus increasing the energy stored in that source [162]. This cycle consists in these three steps, with reference to the circuit in fig. 3.20 and the cycle schematized in fig. 3.21(a):

Pre-charge (1-2): the capacitor C_v is pre-charged to a set voltage V whilst it is at its maximum value C_{max}. $SW1$ is closed, $SW2$ is opened and $C_v = C_{max}$.

Generate (2-3): whilst the capacitance is connected to a voltage source V, C_v is reduced, forcing charge back into the voltage source. This is the generation part of the cycle. $SW1$ is closed, $SW2$ is closed and C_v goes from C_{max} to

C_{min} because of the relative displacement z of the mechanical coupling structure.

C increases (3-1): switches then disconnect C_v from the voltage source V before it is increased at constant charge (3-1) ready for the cycle to start again. $SW1$ is opened, $SW2$ is opened and C_v goes from C_{min} to C_{max}.

The area enclosed by the vertex 1, 2 and 3 in the Charge-Voltage diagram in fig. 3.21(a) represents the electrical energy E harvested in a cycle and is modeled in (3.15), where parasitic effects have been neglected.

$$E = \frac{1}{2}(C_{max} - C_{min})V^2 \tag{3.15}$$

In the constant charge mode, the variable capacitor C_v is pre-charged at maximum capacitance C_{max} and then disconnected from any external circuitry before the geometry of the capacitor is changed by the relative displacement z of the mechanical coupling structure, additional energy will be stored in the electric field between the electrodes as work has been done against the electrostatic force [162]. This cycle consists

in these three steps, with reference to the circuit in fig. 3.20 and the cycle schematized in fig. 3.21(b):

Pre-charge (A-B): the capacitor C_v is pre-charged to a low voltage V_{start} by making a connection to a voltage source. $SW1$ is closed, $SW2$ is opened and $C_v = C_{max}$.

Generate (B-C): the capacitor C_v is disconnected from the source and the load in order to be separated under constant charge during this part of the cycle. This is the generation part of the cycle. $SW1$ is opened, $SW2$ is opened, C_v goes from C_{max} to C_{min} because of the relative displacement z of the mechanical coupling structure and the voltage goes from V_{start} to V_{max}.

C discharge (C-A): The capacitor C_v is discharged to the load C_{stor} in the third part of the cycle. The capacitance is then increased ready for the cycle to restart. $SW1$ is opened, $SW2$ is closed. When $V = 0$, C_v goes from C_{min} to C_{max} due to the relative displacement z of the mechanical coupling structure.

The area enclosed by the vertex A, B and C in the Charge-Voltage diagram in fig. 3.21(b) represents the electrical energy

E harvested in a cycle and is modeled in (3.16), where parasitic effects have been neglected.

$$E = \frac{1}{2}(C_{min}{V_{max}}^2 - C_{max}{V_{start}}^2) \tag{3.16}$$

By considering (3.15) and (3.16), larger applied voltages V lead to larger energy extracted in a cycle, even if more energy must be initially supplied to polarize the capacitance C_v. Besides, larger displacements of the mechanical coupling structure result in a larger energy output.

Several devices adopting switching operating modes have been proposed in literature [112, 136], even if they exhibit many limits.

First of all, electrostatic switching transducers require the application of an external voltage to polarize the variable capacitances. Furthermore, there is the necessity of a control logic to handle the polarization and the depolarization of the capacitance C_v (i.e. the opening and the closing of the switches $SW1$ and $SW2$ in the circuit in fig. 3.20); this requires the use of electronics circuits, increasing design complexity and power requirement of electrostatic harvesters. Mechanical switches

are one of the solutions proposed in literature to help in solving the issue of the polarization and depolarization control of the capacitance C_v [52]. Another issue is given by the necessity of knowing (or sensing) the values of C_{min} and C_{max} in order to effectively control the polarization and the depolarization during the cycles. This limits, first of all, the design of the structures because mechanical stoppers must be designed in order to limits the relative displacement $z(t)$ of the mechanical coupling structure. Secondly, this restricts the range of application of these transducers because the handling of sources of mechanical vibrations having a random dynamics could be problematic for the effective control of polarization/depolarization of the capacitances; in fact, quite all the examples in literature adopt deterministic inputs in laboratory characterization, such as sinusoids [160], to model the vibrational sources.

The aforesaid limitations have been overcome by the use of variable capacitances having a fixed internal charge given by electrets [32].

Electrets are dielectric materials having a quasi-permanent electric charge or dipole polarization. An electret generates and keeps internal and external electric fields (and a surface voltage V) for years, thanks to charge trapping, and is the electrostatic equivalent of a permanent magnet. They are obtained by implanting electric charges into dielectrics. Theoretically, dielectrics do not conduct electricity; therefore, the implanted charges stay trapped inside. Many techniques exist to manufacture electrets, one of them is the corona discharge [49]. Nevertheless, dielectrics are not perfect insulators and implanted charges can move inside the material or can be compensated by other charges or environmental conditions, and finally disappear. Nowadays, many materials are known as good electrets able to keep their charges for years: for example, Teflon and Silicon Dioxide whose stability is estimated to more than 100 years [32]. Actual microfabrication technologies allow the deposition of electrets on sidewalls of comb capacitors [261].

An example of electret based harvester using a cantilever beam as mechanical coupling structure is presented in fig. 3.22 [32].

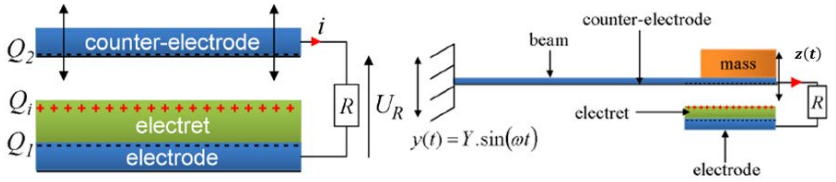

Fig. 3.22 – Electret based harvester using a cantilever beam as mechanical coupling structure [32].

The system in fig. 3.22 is composed of a counter-electrode and an electrode on which is deposited an electret, spaced by an air gap and connected by an electrical load (e.g., a resistor R in fig. 3.22). The electret has a constant charge Q_i, and, due to electrostatic induction and charges conservation, the sum of charges on the electrode and on the counter-electrode equals the charge on the electret: $Q_i = Q_1 + Q_2$. When a vibration occurs leading to a displacement z, it induces a change in the capacitor geometry (e.g. the counter-electrode moves away from the electret, changing the air gap and then the electret influence on the counter electrode) and a reorganization of charges between the electrode and the counter-electrode through the load. This induces a current across the load R and part of the mechanical energy is then turned into electricity [32].

This system can be modeled through the 1 DOF lumped parameter model, derived from (3.1) and exposed in (3.17) [32].

$$\begin{aligned} m\ddot{z} + c_m\dot{z} + kz - \frac{\partial}{\partial z}\left(\frac{Q^2}{2C_v}\right) &= -m\ddot{y} \\ \frac{\partial Q}{\partial t} &= \frac{V}{R} - \frac{Q}{RC_v} \\ C_v &= \epsilon\frac{l_E w_E}{[g_0 \pm z]} \end{aligned} \tag{3.17}$$

where Q is the charge on the electret, V surface voltage on the electret, R the resistive load, l_E the length of the capacitance plates, w_E the length of the capacitance plates and g_0 the initial gap between the capacitance plates. The electrical output is given by the current $\frac{\partial Q}{\partial t}$.

Several examples of electret based devices can be found in literature [33, 230] and a special attention is deserved to harvesters having three axes scavenging capability [158].

Electromagnetic transduction strategies

Electromagnetic mechanical-to-electrical transducers exploit the electromagnetic induction phenomenon [212]. In this case, an electro-motive force is induced across a coil if the magnetic flux coupled to the inductor changes as a function of time

and space. Typically, a magnetic field source (e.g., permanent magnet) is attached to the mechanical coupling structure and oscillates because of mechanical vibrations. If the resultant time-varying magnetic flux couples a fixed solenoid/inductor (and/or vice versa), a voltage difference is generated as output [47].

Considering the model (3.1), a general model for a harvester adopting electromagnetic mechanical-to-electrical transduction can be derived in (3.18) [189].

$$\begin{aligned} & m\ddot{z} + c_m\dot{z} + kz + D_{em}\dot{z} = -m\ddot{y} \\ & -\frac{d\Phi}{dz}\dot{z} - (R_c + R_L)i - L\frac{di}{dt} = 0 \\ & D_{em} = \frac{1}{(R_c + R_L)i + L\frac{di}{dt}}\left(\frac{d\Phi}{dz}\right)^2 \end{aligned} \tag{3.18}$$

where D_{em} is the electromagnetic damping (i.e. the energy subtracted from the mechanical system), R_c the electric resistance of the coils/solenoid, R_L the resistive load, L the inductance of the coils/solenoid, Φ the total magnetic flux linkage and i the electrical output current induced in the solenoid/coil. The output voltage is given by the product between the output current i and the load resistance R_L.

Several examples of electromagnetic MEMS generators can be found in literature [28, 75, 208].

Advantages of electromagnetic transducers are represented by [189]:

- no separate external voltage source is needed;
- no mechanical stops are requested;
- no smart materials are needed (with the exception of permanent magnets).

However disadvantages are given by [189]:

- bulky size;
- difficult to integrate with microsystems;
- difficulty in fabricating integrated coils.

A special case of electromagnetic transducers is represented by the devices exploiting magnetostrictive materials.

Magnetostriction is a property of ferromagnetic materials that causes them to change their physical shape under the influence of external magnetic fields. The inverse magnetostrictive effect (also known as Villari effect) is the name given to the change of the magnetic susceptibility of a material when

subjected to a mechanical stress. Magnetostrictive materials can convert magnetic energy into kinetic energy, or the reverse. Examples of magnetostrictive materials are: Cobalt, Terfenol-D, Galfenol and Metglas 2605SC®.

According to Villari effect, the application of a time variable stress (in this case coming from a mechanical coupling structure) to a magnetostrictive material causes a changing magnetic field that induces an electro-motive force across a coil/solenoid through magnetic induction, thus generating electrical energy [245].

3.2 Bistable MEMS devices for vibration energy harvesting in the CNM BESOI process

The development of bistable strategies for energy harvesting from mechanical vibrations represents one of the key research fields to improve the efficiency of MEMS scavengers [107].

In this section, a novel approach involving purely mechanical, fully-compliant, bistable MEMS devices in the BESOI process (see subsection 2.1.1) from the CNM of Barcelona (Spain) is proposed to improve the efficiency of vibration energy harvesters when wideband vibrations at low frequencies (e.g., the frequency spectrum below 500 Hz, where vibrations contain more energy [202]) have to be addressed.

MEMS devices resembling those considered in this section have been proposed [179] as bistable switches [35, 236]: all these mechanisms have been actuated by thermal, electrostatic forces or mechanical probes.

Differently from what has been previously proposed in literature, the bistable microstructures proposed in this section are actuated by external random mechanical vibrations, which result in forces acting on an inertial mass placed at the center of the bistable micromechanism in order to make it "snapping" from one stable equilibrium state to the other one when target vibrations are taken as input. Both the MEMS inertial mass displacements and velocities will be taken into account. In fact these quantities are both crucial in the mechanical-

to-electrical conversion step: whichever mechanism is used to produce electrical energy, a higher response in terms of displacement and velocity will result in a higher power harvested from random vibrations.

The analytical model of the microsystem will be discussed in the subsection 3.2.1. Numerical analyses and their results will be presented in the subsection 3.2.2 about the behaviour of the MEMS device. Afterwards, a realistic case study has been considered taking into account the range of accelerations that can be experienced in automotive applications and a geometrically optimized structure for these applications is proposed and compared with an "equivalent" monostable device in subsection 3.2.3. Finally, the mechanical-to-electrical transduction will be discussed in subsection 3.2.4 taking into account the electrostatic transduction principle.

3.2.1 Device modeling

The mechanical structure investigated here is composed of a central mass (CM) connected, via two short flexural pivots (LCFP and RCFP), to two slanted rigid links (LRL and RRL). These links are joined, via two short flexural pivots

(LSFP and RSFP), to two lateral fixed-fixed beams (LFB and RFB). The basic structure is shown in fig. 3.23 where all the acronyms are defined.

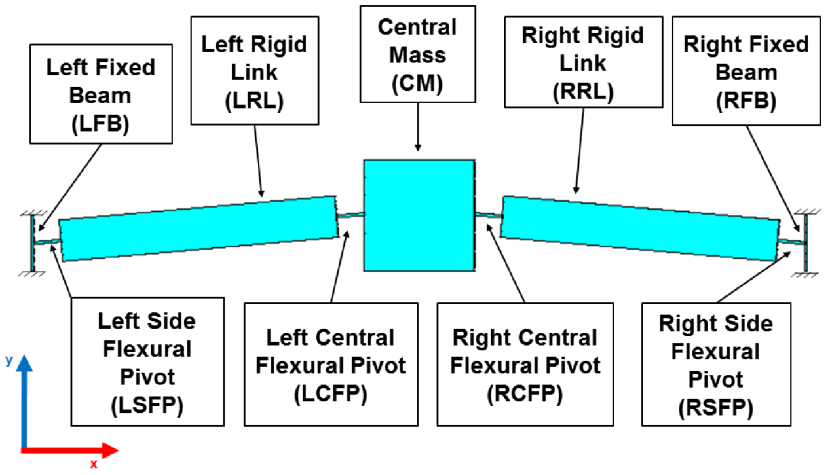

Fig. 3.23 – Two-dimensional structure of the proposed device to be realized in the BESOI process.

Flexural pivots allow for the displacements of the entire structure interconnecting, as elastic joints, rigid links (LRL and RRL) and side fixed-fixed beams (RFB and LFB), while the central mass (CM) accounts for the force applied to the structure as a consequence of external accelerations.

Three equilibrium positions can be identified: two stable, S1, i.e. the "fabrication" position, and S2, and one unstable U, as illustrated in fig. 3.24.

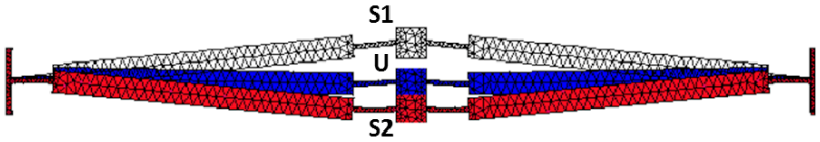

Fig. 3.24 – The initial position (S1') is shown together with the unstable (U) and the second stable equilibrium position (S2) as resulting from FEM simulations.

When a force is applied to the central mass along the y-axis, the rigid links LRL and RRL transmit the displacement to the flexural pivots LSFP and RSFP; the displacement along y-axis originated by central mass CM is converted into a motion along x-axis and a rotation thanks to the deformation of the two fixed-fixed beams LFB and RFB. Because of their elastic deformations, lateral fixed-fixed beams are charged with elastic energy when the system deviates from the initial stable equilibrium state S1; the energy stored is released

when the system exceeds the unstable equilibrium position U and converges to the other stable equilibrium position S2.

The application of the theory of the Pseudo-Rigid Body Model (PRBM) [116] leads to describe the previously qualitatively described compliant mechanism as a multibody system of rigid links and torsional and linear springs. The obtained 1 DOF (Degree of Freedom) PRBM of the device is shown in fig. 3.25.

It should be remarked that only the one dimensional behaviour is studied in this work. Forces along the x-axis are nulled by the device symmetry, while excitations along z-axis, which may eventually induce some precession, are for the moment neglected. These forces will eventually reduce the overall system performance but will not affect the significance of the presented results.

The general form of the elastic potential energy function can be expressed as in (3.19).

$$U(y_m) = \frac{1}{2}\Big(2K_1\psi_1^2(y_m)+2K_2\psi_2^2(y_m)+2K_{sb}\chi_{sb}^2(y_m)\Big) \quad (3.19)$$

with:

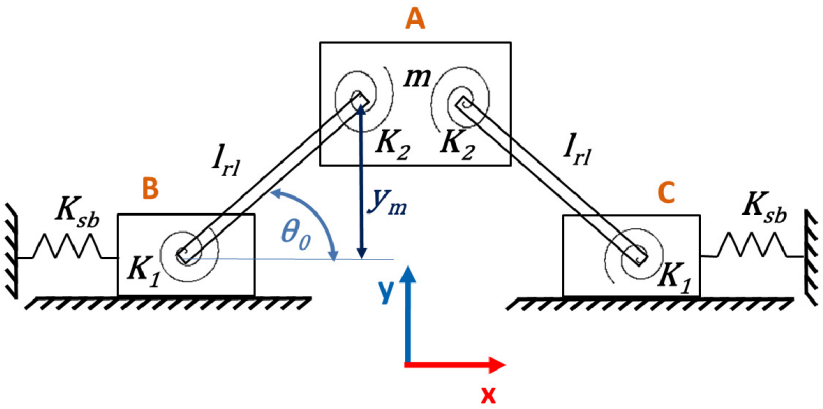

Fig. 3.25 – Pseudo-rigid body model of the microstructure. The terms K_1 and K_2 refer to (3.20), and K_{sb} to the (3.21).

$$K_i = \frac{(EI)_{l_i}}{l_i}(i = 1, 2) \tag{3.20}$$

$$K_{sb} = 192\frac{EI_{sb}}{l_{sb}^3} \tag{3.21}$$

$$\psi_1(y_m) = \arcsin\left(\frac{y_m}{l_{rl}}\right) - \theta_0 \tag{3.22}$$

$$\psi_2(y_m) = \arcsin\left(\frac{y_m}{l_{rl}}\right) - \theta_0 \tag{3.23}$$

$$\chi_{sb}(y_m) = l_{rl}\cos\left(\arcsin\left(\frac{y_m}{l_{rl}}\right)\right) - l_{rl}\cos(\theta_0) \tag{3.24}$$

where: K_i are the torsional spring constants of small-length flexural pivots (with reference, for the sake of simplicity, only

to the left side of the structure it will be: LSFP for $i = 1$ and LCFP for $i = 2$, see fig. 3.25); K_{sb} is the spring constant of side beams (see fig. 3.25); E is the Young modulus of single crystal silicon; I_i and I_{sb} are the moments of inertia of flexural pivots and side beams; l_i, l_{sb} and l_{rl} are the length of flexural pivots, side beams and rigid links, respectively; y_m is the vertical position of central mass; ψ_1 and ψ_2 are respectively the angular displacements of torsional springs K_1 and K_2 and χ_{sb} is the linear displacement of spring K_{sb}.

By taking into account definitions introduced in (3.20)–(3.24), the potential energy function in (3.19) can be rewritten in a more explicit form as in (3.25).

$$U(y_m) = (K_1 + K_2)\left[\arcsin\left(\frac{y_m}{l_{rl}}\right) - \theta_0\right]^2 + K_{sb} l_{rl}^2 \left[\sqrt{1 - \left(\frac{y_m}{l_{rl}}\right)^2} - \cos(\theta_0)\right]^2 \tag{3.25}$$

This system has been studied, both analytically and numerically, in order to assess its bistable behaviour and to optimize its performances towards an efficient energy harvesting from environmental vibrations. Considering the geometrical

dimensions of the proposed microstructure as design parameters (they are listed in table 3.4), an accurate parameter analysis has been performed in order to characterize the effects of the bistable behaviour.

An optimization has been carried out over several parameters in order to minimize the acceleration necessary to obtain the switching behaviour between the two stable equilibrium configurations and the resulting set of values is reported in table 3.4. Design rules and the mechanical material properties (see table 3.3) of the structural layer in the BESOI process described in subsection 3.2.3 have been taken into account as design constraints.

Table 3.3 – Mechanical material properties of single crystal silicon [213] in BESOI technology.

Properties	**Value**
Mass density	2330 kg/m^3
Young modulus	169 GPa
Poisson's ratio	0.3

Results of the parameter analysis are reported in table 3.4 and a scheme of the variables listed in table 3.4 is shown in fig. 3.26.

Table 3.4 – Geometric parameters of the microstructure in fig. 3.23. The microstructure is symmetric along y-axis. A basic schematic of the variables listed is shown in fig. 3.26.

Variable	Value	Description
θ_0	5.5°	Slope of rigid links and flexural pivots
l_{sfp}	200 µm	Length of side flexural pivots
l_{rl}	1500 µm	Length of rigid links
l_{cfp}	200 µm	Length of central flexural pivots
l_{sb}	150 µm	Length of side beams
w_{sfp}	10 µm	Width of side flexural pivots
w_{rl}	70 µm	Width of rigid links
w_{cfp}	10 µm	Width of central flexural pivots
w_{sb}	10 µm	Width of side beams
t	15 µm	Thickness (except the central mass)
t_{cm}	467 µm	Thickness of the central mass

The parameters values in table 3.4 have been used to evaluate the elastic potential energy function $U(y_m)$ through

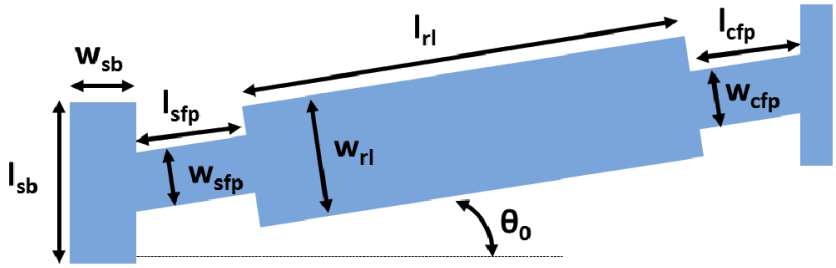

Fig. 3.26 – Basic schematic of the variables listed in the tab. 3.4 for the microstructure in fig. 3.23. The picture is not in scale.

the (3.25) for different positions of the central mass. Results of this computation are reported in fig. 3.27.

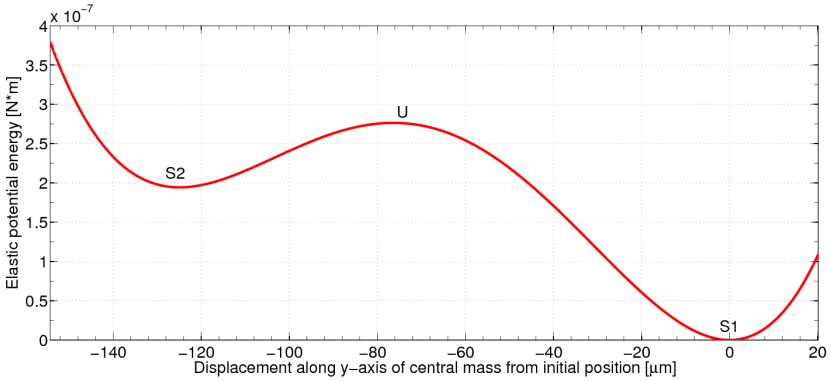

Fig. 3.27 – Elastic potential energy evaluated by PRBM with θ_0=5.5°. The stables, S1 and S2, and the unstable U equilibrium positions are marked.

The bistable potential is not symmetrical, this is due to the slope θ_0 assigned as a design parameter to the junction between the flexures and the rigid links. This means that flexural pivots are deflected in the second stable equilibrium position S2 and, consequently, the torsional springs K_1 and K_2 are not at rest and give a nonzero contribution to the elastic potential energy. As a consequence, a higher energy threshold must be overcome to switch from S1 to S2 than from S2 to S1. The asymmetrical trend in fig. 3.27 can be seen as the sum of two contributions: one, symmetrical, due to the spring K_{sb} and another, asymmetrical, generated by torsional springs K_1 and K_2.

Among all parameters, a special attention has been paid to the angle θ_0, that is the slope (referenced to the horizontal axis) of the rigid links at the intersection with the side beams. In fact, this angle is one of the fabrication parameters that strongly affects the bistable behaviour, as can be later in fig. 3.28 where several elastic potential energy functions $U(y_m)$ for different values of the angle θ_0.

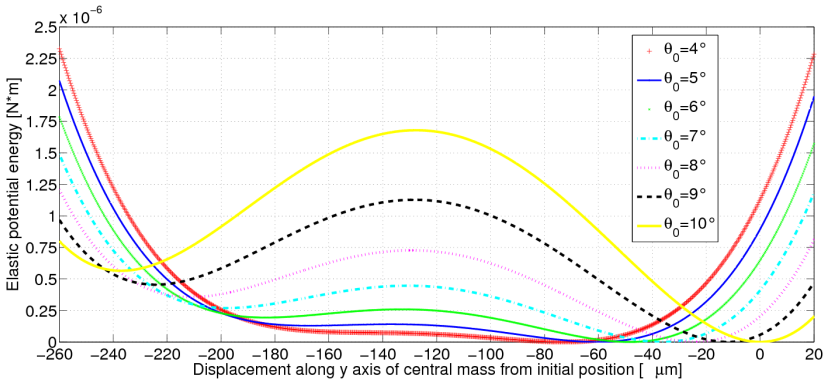

Fig. 3.28 – Elastic potential energy evaluated for different values of the parameter θ_0. For θ_0=4° and the other parameters in table 3.4, the microstructure has a monostable behaviour. Results refer to parameters different from those in the tab. 3.4.

3.2.2 Numerical analyses and results

Finite Elements Model (FEM) analyses on ANSYS® platform have been carried out in order to investigate the device bistable behaviour in static conditions and to confirm results obtained from PRBM.

The methodology adopted in these simulations consists of nonlinear static mechanical analyses: a very small displacement along y-axis is applied, step by step, to the central mass of the microstructure and the resultant reaction force along

y-axis on central mass is computed. The positions where reaction force is equal to zero are the equilibrium points, according to (1.2), and the elastic potential energy is obtained by numerical integration of reaction forces over displacements along y-axis.

Figure 3.29 shows reaction force along y-axis on central mass when its position changes, while fig. 3.30 presents results of numerical integration of reaction forces.

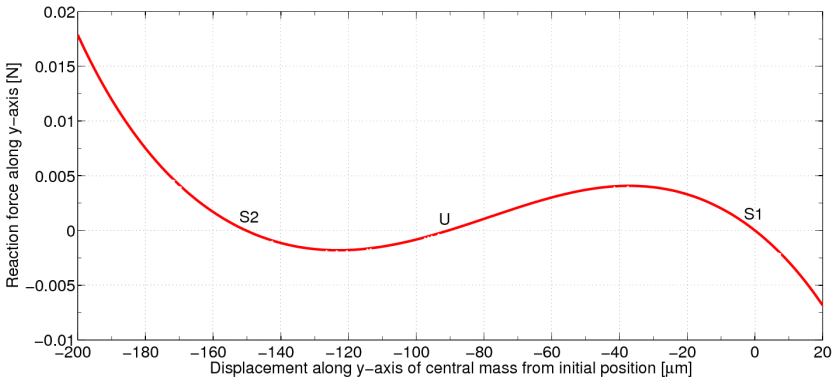

Fig. 3.29 – Reaction force on central mass after displacement numerically evaluated by FEM.

Figure 3.30 confirms the expected bistable behaviour. A small difference between the equilibrium positions evaluated

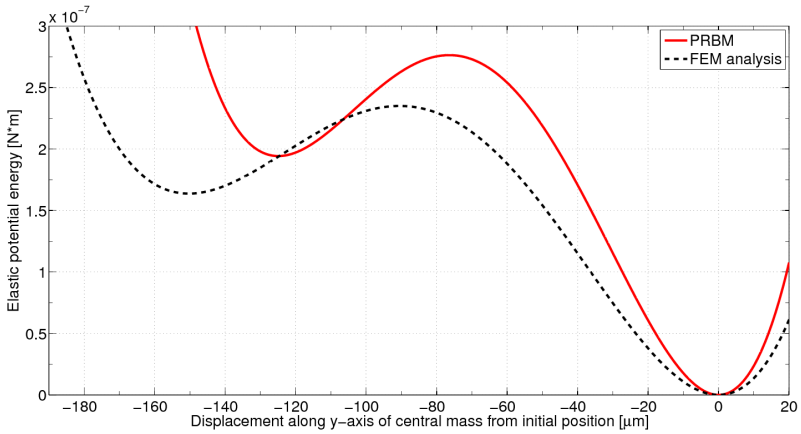

Fig. 3.30 – Elastic potential energy numerically evaluated by FEM (dashed line) compared with the potential (continuous line) obtained from PRBM (fig. 3.27).

from PRBM and from FEM is observed, this is due to the overestimation of the energy contribution of flexural joints in the PRBM [116].

The deformed structures in U and in S2 are shown in figure 3.24 together with the undeformed system in S1.

In order to investigate dynamic behaviours of the bistable microstructure in the case of random input vibrations, the corresponding stochastic differential equations (SDEs) model has been considered.

The nonlinear dynamic model is indicated in (3.26) and derived from (3.5).

$$m\ddot{y} + c\dot{y} + \Psi(y) = -ma_{ext} \tag{3.26}$$

where m is the central mass of the system, c is the mechanical damping coefficient, y is the displacement of central mass along y-axis with respect to the external frame, a_{ext} is the input acceleration applied to the external frame and $\Psi(y)$ is the nonlinear elastic term expressed by (3.27):

$$\Psi(y) = \frac{dU(y)}{dy} \tag{3.27}$$

where $U(y)$ is the elastic potential energy function, evaluated via a fourth-order polynomial fitting of the FEM results shown in fig. 3.30.

From (3.26), the two-dimensional stochastic differential equations system in Itō form [129] can be derived in (3.28):

$$\begin{cases} dy = y_v dt \\ dy_v = \frac{1}{m}\Big[- cy_v - \Psi(y)\Big]dt + \frac{\sigma}{m}dW_t \end{cases} \tag{3.28}$$

where y_v represents the velocity of the central mass, W_t represents the Wiener process, which increments by dW_t. Wiener process models the stochastic input due to external mechanical random vibrations. Finally σ represents the diffusion coefficient which set the magnitude of the stochastic input a_{ext} by (3.29) [139]. The input signal is therefore modeled as:

$$a_{ext} = \frac{\sigma}{m}\frac{dW_t}{dt} = \frac{\sigma}{m}\epsilon_t\frac{1}{\sqrt{dt}} \tag{3.29}$$

where ϵ_t is a dimensionless, random, serially uncorrelated, normally distributed variable.

The Euler-Maruyama method has been used to solve numerically the SDEs model in (3.28) by using Matlab and to evaluate the dynamic behaviour of the system [129]. Setting $\sigma = 12$ µNs$^{1/2}$, the integration time step t_s is equal to 1 µs and taking into account BESOI technology parameters, results shown in figs. 3.31–3.32 have been obtained and bistable behaviour is evident in the simulated dynamics.

In order to compare the behaviour of the device proposed with an equivalent monostable system, simulations benchmarks have been performed by considering the same struc-

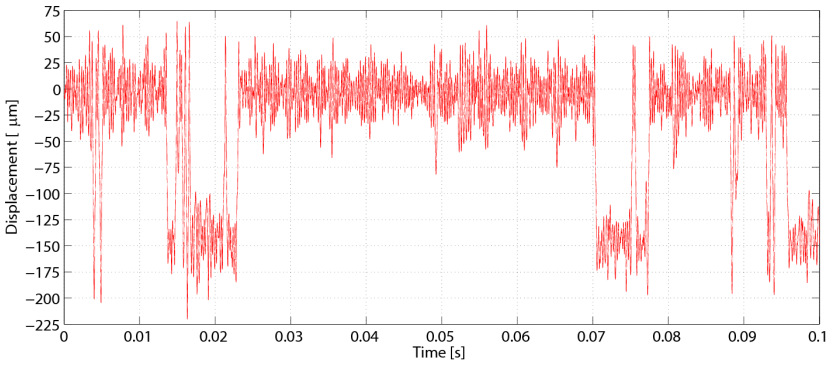

Fig. 3.31 – Time series of the central mass displacement as resulting from the numerical evaluation of SDEs model by Euler-Maruyama method.

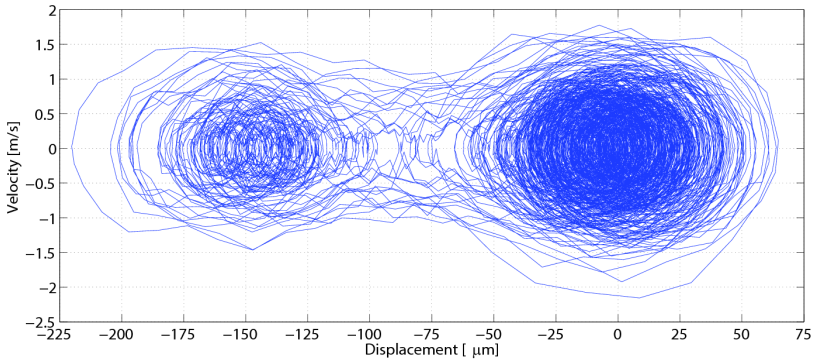

Fig. 3.32 – Trajectory map of the two system states variables (displacement and velocity) under stochastic input dW_t, as resulting from the numerical evaluation of SDEs model by Euler-Maruyama method.

ture as in tab. 3.4 but having $\theta_0 = 0°$. This device is regarded as "equivalent" because it is of the same geometrical parameters of the proposed bistable structure with the exception of the base angle θ_0 which is equal to zero in order to induce a monostable elastic behaviour. In fact it is shown in fig. 3.28 that for $\theta_0 = 0°$ the potential function is monostable, in these conditions the behaviours are similar (apart some obvious distortions) to those of a conventional linear resonant oscillator.

The same random stochastic input signal has been applied to both systems. Power Spectral Densities (PSDs) of the mass displacement are shown in fig. 3.33 for both the bistable and the monostable system.

It can be observed that bistable system exhibits both a wider spectrum and a higher gain, at low frequencies, than the monostable one which shows the peak similarly to a linear resonant device.

Therefore, when subjected to vibrations with wide spectrum at low frequencies, the bistable device is capable to scavenge a larger fraction of the incoming energy than the equivalent monostable device. This means that a larger frac-

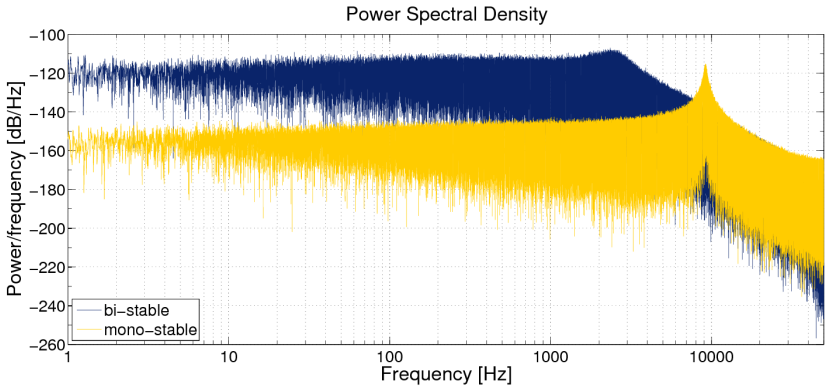

Fig. 3.33 – Comparison between power spectrum densities of central mass displacements of bistable microstructure and monostable one under the same stochastic stimulus dW_t.

tion of mechanical energy is scavenged from input vibrations and transferred to the mechanical-to-electrical transducer.

This difference will result also in a large amount of electrical energy whatever mechanical-to-electrical energy conversion strategy will be used in this energy harvester.

3.2.3 Design of the vibration MEMS energy harvester

In this subsection, the design of a bistable MEMS structure that can profitably harvest energy from low level vibrations,

whose energy is spread over a large bandwidth at low frequencies, is proposed.

Several scenarios are considered, including automotive, where vibrations appear as a noisy signal [202] with acceleration peak of about 12 m/s^2 and bandwidth of few hundreds Hertz, eventually up to about 500 Hz.

The design goal is focused on a bistable MEMS device that can show low critical forces, mechanical robustness, rejection of unwanted vibrational modes and a limited occupation of wafer area taking into account the BESOI technology parameters.

The worst case to allow switching between stable equilibrium states is represented by the critical force required to statically commutate from S1 to S2 and that can be evaluated by FEM (see, for example, fig. 3.29 in the case of the previous structure), while a more accurate estimation of the minimal forces required to obtain switching must be performed by taking into account the dynamic behaviour. The design strategy will be based on FEM simulations results to estimate the force level to be applied to the inertial mass in order to induce

switching between the two stable equilibrium states of the device; the worst case, represented by the commutation from S1 to S2, will be obviously taken into account. The dynamic behaviours will therefore be taken into account to refer these results to the external acceleration a_{ext}.

The basic bistable structure studied in the previous section has been considered as first device candidate. For this device it has been not possible to satisfy all the design goals as the minimum acceleration level required for inducing switchings was larger than the considered design goal.

A modified structure has been therefore considered where a different geometry for the flexural beam has been taken into account in order to increase the device flexibility. The fixed-fixed beams (LFB and RFB) have been replaced by a rigid part (Left Rigid Part, LRP, and Right Rigid Part, RRP) interconnecting respectively each of the original side flexural pivots (LSFP and RSFP) to two flexural pivots (Left Side Upper Flexural Pivot, LSUFP, and Left Side Lower Flexural Pivot, LSLFP, Right Side Upper Flexural Pivot, RSUFP, and Right Side Lower Flexural Pivot, RSLFP). These two addi-

tional flexural pivots are joined to two fixed-fixed beams (Left Upper Fixed Beam, LUFB, Left Lower Fixed Beam, LLFB, Right Upper Fixed Beam, RUFB, and Right Lower Fixed Beam, RLFB). Figure 3.34 illustrates the aforesaid changes on the microstructure and the nomenclature of the new components of the microstructure, for the left side.

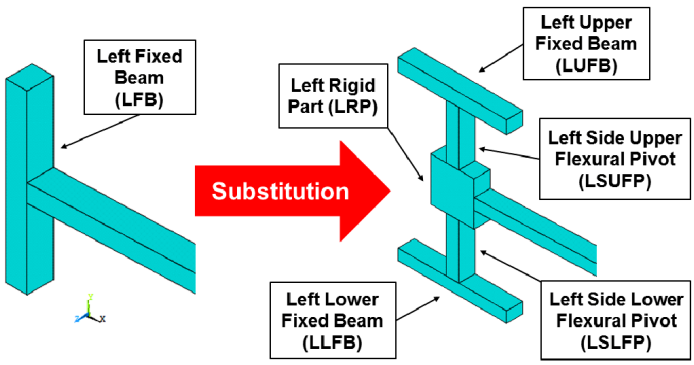

Fig. 3.34 – Basic illustration of the substitutions, only for the left side, made to the microstructure in fig. 3.23 in order to make it more flexible. Changes and nomenclature are analogous on the right side.

In order to improve the mechanical stability of the microstructure and to reduce the incidence of some unwanted vibrational modes, the number of arms holding the central

mass has been increased to four and the total thickness of the BESOI wafer (467 µm) has been exploited in the implementation of these arms. This also allows the use of larger central masses without affecting the robustness of the structure and its main vibrational mode (along y-axis). A complete picture of the new microstructure is shown in fig. 3.35.

Thanks to these substitutions, the new structure is more compliant than the previous one and its increased mechanical flexibility leads to lower values of critical forces required for commutations between stable equilibrium states.

A parameter analysis like the one shown in fig. 3.28 gives the optimum parameters in tab. 3.5 for the structure shown in fig. 3.35. A basic schematic of the variables listed in tab. 3.5 is illustrated in fig. 3.36. Switchings between the two stable states is now allowed by external vibrations with peak acceleration of 12 m/s^2. The square central mass of 1200 µm side length allows to convert the external acceleration into a force applied to the structure. The microstructure occupies an area 3.74 mm long and 1.33 mm wide.

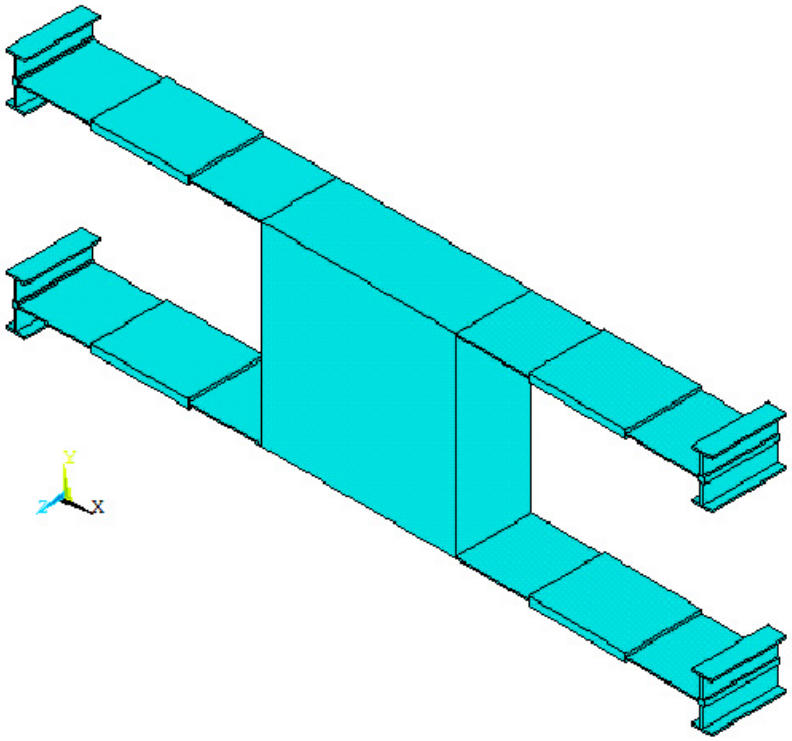

Fig. 3.35 – Three-dimensional model of the new proposed microstructure.

Results of the reaction forces against structure displacements, evaluated by FEM analysis, and the corresponding elastic potential energy are shown in fig. 3.37.

The unstable equilibrium position U is at -13.75 µm from initial position along y-axis and the second stable equilibrium

Table 3.5 – Geometric parameters of the microstructure in fig. 3.35. The microstructure is symmetric along y-axis. A basic schematic of the variables listed is shown in fig. 3.36.

Variable	Value	Description
θ_0	0.5°	Slope of rigid links and flexural pivots
l_{sfp}	450 µm	Length of side flexural pivots
l_{rl}	600 µm	Length of rigid links
l_{cfp}	450 µm	Length of central flexural pivots
l_{rp}	35 µm	Length of rigid parts
l_{sufp}	120 µm	Length of side upper flexural pivots
l_{slfp}	120 µm	Length of side lower flexural pivots
l_{ufb}	120 µm	Length of upper fixed beams
l_{lfb}	120 µm	Length of lower fixed beams
w_{sfp}	10 µm	Width of side flexural pivots
w_{rl}	60 µm	Width of rigid links
w_{cfp}	10 µm	Width of central flexural pivots
w_{rp}	35 µm	Width of rigid parts
w_{sufp}	12 µm	Width of side upper flexural pivots
w_{slfp}	12 µm	Width of side lower flexural pivots
w_{ufb}	12 µm	Width of upper fixed beams
w_{lfb}	12 µm	Width of lower fixed beams
t	467 µm	Thickness of the entire structure

position S2 is at -26.7 µm from initial position. The critical

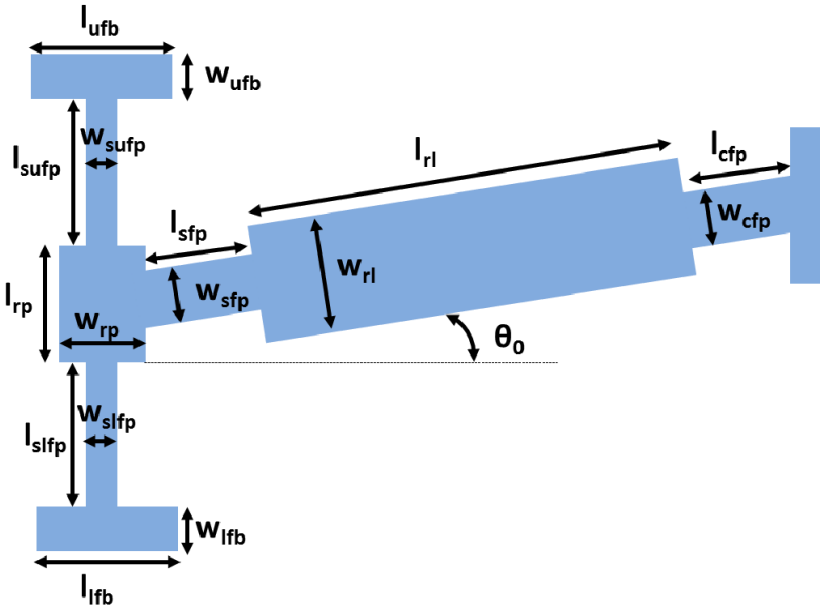

Fig. 3.36 – Basic schematic of the variables listed in the tab. 3.5 for the microstructure in fig. 3.35. The picture is not in scale.

force to switch from S1 to S2 is 29.1 µN, while the required static force to commutate from S2 to S1 is about 8.2 µN.

Several dynamic analyses, using the model in (3.28) have been performed in order to characterize the behaviour of the new structure in fig. 3.35, when the parameter values reported in tab 3.5 are adopted.

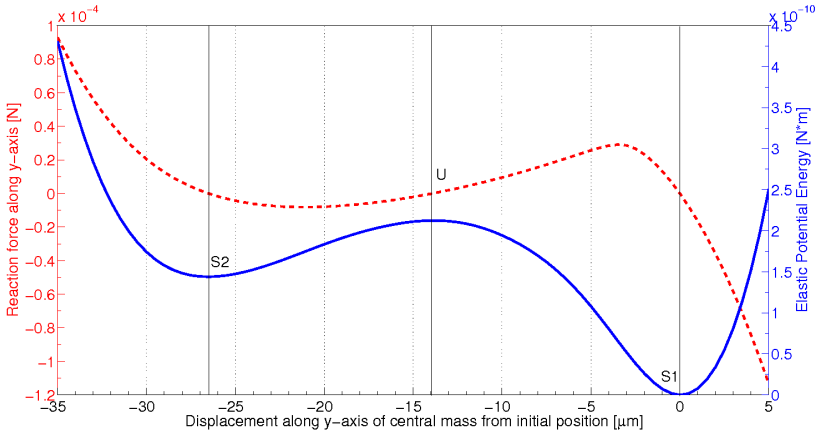

Fig. 3.37 – Reaction force (dashed line) on central mass and elastic potential energy (continuous line) evaluated by FEA for configuration on table 3.5 of the microstructure proposed in figure 3.35. Equilibrium positions are indicated.

The number of commutations between the two stable equilibrium states as a function of the RMS value of the external acceleration, considered as a stochastic signal, has been considered as quantifier of the device performance. In fig. 3.38 obtained results are shown in terms of average number of switching events, over a simulation time of 60 s, and standard deviation. The largest energy value reported in the horizontal axis corresponds to peak accelerations up to about 14 m/s^2.

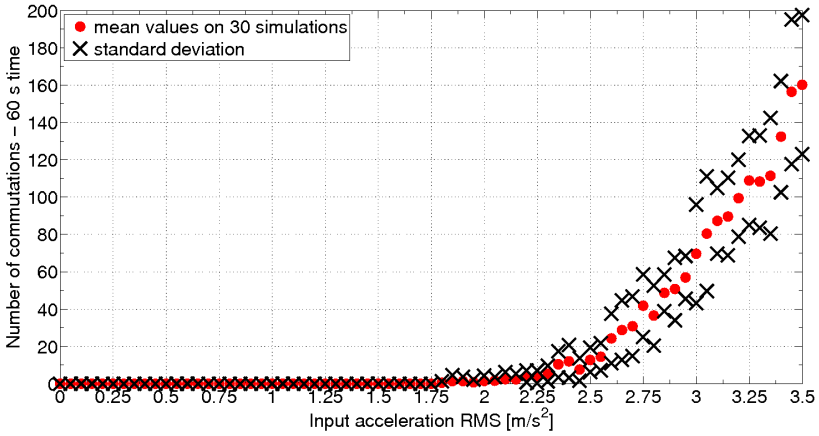

Fig. 3.38 – Results from several stochastic analyses for accelerations having different RMS values. Points represent the mean values of the number of commutations between stable equilibrium states in a time interval of 60 s and 30 simulations for each simulated value of input peak accelerations; while "x" represents the standard deviation.

A comparison between this bistable behaviour and its "equivalent" monostable is performed again by taking into account the same structure but having $\theta_0 = 0°$. The elastic potential of the equivalent monostable device is shown in fig. 3.39 in comparison with the elastic potential of the bistable microstructure.

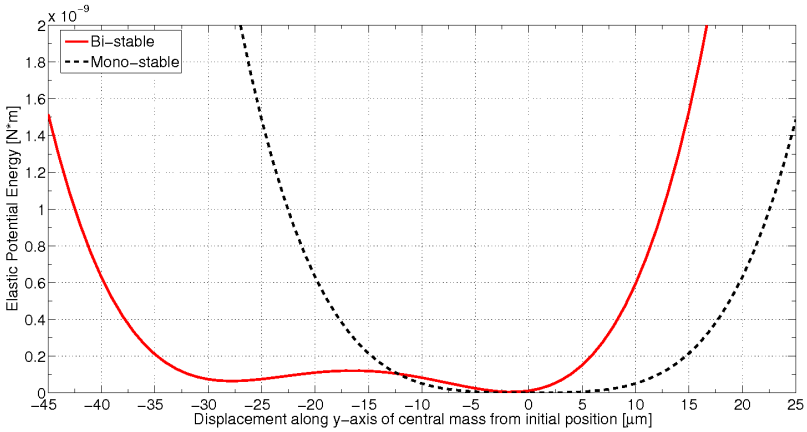

Fig. 3.39 – Elastic potential energy numerically evaluated by FEM of the monostable device (dashed line) compared with the elastic potential (continuous line) of the bistable one.

In figs. 3.40–3.41 the PSDs of central mass displacements are reported both for the bistable and for the monostable device: the case of a stochastic input acceleration smaller than the minimum value allowing for device switchings is shown in fig. 3.40; the case of input acceleration large enough to allow commutations between the two stable states of the device are shown in fig. 3.41.

The integral of the PSD of central mass displacement in the frequency range of interest (0.1 Hz–500 Hz) represents

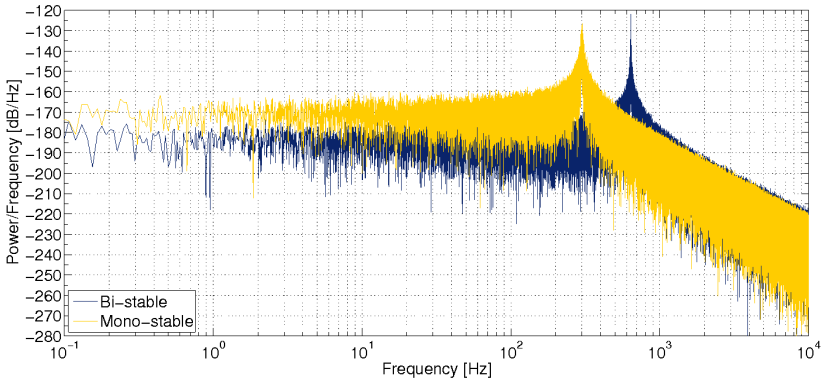

Fig. 3.40 – Simulation results: plot of PSD of central mass displacement for the bistable (blue curve) and the monostable (yellow curve) in the case of under-threshold excitation (acceleration peak value of about 4 m/s^2 when the bistable system oscillates around its first stable equilibrium state.

the mechanical energy scavenged by the microstructure from the random environmental input vibrations; the device performance is estimated as the ratio between the energy transferred to the mechanical-to-electrical conversion system and the external vibrations energy in the frequency range of interest.

A slightly better performance at low frequencies is observed in the monostable structure when the bistable one does not switch between its stable equilibrium states (fig. 3.40): this is due to a lower resonant frequency with respect the bistable

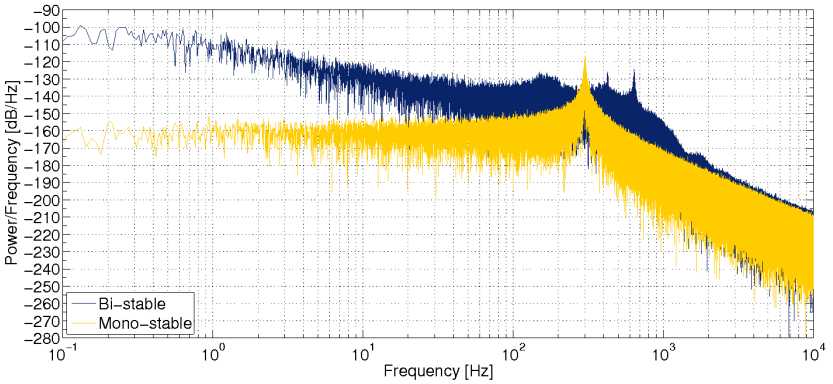

Fig. 3.41 – Simulation results: plot of PSD of central mass displacement for the bistable (blue curve) and the monostable (yellow curve) in the case of underthreshold excitation (acceleration peak value of about 13 m/s^2 when the bistable system oscillates around its first stable equilibrium state.

one. When the bistable structure begins to switch between its stable equilibrium states, its behaviour is considerably more efficient than the monostable one (fig. 3.41).

In fig. 3.42 the total energy gathered is plotted, for both the monostable and the bistable structures, as a function of the RMS value of input acceleration. The energy is evaluated as the normalized PSD integral, in the frequency range of 0.1 Hz–500 Hz of the central mass displacement. Normalization is

performed with respect to the input acceleration energy in the same frequency range.

In fig. 3.42 it is shown that the bistable device harvests more mechanical energy than the monostable one as soon as the excitation signal becomes large enough to induce switchings between the two stable equilibrium states.

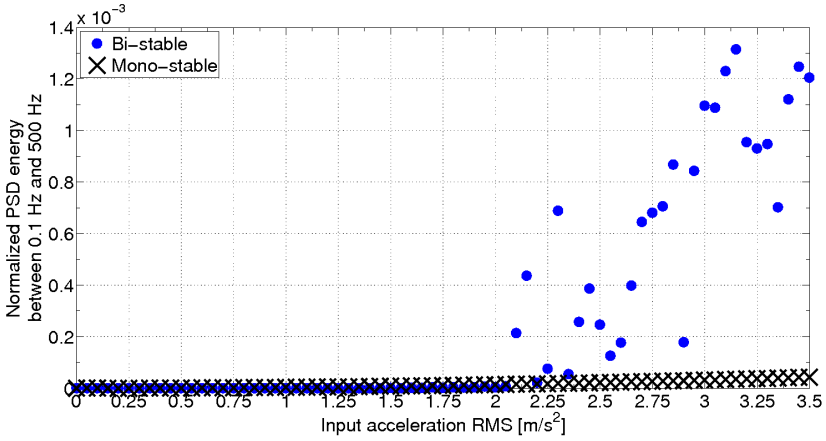

Fig. 3.42 – Energy of central mass displacements normalized with input energy from vibrations versus the RMS value of the input acceleration signal. Points represent the computed values for the bistable microstructure at each acceleration peak value, while the "x" for the monostable device.

3.2.4 Considerations on mechanical-to-electrical energy conversion

The electrostatic mechanical-to-electrical transduction strategy is considered for this device. Voltage constrained [157], in-plane overlap varying [27] interdigitated capacitors (see subsection 3.1.7) have been designed on both the upper and lower sides of the central mass in order to exploit the displacements along y-axis in the energy transduction. A three dimensional model of the device is illustrated in fig. 3.43.

The fingers of the capacitors have a total thickness of 467 µm, as all the three layers of the BESOI substrate (see fig. 2.1) have been considered. This gives higher mechanical robustness to the fingers and increases the inertial mass applied to the microstructure. However, only 15 µm in single crystal silicon are exploited for the electrical capacitors because of electrical insulation due to buried oxide layer between the single crystalline silicon and the substrate.

The two overlap varying interdigitated capacitors C_{AC} (between the stator "A" and the rotor "C" in fig. 3.43) and C_{BC}

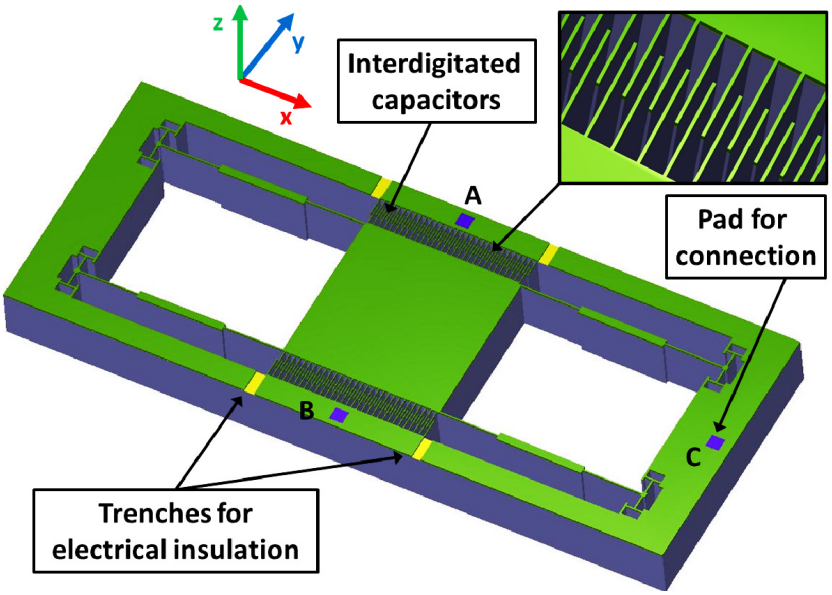

Fig. 3.43 – Three dimensional model of the device incorporating the microstructure in fig. 3.35 and the mechanical-to-electrical transduction mechanism. The letters "A", "B" and "C" indicate the pads for the electrical connection of the plates of the interdigitated capacitors.

(between the stator "B" the rotor "C" in fig. 3.43) are defined in (3.30) and in (3.31) [22], with reference to (3.10).

$$C_{AC}(y) = 2\frac{N_f \epsilon_0 t_f \left(l_{f0} - y\right)}{g} \tag{3.30}$$

$$C_{BC}(y) = 2\frac{N_f \epsilon_0 t_f \left(l_{f0} + y\right)}{g} \tag{3.31}$$

where N_f is the number of fingers (on the rotor side of the capacitor), ϵ_0 is the electrical permittivity of air, t_f is the thickness of the electrical layer in the capacitor, g is the air gap, l_{f0} is the length of the overlap between two fingers facing each other and y is the displacement of the central mass along the y-axis from its initial position.

Taking into account the applied mechanical-to-electrical conversion system(see subsection 3.1.7), the model in (3.26)) modifies [202] in (3.32), according to (3.13).

$$m\ddot{y} + c^*\dot{y} + b_e(y) + \Psi(y) = -ma_{ext} \tag{3.32}$$

The parameter c^* in (3.32) represents the mechanical damping caused predominantly by the slide film effect in the interdigitated capacitors and is stated by (3.33) [53].

$$c^* = 4\frac{N_f \eta t_f l_{f0}}{g} \tag{3.33}$$

where η is the dynamic viscosity of air (η = 18 µPa·s).

The term b_e is the electrical damping that models the effect of the electrical polarization of the two interdigitated capaci-

tors $C_{AC}(y)$ and $C_{BC}(y)$ on the mass movement and is defined by (3.34) [202], according to (3.14).

$$b_e(y) = \frac{\epsilon_0 N_f t_f}{g} {V_{AC}}^2 - \frac{\epsilon_0 N_f t_f}{g} {V_{BC}}^2 \tag{3.34}$$

where the terms V_{AC} and V_{BC} are respectively the polarization voltages of the capacitors C_{AC} and C_{BC}. The signs in (3.14) indicate the directions of the damping forces from the two capacitors (when each of them is polarized) that are opposite to the direction of the motion of the central mass. According to (3.30)–(3.31) and considering the bistable dynamic operation of the proposed device, if any overshoots in the displacement of the central mass are neglected, the capacitance C_{AC} presents its maximum value in S1 while C_{BC} its minimum; analogously, in S2, C_{AC} is at its minimum while C_{BC} at its maximum.

On the basis of the operating cycle of voltage constrained electrostatic mechanical-to-electrical transduction systems [162], the voltage V_{AC} is equal to the applied voltage V_{in} only when the central mass goes from S1 to S2 and in the other cases V_{AC} is equal to 0 V, while V_{BC} is equal to V_{in} when the cen-

tral mass comes from S2 to S1 and in the other cases V_{BC} is equal to 0 V. The energy harvested respectively by the capacitor C_{AC} in each cycle of commutation from S1 to S2 and by the capacitor C_{BC} in each cycle of commutation from S2 to S1 are expressed by E_{AC} and E_{BC} in (3.35) and (3.36) [157], according to (3.15).

$$E_{AC} = \frac{1}{2}\big(C_{AC}(S1) - C_{AC}(S2)\big){V_{in}}^2 \tag{3.35}$$

$$E_{BC} = \frac{1}{2}\big(C_{BC}(S2) - C_{BC}(S1)\big){V_{in}}^2 \tag{3.36}$$

If a time series of length ts is observed, an estimation of the power harvested P by the whole system during the observation time ts can be done by counting the number of commutations from S1 to S2, N_{12}, and from S2 to S1, N_{21}, and taking into account (3.35)–(3.36) in (3.37) [157].

$$P = \frac{N_{12}}{ts}E_{AC} + \frac{N_{21}}{ts}E_{BC} \tag{3.37}$$

The computed values of the parameters of the interdigitated fingers for the mechanical-to-electrical energy conversion are listed in the tab. 3.6. The choice of these values is

motivated by the need to ensure an adequate extraction of energy without affecting the robustness of the fingers and taking into account the movements of the structure between the two stable equilibrium states.

Table 3.6 – Parameters of the adopted mechanical-to-electrical transduction mechanism for the device in fig. 3.43. Values are equal for both the capacitances C_{AC} and C_{BC}.

Variable	Value	Description
N_f	29	Number of fingers on rotor
l_f	150 µm	Total length of each finger
l_{f0}	75 µm	Initial overlap length between two fingers
t	467 µm	Mechanical thickness of each finger
t_f	15 µm	Thickness of the conductive layer
w_f	5 µm	Width of each finger
g	15 µm	Air gap between two fingers

A possible solution to increase the energy harvested in each cycle of commutation E_{AC} and E_{BC} in (3.35)–(3.36) is to increase the difference in the maximum and minimum values of the capacitances C_{AC} and C_{BC}. This can be achieved by exploiting also the thickness of the silicon substrate in the in-

terdigitated capacitors through an adaptation of the BESOI technology process (see fig. 2.1). The modification consists in the creation of an electrical connection between the single crystal silicon layer and the silicon substrate through a pattern of the buried oxide and a selective deposition of metal (probably aluminium). The creation of suitable trenches in the silicon substrate, from the bottom, and in the single crystal silicon, from the top, ensures the separation of the areas at different electric potential, with also the help of the buried oxide layer. This concept is illustrated in fig. 3.44.

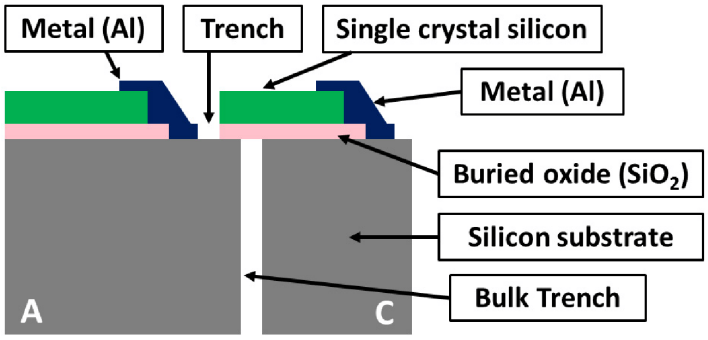

Fig. 3.44 – Basic conceptual schematic of the proposed modifications in the BESOI technology. "A"and "C" represent areas at different electric potential. The picture is not in scale.

Thanks to this eventual modification in the technology process, the thickness of the conductive layer on each finger t_f comes from 15 µm to 465 µm (see fig. 2.1). This increases the values of the two capacitances C_{AC} and C_{BC} from (3.30)–(3.31), the difference between their maximum and minimum values and, from (3.35)–(3.36), the amount of the electrical harvested energy.

In order to estimate the power harvested by the whole system from (3.37) as a benchmark of the proposed concept, the same microstructures studied in subsection 3.2.2 (the bistable microstructure and its "equivalent" monostable one) with the same mechanical-to-electrical transducers have been compared in simulations for several accelerations having different associated energy, random dynamics and a spectrum wide about 500 Hz [202]. This range of low frequency vibrations is the most critical to be explored in order to exploit the benefits of the proposed bistable device with respect to linear or monostable systems. Models in (3.32)–(3.37) have been taken into account and parasitic effects are neglected.

As the displacements of the central mass in the monostable structure do not always have the same amplitude (neglecting any overshoots) when the device is forced by noisy vibrations, there are no fixed maximum and minimum values for the capacitances C_{AC} and C_{BC} in the system dynamics, differently from the bistable device. In order to adopt the models in (3.32)–(3.37) and the same strategies of the bistable device in the polarization of the capacitances C_{AC} and C_{BC}, two values of displacements t_l to t_h have been imposed as thresholds to control the polarization and the depolarization of the transduction capacitors (in the same way of the positions S1 and S2 in bistable device). So, in the monostable case, C_{AC} is polarized by V_{in} when the central mass comes from the higher threshold t_h to the lower threshold t_l, analogously C_{BC} is polarized when the system goes from t_l to t_h. Three different pairs of thresholds have been analyzed in the comparisons with the bistable device: t_h =1 5 µm and t_l = -5 µm, t_h = 10 µm and t_l = -10 µm and, finally, t_h = 13.35 µm and t_l = -13.35 µm. The last pair (t_h = 13.35 µm and t_l = -

13.35 µm) presents the same length of displacements between the two equilibrium stable states of the bistable device.

Results are presented as the mean values over 30 time series of 100 s each of the power harvested evaluated through (3.37) for different RMS input accelerations. Figure 3.45 summarizes the results for $V_{in} = 30$ V.

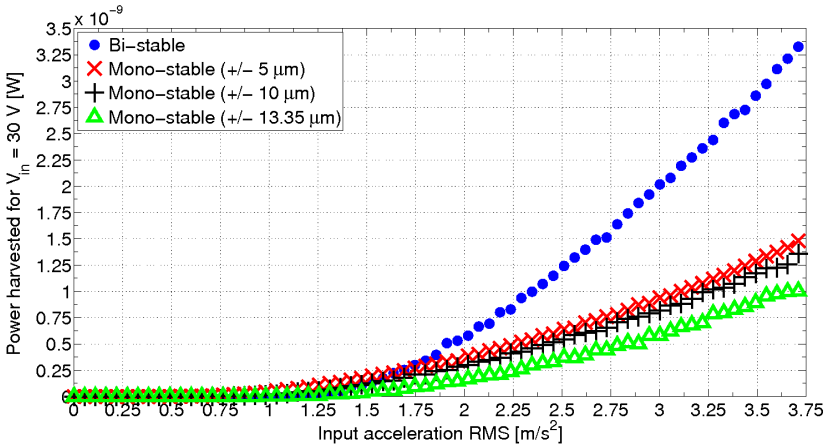

Fig. 3.45 – Power harvested at several RMS value of input acceleration for the bistable device and its "equivalent" monostable one. A polarization voltage of 30 V and the parameters for the transduction mechanism in the tab. 3.6, with $t_f = 465$ µm, are considered.

Results in fig. 3.45 confirm the improvement in performance of the bistable device over the monostable one as soon as the input acceleration is able to put it in commutation between its two stable equilibrium states.

3.3 Bistable MEMS devices for vibration energy harvesting in the STMicroelectronics ThELMA® process

The same methodology followed in the section 3.2 for designing a bistable MEMS harvester exploiting electrostatic transduction has been adopted in this section to design a MEMS device for vibration energy harvesting in the STMicroelectronics ThELMA® process.

As discussed in the subsection 2.1.4, ThELMA® technology is a surface micromachining process that ensures smaller structural dimensions than bulk micromachining processes, such as BESOI process. Differences in device sizes and performances will be evidenced in the following subsections.

3.3.1 The mechanical microstructure

In order to reduce the overall dimensions of the structure and its wafer occupancy, although the shape of flexural beams is the same as the ones of the BESOI device in subsection 3.2.3, the position of the four flexural beams holding the central mass has been changed (with respect to the BESOI device in subsection 3.2.3) to get a more compact microstructure.

An image of the concept of the studied structure is illustrated in fig. 3.46 and the geometry of the flexural beams is reported in fig. 3.47.

The 22 µm thick epitaxial polysilicon layer has been exploited for the device structure.

3.3.2 FEM analyses of the microstructure

The proposed microstructure has been simulated through FEM analyses on ANSYS® platform by adopting the same methodology applied to the structure in subsection 3.2.2. The aim is to properly design structure geometrical parameters in order to achieve bistable behaviour with a proper poten-

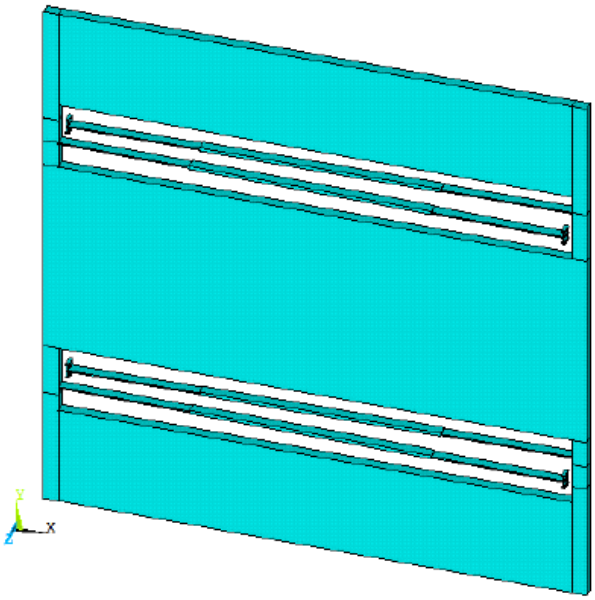

Fig. 3.46 – 3D model of the proposed mechanical structure in the STMicroelectronics ThELMA® process.

tial energy barrier for scenarios where vibrations appear as a noisy signal [202] with acceleration peak of about 12 m/s^2 (typical of automotive applications [202]) and bandwidth of few hundreds of Hertz, eventually up to about 500 Hz (the same target as in the subsection 3.2.3).

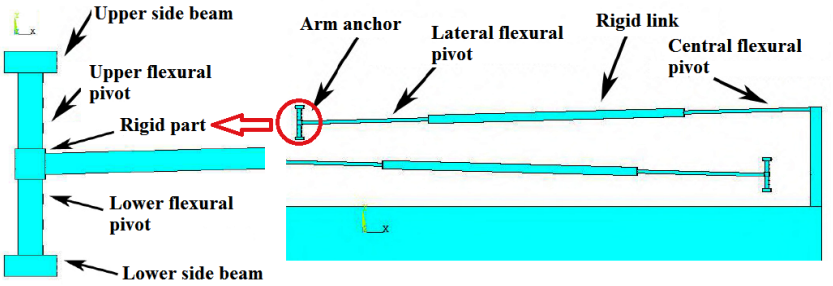

Fig. 3.47 – Flexural beams of the proposed mechanical structure in the STMicroelectronics ThELMA® process. Their shape is the same as the one of the device in the BESOI process in subsection 3.2.3 but their positioning within the structure changes.

Design constraints are represented by ThELMA® process design rules [225], epitaxial polysilicon thickness (22 µm) and by epitaxial polysilicon properties in the tab. 3.7 [225].

Table 3.7 – Material properties of the epitaxial polysilicon in ThELMA® process used in the FEM simulations [225].

Property	**Value**
Young modulus	160 GPa
Poisson's ratio	0.22
Mass density	2230 kg/m^3

Several geometric configurations have been simulated to adapt the mechanical coupling structure to the vibrational source. One of the geometrical configurations resulting in a suitable potential barrier for the aforesaid applications is reported in the tab. 3.8.

Results of the static FEM analysis of the microstructure with the geometrical configuration in tab. 3.8 are displayed in figs. 3.48–3.49: reaction forces along y-axis of the device mass for different positions along y-axis are reported in fig. 3.48 and the elastic potential energy obtained after numerical integration of the reaction forces plotted in fig. 3.48 is shown in fig. 3.49.

Among different geometrical parameters of the device, a special attention has been deserved to the angle θ_0, the slope of rigid links and flexural pivots in the fabrication position of the microstructure. The trend of the elastic potential energy resulting from FEM simulations for different values of the angle θ_0, maintaining the other geometrical parameters equals to those in tab. 3.8, is reported in fig. 3.50.

Table 3.8 – Geometric parameters of the microstructure in fig. 3.46. The microstructure is symmetric along y-axis. A basic schematic of the variables listed is shown in fig. 3.36.

Variable	Value	Description
θ_0	1.5°	Slope of rigid links and flexural pivots
l_{sfp}	110 µm	Length of side flexural pivots
l_{rl}	220 µm	Length of rigid links
l_{cfp}	110 µm	Length of central flexural pivots
l_{rp}	7 µm	Length of rigid parts
l_{sufp}	150 µm	Length of side upper flexural pivots
l_{slfp}	150 µm	Length of side lower flexural pivots
l_{ufb}	150 µm	Length of upper fixed beams
l_{lfb}	150 µm	Length of lower fixed beams
w_{sfp}	10 µm	Width of side flexural pivots
w_{rl}	7 µm	Width of rigid links
w_{cfp}	2.8 µm	Width of central flexural pivots
w_{rp}	7 µm	Width of rigid parts
w_{sufp}	4 µm	Width of side upper flexural pivots
w_{slfp}	4 µm	Width of side lower flexural pivots
w_{ufb}	4 µm	Width of upper fixed beams
w_{lfb}	4 µm	Width of lower fixed beams
t	22 µm	Thickness of the entire structure
l_m	1100 µm	Length of the device mass
w_m	500 µm	Width of the device mass

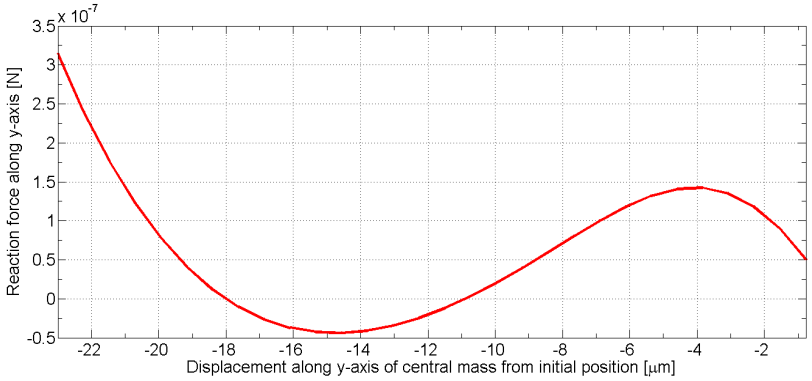

Fig. 3.48 – Reaction forces along y-axis versus device mass displacement along y-axis as resulting from FEM simulations.

3.3.3 Considerations on mechanical-to-electrical transduction

In order to estimate the power harvested by the microstructure designed in subsection 3.3.2 and having the geometrical parameters listed in tab. 3.8, voltage constrained [157], in-plane overlap varying [27] interdigitated capacitors (see subsection 3.1.7) have been designed on both the upper and lower sides of the central mass, in the epitaxial polysilicon layer, with the aim of exploiting device displacements along y-axis for the energy transduction.

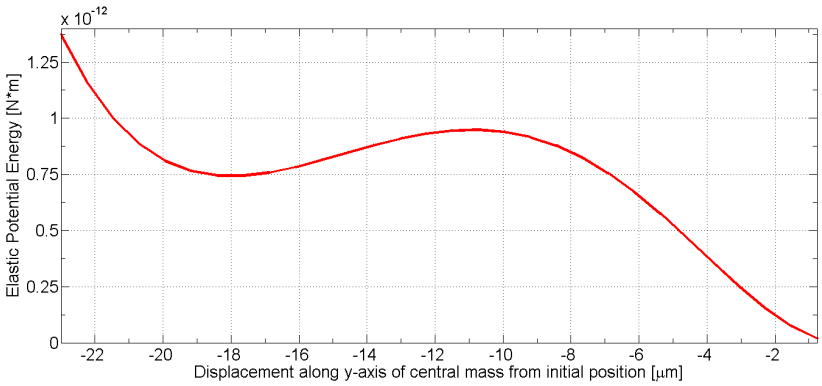

Fig. 3.49 – Elastic potential energy numerically evaluated through numerical integration of FEM analyses results in fig. 3.48.

Due to the characteristics of the ThELMA® process, other capacitor configurations (such as in-plane gap closing capacitors, for example) can be studied and added to the device in order to exploit device displacements along different axes in the energy conversion an, consequently, to increase the amount of energy scavenged, but for the sake of brevity and for the aim of this work only in-plane overlap varying interdigitated capacitors will be treated here.

A three dimensional model of the upper side of the device is illustrated in fig. 3.51.

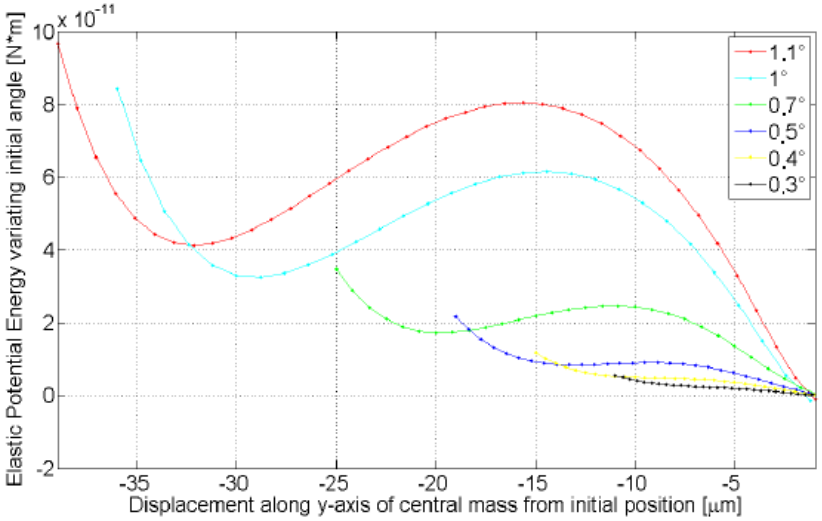

Fig. 3.50 – Elastic potential energy numerically evaluated from FEM analyses for different values of the angle θ_0.

The model expressed by equations in (3.30)–(3.37) and discussed in subsection 3.2.4 has been used to estimate the power harvested by the device when accelerations having different associated energy, random dynamics and a spectrum wide about 500 Hz [202] are considered as input.

Several geometric configurations of the interdigitated capacitors have been considered, results presented in this work refer to the geometrical configuration in tab. 3.9 and to three

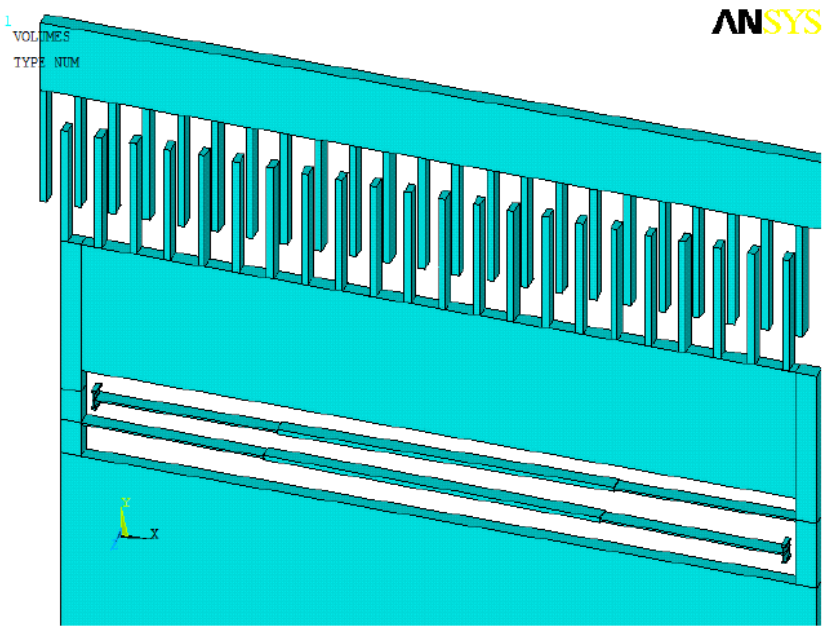

Fig. 3.51 – Comb electrodes designed on the microstructure in fig. 3.46.

different values of air-gap g between two fingers facing each other (1.1 µm, 2 µm and 3 µm).

Because the air-gap between two finger facing each other changes in the three studied configurations (1.1 µm, 2 µm and 3 µm) and the length of the device mass is fixed to 1100 µm (see tab. 3.8), a different number of fingers N_f will result. So, an

Table 3.9 – Parameters of the adopted mechanical-to-electrical transduction mechanism for the device in fig. 3.51.

Variable	Value	Description
l_f	40 µm	Total length of each finger
l_{f0}	15 µm	Initial overlap length between two fingers
t	22 µm	Mechanical thickness of each finger
w_f	2.7 µm	Width of each finger

air-gap of 1.1 µm leads to 141 fingers, 2 µm to 114 and 3 µm to 94.

The different air-gap and the different number of fingers affect the mechanical damping c^*, according to (3.33), and the amount of the capacitance variation, see (3.30)–(3.31).

The mean electrical power harvested by the system and the mean number of commutations between stable equilibrium states (over 30 simulations) have been evaluated for several values of the polarization voltage V_{in}, for the three studied configurations and for an input acceleration a_{ext} having an RMS value of 7 m/s^2 and a bandwidth of 500 Hz. Results are reported in tab. 3.10 when the air-gap is 1.1 µm, in tab. 3.11

when the air-gap is 2 µm and in tab. 3.12 when the air-gap is 3 µm.

Table 3.10 – Mean electrical power harvested by the system and mean number of commutations between stable equilibrium states (over 30 simulations) for several values of the polarization voltage V_{in}, when an air-gap of 1.1 µm and an input acceleration a_{ext} having an RMS value of 7 m/s^2 and a bandwidth of 500 Hz are applied to the system.

Voltage	**Mean power harvested**	**Mean number of commutations**
1 V	64 pW	932
2 V	242 pW	867
3 V	446 pW	712
4 V	580 pW	519
5 V	600 pW	344
6 V	522 pW	208
7 V	483 pW	114

In order to show the improvement due to bistability in the amount of harvested power, the power scavenged by the designed bistable device (with capacitor fingers having an air-gap of 3 µm) has been compared with its "equivalent" monostable (i.e. the device having the same geometrical parameters as the bistable one except for the angle θ, which is equal to

Table 3.11 – Mean electrical power harvested by the system and mean number of commutations between stable equilibrium states (over 30 simulations) for several values of the polarization voltage V_{in}, when an air-gap of 2 µm and an input acceleration a_{ext} having an RMS value of 7 m/s^2 and a bandwidth of 500 Hz are applied to the system.

Voltage	Mean power harvested	Mean number of commutations
3 V	366 pW	1314
4 V	546 pW	1101
5 V	700 pW	902
6 V	802 pW	720
7 V	902 pW	601
8 V	828 pW	417
9 V	792 pW	315
10 V	764 pW	246

0°, thus causing a monostable behaviour), in the same way as in subsection 3.2.4.

Results of one of these benchmarking simulations are reported in fig. 3.52 for different values of the polarization voltage V_{in}, when an input acceleration a_{ext} having an RMS value of 7 m/s^2 and a bandwidth of 500 Hz has been considered. As the displacements of the central mass in the monostable structure do not always have the same amplitude (neglect-

Table 3.12 – Mean electrical power harvested by the system and mean number of commutations between stable equilibrium states (over 30 simulations) for several values of the polarization voltage V_{in}, when an air-gap of 3 µm and an input acceleration a_{ext} having an RMS value of 7 m/s^2 and a bandwidth of 500 Hz are applied to the system.

Voltage	Mean power harvested	Mean number of commutations
5 V	664 pW	1512
6 V	838 pW	1365
7 V	926 pW	1106
8 V	1010 pW	924
9 V	1092 pW	760
10 V	1234 pW	723
11 V	1282 pW	620
12 V	1334 pW	462
13 V	1178 pW	408

ing any overshoots) when the device is forced by noisy vibrations, there are no fixed maximum and minimum values for the capacitances C_{AC} and C_{BC} in the system dynamics, differently from the bistable device. In order to adopt the models in (3.32)–(3.37) and the same strategies of the bistable device in the polarization of the capacitances C_{AC} and C_{BC}, two values of displacements t_l to t_h have been imposed as a threshold

to polarize the device, equal respectively to -9 µm and 9 µm, in order to match the distance between the stable equilibrium states (equal to 18 µm) in the bistable device (see fig. 3.48).

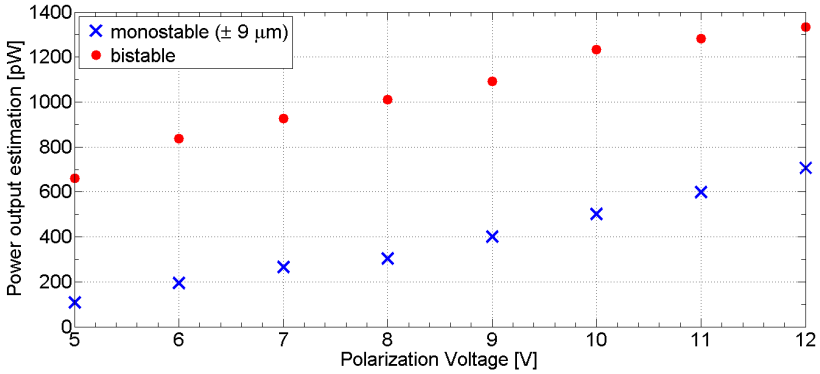

Fig. 3.52 – Comparison in the power output estimation between the bistable device and its "equivalent" monostable for different values of the polarization voltage, when an input acceleration a_{ext} having an RMS value of 7 m/s^2 and a bandwidth of 500 Hz is applied and an amplitude threshold of 18 µm is adopted in the monostable device.

Results in fig. 3.52 confirm the improvement in harvesting performance descending from the adoption of a bistable coupling mechanical structure.

3.4 Bistable microstructure in the MEMSCAP™ MetalMUMPs® process

In order to test the capabilities of the MetalMUMPs® process from MEMSCAP™ (see subsection 2.1.2) in the implementation of bistable microstructures, a MEMS structure, previously microfabricated for thermal microsensors [18], has been simulated and tested at the Nanotechlab of the University of Catania (Italy).

3.4.1 Cascaded triple bent-beam structure

The structure is based on a cascaded triple bent-beam suspended architecture realized in the 20.5 µm thick electroplated nickel layer of the MetalMUMPs® process [62].

The layout of the microstructure along with its geometric specifications is shown in fig. 3.53; descriptions and values of its geometric specifications are listed in tab. 3.13.

The 3D model of the device is illustrated in fig. 3.54.

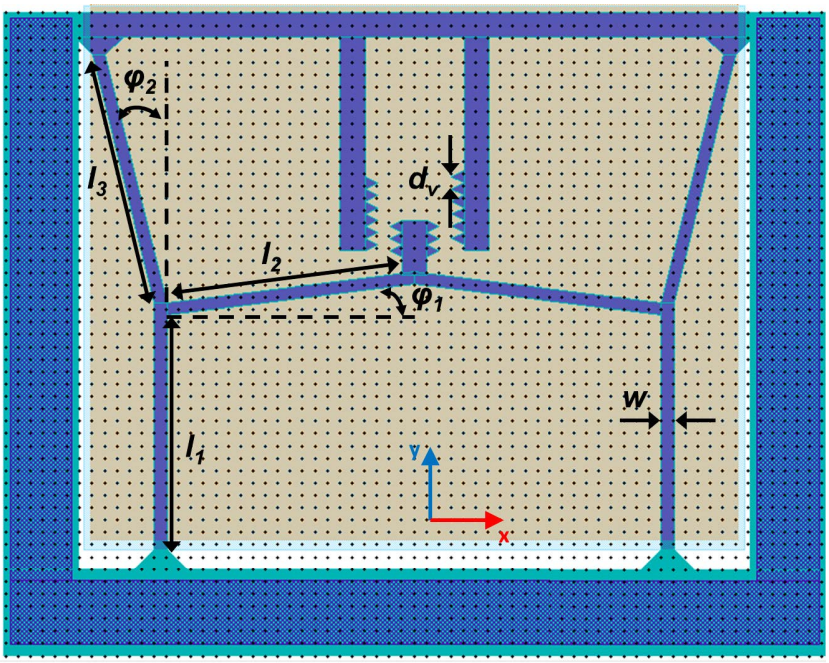

Fig. 3.53 – Layout of the cascaded triple bent-beam microstructure with the definition of its geometric specifications, whose values and descriptions are listed in the tab. 3.13.

3.4.2 FEM simulations

The microstructure has been simulated through FEM analyses on COMSOL Multiphysics® platform adopting the same methodology as the numerical simulations on subsection 3.2.2.

Table 3.13 – Geometric specifications of the cascaded triple bent-beam microstructure defined in fig. 3.53. Due to the symmetry of the device along y-axis, values are equal for the left and the right side of the microstructure.

Variable	Value	Description
l_1	200 µm	Length of the lower vertical beam
l_2	192 µm	Length of the slanted horizontal beam
l_3	205 µm	Length of the upper slanted vertical beam
w	10 µm	Width of all the beams composing the structure
ϕ_1	8.27°	Slope of the slanted horizontal beam on the x-axis
ϕ_2	12.68°	Angle between horizontal and upper slanted vertical beams
t	20.5 µm	Thickness of the microstructure
d_v	10 µm	Distance between two adjacent verniers

Material properties of the electroplated nickel adopted in FEM simulations are reported in the tab. 3.14.

Results of FEM simulations are reported in figs. 3.55– 3.56: reaction forces along y-axis at the device shuttle for different positions along y-axis are reported in fig. 3.55 and the elastic potential energy obtained after numerical integration of the reaction forces plotted in fig. 3.55 is shown in fig. 3.56.

It is worth noting that the maximum level of stress, computed by the FEM software, in the structure for all the simu-

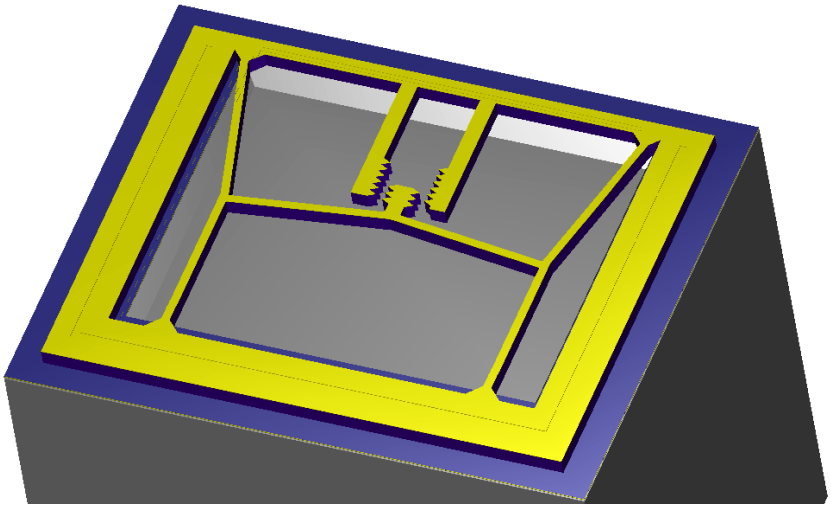

Fig. 3.54 – 3D model of cascaded triple bent-beam microstructure.

Table 3.14 – Material properties of the electroplated nickel used in the FEM simulations.

Property	**Value**
Young modulus	160 GPa [109]
Poisson's ratio	0.31 [213]
Film residual stress	50 MPa [62]
Yield stress	35 MPa [115]
Mass density	8910 kg/m^3 [213]

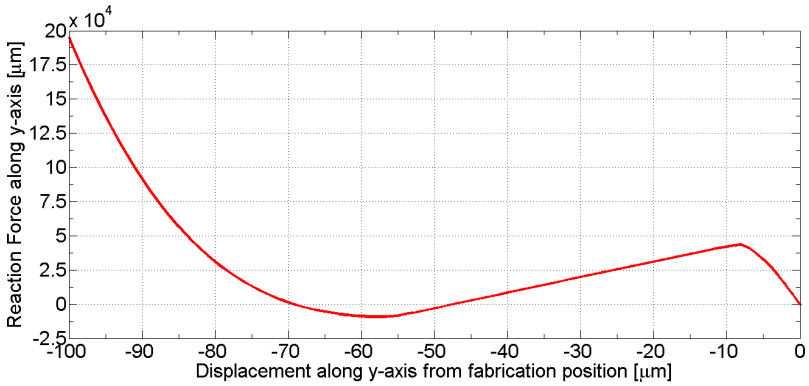

Fig. 3.55 – Reaction forces along y-axis versus device shuttle displacement along y-axis as resulting from FEM simulations.

lated positions is below the value of yield stress listed in the tab. 3.14: this means that the device experiences only elastic deformations.

The shapes of the deformed microstructure in its unstable and second stable equilibrium positions (respectively at about 41 µm and about 69 µm from fabrication position) are reported in fig. 3.57, as resulting from FEM analyses.

3.4.3 Test of the microstructure

In order to assess the bistable behaviour of the simulated structure and to validate results from FEM simulations in

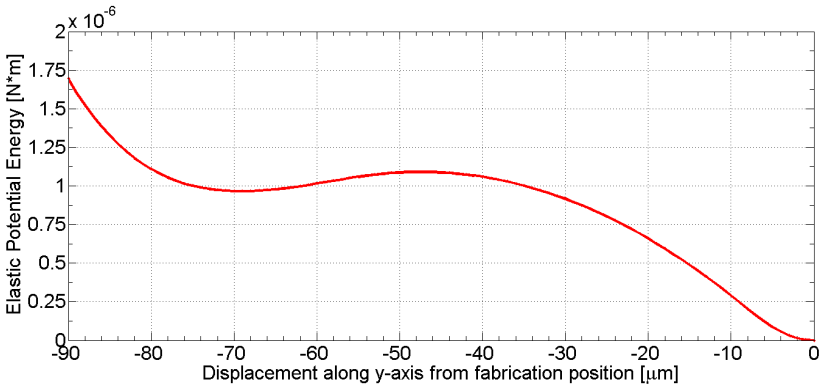

Fig. 3.56 – Elastic potential energy numerically evaluated from FEM analyses results in fig. 3.55).

subsection 3.4.2, the microfabricated structure has been tested at the Nanotechlab of the University of Catania (Italy).

The test consists in actuating the shuttle of the device through a microprobe in order to move it from its first stable equilibrium state (i.e. the fabrication position) to its second one and, then, after removing the probe, observe through an optical microscope if the device will maintain its second stable equilibrium position.

The test was successful and it was also positively repeated by moving the device shuttle from the second to the first stable equilibrium state.

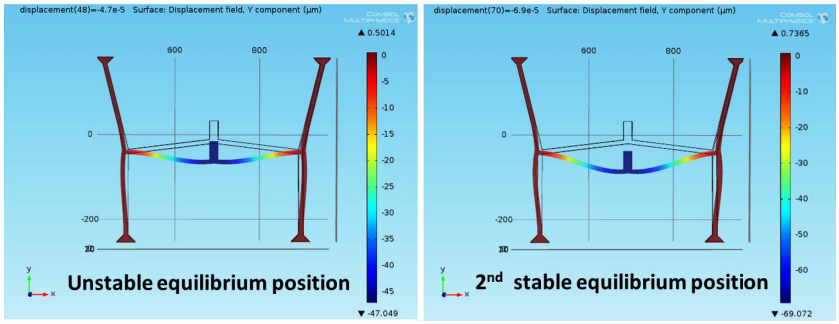

Fig. 3.57 – Deformed shapes of the microstructure in its unstable (left) and second stable (right) equilibrium positions, as computed in the FEM simulations. Both deformed shapes are compared with the undeformed shape (i.e. the fabrication position).

Several additional commutations between stable equilibrium states have been generated by the probe without affecting the device behaviour and its reliability.

A movie of the previously described test, recorded through the camera of the optical microscope, is available on internet [143]. The two stable equilibrium positions observed during the test through the optical microscope are reported in the pictures in fig. 3.58.

The comparison of the deformed shapes of the device in figs. 3.57–3.58 shows that the FEM analyses tend to overesti-

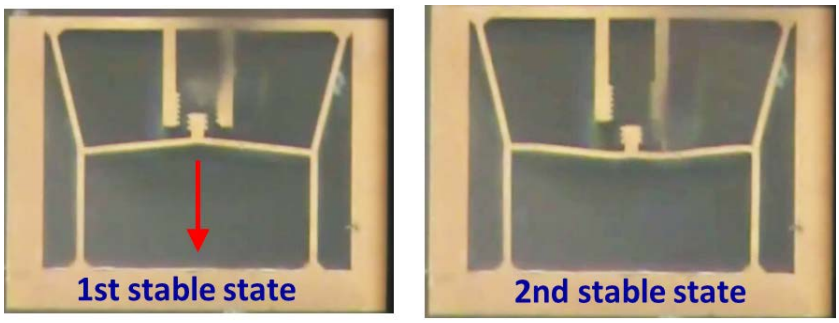

Fig. 3.58 – Optical microscope pictures of the two stable equilibrium positions of the device, as resulting from its test at the Nanotechlab of the University of Catania (Italy). The probe used for the device shuttle actuation is barely visible out-of-focus in the upper side of both pictures, as it does not touch the device.

mate the position of the second stable equilibrium state with respect to the shape resulting from the test. This is caused probably by approximations in the numerical FEM simulations and by tolerances in the device parameters. However, no plastic stress has been observed during the test as predicted from FEM analysis and the microstructure bistable behaviour has been validated.

Results exposed in this section reveals the suitability of the MetalMUMPs® process from MEMSCAP™ to develop bistable structures for energy harvesting.

3.5 Bistable devices for vibration energy harvesting in in direct printing technology

Direct printing technology process at the Sensor Lab of the University of Catania (Italy), described in section 2.3, has been exploited to develop a macroscale prototype of a nonlinear piezoelectric energy harvester based on a bistable snap-through buckled beam [4].

Buckled beams represent a strategy to obtain a bistable structure by simply applying an axial stress (tensile or compressive) or an axial loading or an axial compressive displacement to a clamped-clamped beam respectively larger than critical stress σ_{cr} defined in (3.38), critical axial load P_{cr} defined in (3.39) and critical compressive displacement Δ_{cr} defined in (3.40) [199].

$$\sigma_{cr} = \frac{4\pi^2 EI}{Al} \tag{3.38}$$

$$P_{cr} = \frac{4\pi^2 EI}{l^2} \tag{3.39}$$

$$\Delta_{cr} = \frac{4\pi^2 I}{Al} \tag{3.40}$$

where E is Young modulus, I is the cross section moment of inertia (in the plane of bending), A is the cross section area, and l is the in-plane length of the beam. The plane of buckling will correspond to the smallest moment of inertia: in-plane if $I_{yy} < I_{zz}$ and out-of-plane if $I_{yy} > I_{zz}$, where $I_{yy} = (1/12)w^3t$ (in-plane) and $I_{zz} = (1/12)wt^3$ (out-of-plane) for rectangular cross-sections of out-of-plane thickness t and in-plane width w.

There is a bifurcation in the buckling equations (i.e., the direction of buckling of an ideal beam can be in either direction within the plane of buckling). Thus the beam has two stable equilibrium positions, separated by an unstable equilibrium position which corresponds to either a supercritically stressed, unbuckled position or an intermediate elastica. The beam may be actuated from one stable position and comes to rest in the second stable position through the unstable

position. Figure 3.59(a) shows a beam buckled due to supercritical stress, as given in (3.38). Figure 3.59(b) illustrates a beam subjected to a compressive external load (or displacement) that exceeds the critical levels for the beam geometry and properties as given by (3.39) or (3.40).

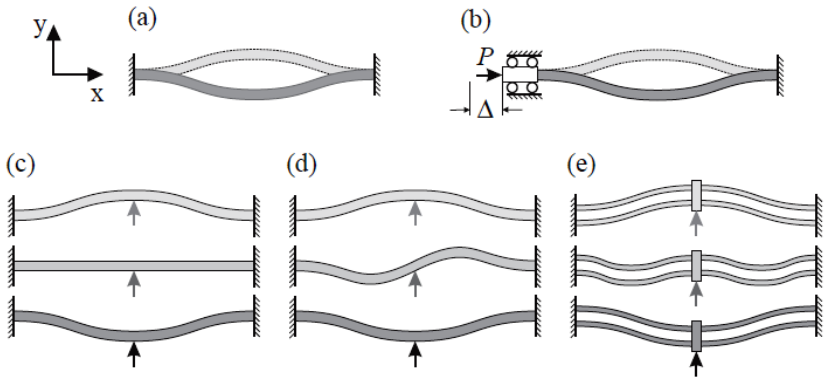

Fig. 3.59 – (a) Ideal buckled beam ("Mode 1") subject to residual stress, showing two possible states. (b) Ideal buckled beam subject to a critical load P_{cr} or displacement Δ_{cr}. (c) Ideal (and unlikely) "Mode 0" transition (or supercritical buckling) between buckled positions. (d) "Mode 2" transition between buckled positions, with rotation of center point. (e) "Mode 3" transition is made possible by the addition of multiple beams and central shuttle for symmetry.

The stable and transitional shapes of the buckled beams will be classified by mode-shapes. The terminology for the

mode-shapes comes from the number of waveform modes corresponding to the number of times the beam crosses the x-axis (not including the origin of the beam). The familiar buckled shape, see fig. 3.59(a), is "Mode 1" buckling. The supercritically stressed transition corresponds to what will be termed "Mode 0" buckling, or unbuckled deflection. The mode shape of the intermediate elastica is "Mode 2", see fig. 3.59(d). This mode is undesirable for bistable switching applications as it introduces rotations that may not be compatible with actuation systems or contacts. This mode does however correspond to the path of lowest potential energy between the stable positions (i.e. the path of least mechanical resistance). This is because a "Mode 0" is highly unlikely and other mode-shapes are always higher energy states. "Mode 2" transition can be avoided by using multiple beams and a central shuttle, see fig. 3.59(e), to provide stabilizing symmetry. The resulting structure is stiffer than a single beam, due to the additional beam and the "Mode 3" transitional mode-shape, but will be less prone to rotational deformations.

Bistable MEMS based on buckled beams have been proposed utilizing beams buckled by residual stress [103, 239], thermally induced stress [50], or by applying external loading by on-chip actuation [207]. Another possible technique is to fabricate the beam in one of the stable positions [192]. Although not buckled in the initial (as fabricated) state, the beam (or beams) can be designed to have a snap-through behaviour and they will however remain biased to the initial position.

In this work the rapid prototyping of piezoelectric buckled beams of centimeter size exploiting the benefits of the bistable dynamics and assuring a wide bandwidth at low frequencies is presented. Low cost strategies based on direct printing technologies are adopted in order to ensure the reducing of both costs and time of realization.

3.5.1 The device and its working principle

The device consists of a PET substrate ("Novele^{TM} IJ-220 coated PET" from Novacentrix®, see fig. 2.30) having a thickness of about 165 µm that implements a clamped-clamped beam. The length l and the width w of the beam are design

parameters. On the top of this beam, a layer containing two pads and two InterDigiTed Electrodes (IDT) has been realized by inkjet printing of a conductive pattern of the silver nanoparticles solution ink "Metalon® JS-B15P" by Novacentrix (see section 2.3) [172], through a cheap commercial EPSON® piezo inkjet printer. IDT fingers width, length and thickness are respectively about 200 µm, 5 mm and 250 nm, while the track spacing is about 300 µm. The function of the IDT is the electrical connection of the Lead Titanate Zirconate (PZT) piezoelectric layer (from Piezokeramica APC 855 [20]) which have a thickness of about 25 µm and is deposited above them through screen printing at the Department of Information Engineering of the University of Brescia (Italy). After its deposition, the PZT layer is cured at 100℃ for 10 minutes. A clamping system allows for both the fixing of the beam ends and the connection of the pads through proper sockets.

A picture of the realized prototype in its upper stable equilibrium state and fixed by the clamping system is reported in fig. 3.60 and diagram (not in scale) of the device layers compared with a picture of the device is reported in fig. 3.61.

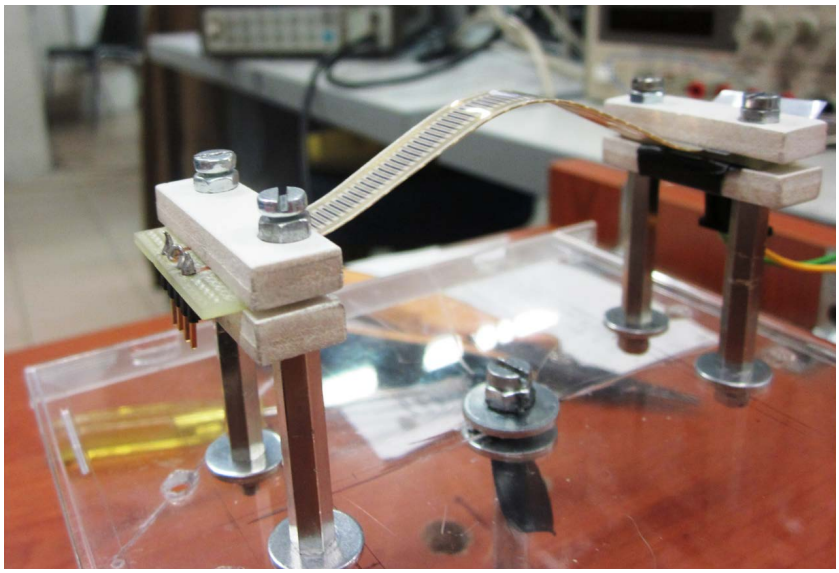

Fig. 3.60 – Picture of the realized prototype in its upper stable equilibrium state and fixed at both ends by the clamping system. Length and width of the device in the picture are respectively 10 cm and 1 cm.

When a suitable axial displacement precompression ΔY, larger than the critical compressive displacement Δ_{cr} defined by (3.40), is applied by the clamping system to both beam ends, buckling occurs in the out-of-plane direction and the clamped-clamped beam exhibits a bistable behaviour. An upper and a lower stable equilibrium positions appear having a distance ΔX. An increase of ΔY results in an increase of ΔX.

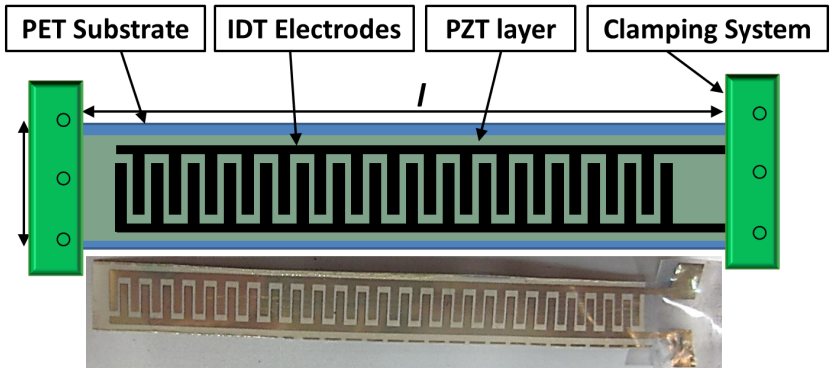

Fig. 3.61 – Diagram (not in scale) of the device layers compared with a picture of the device in fig. 3.60.

In order to achieve commutations between these stable equilibrium states, a force F having amplitude larger than a certain threshold (imposed by the bistability) must be applied approximately at the center of the beam in its out-of-plane direction. In this case, this force is given by the product of the acceleration coming from external vibrations and of the beam mass (that can be increased by placing a proof mass at the center of the beam). Strains due to the beam commutations are converted into an output voltage by the PZT layer. An increase of the distance between stable equilibrium states ΔX

leads to a growth of both the output voltage V and the force amplitude F required for commutations.

A proof mass m_{add} can be added at centre of the beam to reduce the level of the external acceleration a_{ext} descending from mechanical vibrations required to make the device switching between its stable equilibrium states.

3.5.2 Design flow

The beam length l, width w, the applied displacement precompression ΔY and the eventual added proof mass m_{add} are the parameters to be designed before device realization. Process parameters, such as layers thickness, are considered unchangeable design constraints. The specification of this design is the minimization of the minimum external static acceleration a_{static} required to achieve device commutations by having a minimum added proof mass a_{ext}.

The value of applied displacement precompression ΔY is bounded below by the critical compressive displacement Δ_{cr} determined by the values of beam length l and width w through the (3.40). The energy specification of the system is indicated by the system critical force F_c which is strictly

related to the distance ΔX between stable equilibrium states for each pair of values of beam length l and width w and applied displacement precompression ΔY. Critical force F_c and distance ΔX can be determined through both FEM analyses and mechanical characterization of the device prototypes.

By fixing the minimum required static acceleration a_{ext} from the vibrational source taken into account, critical force F_c is computed through the Newton's Second Law [212] by defining the eventual proof mass m_{add} to be added to beam mass. External static acceleration a_{ext} and eventual added proof mass m_{add} define the distance ΔX between stable equilibrium states which, then, determines the value of the displacement precompression ΔY for each pair of beam length l and width w (selected to optimize system dimension). Design flow is summarized in fig. 3.62.

In this specific case study, the proposed design flow has been applied to design a device capable of harvesting energy from accelerations coming from a running/walking person. An example of the typical waveforms and magnitude levels of these accelerations is reported in figs. 3.2–3.3.

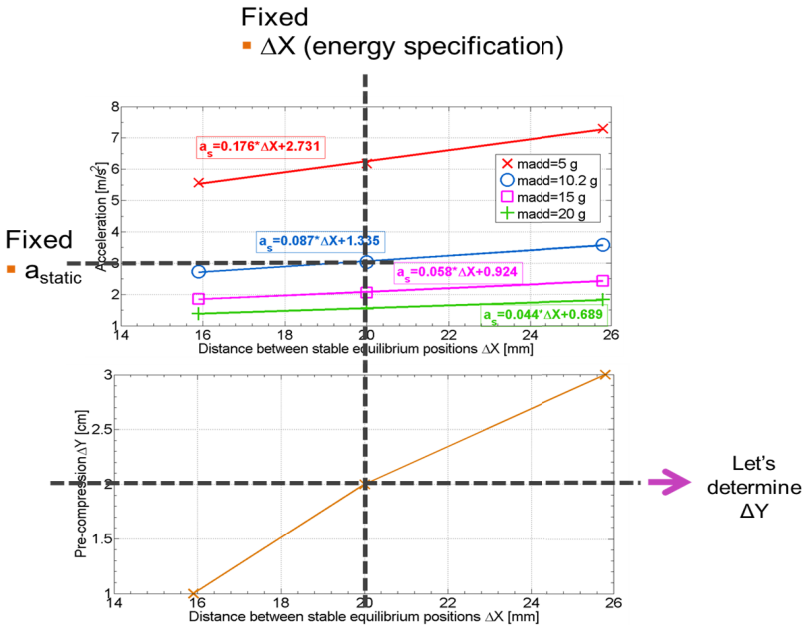

Fig. 3.62 – Diagram summarizing the design flow of the device.

3.5.3 Mechanical Characterization

Several tests have been performed to define the device mechanical behaviour and to assess the relationships among device parameters useful for the definition of the geometry in the design flow.

The bistable behaviour of the precompressed beam has been investigated by forcing the centre of the buckled beam

through a micropositioner coupled with a load cell. For each displacement of the micropositioner, the beam moves from its stable equilibrium positions and the load cell measures the beam reaction forces in the out-of-plane direction. Measurement setup is shown in the photo in fig. 3.63 and an example of measurement results for a beam 10 cm long and 1 cm wide subjected to a displacement precompression ΔY of 2.7 mm is shown in the plot in fig. 3.64.

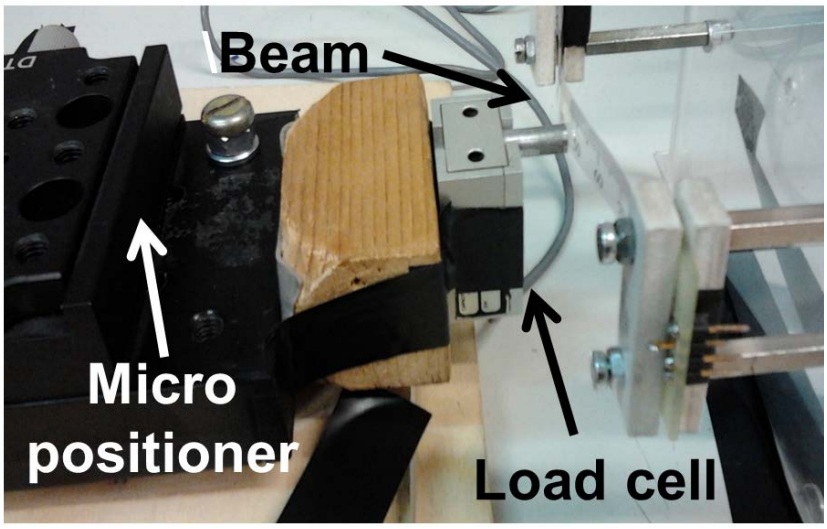

Fig. 3.63 – Experimental setup for the mechanical characterization of the reaction forces of the buckled beam.

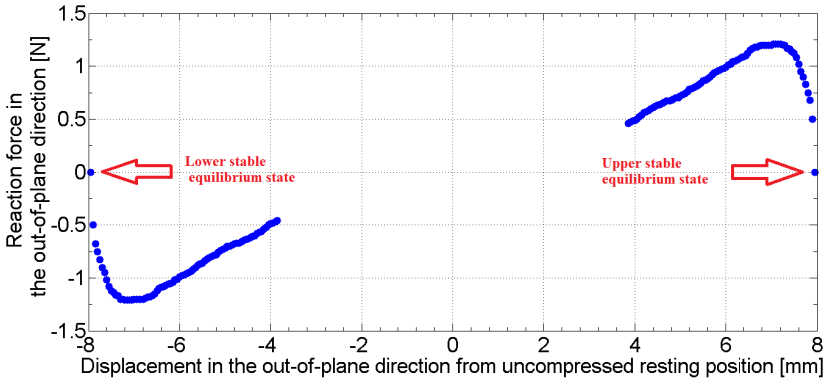

Fig. 3.64 – Measurement results of the reaction forces in the out-of-plane direction for a beam 10 cm long and 1 cm wide subjected to a displacement precompression ΔY of 2.7 mm. Results refers to the stable zones of the beam.

The application of the same measurement methodology leads to identify the distance ΔX between stable equilibrium states in a beam of defined sizes for different applied displacement precompressions ΔY. Results from measurements have been compared with results of FEM static simulations (on ANSYS® platform) adopting the same methodology. An example of measurement results for a beam 10 cm long and 1 cm wide is reported in the plot in fig. 3.65.

The static relation between the distance ΔX between stable equilibrium states and the minimum required static accel-

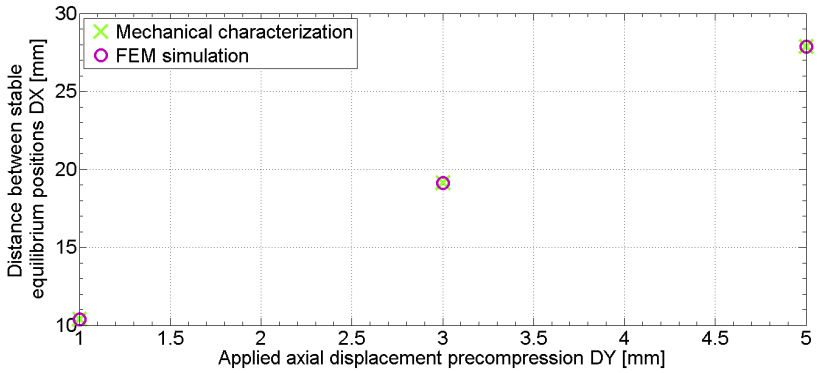

Fig. 3.65 – Measurement results and FEM simulations results of the relation between the applied displacement precompressions ΔY and the distance ΔX between stable equilibrium states for a beam 10 cm long and 1 cm wide.

eration a_{ext} for achieving device commutations has been experimentally investigated by applying several loading masses m_{add} (i.e. several steel nuts), having a known weight, subjected to gravitational acceleration g at the centre of the beam. So, the applied force F in the out-of-plane direction will be the product between the overall mass of the system (i.e. the sum of the beam mass m_{beam} and of the added mass m_{add}) and of the gravitational acceleration g. The critical force allowing a commutation from one stable equilibrium state to the

other one has been measured in this way. A picture of the measurement setup is shown in fig. 3.66.

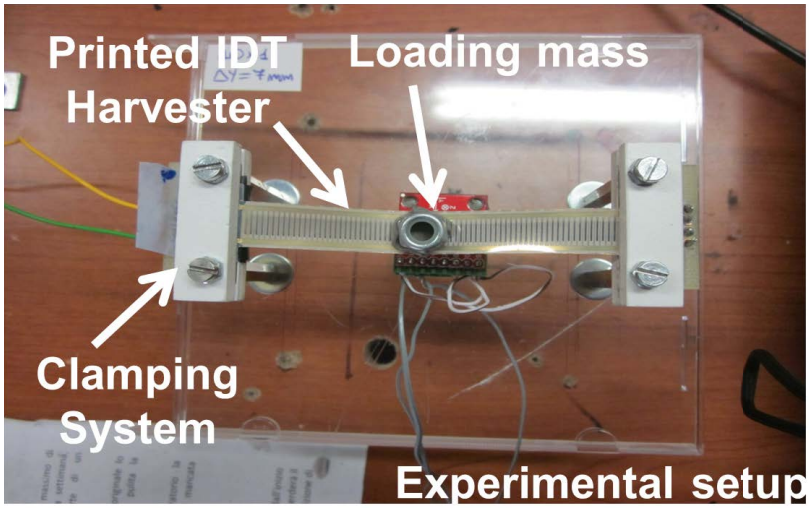

Fig. 3.66 – Experimental setup of the mechanical characterization of the relation between the distance ΔX between stable equilibrium states and the minimum required static acceleration a_{ext} for achieving device commutations. Proof mass is represented by a steel dice attached to the centre of the beam.

The application of an additional proof mass m_{add} to the centre of the beam reduces drastically the critical acceleration required to commutate between the two stable equilibrium states, increasing the device sensitivity to vibrations, as shown

in the measurement results in fig. 3.67 for a beam 10 cm long and 1 cm wide.

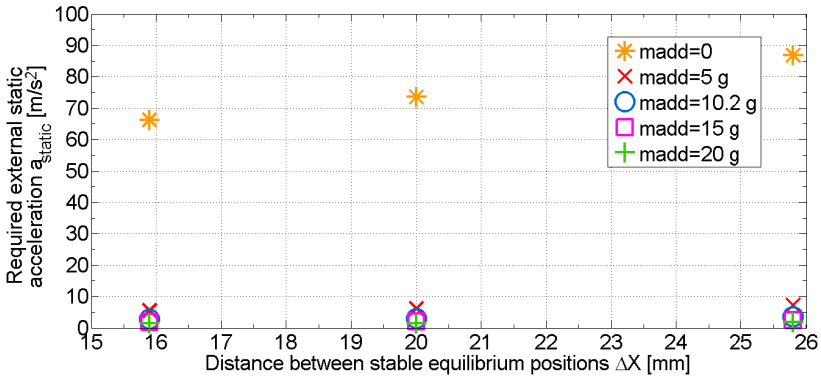

Fig. 3.67 – Measurement results of the static relation between the distance ΔX between stable equilibrium states and the minimum required static acceleration a_{ext} for achieving device commutations for a beam 10 cm long and 1 cm wide.

3.5.4 Electrical Characterization

In order to investigate experimentally the behaviour of the proposed device, several tests have been performed by stimulating the device (without proof mass) through a periodic mechanical burst generated by an electromechanical shaker con-

nected to a function generator. The mechanical input coming from the shaker has been measured through an accelerometer (MMA7361 from Freescale^{TM} [221]); the output voltage of the device on a resistive load of 1 MΩ has been acquired through a digital oscilloscope; the mechanical displacement in the out-of-plane direction of the device has been monitored through a laser distance meter (Baumer OADM 12U6460/S35A [26]). A schematic of the setup is illustrated in fig. 3.68.

The choice of a mechanical burst as excitation signal is due to the fact that it suitably represents the waveform of the accelerations measured by running/walking person (i.e. the target vibrational source chosen), as shown in the example plots in figs. 3.2–3.3.

The output voltage from piezoelectric output has been measured on a resistive load of 1 MΩ, when the device has been stimulated through a periodic mechanical burst with fixed amplitude and several frequencies (1 Hz, 10 Hz, 30 Hz and 70 Hz). The acceleration amplitude related to the input vibrations imposed by the shaker ranges from 1g RMS to 6g RMS and increases with the frequency of the burst, as

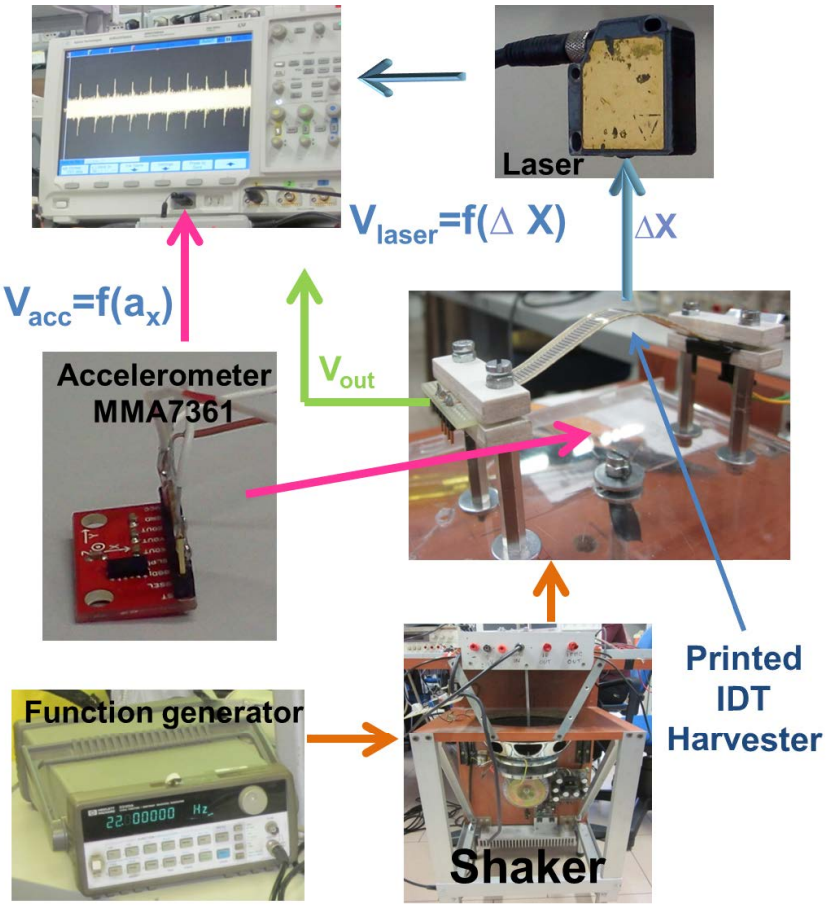

Fig. 3.68 – Experimental setup for the electrical characterization of the device.

measured by the accelerometer. The waveforms of the voltage output are reported in figs. 3.69–3.72 for a beam 10 cm long

and 1 cm wide subjected to a displacement precompression ΔY of 3 mm.

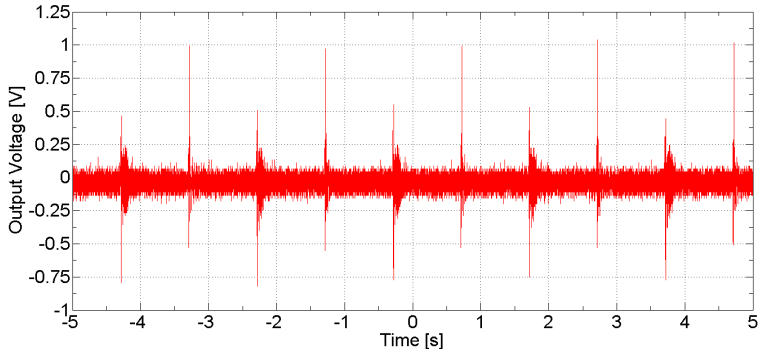

Fig. 3.69 – Output voltage of a beam 10 cm long and 1 cm wide subjected to a displacement precompression ΔY of 3 mm and forced by a periodic mechanical burst having a frequency of 1 Hz.

The waveforms of the applied mechanical burst (as resulting from the accelerometer measurement) and of the displacement of the centre of the beam (as resulting from the laser measurement) are reported in fig. 3.73, when the device is forced by a periodic mechanical burst having a frequency of 10 Hz.

The measured RMS value of the output voltage on a resistive load of 1 MΩ for different frequencies of the applied burst

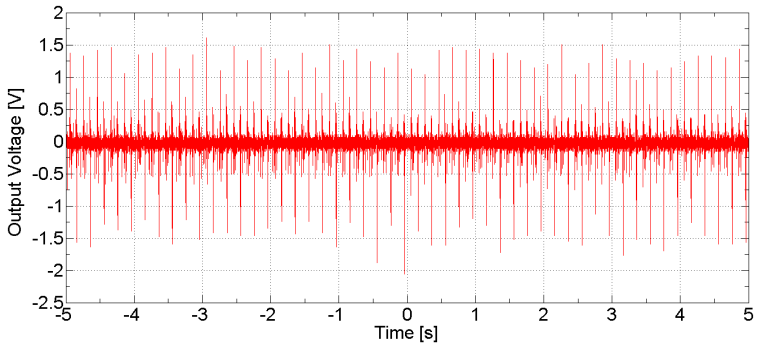

Fig. 3.70 – Output voltage of a beam 10 cm long and 1 cm wide subjected to a displacement precompression ΔY of 3 mm and forced by a periodic mechanical burst having a frequency of 10 Hz.

and several peak-to-peak amplitudes A_b of the electric signal used to excite the electromechanical shaker are reported in fig. 3.74, as resulting from measurements on a beam 10 cm long and 1 cm wide, without proof mass, subjected to a displacement precompression ΔY of 3 mm.

According to (4.19) and results in fig. 3.74, the maximum measured harvested power is about 290 nW (when the electrical signal used to excite the electromechanical shaker is a periodic burst with a frequency of 60 Hz and a peak-to-peak amplitude A_b of 440 mV and a resistor load of 1 MΩ).

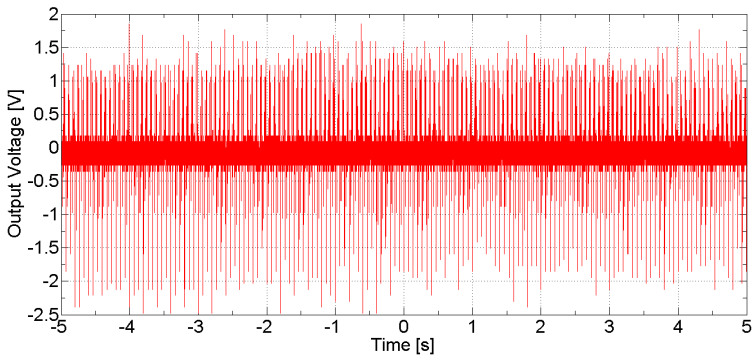

Fig. 3.71 – Output voltage of a beam 10 cm long and 1 cm wide subjected to a displacement precompression ΔY of 3 mm and forced by a periodic mechanical burst having a frequency of 30 Hz.

The working frequency band of the device is estimated around 70 Hz, as above this frequency the device does not exhibit interwell commutations.

The estimated bandwidth of the 10 cm long and 1 cm wide beam, without proof mass, subjected to a displacement precompression ΔY of 3 mm and the level of accelerations required suggest the application of the realized prototype for harvesting vibrations from a running/walking person (whose typical acceleration is reported as example in figs. 3.2–3.3).

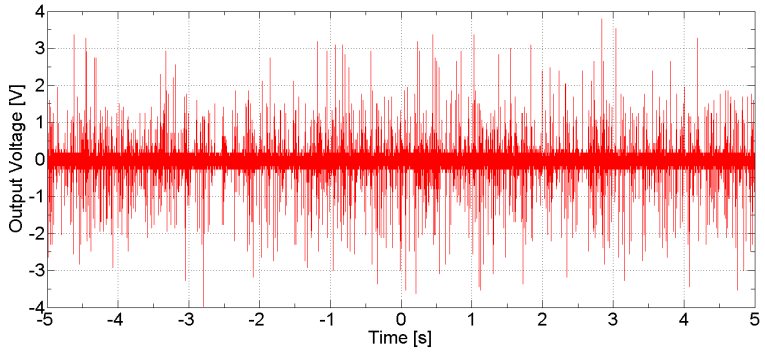

Fig. 3.72 – Output voltage of a beam 10 cm long and 1 cm wide subjected to a displacement precompression ΔY of 3 mm and forced by a periodic mechanical burst having a frequency of 70 Hz.

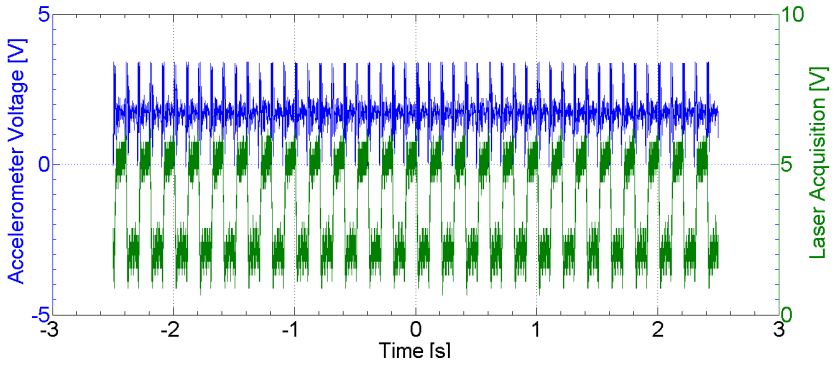

Fig. 3.73 – Waveforms of the applied mechanical burst (as resulting from the accelerometer measurement) and of the displacement of the centre of the beam (as resulting from the laser measurement) when the device is forced by a periodic mechanical burst having a frequency of 10 Hz. Units on y-axes are reported in voltage (i.e. the direct output from the accelerometer and from the laser distance meter. A beam 10 cm long and 1 cm wide subjected to a displacement precompression ΔY of 3 mm has been considered.

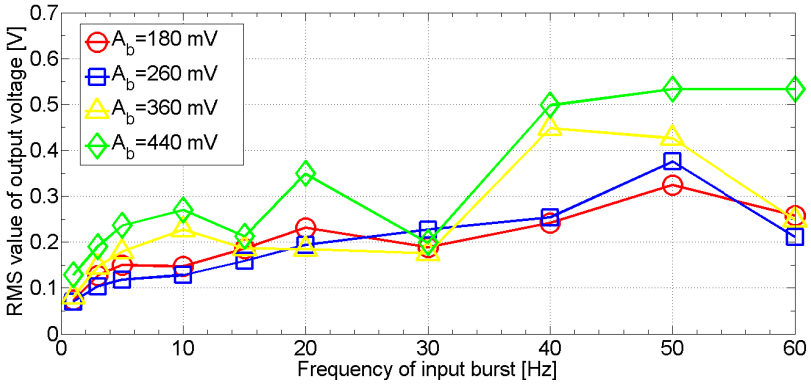

Fig. 3.74 – RMS value of the output voltage of a beam 10 cm long and 1 cm wide subjected to a displacement precompression ΔY of 3 mm forced by a periodic mechanical burst having several frequencies and several amplitudes A_b.

4

Bistable devices for AC current sensors

I happen to have discovered a direct relation between magnetism and light, also electricity and light, and the field it opens is so large and I think rich.

Michael Faraday

In this chapter, a nonlinear methodology to improve the sensitivity in measuring AC electrical currents in certain operating conditions and to ensure autonomous sensor operation will be presented along with device simulations and experimental results to assess the feasibility of the proposed approach.

4.1 State of art for AC current sensors

The need for ubiquitous and autonomous sensors for sensing electrical quantities represents one of the most important motivating reasons for research efforts spent in the scientific field. In fact, increasing global requests for energy efficiency, development of smart-grids and advances in compact sensor network technologies push researchers to study novel types of sensors in order to efficiently monitor electricity usage in power lines both in residential, industrial and commercial environments and in distribution and transmission power systems [153].

Among electrical quantities a special attention is deserved to AC electrical currents in order to monitor power consumption in electric systems [250].

An overview on techniques for current sensing is presented in subsection 4.1.1 and, due to the topic in this work, more details on MEMS AC current sensors will be discussed in subsection 4.1.2.

4.1.1 Techniques for current sensing

Shunt resistor, transformers, and magnetic field sensors are traditional technologies adopted to measure a current flowing in a wire [249].

Shunt resistors techniques are used to directly measure the amount of current through a resistive element placed in series with the load. The principle is based on Ohm's law where the voltage drop across the device is proportional to the flowing current. This technology can provide an accurate measurement for low currents, but in the case of large currents it is very impractical because the shunts become bulky and heavy and the voltage drop causes large heat dissipation. Furthermore, some mounting issues are noticed, their measurement is affected by insertion loss and other circuitry, such as instrumentation amplifiers, are needed to generate distinguishable signals for measurement [130].

Transformer techniques are passive methodologies adopted to indirectly measure the current through the secondary winding of a current transformer. Current transformers are relatively simple to implement and are passive devices that do not

require driving circuitry to operate. These transformers have a primary coil with a few turns and a secondary coil which should ideally be short circuits, see fig. 4.1(a). The primary AC current will generate a magnetic field which is coupled into secondary coil by Faraday's law. The magnitude of the secondary current is proportional to the number of turns in the coil, which is typically higher than 1000. Secondary current is then sensed through a sensing resistor to convert the output to voltage. Current transformers amplitude and phase errors depend on the core material and size, coil geometry, amplitude and frequency of the measured current, and also on the value of the load. Advantages of current transformers are: contact-less current measurement, detecting of high currents, low power consumption, and low temperature shift [259].

Several techniques of current sensing have been developed by exploiting magnetic field sensors, whose technology and applications have been in a great interest and in a constant growth in scientific research in last decades [140, 141]. The main advantage of this current sensing technique is sensing the magnetic field produced by the current under test in a

contactless measurement, due to the safety needed in the case of high current measurement.

Hall sensors are among the most commonly used types of magnetic field sensors. According to the Hall Effect principle, the magnetic force on a moving electron in a conductor will produce a slight displacement between the electrons and the positive ions of the stationary lattice structures. As a result of this, a voltage will be generated perpendicular to both the current and the field. This principle is known as Hall Effect [186]. In the case of current sensors based on Hall Effect, when a magnetic field is perpendicular to a current in a thin metal sheet, a Lorentz force is exerted on the current. This force disturbs the current distribution, resulting in a potential difference across the output, see fig. 4.1(b). This voltage is called "Hall voltage" and is directly proportional to the current and the magnetic field, albeit of being of very small in order (micro-Tesla) [69]. The most sensitive Hall sensors are made of Indium antimonide (InSb) and III-V semiconductors, which require dedicated fabrication processes [219].

Rogowski coil, also known as "di/dt coil", is used to measure AC current, transient current and changes in DC current. It is based on search coil technique for sensing magnetic field. It is made of coil with or without core [121, 247]. The operation principle of these sensors is based on Faraday's Law of Induction [212]. If the magnetic flux inside the coil changes, a voltage proportional to the rate of change of the flux is generated between the coil leads. The sensitivity of the search coil depends on the magnetic permeability of the core material (ferromagnetic core increases the sensitivity), the area of the coil, the number of turns and the rate of change of the magnetic flux through the coil. The Rogowski coil is designed to cancel the far field while the near field will remain. This is to avoid the possibility of interference occurring which is usually far field related. Rogowski devices are extremely linear and have air cores which make construction simple. However, in terms of signal processing, the output of the coil should be integrated because it is sensitive to the rate of the current, see general scheme in fig. 4.1(c). The advantage that the Rogowski coil has in addition to current transformers is

that no DC or high current saturation is possible. This is because the saturation of the air-core in a Rogowski coil is extremely high compared with ferrite cores of normal current transformers. The air core also has a linear phase response and low cost [197].

Fluxgate sensors measure the magnitude and direction of the DC or low AC magnetic field with high sensitivity in the range between several tens of nano-Tesla and tens of milli-Tesla [198]. As all ferromagnetic materials exhibit hysteresis, a sinusoidal current applied to drive coil causes the core to reach its saturation magnetization once every half cycle. The sense coil then detects a nonlinearIy distorted signal, see general scheme in fig. 4.1(d). The output signal includes even harmonics of the drive signal, and most importantly, the second harmonic. The voltage associated with harmonics is proportional to the external magnetic field [68].

Superconducting Quantum Interference Devices (SQUID) are one of the most sensitive magnetic sensors available. The sensitivity of these sensors is on the order of femto-Teslas [71]. Besides their use in the laboratory, they have a rich applica-

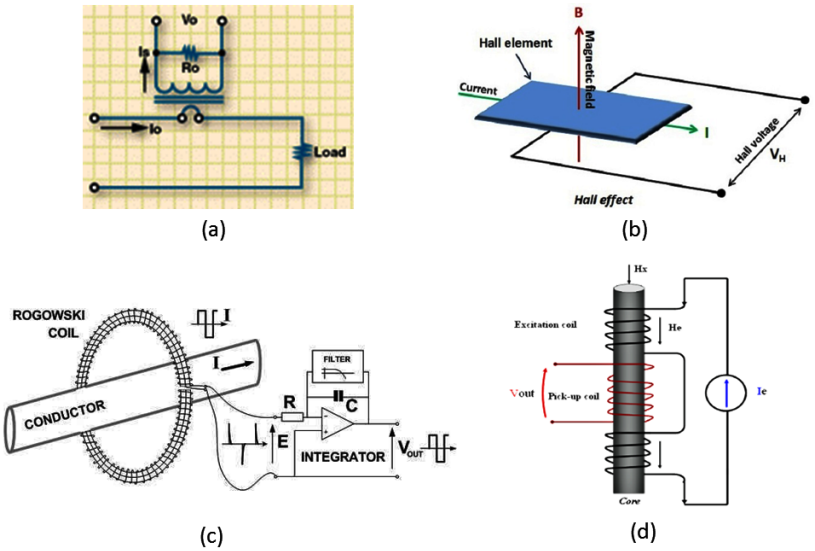

Fig. 4.1 – General schemes of current sensing techniques: (a) current transformer, (b) Hall Effect, (c) Rogowski coil and (d) fluxgate magnetometer.

tion potential in areas such as geophysics, bio-magnetism and non-destructive testing of materials. The basic phenomena governing the operation of SQUID devices are flux quantization in superconducting loops and the Josephson Effect [251]. One of the main applications besides current measurement is in medical imaging purposes, whereby measuring the neuromagnetic field of the humans [72].

Other techniques for current measurement are based on nuclear precession [149], fiber optic with magnetostrictive materials [209], magnetoresistors [119], magnetodiodes [185] and magnetotransistors [233].

Because of the scope of this work, a special attention is deserved to micromechanical AC current sensors, which will be illustrated with more details in subsection 4.1.2.

4.1.2 MEMS AC current sensors

Most MEMS sensors are based on mechanical microstructures technology, which uses a broad range of design materials and mechanical structures. The benefit of MEMS technology is in the development of miniaturized devices with a lower cost, lower power consumption, higher performance and greater integration for batch production [131].

The deposition of functional magnetic materials on microstructures, such as cantilever beams, enables the possibility to exploit MEMS devices in magnetic field sensing applications and, thus, to detect and measure time-variable electric currents, that are sources of magnetic fields. Among time-variable currents, AC electrical currents (thus generating an

oscillating alternate magnetic field) play a central role in electric systems because the current delivered by power systems is sinusoidal (at a frequency of 50 Hz or 60 Hz, depending on the countries) and switching systems are widely used in power converters [163].

Using this approach, several microcantilevers capable of detecting magnetic fields [61] have been developed. Some of them have also an accurate angle detection capability [123].

Traditionally, MEMS sensors for AC electrical currents are based on the interaction between a magnetic field generated by the electrical current to be measured and a magnetic field produced by the sensor [137]. The magnetic field coming from the sensor can be generated either by using coils where a secondary electrical current is forced by the sensor [23] or by adopting magnetic materials like permanent magnets [197]. To this aim, other materials capable of interacting with the external magnetic field, such as cobalt, have been used in coatings of cantilever beams too [96]. Sensors exploiting Lorentz forces [122] and eddy currents [206] have been also proposed.

This strategy has the advantage of contactless operation, even if the distance between the sensor and the source should be very small for the feasibility of the principles.

The approach based on permanent magnets is preferred because permanent magnets do not require power and conditioning circuitry to generate a magnetic filed. However solutions using actuation currents or magnetic coatings are desirable in microsystems applications where the microfabrication of permanent magnets, especially having a given magnetization, can be seriously challenging.

The magnetic force generated by the aforesaid magnetic interaction is commonly used to actuate a mechanical vibrating structure. Typically, this structure consists of a linear resonant mechanism tuned with the frequency of the AC electrical current to be measured (e.g. a cantilever beam equipped with a permanent magnet or coils on its free end) and that gives a linear response [111], in terms of relation between the magnitude of AC current and the amplitude of mechanical oscillation of the microstructure. Resonating microstructures have the advantage of providing a large output signal. For

this reason, many micromechanical sensors have exploited this advantage to improve their sensitivity or dynamic range, although they could suffer from certain operating conditions, such as noisy environments, or low levels of target currents (see subsection 1.3.1) [122].

Displacements and strains of the oscillating structure due to magnetic interaction forces are electrically sensed through piezoresistors [30] or variable capacitors [78]: these approaches require external powering. Sometimes capacitive sensing has been used to correct nonlinearities of resonant sensors through a feedback logic [122]. Optical readout [124] is also adopted at the price of higher complexities (e.g., use of laser and/or optical fibres). Another readout strategy is based on piezoelectric strategies employing self-generating materials, such as Lead Titanate Zirconate (PZT) and Aluminium Nitride (AlN), which provide autonomous solutions without external powering [178]; an example of piezoelectric resonant AC current sensor proposed in literature is illustrated in fig. 4.2

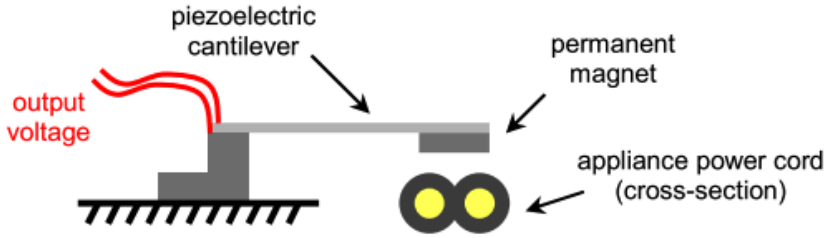

Fig. 4.2 – Schematic of a piezoelectric resonant AC current sensor proposed in literature [137].

4.2 Bistable AC current sensor

The device proposed in this work is based on a cantilever beam with a permanent magnet on its free end. Another permanent magnet with opposed magnetization is externally fixed and placed at a given distance Δ on the x-azis from the first one to achieve bistable behaviour through the magnetic repulsion of these two magnets [7]. A scheme of the proposed sensor is illustrated in fig. 4.3.

This configuration has been previously proposed in literature for harvest energy from mechanical vibrations exploiting nonlinear oscillators in order to achieve improved performance when wideband and low frequency vibrations are addressed [9].

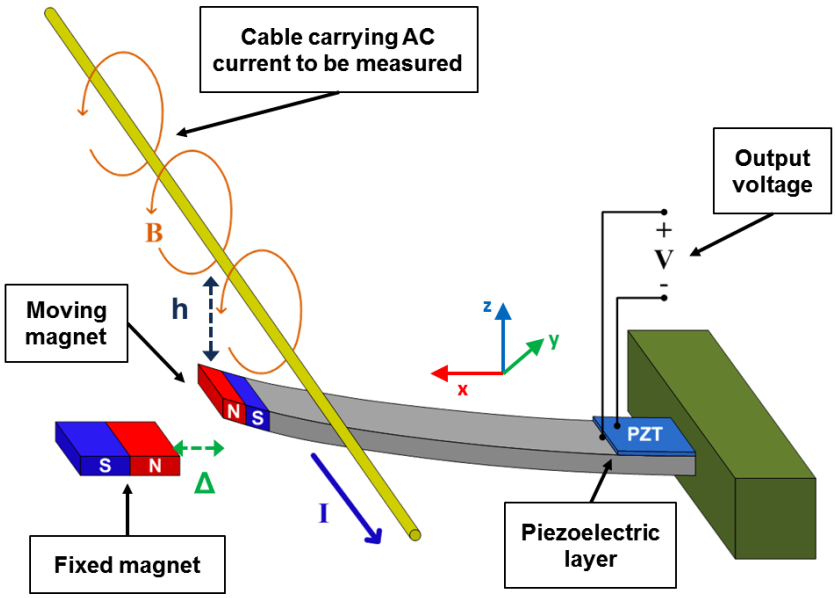

Fig. 4.3 – Schematic of the proposed nonlinear AC current sensor.

Differently from energy harvesting applications, the cantilever beam is actuated by means of the magnetic force given by the interaction of the "moving" permanent magnet, on the tip of the beam, and the magnetic field coming from the target AC electrical current. When the magnitude of the incoming magnetic force (due to the AC current) is larger than the threshold imposed by the distance of the two permanent mag-

nets, the system snaps from one stable equilibrium state to the other one, triggering some commutations.

A piezoelectric layer provides a mechanical-to-electrical transduction of the mechanical displacements and velocities of the structure and ensures the autonomous operation of the device.

The number of commutations between the two stable states, in a defined period of time and with a fixed bistable threshold, grows by increasing the amount of the incoming electrical current until a saturation level is reached: this directly provides a digital measurement of the current. In fact, systems commutations can be easily counted through digital counters by considering the output from the piezoelectric layer.

Another advantage is given by the increased sensitivity of the device: in fact, whichever will be the amount of the electrical current above the fixed bistable thresholds and in the operative range of the sensor (easily tuned by adjusting the distance Δ between permanent magnets), the amplitude and the duration of each commutation and, consequently, the amplitude of the output piezoelectric signal will not roughly change,

differently from strategies based on resonant cantilevers that provide a linear output. This makes the system more robust to external noise (e.g., electrical noise in power lines and mechanical noise from mechanical vibrations in the operative environment of the device), especially when weak electric currents have to be measured [92].

Considering the bistable transduction mechanism implemented in this sensor, this device takes advantage of all the benefits descending from stochastic resonance and the interplay between nonlinearity and noise in "Noise Activated Nonlinear Dynamic Sensors" [88], as discussed in subsection 1.3.1. In fact, electrical noise in power lines, mechanical noise from mechanical vibrations in the operative environment of the device and the deterministic sinusoidal signal of the AC target current can be related to the theory of stochastic resonance (see eq. (1.8) in subsection 1.3.1) and exploited to enhance sensing performance of the device, in terms of sensitivity and responsivity, in certain operating conditions that can be unfavorable to linear resonant sensors (e.g., high levels of noise and weak target signals).

The output voltage from the piezoelectric layer can be used both as signal to carry information from the sensor operation of the device and as energy harvested from the beam commutations (that can be used to power the sensor and/or other electronic circuits ensuring sensor operation, e.g., in a wireless sensor node). In fact, beam commutations can be caused by both the magnetic field from the target current and also by mechanical vibrations in the operating environment of the device, thus, including in the same device a sensor and an energy harvester [7]. In this case, the benefits of the interplay between noise and nonlinearity in periodically-forced nonlinear oscillators is exploited both in enhancing quality and quantity of extracted information and in scavenging more energy [40, 235].

The adoption of a nonlinear oscillating structure, thus avoiding the use of resonant structures, prevents the issues of matching the frequency of the resonant structures with the one of the electrical current to be measured. In fact, the realization of linear resonant structures with very low resonant frequencies (such as 50 Hz or 60 Hz, i.e. the most used fre-

quency of the delivered currents in the power lines in many countries) is very difficult at microscale [17].

The development of this device at microscale (e.g. its integration in a chip) will allow its insertion into the shields of cables (i.e. between the cables and their shields). The reduction of the system dimensions (the cantilever beam and the permanent magnets) will also decrease the amount of the magnetic force required for the commutations of the beam and will allow its placement at a distance of or below a millimeter size.

The model of the proposed device will be discussed in section 4.3.

4.3 Bistable AC current sensor modeling

The system is composed of a vibrating structure and two permanent magnets, one fixed and one moving. With reference to the scheme in fig. 4.3, the vibrating structure of the system consists in a cantilever beam having a length l (on x-axis), a width w (on y-axis) and a thickness t (on z-axis). A piezoelectric layer of thickness t_{PZT} (on z-axis), width w_{PZT}

(on y-axis) and length l_{PZT} (on x-axis) is placed on the mechanical layer of the cantilever beam in order to implement a self-generating piezoelectric readout for the sensor. A permanent magnet (i.e. the moving permanent magnet) of volume V_m, mass density ρ_m and magnetic remanence B_r is attached to the top of the free end of the beam, while another magnet, the fixed permanent magnet, having the same properties as the moving permanent magnet, but opposed magnetization, is placed on a fixed base at a distance Δ from the moving magnet. The length of the cantilever beam is along x-axis and the main displacement of its free end is along z-axis. The AC electrical current to be measured $I(t)$ flows in a wire placed along the z-axis and at a minimum distance h (measured along x-axis) from the magnet placed at the tip of the beam. Let z be the relative displacement of the cantilever beam from its fabrication position ($z = 0$), the 1 DOF lumped parameter model is defined by (4.1) (derived from (3.7), after slight modifications).

$$m\ddot{z} + c_m\dot{z} + \frac{dU(z)}{dz} + \frac{dU_g(z)}{dz} - \theta V = F_m(t) + ma_{ext}(t)$$

$$\dot{V} = -\frac{\theta}{C_p}\dot{\dot{z}} - \frac{1}{R_L C_p}V \tag{4.1}$$

where z, $\dot{z}$ and $\ddot{z}$ are respectively relative displacement (with respect to fabrication position, $z = 0$), velocity and acceleration of the free end of the cantilever beam; m is the sum of the mass of the cantilever beam, m_{beam}, and the mass of the moving permanent magnet, m_m, given by $m_m = \rho_m V_m$; c_m is the mechanical damping; $U(z)$ and U_g are respectively the magneto-elastic potential, due to the cantilever beam stiffness k and the interaction force between moving and fixed permanent magnets (which will calculated in (4.10)), and the potential of the gravitational forces defined in (4.13); θ is the piezoelectric coupling term for the beam and it is defined as $\theta = -e_{31}w_{PZT}$ [81], in which e_{31} is the piezoelectric coupling coefficient, in stress-charge form, in 31 direction of the material in the piezoelectric layer; $F_m(t)$ is the input force caused by the interaction of the magnetic field of the moving magnet and the magnetic field generated by the AC current to be

measured (which will be computed in (4.17)); $a_{ext}(t)$ is the mechanical acceleration descending from the environmental mechanical noise (e.g., mechanical vibrations) and acting on the mass m; V is the output voltage, R_L, the electrical load resistance attached to the output and C_p is the piezoelectric capacitance, defined in (4.2) [81].

$$C_p = \frac{\epsilon_{33} w_e l_e}{t_{PZT}} \tag{4.2}$$

where ϵ_{33} is the electrical permittivity in the 33 direction of the material in the piezoelectric layer, w_e and l_e are respectively the width and the length of the metal electrodes used in the piezo-stack to read the voltage difference V generated by the piezoelectric layer.

The magneto-elastic potential $U(z)$ is obtained by integrating the sum of two forces. The first force is the component along z-axis F_{kz} of the restoring elastic force of the cantilever beam and is defined in (4.3) [212].

$$F_{kz} = -kz \tag{4.3}$$

where k is the elastic coefficient of the cantilever beam given by (4.4) [199].

$$k = 3\frac{EI}{l^3} = \frac{1}{4}\frac{Ewt^3}{l^3} \tag{4.4}$$

where E is the Young Modulus of the material of the cantilever beam and I its moment of inertia. In the case of multilayered structures the Equivalent Section Method must be applied to properly compute E and I [110].

The second term is given by the component along z-axis of the magnetic interaction force $\overrightarrow{F_{im}}$ between the moving and the fixed magnets that are approximated as two magnetic dipoles: let $\overrightarrow{m_1}$ be the magnetic dipole moment of the moving magnet and $\overrightarrow{m_2}$ the magnetic dipole moment of the fixed magnet. This approximation is valid only if the modulus of the distance vector $\overrightarrow{r}$ between the two magnets is much larger than their sizes. Under the hypothesis that the two magnetic dipole moments are approximated as two linear and circular circuits carrying a current, it is possible to express an analytic formula describing the force between two magnetic dipoles in (4.4) [243] that approximates the mag-

netic interaction force $\overrightarrow{F_{im}}$ between the moving and the fixed magnets.

$$\overrightarrow{F_{im}} \simeq \frac{3\mu_0}{4\pi r^4}\{(\widehat{r}\times\overrightarrow{m_1})\times\overrightarrow{m_2}+(\widehat{r}\times\overrightarrow{m_2})\times\overrightarrow{m_1}-2\widehat{r}(\overrightarrow{m_1}\cdot\overrightarrow{m_2})+ \\ +5\widehat{r}[(\widehat{r}\times\overrightarrow{m_1})\cdot(\widehat{r}\times\overrightarrow{m_2})]\} \tag{4.5}$$

where μ_0 is the magnetic permeability of vacuum (equal to $4\pi 10^{-7}$ H/m), and r and $\widehat{r}$ are respectively the modulus and the unit vector of the vector $\overrightarrow{r}$ indicating the spatial distance between the two magnets.

Considering the orientation of the two permanent magnets and the displacement of the free end of the cantilever beam according to (3.7) and neglecting the displacement of the free end of the cantilever beam along the y-axis and the x-axis, it is possible to write the vectorial expression of the magnetic dipole moments $\overrightarrow{m_1}$ and $\overrightarrow{m_2}$ and of their mutual distance $\overrightarrow{r}$ in (4.6) in order to substitute them into (4.5).

$$\begin{aligned} \overrightarrow{m_1} &= \{m\cos[\arctan(z/\Delta)]\ ,\ m\sin[\arctan[z/\Delta)]\ ,\ 0\} \\ \overrightarrow{m_2} &= \{-m\ ,\ 0\ ,\ 0\} \\ \overrightarrow{r} &= \{-\cos[\arctan(z/\Delta)]\ ,\ 0\ ,\ \sin[\arctan(z/\Delta)]\} \end{aligned} \tag{4.6}$$

where m is the modulus of the magnetic dipole moments of both the magnets, Δ is the distance along the x-axis between the magnets. For the sake of clarity, the spatial position of these three vectors $\overrightarrow{m_1}$, $\overrightarrow{m_2}$ and $\overrightarrow{r}$ in (4.6) is illustrated in the scheme in fig. 4.4.

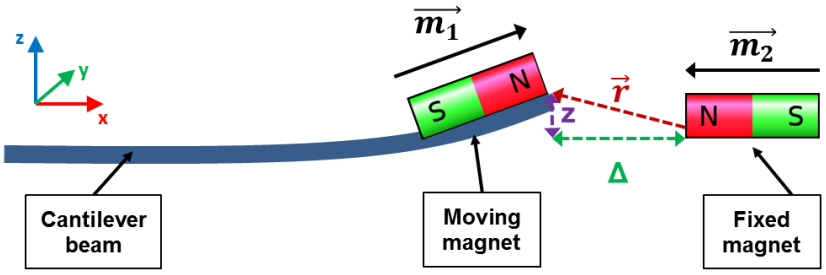

Fig. 4.4 – Schematic representation of the spatial positions of the vectors in (4.6). The image is not in scale.

The substitution of (4.6) into (4.5) leads to the evaluation of the component along z-axis F_{imz} of the magnetic interaction force $\overrightarrow{F_{im}}$, as reported in (4.7).

$$F_{imz} = \frac{9m^2\Delta\mu_0 z}{4\pi(\Delta^2 + z^2)^3} \tag{4.7}$$

Considering that the modulus m of the magnetic dipole moment $\overrightarrow{m}$ can be written as $m = MV_m$, where M is the

modulus of the magnetization vector $\overrightarrow{M}$ [212], and taking into account that the magnetic remanence B_r of the permanent magnets can be written as $B_r = \mu_0 M$ [212], the modulus m of the magnetic dipole moment can be related to the magnetic remanence B_r of the permanent magnets as in (4.8).

$$m = \frac{B_r V_m}{\mu_0} \tag{4.8}$$

The substitution of the (4.8) into (4.7) results in (4.9).

$$F_{imz} = \frac{9{B_r}^2{V_m}^2 \Delta z}{4\pi\mu_0(\Delta^2 + z^2)^3} \tag{4.9}$$

By summing and integrating F_{kz} from (4.9) and F_{imz} from (4.3), the expression of the magneto-elastic potential $U(z)$ in (4.10) is obtained, up to an additive constant.

$$U(z) = \frac{1}{2}kz^2 + \frac{9{B_r}^2{V_m}^2 \Delta}{16\pi\mu_0(\Delta^2 + z^2)^2} \tag{4.10}$$

The magneto-elastic potential $U(z)$ in (4.10) exhibits bi-stable behaviour only if condition in (4.11) is satisfied and in this case the unstable equilibrium position is in $z = 0$ and the two stable equilibrium positions $z_{1,2}$ are given in (4.12).

$$\sqrt[3]{\frac{9}{4}\Delta\frac{{B_r}^2 V_m}{\pi\mu_0 k}} - \Delta^2 > 0 \tag{4.11}$$

$$z_{1,2} = \pm\sqrt{\sqrt[3]{\frac{9}{4}\Delta\frac{{B_r}^2 V_m}{\pi\mu_0 k}} - \Delta^2} \tag{4.12}$$

The potential U_g of the gravitational forces is defined in (4.13) [212].

$$U_g = -mg(z_0 + z)\cos(\theta) \tag{4.13}$$

where g is the acceleration of gravity, approximately equal to 9.81 m/s^2, z_0 is the "zero-level" assumed for the force of gravity along the direction of the cantilever beam bending and θ is the angle between the direction of the cantilever beam displacement z and the direction along which the force of gravity acts. If $\cos(\theta)$ is different from zero, the total potential energy of the system [i.e. $U(z) + U_g$] will assume different values in the two stable equilibrium states and the system will have a larger probability of oscillation around one stable equilibrium state than around the other one.

The input force $F_m(t)$ caused by the interaction of the magnetic field of the moving magnet and the magnetic field generated by the AC current to be measured is given by (4.14) [137].

$$F_m = \int \frac{d}{dr} H_h(t) dV_m \tag{4.14}$$

where $H_h(t)$ is the component on h direction (i.e. the direction of the minimum distance between the wire carrying the AC target current and the moving magnet) of the magnetic field irradiated by the AC electrical current to be measured and it is defined in (4.15) [137]

$$H_h(t) = \frac{I(t)}{2\pi h} \tag{4.15}$$

where h is the radial distance of the moving magnet from the wire and $I(t)$ is the AC current to be measured, that is assumed in the form in (4.16).

$$I(t) = A \sin(2\pi f t) + n(t) \tag{4.16}$$

where A is the amplitude of the current (the term to be measured), f is its frequency (equal to 50 Hz or 60 Hz, depend-

ing on the countries) and $n(t)$ is the electrical noise carried by the current.

Through the combination of (4.14), (4.15) and (4.16) and evaluating the integral in (4.14) (where the integrand is constant with respect to the variable of integration, therefore it is possible to take it out of the integral significantly simplifying its calculation), the expression of the input force F_m, acting along the z-axis, in (4.17) is obtained

$$F_m = B_r V_m \frac{A\sin(2\pi f t) + n(t)}{2\pi h^2} \tag{4.17}$$

In (4.17), the distance h is considered larger than the cantilever beam tip deflection z and for this reason the influence of the displacement z is neglected in (4.17).

4.4 Bistable AC current microsensor in PiezoMUMPs® process

A bistable AC current microsensor has been designed for a future fabrication in the PiezoMUMPs® process from MEMSCAP™.

The characteristics, the specifications and the design rules of the PiezoMUMPs® process are discussed in subsection 2.1.3 [63] and the model in (4.1) has been taken into account.

The mechanical layer of the cantilever beam is composed of a n-doped silicon (Si) layer having a thickness t of 10 µm. After the consideration of several sizes, the length l and the width w have been designed respectively to 2.5 mm and 900 µm in order to not exceed with the beam dimensions and to favourite the deposition by hand of the moving permanent magnet on the free end of the cantilever beam.

On the silicon layer, a 0.5 µm thick (t_{PZT}) layer of piezoelectric aluminium nitride layer (AlN) is deposited by hand to implement the piezoelectric conversion in the device. The layer of the AlN has been patterned in order to respect PiezoMUMPs® design rules [63] and has a length l_{PZT} and a width w_{PZT} of 2.495 mm and of 890 µm, respectively.

The electrodes of the piezoelectric layer are implemented by the n-doped mechanical silicon layer in the bottom side, that also acts as bottom electrode, and by a 1.1 µm thick aluminium (Al) layer that acts as top electrode. In order to

respect PiezoMUMPs® design rules [63], the length l_e and the width w_e of the Al top electrode are respectively 2.492 mm and of 887 µm. The top electrode is separated into two sub-electrodes (one on the right side and the other on the left side separated by a spacing of 10 µm), however, these two electrodes are connected in short circuit in this device and considered as a single electrode in this work.

According to this configuration, the device operates in d_{31} mode.

A 0.2 µm thick silicon dioxide layer has been used as electrically isolating layer to separate conductive layers, implementing top and bottom electrodes, in the routing of the piezo stack.

At the free end of the cantilever beam, a silicon (Si) mechanical proof mass is attached (on its bottom side) in order to increase the device sensitivity to both the external magnetic force $F_m(t)$ and the acceleration from the mechanical noise $a_{ext}(t)$ by providing a larger value of the mass m in (4.1). The proof mass is composed of the SOI substrate of the PiezoMUMPs® process and has a length of 695 µm, a

width of 900 µm and a thickness of 400 µm. The buried oxide of the SOI substrate has been neglected.

As the cantilever beam is a multilayer structure, its elastic constant k has been evaluated through the equivalent section model.

The 3D model of the discussed cantilever beam is shown in fig. 4.5.

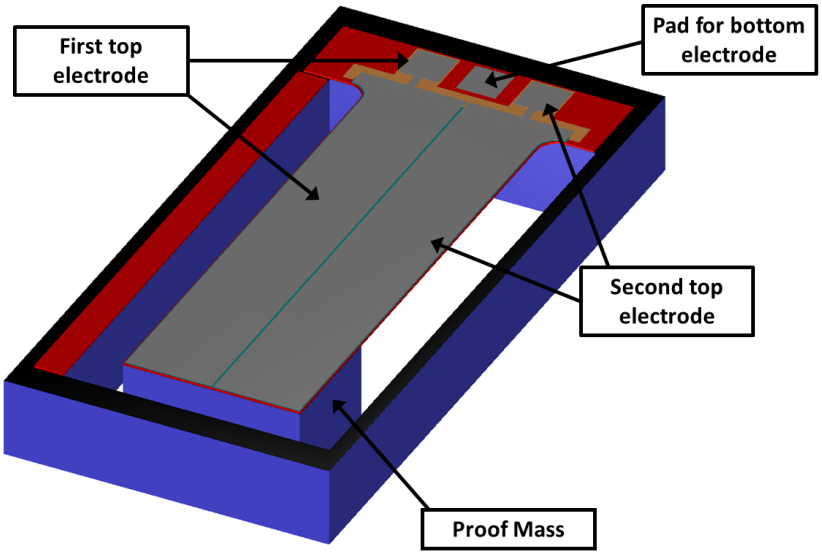

Fig. 4.5 – 3D model of the cantilever beam designed to implement the AC current microsensor proposed in this work. The two top electrodes are connected in short circuit in this device and considered as a single electrode.

The moving permanent magnet is deposited in post-process on the free end of the beam in order to obtain the structure in fig. 4.3. In this case, a neodymium (NdFeB) magnet having a cylindrical shape with a height of 1 mm and a radius of 0.5 mm has been chosen. An equal magnet is placed at the distance Δ from the moving magnet to implement the fixed magnet.

Material properties used in this design are listed in table 4.1.

The distance h between the cable carrying the AC current to be measured and the moving magnet has been fixed to 1 mm. A mechanical damping coefficient c_m of 1e-9 kg/m [9] and an electrical load resistance of 330 kΩ have been adopted.

Finally, it has been assumed that the gravity force acts in the orthogonal direction ($\theta = 90°$) with respect to the axis of the cantilever beam displacement z.

The achieved results from the simulations of the microsensor will be presented in the subsection 4.4.1 in order to assess the device behaviour and the model proposed in (4.1).

Table 4.1 – Material properties used in the design and simulations of the AC microsensor [213].

Properties	**Values for Si**
Mass density	2329 kg/m^3
Young Modulus	170 GPa
	Values for AlN
Mass density	3260 kg/m^3
Young Modulus in 33 direction	410 GPa
Piezoelectric coupling in 31 direction e_{31}	-0.58 C/m^2
Electrical permittivity in 33 direction ϵ_{33}	7.97 pF/m
	Values for Al
Mass density	2700 kg/m^3
Young Modulus	70 GPa
	Values for NdFeB
Mass density	7400 kg/m^3
Magnetic remanence B_r	1170 mT [187]

4.4.1 Device simulations

The model of the device in (4.1), along with the parameter values presented in section 4.4, has been simulated in the Simulink® environment of Matlab® platform.

The aim is to assess, through the validation of the device model, that a bistable system can achieve better performance

than a linear resonant system in terms of sensing capabilities (in certain operating conditions) and energy harvested.

Design of the distance between permanent magnets

After the consideration of the device model in (4.1) and the examination of the given parameter values in section 4.4, the distance Δ between permanent magnets must be defined. The application of those parameter values to (4.11) leads to a limit value of $\Delta = 3.32$ mm in order to achieve bistable behaviour: for values of Δ smaller than 3.32 mm, the system exhibits bistable behaviour, for larger distances linear resonant behaviour is expected. This means that the distance Δ plays a crucial role in the device operation.

In fact, in the bistable operative range ($\Delta \leq 3.32$ mm), taking into account (4.10), different values of the parameter Δ result in bistable magneto-elastic potentials $U(z)$ having distinct shapes, as shown in the plot in fig. 4.6 for four different values of the distance Δ (2.1 mm, 2.2 mm, 2.25 mm, 2.3 mm).

In particular, since the distance Δ affects the magnetic levitation force between permanent magnets, higher values of Δ in the bistable operative range lead to smaller inter-

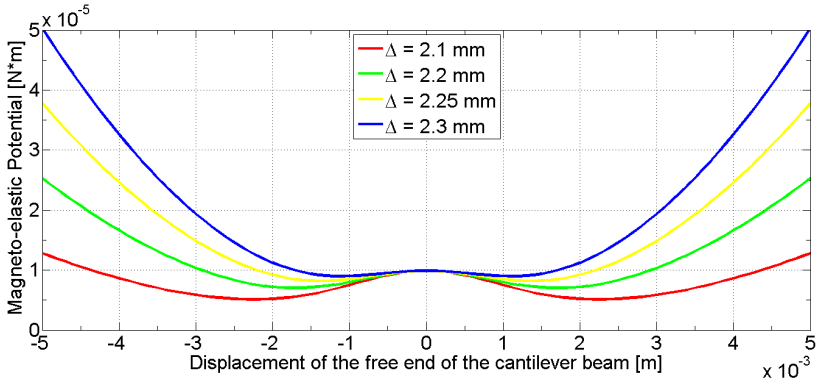

Fig. 4.6 – Comparison of four bistable magneto-elastic potentials $U(z)$, computed through (4.10) and the parameter values in section 4.4, obtained with four different values of the distance Δ (2.1 mm, 2.2 mm, 2.25 mm, 2.3 mm).

action forces and, then, lower energy is required to trigger commutations in the bistable device as the potential barrier in the magneto-elastic potential $U(z)$ is reduced as shown in fig. 4.6. This causes that a given level of the input force $F_m(t)$, linked to the AC target input current $I(t)$ through the (4.17), will induce more commutations for increasing values of Δ in the bistable operation range. As the measurement of the input current $I(t)$ is performed by counting the number of the beam commutations, the output of the sensor and its operative range are strongly affected by the distance Δ.

Accurate attention should also be paid to the level of input mechanical noise: In fact, the ranges of the acceleration a_{ext} induced by mechanical noise and its effect on the bistable system (given its magneto-elastic bistable potential) must be investigated. If an energy harvesting application must be addressed, external noise should be enough to guarantee the presence of beam switchings (i.e. high energy orbits behaviour). In this sensing application, however, the measurement of the unknown quantity is performed by counting of the number of beam commutations; therefore, it is evident that commutations triggered by mechanical noise cannot be counted in the evaluation of the target current.

For this reason, in the designing of the distance Δ, first of all, it is necessary to verify the minimum and the maximum amplitude of the AC current that the sensor is able to detect and, then, the maximum level of vibrational noise should be investigated to avoid device commutations induced by the input vibrational acceleration.

Model simulations

Before running the simulations of the device, the specifications of the system inputs have been investigated. Given the sizes of the microstructure, external accelerations a_{ext} having a Root Mean Square (RMS) value smaller than 1g have been considered to speed up and simplify the design.

The input mechanical noise a_{ext} has been modeled through a band-limited white noise with a given gain to regulate its RMS value and filtered by a eighth-order Butterworth low-pass filter having a cut-off frequency of 500 Hz.

Examples of the time series of the input acceleration a_{ext} and its Power Spectrum Density (PSD) are shown in figs. 4.7–4.12 for three distinct RMS values of the input acceleration (0.031g, 0.31g and 0.98g).

Considering as input several AC current magnitudes without electrical noise $n(t) = 0$, several levels of input mechanical noise a_{ext} and the parameters described in section 4.4, the system in (4.1) has been numerically simulated in Simulink® using Runge-Kutta "ODE45" integration formula [44]. As results of simulations, the number of commutations between the

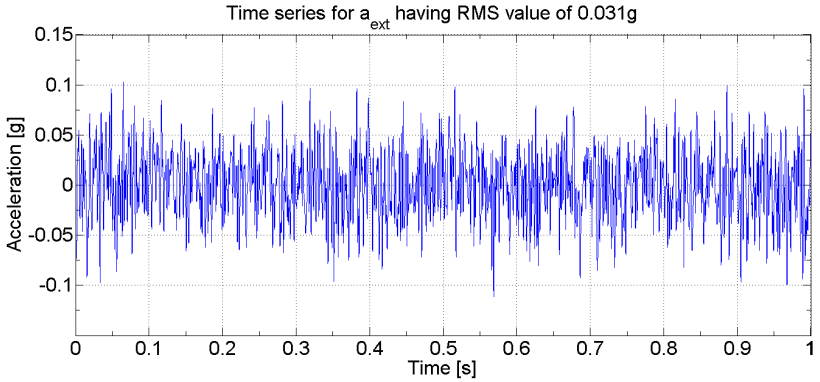

Fig. 4.7 – Time series of the input acceleration a_{ext} having a RMS value of 0.031g.

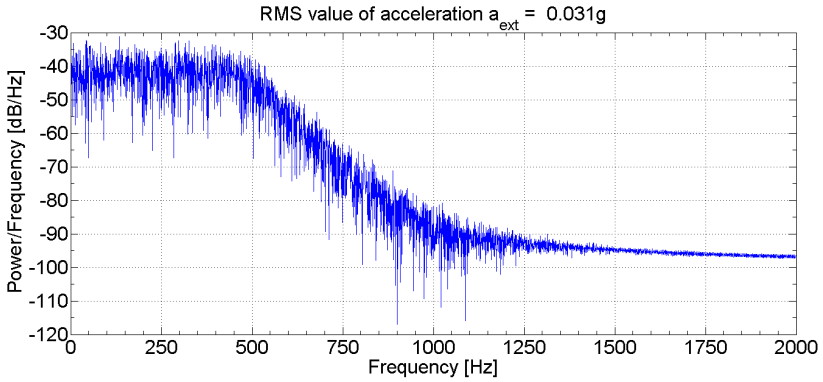

Fig. 4.8 – PSD of the input acceleration a_{ext} having a RMS value of 0.031g.

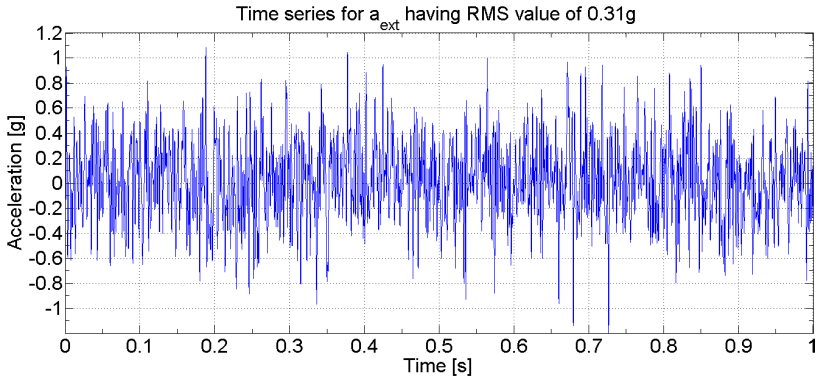

Fig. 4.9 – Time series of the input acceleration a_{ext} having a RMS value of 0.31g.

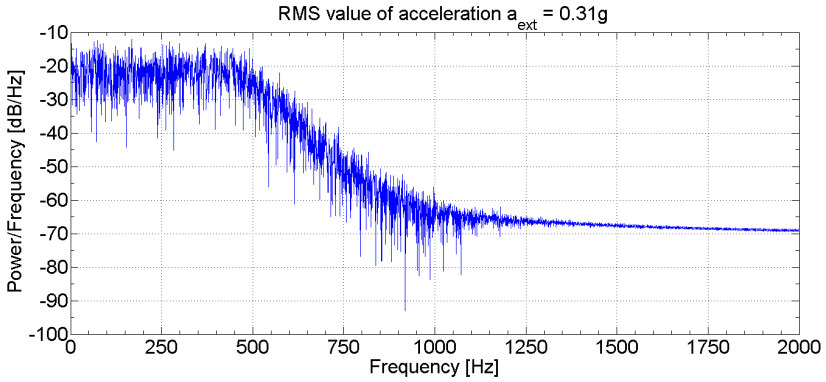

Fig. 4.10 – PSD of the input acceleration a_{ext} having a RMS value of 0.31g.

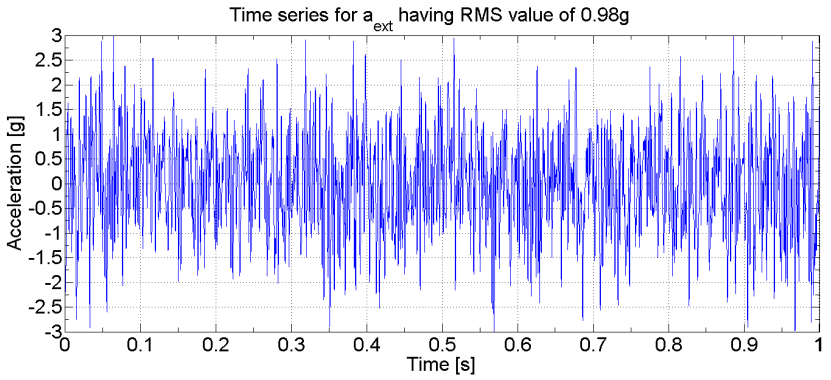

Fig. 4.11 – Time series of the input acceleration a_{ext} having a RMS value of 0.98g.

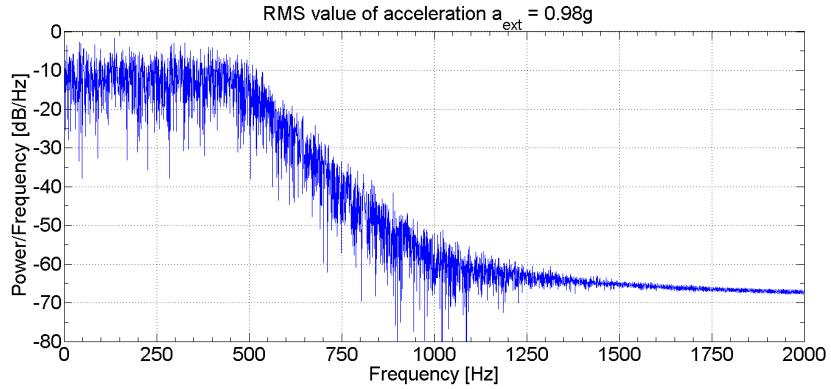

Fig. 4.12 – PSD of the input acceleration a_{ext} having a RMS value of 0.98g.

stable equilibrium states has been counted in a time interval of 1 s, when the system is in its steady state. For each AC current magnitude taken into account, 30 simulations have been carried out to characterize the number of commutations in terms of average values and standard deviations.

Four different values of the distance Δ (2.1 mm, 2.2 mm, 2.25 mm, 2.3 mm), two values of the frequency f of AC target current (50 Hz and 60 Hz) and five RMS values of the the input acceleration (0.031g, 0.16g, 0.31g, 0.91g and 0.98g) have been investigated in the simulations. Results for AC current frequency of 50 Hz are presented in figs. 4.13–4.17.

Results for AC current frequency of 60 Hz are presented in figs. 4.18–4.22.

Results in figs. 4.13–4.22 show that there are not so great differences in the behaviour of the system at 50 Hz and 60 Hz of AC current frequency.

It should be noted also that three operative regions can be identified on the basis of the AC target current magnitude. In the first region, the magnitude of the AC current $I(t)$ leads to an input force F_m (through 4.17) lower than the bistable po-

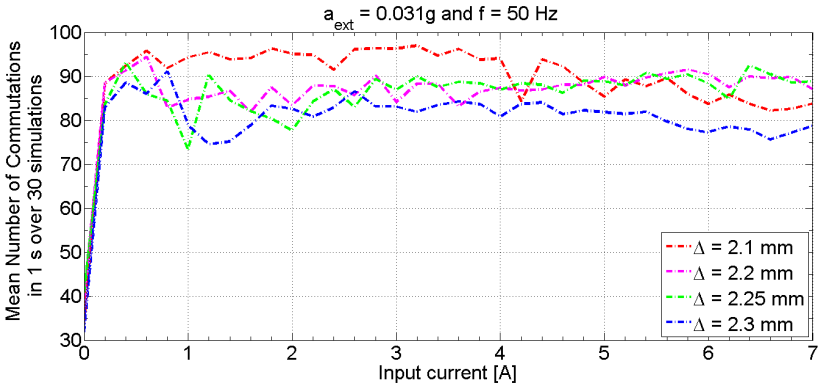

Fig. 4.13 – Mean number of commutations in 1 s, over 30 simulations, versus AC current magnitude at a frequency of 50 Hz, when the RMS value of input acceleration a_{ext} is 0.031g, for four values of the distance Δ (2.1 mm, 2.2 mm, 2.25 mm, 2.3 mm).

tential barrier; in this case, the system oscillates only around one of its stable equilibrium states or exhibits some commutations induced by the external mechanical noise a_{ext}; this region can be named "subthreshold" region. In the second region, the level of the force F_m generated by the AC target current is able to put the system in commutation between its stable equilibrium states and the number of commutations increases when the AC current magnitude grows and the level of mechanical noise is fixed: in this case the system can be used

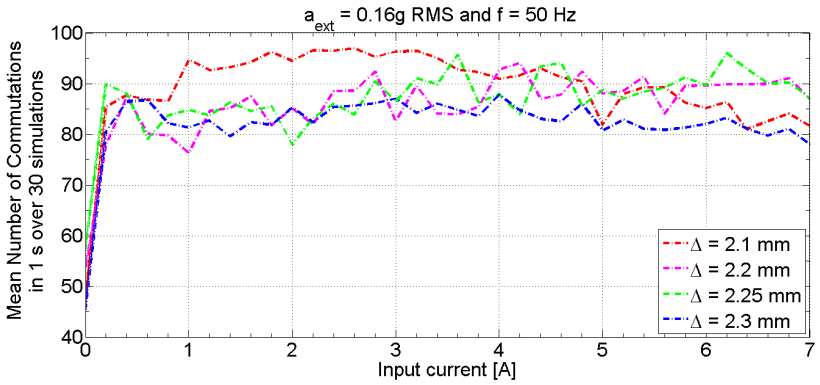

Fig. 4.14 – Mean number of commutations in 1 s, over 30 simulations, versus AC current magnitude at a frequency of 50 Hz, when the RMS value of input acceleration a_{ext} is 0.16g, for four values of the distance Δ (2.1 mm, 2.2 mm, 2.25 mm, 2.3 mm).

to measure the magnitude of the AC current and the limits of this region, given by the AC current magnitude, define the operative range of the sensor; this region can be named "operative" region. In the third region, due to the high level of the input current, the number of commutations saturates to a fixed value, in a time interval, imposed by the nonlinear system and by the frequency f of the current $I(t)$, in this region variations in the number of commutations are caused

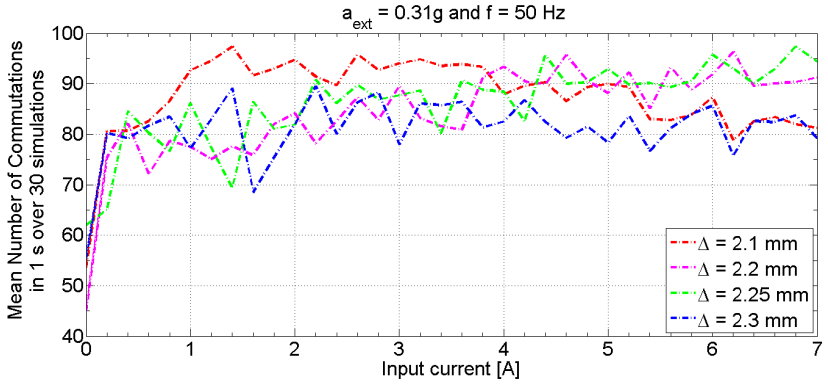

Fig. 4.15 – Mean number of commutations in 1 s, over 30 simulations, versus AC current magnitude at a frequency of 50 Hz, when the RMS value of input acceleration a_{ext} is 0.31g, for four values of the distance Δ (2.1 mm, 2.2 mm, 2.25 mm, 2.3 mm).

only by the mechanical noise a_{ext}; this region can be named "saturation" region.

The operative range of the sensor (i.e. the limits of the second operative region) can be adapted by properly designing of the distance Δ which tunes the potential barrier and can be used to reduce the effect of the mechanical noise on the system. However, the presence of the mechanical noise helps the system in commutating even if the level of the AC current magnitude is low. In this way, the operative range of the sen-

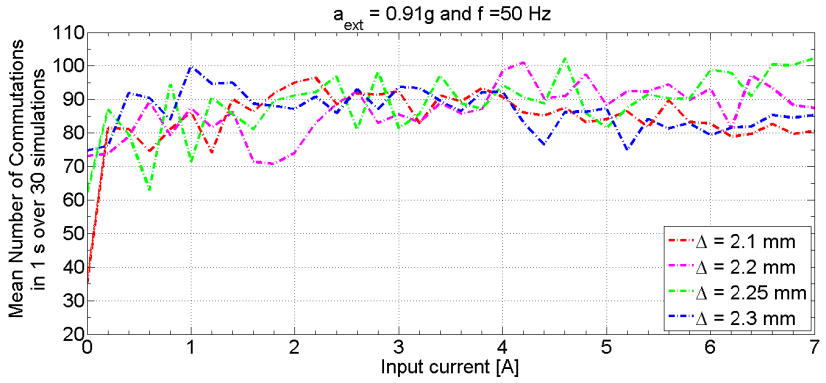

Fig. 4.16 – Mean number of commutations in 1 s, over 30 simulations, versus AC current magnitude at a frequency of 50 Hz, when the RMS value of input acceleration a_{ext} is 0.91g, for four values of the distance Δ (2.1 mm, 2.2 mm, 2.25 mm, 2.3 mm).

sor can be modified and, in a favourable situation, extended by the external noise as expected in the "Noise Activated Nonlinear Dynamic Sensors" [88].

It is also worth noting that only the number of commutations caused by the force F_m has to be considered in the AC current measurement and, for this reason, techniques to "discriminate" the useful signal from the noise, like the characterization of the system commutations in terms of mean and standard deviation in time intervals and the adoption of al-

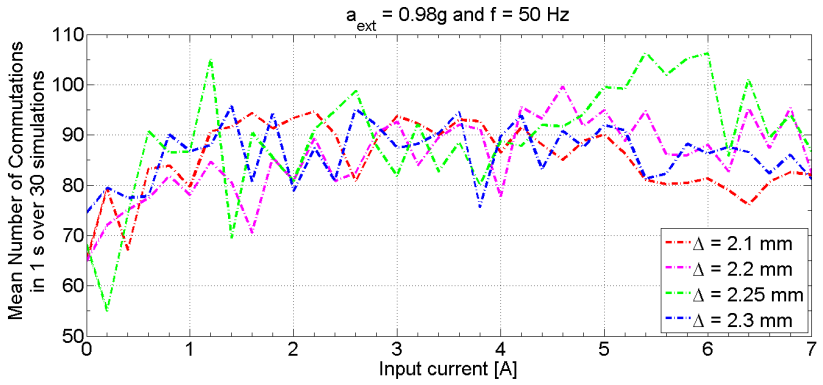

Fig. 4.17 – Mean number of commutations in 1 s, over 30 simulations, versus AC current magnitude at a frequency of 50 Hz, when the RMS value of input acceleration a_{ext} is 0.98g, for four values of the distance Δ (2.1 mm, 2.2 mm, 2.25 mm, 2.3 mm).

gorithms based on multiple thresholds in the counting of the commutations, should be adopted. The aforesaid techniques are applied to all the simulations presented in this work.

An example of the waveform of the beam displacement compared with the sinusoidal AC input current, when the device is at steady state in its operative region is illustrated in the plot in fig. 4.23 for the sake of completeness.

In order to evaluate the sensor operation in some "real" operative conditions, four simulation case studies have been car-

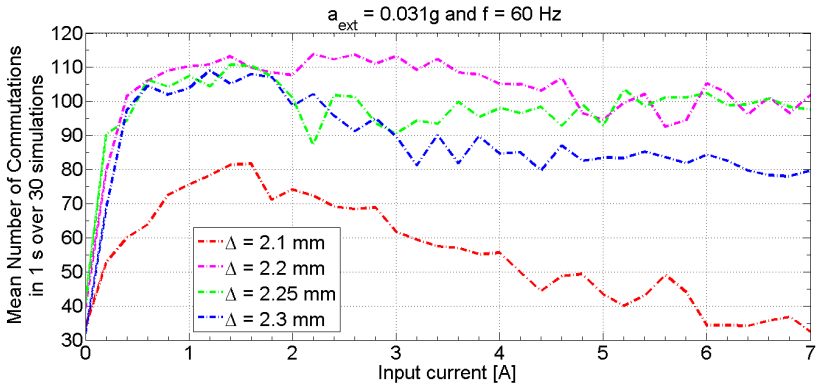

Fig. 4.18 – Mean number of commutations in 1 s, over 30 simulations, versus AC current magnitude at a frequency of 60 Hz, when the RMS value of input acceleration a_{ext} is 0.031g, for four values of the distance Δ (2.1 mm, 2.2 mm, 2.25 mm, 2.3 mm).

ried out by considering the electric current absorbed by some household appliances powered at a voltage V of 220 V and a frequency of 50 Hz. In these cases, considering the power consumption P required by the single appliance (obtained from its datasheet) and the powering voltage V required (i.e. 220 V in Europe), the nominal absorbed AC current I is calculated through the manipulation of the (4.18) [212].

$$P = VI \tag{4.18}$$

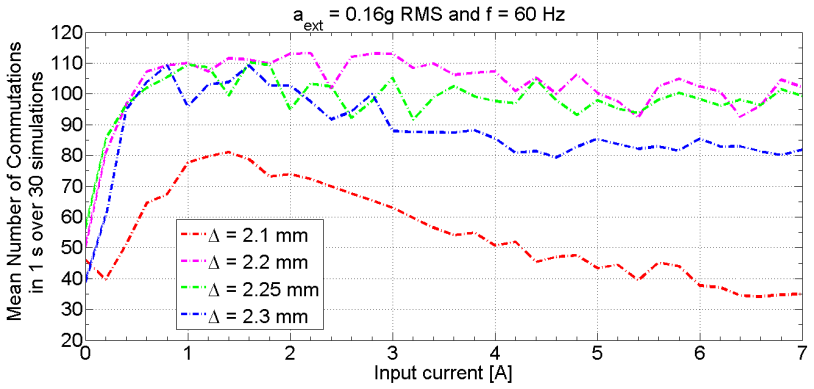

Fig. 4.19 – Mean number of commutations in 1 s, over 30 simulations, versus AC current magnitude at a frequency of 60 Hz, when the RMS value of input acceleration a_{ext} is 0.16g, for four values of the distance Δ (2.1 mm, 2.2 mm, 2.25 mm, 2.3 mm).

The four case studies are listed in table 4.2 [66].

Table 4.2 – Data of the power required by the home appliances studied [66].

Household appliance	Power required	Nominal absorbed current
Washing machine	2000 W	9 A
Air conditioner	1000 W	4.5 A
Refrigerator	200 W	1.9 A
TV set	100 W	0.45 A

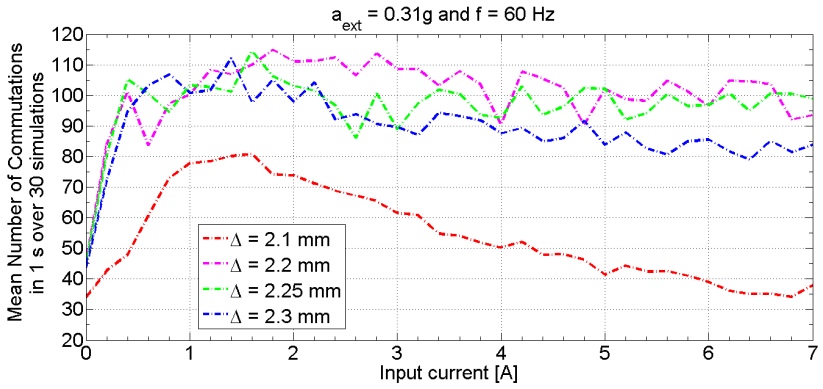

Fig. 4.20 – Mean number of commutations in 1 s, over 30 simulations, versus AC current magnitude at a frequency of 60 Hz, when the RMS value of input acceleration a_{ext} is 0.31g, for four values of the distance Δ (2.1 mm, 2.2 mm, 2.25 mm, 2.3 mm).

It should be noted that each household appliance must respect the legislation about electromagnetic compliance [175].

Because each household appliance considered in table 4.2 has a different level of nominal absorbed current, different values of the distance Δ have been adopted for each case study. In particular, Δ = 2.1 mm has been chosen for case of the washer machine, Δ = 2.2 mm for the air conditioner, Δ = 2.25 mm for the refrigerator and Δ = 2.3 mm for

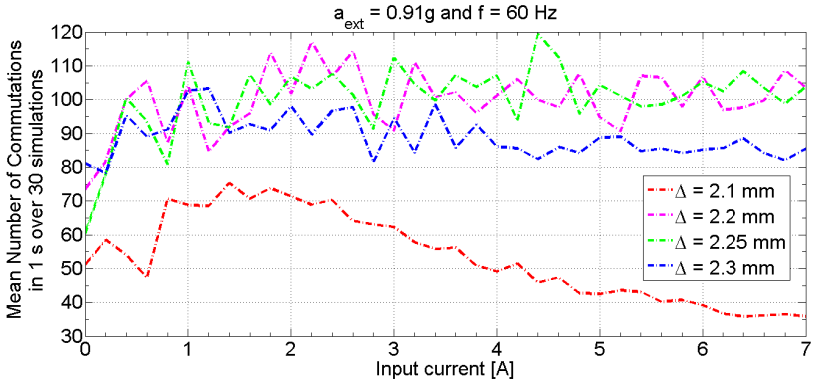

Fig. 4.21 – Mean number of commutations in 1 s, over 30 simulations, versus AC current magnitude at a frequency of 60 Hz, when the RMS value of input acceleration a_{ext} is 0.91g, for four values of the distance Δ (2.1 mm, 2.2 mm, 2.25 mm, 2.3 mm).

the TV set. Obviously, the model in (4.1) and the parameter values in section 4.4 have been used.

Results of each of the four case studies is reported in the following.

Case study: washer machine

The application of a distance $\Delta = 2.1$ mm results in two stable equilibrium positions centered in $z_{1,2} = \pm 889$ µm, according to the (4.12).

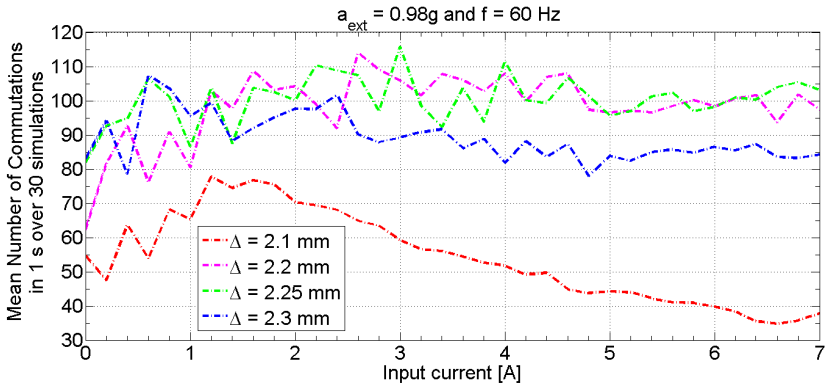

Fig. 4.22 – Mean number of commutations in 1 s, over 30 simulations, versus AC current magnitude at a frequency of 60 Hz, when the RMS value of input acceleration a_{ext} is 0.98g, for four values of the distance Δ (2.1 mm, 2.2 mm, 2.25 mm, 2.3 mm).

The mean number of commutations in 1 s, over 30 simulations, versus several AC current magnitudes at a frequency of 50 Hz, for different RMS values of the input acceleration a_{ext} has been evaluated and simulation results are reported in fig. 4.24

From fig. 4.24, it is easy to identify the operative region of the sensor and how its limits change with the level of the mechanical noise. Furthermore, it is possible to observe that in the saturation region the number of commutations in 1 s

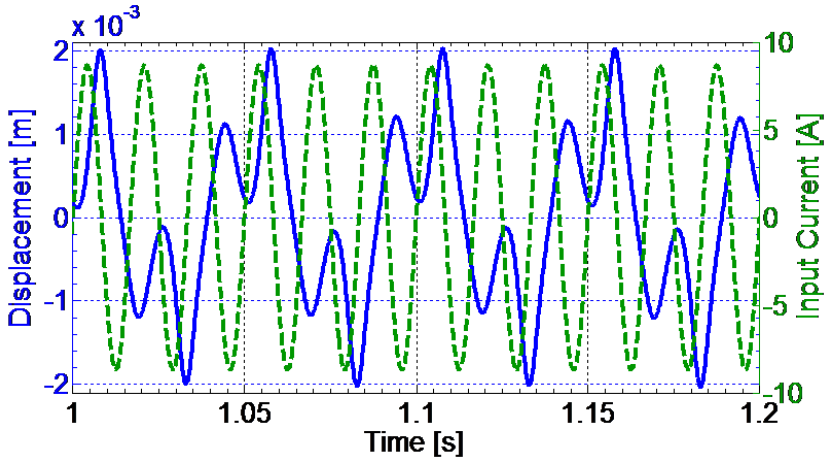

Fig. 4.23 – Waveform of the displacement (straight line) of the tip of the cantilever beam compared with the AC input current (dashed line) when the sensor is in its operative region.

saturates at around twice the frequency f of the AC target current (i.e. 100 commutations in 1 s): this means that the beam commutates at both the rising front of the sinusoid of the current $I(t)$ and the falling front.

At this point, since only switchings coming from AC current have to be considered, it is necessary to identify the minimum level of the mechanical noise that generates commutations when the AC target current is null ($I(t) = 0$ A). Simulation data indicate that the system starts to commu-

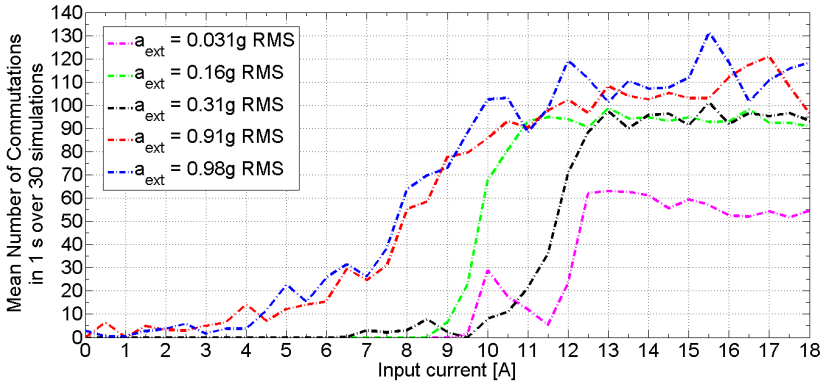

Fig. 4.24 – Mean number of commutations in 1 s, over 30 simulations, versus AC current magnitude at a frequency of 50 Hz, when the distance Δ is 2.1 mm, for five RMS values of the input acceleration a_{ext} (0.031g, 0.16g, 0.31g, 0.91g and 0.98g).

tate for RMS values of the acceleration a_{ext} larger than 0.75g: this means that, in this application, the sensor can work in environments where the level of mechanical noise is below 0.75g RMS.

After the determination of the limit value for the noise level, the operative range of the sensor with $\Delta = 2.1$ mm is evaluated in fig. 4.25 when the mechanical noise level is between 0g and 0.75g RMS.

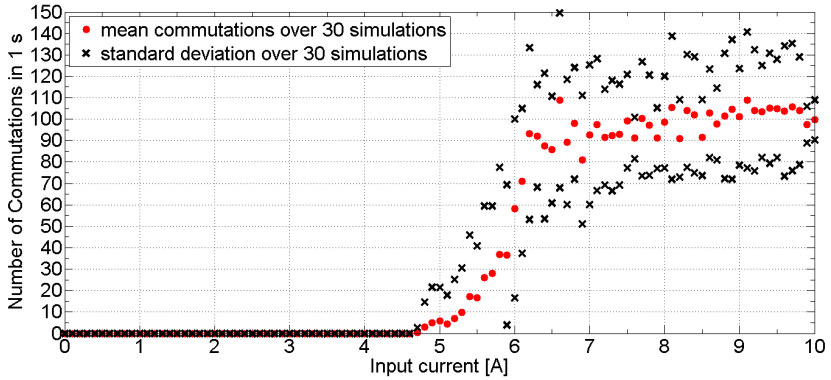

Fig. 4.25 – Mean number of commutations and standard deviation in 1 s, over 30 simulations, versus AC current magnitude at a frequency of 50 Hz, when the distance Δ is 2.1 mm and the input acceleration a_{ext} is between 0g and 0.75g RMS.

From fig. 4.25 it is possible to state that the system can detect AC currents magnitudes between 4.75 A and 9 A (with a reduction of sensitivity around 9 A for high levels of noise), according to the range of absorbed currents by the washer machine.

RMS values of the displacement of the beam and of the voltage output from the piezoelectric layer of the device (i.e. the energy harvested by the system), for different AC cur-

rent magnitudes are reported respectively in fig. 4.26 and in fig. 4.27.

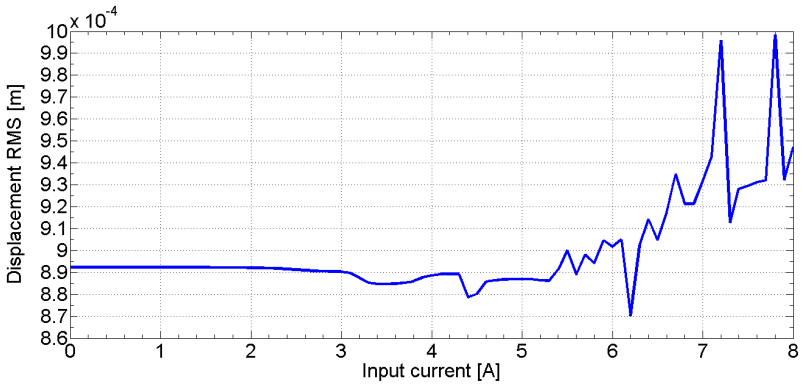

Fig. 4.26 – RMS values of the cantilever beam displacement versus AC current magnitude at a frequency of 50 Hz, when the distance Δ is 2.1 mm and the input acceleration a_{ext} is between 0g and 0.75g RMS.

From fig. 4.26 and in fig. 4.27 it is evident that, when the cantilever beam starts switching, the RMS values of its displacement and of its output voltage strongly increase and the amount of energy harvested grows.

The power harvested P_h by the device can be easily derived considering the RMS value of the output voltage V_{RMS} in fig. 4.27 and the load resistor R_L in (4.19) [212].

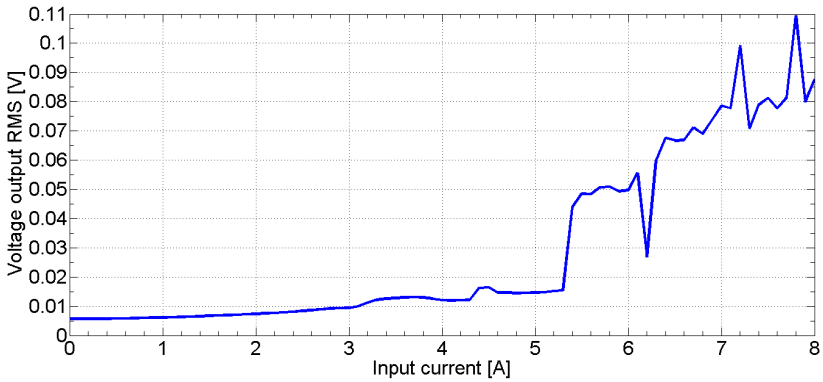

Fig. 4.27 – RMS values of the output voltage of the piezoelectric layer versus AC current magnitude at a frequency of 50 Hz, when the distance Δ is 2.1 mm and the input acceleration a_{ext} is between 0g and 0.75g RMS.

$$P_h = \frac{{V_{RMS}}^2}{R_L} \tag{4.19}$$

According to the results in fig. 4.27 and to (4.19), the nominal power scavenged at the AC current magnitude of 8 A is about 24.5 nW.

The same methodology of study has been applied to other three case studies.

Case study: air conditioner

The application of a distance $\Delta = 2.2$ mm results in two stable equilibrium positions centered in $z_{1,2} = \pm 669$ µm, according to the (4.12).

The mean number of commutations in 1 s, over 30 simulations, versus several AC current magnitudes at a frequency of 50 Hz, for different RMS values of the input acceleration a_{ext} has been evaluated and simulation results are reported in fig. 4.28.

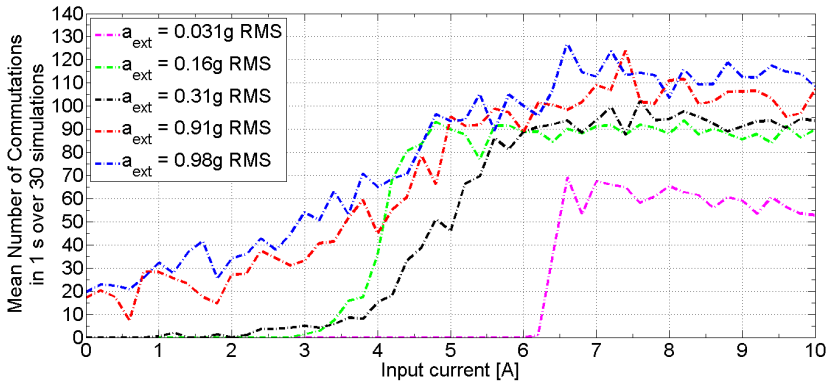

Fig. 4.28 – Mean number of commutations in 1 s, over 30 simulations, versus AC current magnitude at a frequency of 50 Hz, when the distance Δ is 2.2 mm, for five RMS values of the input acceleration a_{ext} (0.031g, 0.16g, 0.31g, 0.91g and 0.98g).

The behaviour exhibited in fig. 4.28 is similar to the one obtained in fig. 4.24, even if operative region has different limits because of the lower value of Δ that reduces the system potential barrier. This results in a smaller limit value for the input mechanical noise a_{ext} in this case study. In fact, as obtainedobtain from simulations with AC current magnitude equal to zero, the RMS limit value of the mechanical noise is 0.5g.

After the determination of the limit value for the noise level, the operative range of the sensor with $\Delta = 2.2$ mm is evaluated in fig. 4.29 when the mechanical noise level is between 0g and 0.5g RMS.

From fig. 4.29 it is possible to state that the system can detect AC currents magnitudes between 0.8 A and 5 A (with a reduction of sensitivity around 5 A for high levels of noise), according to the range of absorbed currents by the air conditioner.

RMS values of the displacement of the beam and of the voltage output from piezoelectric layer of the device (i.e. the energy harvested by the system), for different AC cur-

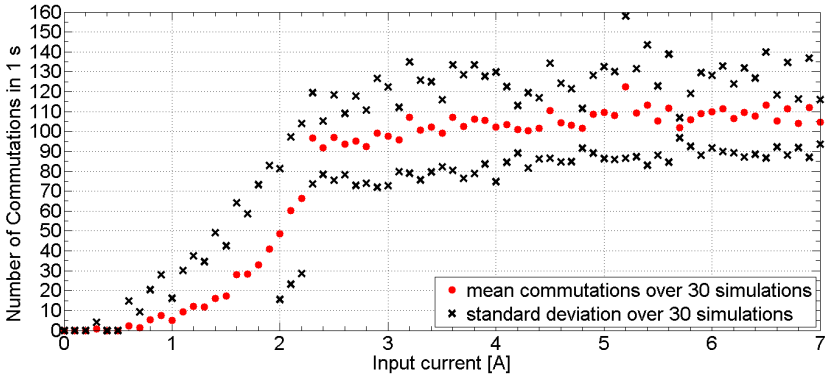

Fig. 4.29 – Mean number of commutations and standard deviation in 1 s, over 30 simulations, versus AC current magnitude at a frequency of 50 Hz, when the distance Δ is 2.2 mm and the input acceleration a_{ext} is between 0g and 0.5g RMS.

rent magnitudes are reported respectively in fig. 4.30 and in fig. 4.31.

From fig. 4.30 and in fig. 4.31 it is evident that, when the cantilever beam starts switching, the RMS values of its displacement and of its output voltage strongly increase and the amount of energy harvested grows.

According to the results in fig. 4.31 and to (4.19), the nominal power scavenged at the AC current magnitude of 4.5 A is about 3.7 nW.

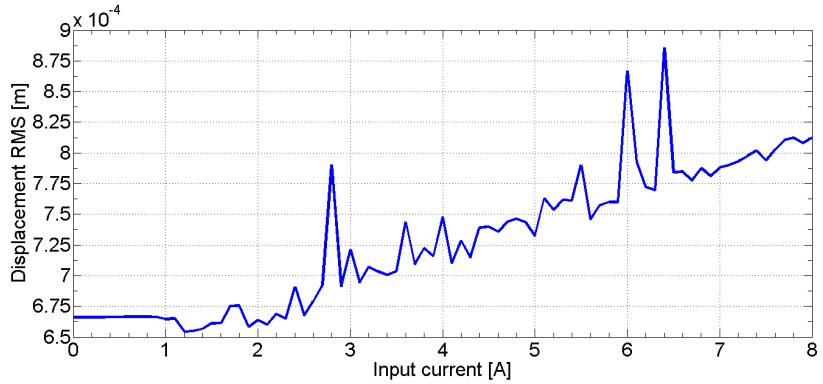

Fig. 4.30 – RMS values of the cantilever beam displacement versus AC current magnitude at a frequency of 50 Hz, when the distance Δ is 2.2 mm and the input acceleration a_{ext} is between 0g and 0.5g RMS.

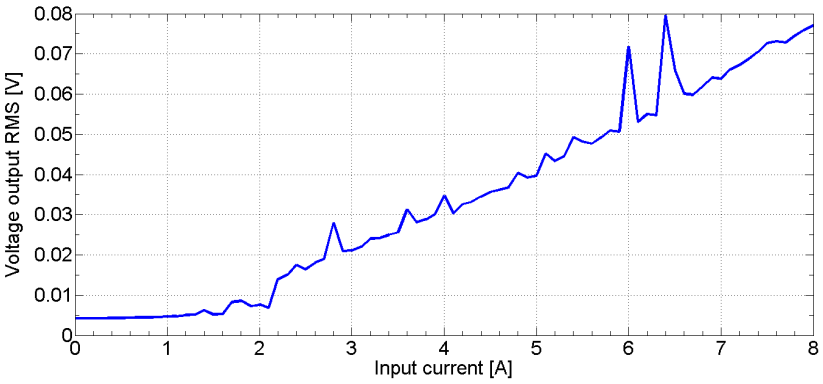

Fig. 4.31 – RMS values of the output voltage of the piezoelectric layer versus AC current magnitude at a frequency of 50 Hz, when the distance Δ is 2.2 mm and the input acceleration a_{ext} is between 0g and 0.5g RMS.

Case study: refrigerator

The application of a distance $\Delta = 2.25$ mm results in two stable equilibrium positions centered in $z_{1,2} = \pm 515$ µm, according to the (4.12).

The mean number of commutations in 1 s, over 30 simulations, versus several AC current magnitudes at a frequency of 50 Hz, for different RMS values of the input acceleration a_{ext} has been evaluated and simulation results are reported in fig. 4.32

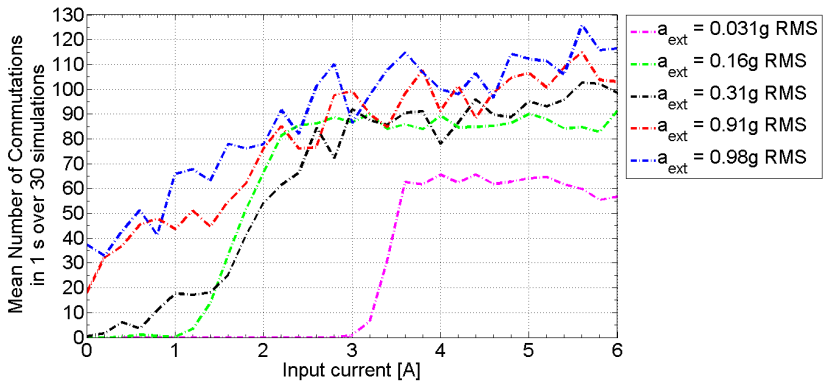

Fig. 4.32 – Mean number of commutations in 1 s, over 30 simulations, versus AC current magnitude at a frequency of 50 Hz, when the distance Δ is 2.25 mm, for five RMS values of the input acceleration a_{ext} (0.031g, 0.16g, 0.31g, 0.91g and 0.98g).

From fig. 4.32, it is evident the effect of the reduction of the potential barrier caused by the decrease of the distance Δ between permanent magnets. This leads to the reduction of the input power required to achieve commutations and decreases the range of input accelerations a_{ext} eligible for the sensor operation, as shown in fig. 4.32, where accelerations like 0.91g induce commutations also when the AC current magnitude is equal to zero.

As resulting from simulations with AC current magnitude equal to zero, the RMS limit value of the mechanical noise is 0.4g.

After the determination of the limit value for the noise level, the operative range of the sensor with $\Delta = 2.25$ mm is evaluated in fig. 4.33 when the mechanical noise level is between 0g and 0.4g RMS.

From fig. 4.33 it is possible to state that the system can detect AC currents magnitudes between 0 A and 2 A, according to the range of absorbed currents by the refrigerator.

RMS values of the displacement of the beam and of the voltage output from piezoelectric layer of the device (i.e.

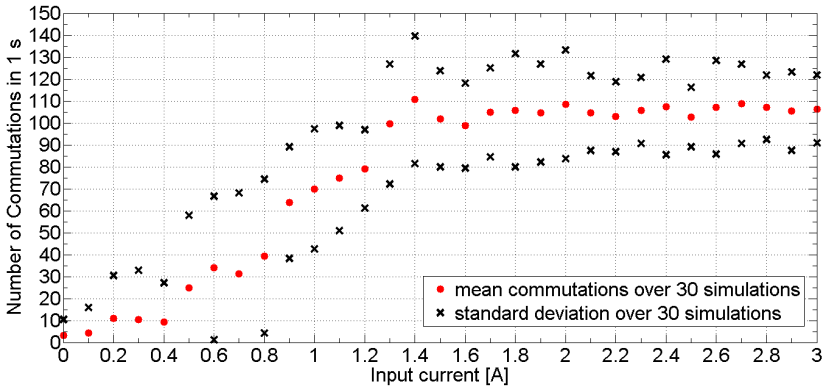

Fig. 4.33 – Mean number of commutations and standard deviation in 1 s, over 30 simulations, versus AC current magnitude at a frequency of 50 Hz, when the distance Δ is 2.25 mm and the input acceleration a_{ext} is between 0g and 0.4g RMS.

the energy harvested by the system), for different AC current magnitudes are reported respectively in fig. 4.34 and in fig. 4.35.

From fig. 4.34 and in fig. 4.35 it is evident that, when the cantilever beam starts switching, the RMS values of its displacement and of its output voltage strongly increase and the amount of energy harvested grows.

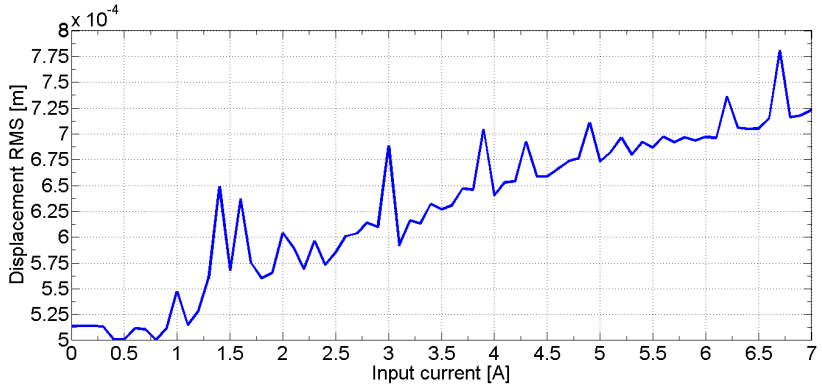

Fig. 4.34 – RMS values of the cantilever beam displacement versus AC current magnitude at a frequency of 50 Hz, when the distance Δ is 2.25 mm and the input acceleration a_{ext} is between 0g and 0.5g RMS.

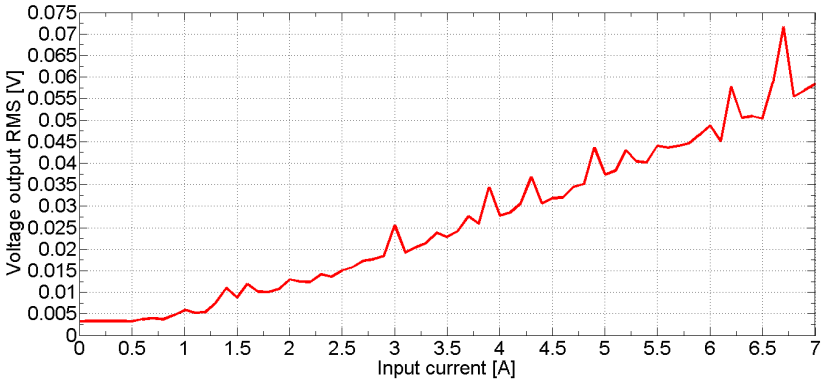

Fig. 4.35 – RMS values of the output voltage of the piezoelectric layer versus AC current magnitude at a frequency of 50 Hz, when the distance Δ is 2.25 mm and the input acceleration a_{ext} is between 0g and 0.5g RMS.

According to the results in fig. 4.35 and to (4.19), the nominal power scavenged at the AC current magnitude of 1.9 A is about 928 pW.

Case study: TV set

The application of a distance $\Delta = 2.3$ mm results in two stable equilibrium positions centered in $z_{1,2} = \pm 280$ µm, according to the (4.12).

The mean number of commutations in 1 s, over 30 simulations, versus several AC current magnitudes at a frequency of 50 Hz, for different RMS values of the input acceleration a_{ext} has been evaluated and simulation results are reported in fig. 4.36

As said in previous case studies, the adopted value of the distance Δ leads to smaller limits for the input mechanical noise. As resulting from simulations with AC current magnitude equal to zero, the RMS limit value of the mechanical noise is 0.1g.

After the determination of the limit value for the noise level, the operative range of the sensor with $\Delta = 2.3$ mm

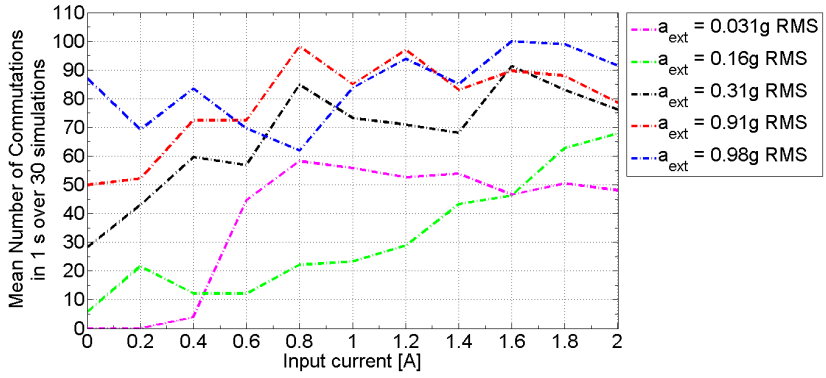

Fig. 4.36 – Mean number of commutations in 1 s, over 30 simulations, versus AC current magnitude at a frequency of 50 Hz, when the distance Δ is 2.3 mm, for five RMS values of the input acceleration a_{ext} (0.031g, 0.16g, 0.31g, 0.91g and 0.98g).

is evaluated in fig. 4.37 when the mechanical noise level is between 0g and 0.1g RMS.

From fig. 4.33 it is possible to state that the system can detect AC current magnitudes between 0 A and 0.8 A, according to the range of absorbed currents by the refrigerator.

RMS values of the displacement of the beam and of the voltage output from the piezoelectric layer of the device (i.e. the energy harvested by the system), for different AC cur-

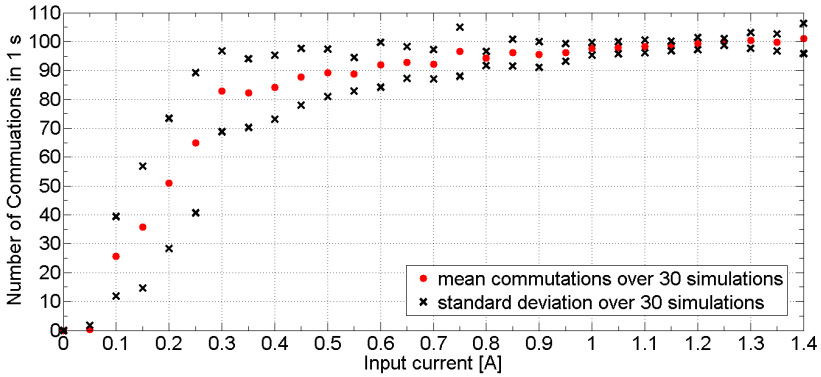

Fig. 4.37 – Mean number of commutations and standard deviation in 1 s, over 30 simulations, versus AC current magnitude at a frequency of 50 Hz, when the distance Δ is 2.3 mm and the input acceleration a_{ext} is between 0g and 0.1g RMS.

rent magnitudes are reported respectively in fig. 4.38 and in fig. 4.39.

From fig. 4.38 and in fig. 4.39 it is evident that, when the cantilever beam starts switching, the RMS values of its displacement and of its output voltage strongly increase and the amount of energy harvested grows.

According to the results in fig. 4.39 and to (4.19), the nominal power scavenged at the AC current magnitude of 0.45 A is about 9.8 pW.

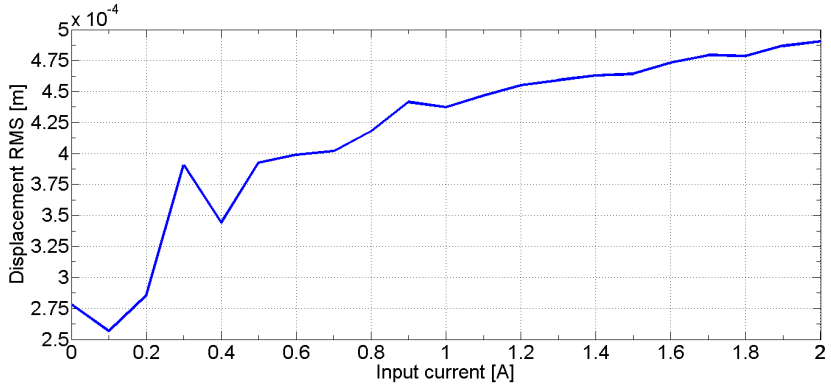

Fig. 4.38 – RMS values of the cantilever beam displacement versus AC current magnitude at a frequency of 50 Hz, when the distance Δ is 2.3 mm and the input acceleration a_{ext} is between 0g and 0.1g RMS.

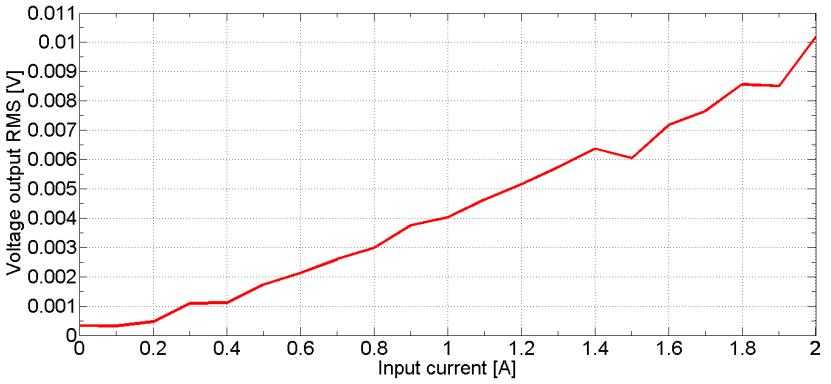

Fig. 4.39 – RMS values of the output voltage of the piezoelectric layer versus AC current magnitude at a frequency of 50 Hz, when the distance Δ is 2.3 mm and the input acceleration a_{ext} is between 0g and 0.1g RMS.

Comparison between bistable and linear AC current sensors

When the condition in (4.11) is not satisfied, the system exhibits linear resonant behaviour. As example, when the distance $\Delta = 3$ mm, the evaluation of the magneto-elastic potential $U(z)$ in (4.10) results in the plot in fig. 4.40.

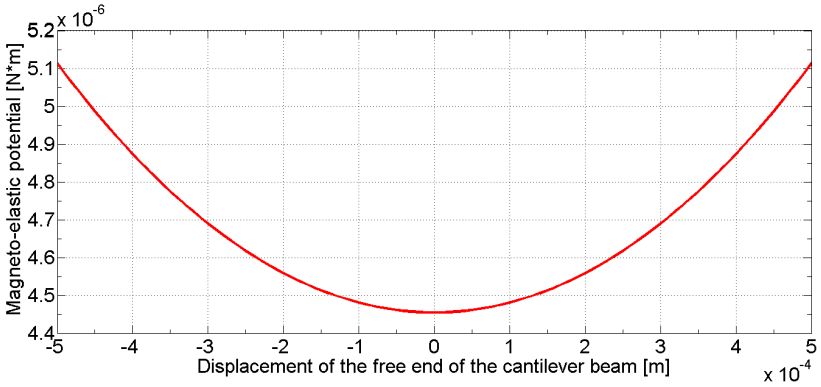

Fig. 4.40 – Monostable linear resonant potential obtained with $\Delta = 2.3$ mm.

The linear device identified by the potential in fig. 4.40 has been used as a comparison term to investigate the benefits descending from the adoption of the bistable sensor in terms of device sensitivity.

The same simulation parameters have been imposed in this comparison, with the exception, obviously, of the magneto-elastic potential $U(x)$, which determines if the device behaves linearly or in a bistable way.

Since the linear sensor performs current measurement through the amplitude of its output voltage, the RMS value of the piezoelectric output voltage from the linear sensor has been compared with the number of commutations in 1 s coming from the bistable device in order to evaluate the sensitivity of the device.

Comparative results for four different values of the distance Δ (2.1 mm, 2.2 mm, 2.25 mm, 2.3 mm) in the bistable device are shown in figs. 4.41–4.44.

The device sensitivity has been evaluated for both devices in the operative ranges defined through dotted lines in figs. 4.41–4.44.

Because the distance Δ in the linear case is fixed at 3 mm, the sensitivity can be considered equal in the four considered cases (figs. 4.41–4.44). The numerical evaluation of the sensitivity of the linear device $S_{lin\%}$ with respect to the maximum

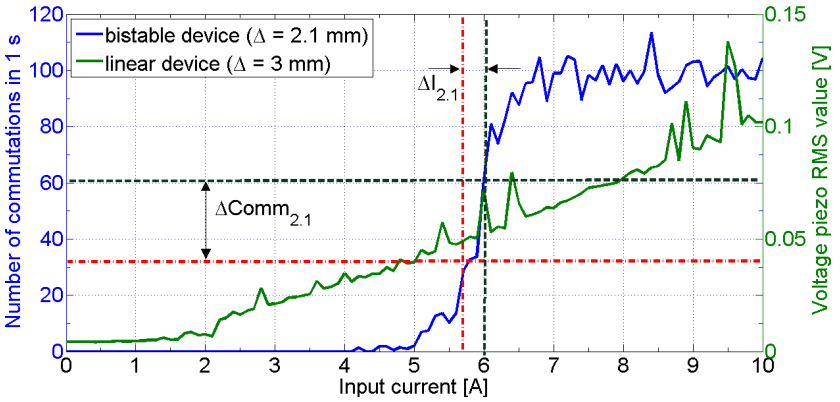

Fig. 4.41 – Number of commutations (blue line) given by the bistable device for Δ = 2.1 mm versus output RMS voltage (green line) from the linear device. The level of mechanical noise a_{ext} is 0.31g and the operative range of the bistable device is indicated through vertical dotted lines.

variation of the output voltage through Matlab® returns 10 % 1/A.

In the bistable device, the sensitivity with respect to the maximum commutations count in the operative ranges of figs. 4.41–4.44 has been evaluated in (4.20)–(4.23) respectively for the four adopted values of Δ (2.1 mm, 2.2 mm, 2.25 mm, 2.3 mm).

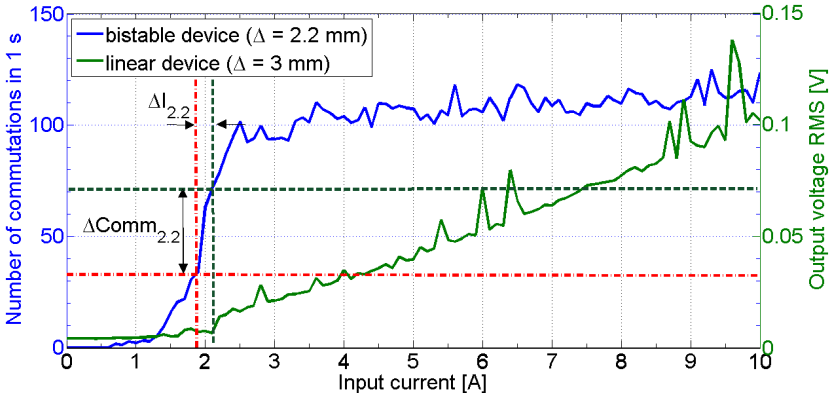

Fig. 4.42 – Number of commutations (blue line) given by the bistable device for Δ = 2.2 mm versus output RMS voltage (green line) from the linear device. The level of mechanical noise a_{ext} is 0.31g and the operative range of the bistable device is indicated through vertical dotted lines.

$$S_{bist\%\ [2.1mm]} = \frac{\Delta Comm_{2.1}}{\Delta I_{2.1}}\% = \frac{(61-32)\ comm}{0.2\ A}\% = 145\%\ 1/A \tag{4.20}$$

$$S_{bist\%\ [2.2mm]} = \frac{\Delta Comm_{2.2}}{\Delta I_{2.2}}\% = \frac{(71-34)\ comm}{0.2\ A}\% = 185\%\ 1/A \tag{4.21}$$

$$S_{bist\%\ [2.25mm]} = \frac{\Delta Comm_{2.25}}{\Delta I_{2.25}}\% = \frac{(75-47)\ comm}{0.2\ A}\% = 140\%\ 1/A \tag{4.22}$$

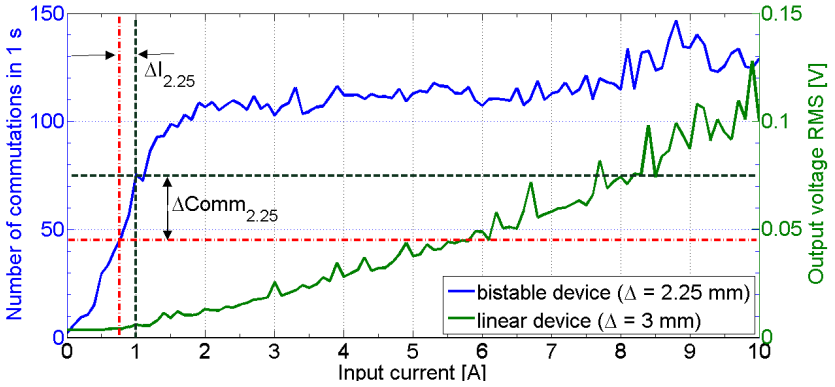

Fig. 4.43 – Number of commutations (blue line) given by the bistable device for Δ = 2.25 mm versus output RMS voltage (green line) from the linear device. The level of mechanical noise a_{ext} is 0.31g and the operative range of the bistable device is indicated through vertical dotted lines.

$$S_{bist\%\ [2.3mm]} = \frac{\Delta Comm_{2.3}}{\Delta I_{2.3}}\% = \frac{(73-32)\ comm}{0.2\ A}\% = 205\%\ 1/A \tag{4.23}$$

Where $S_{bist\%\ [2.1mm]}$, $S_{bist\%\ [2.2mm]}$, $S_{bist\%\ [2.25mm]}$ and $S_{bist\%\ [2.3mm]}$ are respectively the sensitivities of the bistable device in its operative ranges defined by the four values of Δ (2.1 mm, 2.2 mm, 2.25 mm, 2.3 mm). The values of the commutations variations $\Delta Comm_{2.1}$, $\Delta Comm_{2.2}$, $\Delta Comm_{2.25}$ and $\Delta Comm_{2.3}$ and of the current variations $\Delta I_{2.1}$, $\Delta I_{2.2}$, $\Delta I_{2.25}$ and $\Delta I_{2.3}$ can be obtained from graphs in figs. 4.41–4.44.

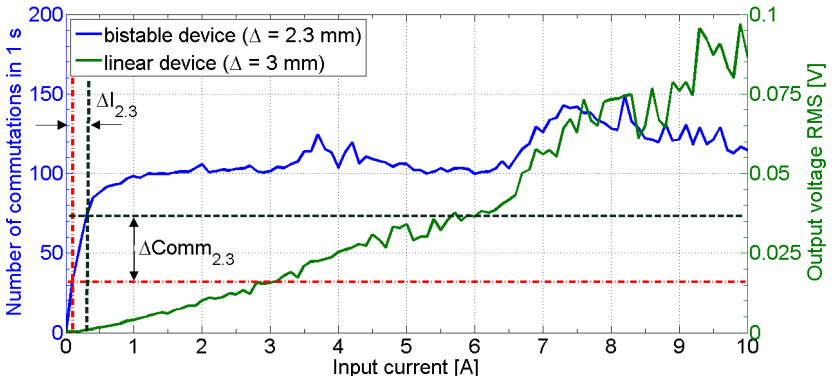

Fig. 4.44 – Number of commutations (blue line) given by the bistable device for Δ = 2.3 mm versus output RMS voltage (green line) from the linear device. The level of mechanical noise a_{ext} is 0.031g and the operative range of the bistable device is indicated through vertical dotted lines.

The comparison of the percentage values of the device sensitivities indicates that the bistable sensor exhibits a larger sensitivity than the linear resonant sensor, even if the operative range of the bistable device is smaller.

Because the adoption of the bistable device leads to an improvement in the device sensitivity as long as the sensor lies in its operative range, the use of the proposed AC current sensor is preferable when small ranges of current must be measured in noisy environments, especially where the linear sensors show difficulties in sensing due to their low sensitivities.

The improvement in sensitivity offered by the nonlinearity in the bistable device is more consistent when small amounts of current have to be sensed, especially in applications requiring the detection of the presence of a current flowing in a wire.

Finally, the possibility of tuning the magneto-elastic potential of the bistable sensor through the distance Δ between permanent magnets can remedy the small operative range in bistable sensor by adapting it to the application requirements.

Another advantage descending from the adoption of the bistable device is related to its capability of scavenging a larger amount of energy than the linear resonant device from its operative environment. As resulting from the device simulations, the power scavenged by the bistable device (for four different values of Δ, 2.1 mm, 2.2 mm, 2.25 mm and 2.3 mm) has been compared with that harvested by the linear resonant device (Δ = 2.1 mm) in fig. 4.45 for several values of AC current magnitude to be measured and a mechanical noise of 0.16g. The values of power in fig. 4.45 have been computed through the (4.19) and considering a resistive load R_L of 330 kΩ.

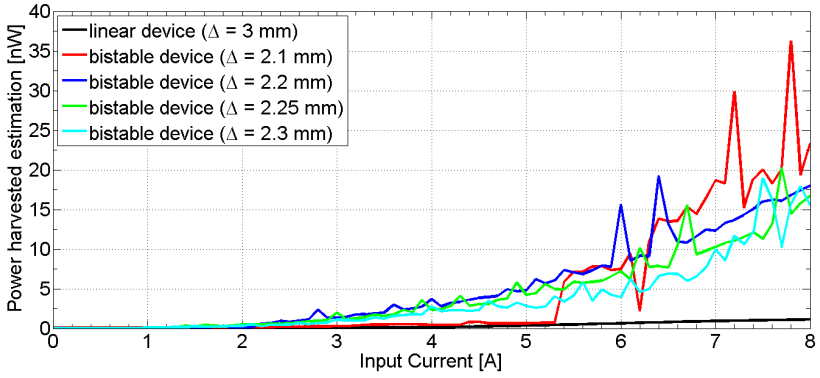

Fig. 4.45 – Estimation of the power harvested by the bistable device (for four different values of Δ, 2.1 mm, 2.2 mm, 2.25 mm and 2.3 mm) and by linear resonant device ($\Delta = 2.1$ mm) for several values of AC current magnitude to be measured and a mechanical noise of 0.16g.

As shown in the results in fig. 4.45, an improvement in the amount of harvested power,with respect to the linear resonant approach, is evident in the performance of the bistable device as soon as it begins to exhibit interwell oscillation.

4.5 Macroscale prototype of the bistable AC current sensor

In order to asses the performance improvement descending from the bistable AC current sensor over linear reso-

nant current sensors through experimental measurements, a macroscale prototype has been developed and studied at the Electrical and Electronic Measurements Laboratory of the University of Catania (Italy).

The current required to power a refrigerator (indicated in table 4.2 [66]) has been chosen as target current for the experimental measurements. In this case, an AC current magnitude of 1 A has to be addressed.

The characteristic of the prototype and the measurement setup are discussed in subsection 4.5.1 and measurement results are presented in subsection 4.5.2.

4.5.1 Prototype characteristics and measurement setup

The macroscale prototype is composed of a brass cantilever beam having a length l of 210 mm, a width w of 10 mm and a thickness t of 200 µm. Mass density of used brass is 8400 kg/m^3 and Young Modulus is 91 GPa [213].

Two Neodymium permanent magnets have been attached to the free end of the beam and one has been fixed at a distance Δ from the others and with opposed magnetization. Two

permanent magnets, instead of one, have been attached to the tip of the cantilever beam in order to increase the overall volume V_m of the moving magnets and, consequently from (4.17), to obtain a larger input magnetic force $F_m(t)$, at the same input current, acting on the beam. The necessity of a larger input magnetic force $F_m(t)$ is caused by the larger dimensions of the beam and by the different material adopted.

Each of the used Neodymium magnets has a cylindrical shape with a radius of 4 mm and a height of 4 mm. Values of mass density and magnetic remanence B_r for Neodymium are listed in table 4.1. The piezoelectric mechanical-to-electrical transduction is performed through a Lead Titanate Zirconate (PZT) disk from Murata®, with integrated electrodes, attached at the clamped end of the cantilever beam. The used PZT disk has a radius of 4.5 mm and a height of 120 µm. A load resistor R_L of 330 kΩ has been connected to the output electrodes of the PZT disk. Piezoelectric coupling in 31 direction in stress-charge form e_{31} of PZT is -20.49 C/m^2 and electrical permittivity in 33 direction ϵ_{33} is 18.5 nF/m [213].

The output voltage on the load resistor R_L is read through an oscilloscope probe and acquired and visualized through a digital oscilloscope.

The cable carrying the AC current to be measured has been placed at a distance h of 1 mm from the moving magnets.

The AC current to be measured is obtained from the mains voltage of 220 V, reduced through a transformer. The value of the AC target current magnitude has been regulated through a potentiometer connected to the output of the aforesaid transformer and verified through an amperemeter.

It should be noted also that the presented prototype is environmental friendly as it has been realized using recycled materials.

A picture of the macroscale prototype of the cantilever beam is reported in fig. 4.46; the transformer and the potentiometer used for generation of the AC target current from mains voltage are shown in fig. 4.47; a photo of the described measurement setup is shown in fig. 4.48.

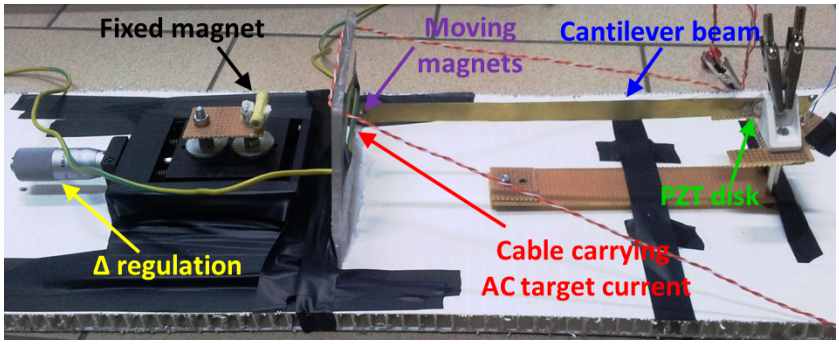

Fig. 4.46 – Macroscale prototype of the cantilever beam with permanent magnets.

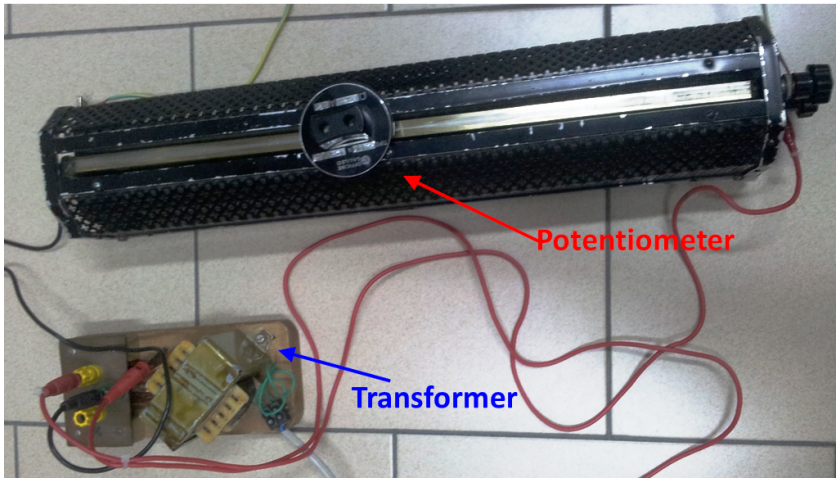

Fig. 4.47 – Transformer and potentiometer used to generate the AC target current from mains voltage at 220 V.

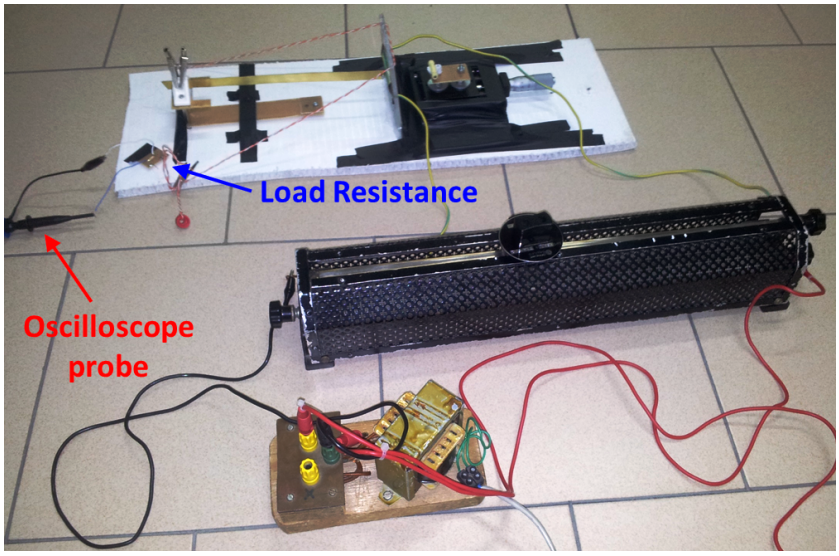

Fig. 4.48 – Picture of the measurement setup.

4.5.2 Measurement results

The application of the (4.11) and of the system parameters presented in subsection 4.5.1 gives a maximum limit value of 57.74 mm for the distance Δ between permanent magnets to achieve bistable behaviour. Consequently, experimental measurements to assess system operation have been carried out applying two different values of the distance Δ: the first one is 45 mm and the second one is 47 mm.

In order to compare performance of the bistable sensor with a linear resonant version of the proposed device, a set of measurements has been fulfilled employing a linear resonant sensor realized through the elimination of the fixed magnet from the measurement setup. Thus, a distance $\Delta \to +\infty$ is imposed and linear resonant behaviour is achieved in this case.

No external mechanical noise a_{ext} has been applied in these measurements.

Results of the measurement campaign are presented in the following and a video of the measurement setup and of the actuated beam is available on internet [218].

Measurement results for $\Delta = 47$ mm

According to (4.12), a distance $\Delta = 47$ mm results in two stable equilibrium positions $z_{1,2}$ placed at ± 30 mm from beam fabrication position ($z = 0$ mm).

Considering the application of the refrigerator, an AC current magnitude of 1 A has been imposed through the potentiometer but no beam commutations have been observed as confirmed by the acquired time series of the piezoelectric output voltage reported in fig. 4.49.

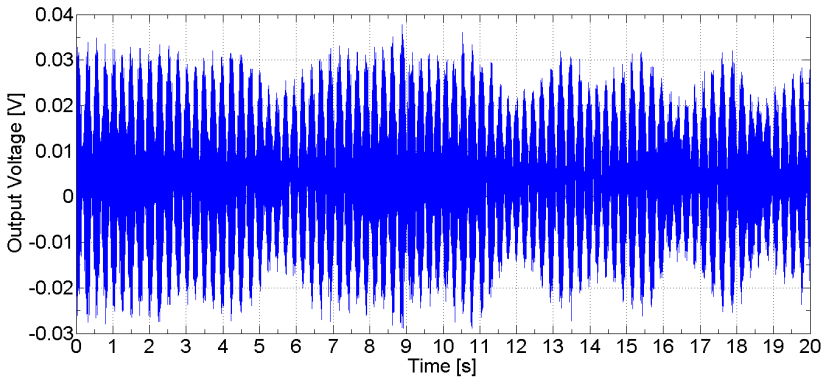

Fig. 4.49 – Piezoelectric output voltage obtained from the measurement setup when an AC current magnitude of 1 A is considered and a distance Δ of 47 mm is applied. From the analysis of these results, no beam commutations are observed.

Considering the (4.19) and the results in fig. 4.49, the measured harvested power is about 820 pW.

After the increase of the AC target current magnitude, the beam starts switching when a current of 1.4 A is considered. Although beam commutations are clearly visible at naked eye, in this setup they are automatically detected and counted exploiting the piezoelectric output voltage, which allows for both signal measurement and energy harvesting. An example

of the output voltage when an AC current magnitude of 3 A flows in the cable is shown in fig. 4.50.

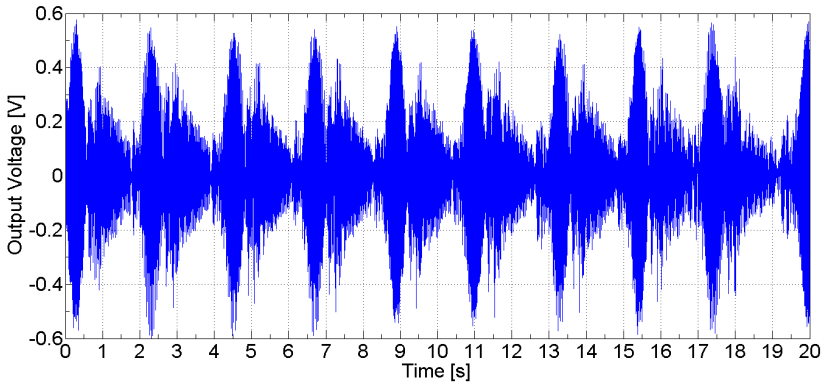

Fig. 4.50 – Piezoelectric output voltage obtained from the measurement setup when an AC current magnitude of 3 A is considered and a distance Δ of 47 mm is applied. From the analysis of these results, 9 beam commutations between stable equilibrium states are observed in a time interval of 20 s.

According to (4.19) and results in fig. 4.50, the measured harvested power is about 187 nW.

9 beam commutations in a time interval of 20 s are detected from the observation of experimental data in fig. 4.50.

The application of several AC current magnitudes leads to a different number of beam commutations (counted through

the piezoelectric output voltage) in a time interval of 20 s, as reported in fig. 4.51.

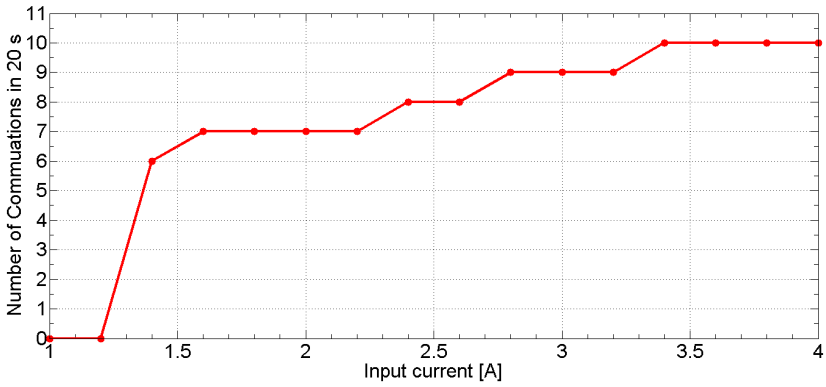

Fig. 4.51 – Number of beam commutations between stable equilibrium states in 20 s for different AC current magnitudes when a distance Δ of 47 mm is applied, , as resulting from the analysis of the measured piezoelectric output voltage.

For the sake of completeness and to show the effectiveness of the piezoelectric output voltage as both output signal for the current measurement and for energy scavenged, the trend of RMS values of the output voltage for different AC current magnitudes is plotted in fig. 4.52.

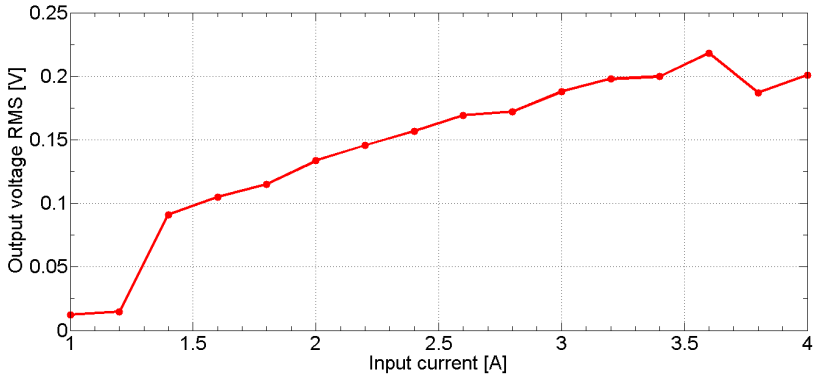

Fig. 4.52 – RMS values of the measured piezoelectric output voltage for different AC current magnitudes when a distance Δ of 47 mm is considered.

Measurement results for $\Delta = 45$ mm

According to (4.12), a distance $\Delta = 45$ mm results in two stable equilibrium positions $z_{1,2}$ placed at $\pm$ 32 mm from beam fabrication position ($z = 0$ mm).

As expected from a smaller distance between permanent magnets, magnet interaction force along z-axis F_{imz} is stronger and, thus, larger external magnetic forces $F_m(t)$ are needed to achieve system switchings between stable equilibrium states. This is confirmed by experimental results reported in fig. 4.53 in terms of beam commutations in a time interval of 20 s for different AC current magnitudes.

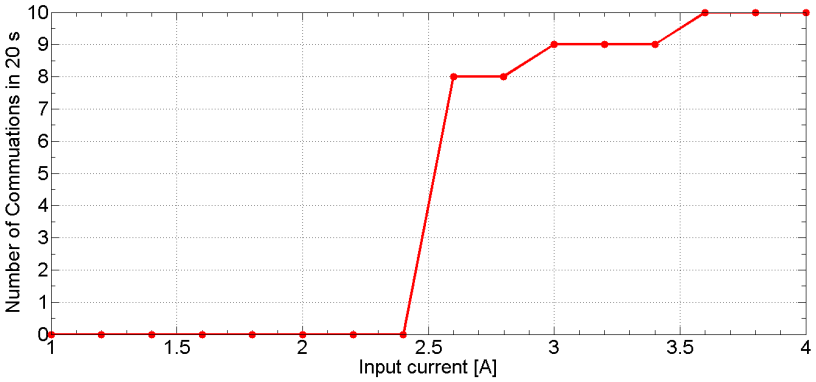

Fig. 4.53 – Number of beam commutations between stable equilibrium states in 20 s for different AC current magnitudes when a distance Δ of 45 mm is applied, as resulting from the analysis of the measured piezoelectric output voltage.

From the observation of the results in fig. 4.53, the system begins commutating when an AC current of 2.4 A is applied: this is an higher value than the one observed with a distance Δ of 47 mm, as expected.

The output voltage acquired when an AC current of 3.75 A is considered is plotted in fig. 4.54

According to (4.19) and results in fig. 4.54, the measured harvested power is about 195 nW.

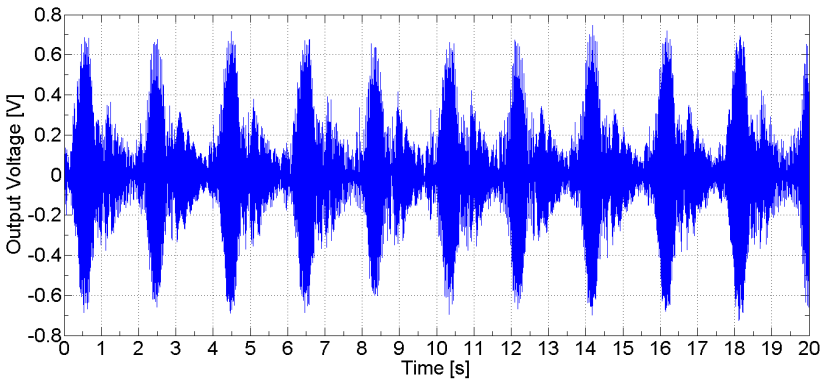

Fig. 4.54 – Piezoelectric output voltage obtained from the measurement setup when an AC current magnitude of 3.75 A is considered and a distance Δ of 45 mm is applied. From the analysis of these results, 10 beam commutations between stable equilibrium states are observed in a time interval of 20 s.

Measurement results for linear resonant sensor

As said, the removal of the fixed magnet from the measurement setup imposes a distance $\Delta \to +\infty$ and consequently a linear resonant behaviour characterized by a single well potential.

In this case, considering the (4.4) and beam parameters, the elastic coefficient of the beam k is about 0.19 N/m. The overall mass of the system is 6.5e-3 kg. The application of the (3.3) results in a resonant frequency of 0.86 Hz.

As already said, because linear systems do not exhibit commutations having a fixed amplitude, the only parameter usable to measure the AC current magnitude is the amplitude of the device oscillations and, consequently, the amplitude of the piezoelectric output voltage.

For this reason, the voltage from the PZT disk has been measured for different values of the AC target current magnitude and results are plotted in the graph in fig. 4.55.

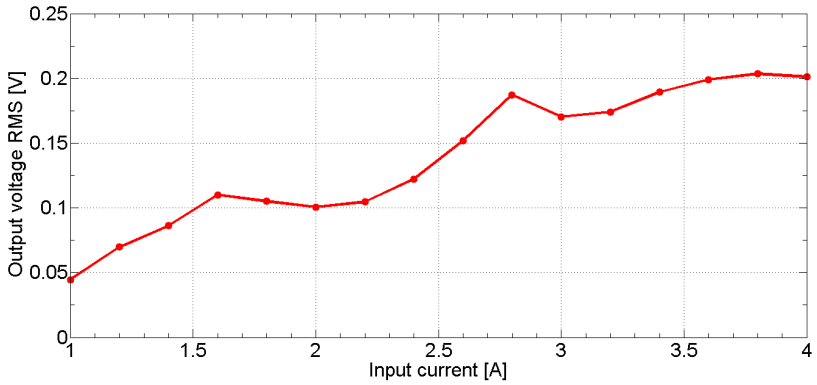

Fig. 4.55 – RMS values of the measured piezoelectric output voltage for different AC current magnitudes for the linear resonant sensor.

The trend of the RMS values in fig. 4.55 is not perfectly linear because of noise in the measurement system.

Comparison among bistable and linear sensors

In order to assess the improvement in performance of the bistable sensor over the linear resonant device in certain operating conditions, the results obtained from measurements in the three considered cases ($\Delta = 47$ mm, $\Delta = 45$ mm and $\Delta \to +\infty$) have been analyzed to compute device sensitivity of the three sensors.

Device sensitivity is the ratio between the output variation (i.e. the number of commutations in the bistable case or the RMS value of the output voltage from the piezoelectric disk in the linear case) and the variation of input that has generated it (i.e. the AC current flowing in the conductor) [70]. It is also noted that the same current range must be considered to properly perform the comparison among devices; in this specific case an AC current magnitude range ΔI of 400 mA has been considered.

The consideration of measurement results presented in fig. 4.51, fig. 4.53 and fig. 4.55 leads to the values of ΔI, $\Delta Comm_{47}$, $\Delta Comm_{45}$, ΔV_1 and ΔV_2 defined in figs. 4.56–4.58.

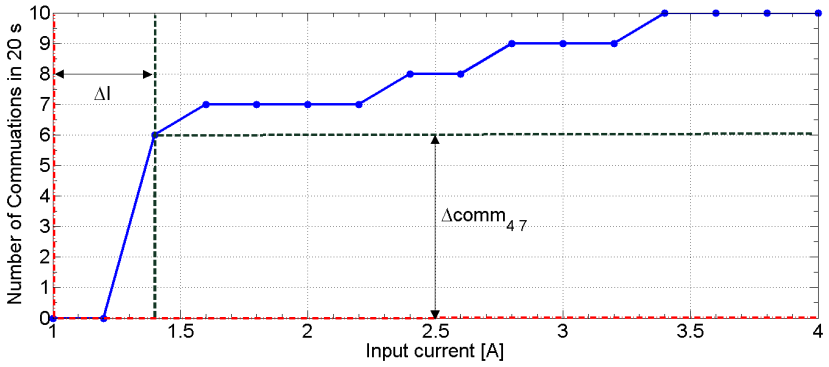

Fig. 4.56 – Number of beam commutations between stable equilibrium states in 20 s for different AC current magnitudes when a distance Δ of 47 mm is applied. Values of ΔI and $\Delta Comm_{47}$ used for the computing of the device sensitivity $S_{bist\%\ [47mm]}$ are indicated.

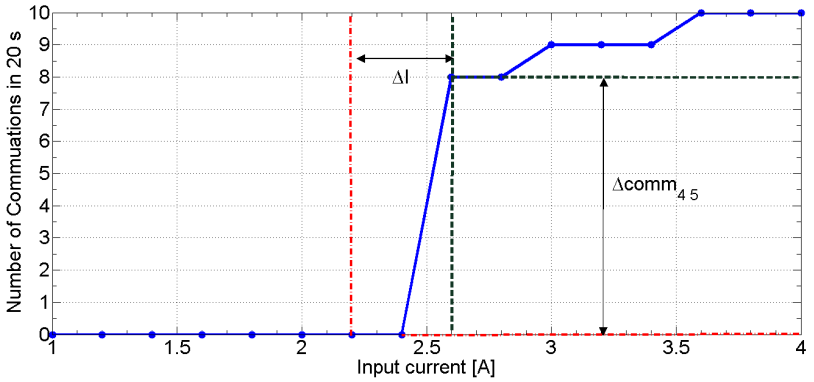

Fig. 4.57 – Number of beam commutations between stable equilibrium states in 20 s for different AC current magnitudes when a distance Δ of 47 mm is applied. Values of ΔI and $\Delta Comm_{45}$ used for the computing of the device sensitivity $S_{bist\%\ [45mm]}$ are indicated.

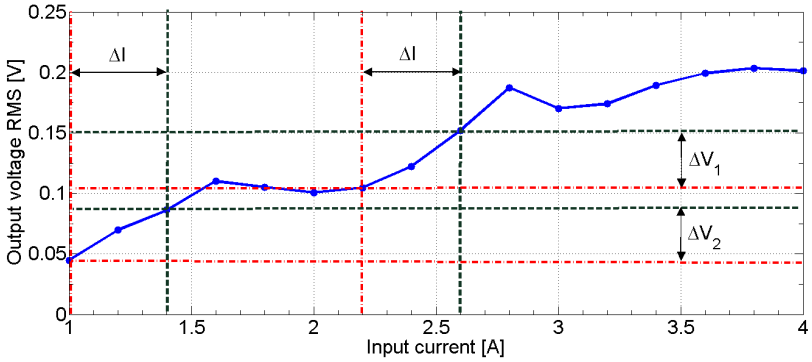

Fig. 4.58 – RMS values of the measured piezoelectric output voltage for different AC current magnitudes for the linear resonant sensor. Values of ΔI, ΔV_1 and ΔV_2 used for the computing of the device sensitivity $S_{lin\%}$ are indicated.

The sensitivity of linear resonant sensor $S_{lin\%}$ is evaluated in (4.24).

$$S_{lin\%} = \frac{max(\Delta V_1, \Delta V_2)}{\Delta I}\% = \frac{max(0.041\ V, 0.05\ V)}{0.4}\% = 29.4\%\ 1/A \tag{4.24}$$

The sensitivity of the bistable sensor $S_{bist\%\ [47mm]}$, when $\Delta\ = 47$ mm, is computed in (4.25).

$$S_{bist\%\ [47mm]} = \frac{\Delta Comm_{47}}{\Delta I}\% = \frac{7\ comm}{0.4\ A}\% = 175\%\ 1/A \tag{4.25}$$

The sensitivity of bistable sensor $S_{bist\%\ [45mm]}$, when $\Delta = 45$ mm, is evaluated in (4.26).

$$S_{bist\%\ [45mm]} = \frac{\Delta Comm_{45}}{\Delta I}\% = \frac{6\ comm}{0.4\ A}\% = 150\%\ 1/A \tag{4.26}$$

Sensitivity results found in (4.24)–(4.26) confirm the improvement in sensitivity of the bistable devices over the linear resonant one when the bistable sensors work in their operative region and all the considerations given at the end of the subsection 4.4.1.

The improvement in the amount of energy scavenged descending from the adoption of bistable mechanisms is shown in fig. 4.59, where the power scavenged by the bistable device (with $\Delta = 47$ mm) has been compared with the power harvested by the linear resonant device (with $\Delta \to +\infty$) for different magnitude values of the AC target current. Results in fig. 4.59 have been obtained by elaborating through the (4.19) the RMS values of the measured output voltage on the resistive load R_L of 330 kΩ.

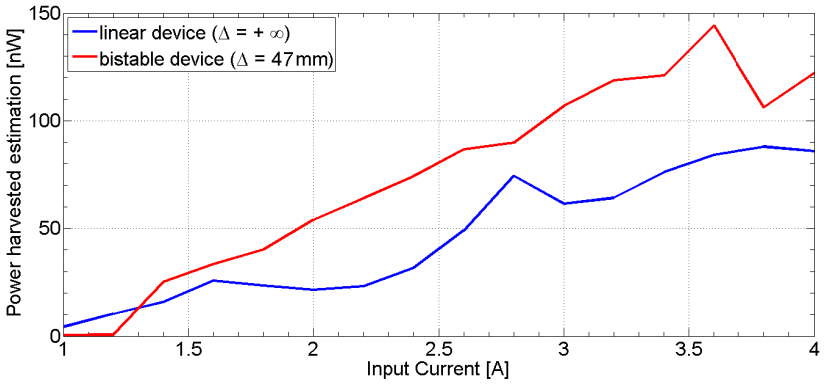

Fig. 4.59 – Estimation of the power harvested by the bistable device (with $\Delta = 47$ mm) and by linear resonant device (with $\Delta \to +\infty$) for several values of AC current magnitude to be measured, as resulting from the set of measurements carried out.

Measurement results in fig. 4.59 confirm the improvement in harvesting performance coming from the adoption of the bistable strategy as soon as interwell oscillations occur in bistable devices.

Conclusions

Imagine a mountain...From the top of this mountain, the view is wonderful. You want to be there, but the summit seems so far away that you lose hope of reaching it. You give up, saying "I will never get there". The truth is, the footsteps of the ones who reached the top were no bigger than yours. But they'd just gone on putting those small footsteps one after the other. It's not miracles which make the impossible happen, it's perseverance.

Serdar Özkan

The main aim of this work is focused on the study of the beneficial effects of the adoption of nonlinear strategies, especially bistable mechanisms, in specific transducers applications.

Efforts have been paid in the identification and in the implementation of technology solutions to fabricate/prototype

bistable devices at several scales. Both standard MEMS batch processes and rapid prototyping strategies have been taken into account. Among rapid prototyping solutions, processes to release cantilever beams through Focused Ion Beam milling and to deposit piezoelectric layers of Zinc Oxide have been developed at micro and nano-scale. At macro-scale (e.g., size of a few centimeters), strategies based on low-cost inkjet printing of electrically conductive inks on plastic flexible substrates have adopted and investigated.

Two large application fields have been explored: one is represented by the energy harvesting from mechanical vibrations and the other one by the sensing of AC currents through micromechanical structures.

In energy harvesting from mechanical vibrations, the application of bistable devices based on fully compliant microstructures and buckled beams, respectively in MEMS standard processes and direct printing technologies, has been investigated through analytical models, FEM simulations and, where prototypes have been fabricated, experimental tests. The widening of the bandwidth of harvesters has been demonstrated

with respect to traditional solutions adopting linear resonant structures. As a consequence, a larger amount of harvested energy has been proven with respect to linear strategies when wideband vibrations at low frequency (e.g., below 500 Hz) are taken as input.

In the field of the AC currents sensors, a novel nonlinear transduction mechanism exploiting the number of beam commutations between its stable equilibrium states to quantify the magnitude of the target AC current has been proposed. This approach leads to an improvement of the device sensitivity in the device operative range over solutions adopting linear resonant strategies. The self-generating operation of the device, due to piezoelectric materials, allows also for the autonomous operation of the device and to exploit ambient noise to harvest energy along with its sensing operation.

Acknowledgements

And in the end the love you take is equal to the love you make.

The Beatles

This thesis concludes three years of work. During this very important period of my life, I had the daily possibility to grow and compare my knowledge and experiences with a great group of researchers and friends. My personal and professional growth and all the results reported in thesis are also due to them.

First of all, I would like to thank Prof. Salvatore Baglio, my tutor during these three years of Ph.D. course. For me, he was a great mentor and an inexhaustible source of constant inspiration, creativity, enthusiasm and motivation. All

my gratitude goes to him for believing in me and for guiding me as a father every day in this important life path.

I would like to thank Prof. Luigi Fortuna, the coordinator of my Ph.D. course, for his constant support and motivation.

I owe a big thank to Prof. Bruno Andò who steadily gave me support and many valuable suggestions which indeed helped me in my personal growth and in improving my experience during these years. His precious help in the research on devices in direct printing technology is part of the results of this work.

I would like to thank Prof. Salvatore Graziani for his suggestions and the important tutorship experience in his course about "Electric and Electronic Measurements".

Special thanks go to all the guys of the "Measurement Group" and "Automation and Control of Complex Systems, Robotic Group" of the University of Catania (Italy) for daily sharing this beautiful experience and for several mutual information exchanges that have been very relevant to improve my knowledge: we lived together a really great adventure. In particular, among them, I want to thank Carlo Trigona, An-

gela Beninato, Elena Umana, Vincenzo Marletta, Salvatore La Malfa, Felice Maiorca, Fabio Antoci, Fabio Giusa, Ilenia Medico, Stefania Medico, Valentina Sinatra, Giuseppe Vitellaro, Antonio Pistorio and Viviana De Luca. I wish you all the best in your lives.

A big thank goes to the people from the company "Advanced Technology Solutions" of Catania (Alfonso D'Agostino, Francesca Cunsolo, Valentina La Paglia and Dr. Ada Di Stefano) for their "logistical" and "friendly" support in my activities at the Nanotechlab of Catania (Italy).

I have to thank Prof. Graziella Malandrino and Prof. Guido Condorelli from Department of Chemistry of the University of Catania (Italy) for the X-Ray Diffraction and Energy Dispersive X-Ray Spectroscopy analyses of the ZnO samples.

A big thank is for Prof. Lucia Romano from the Department of Physics of the University of Catania (Italy) for the Rutherford Backscattering Spectroscopy analyses of the ZnO samples and for her precious suggestions when I started working with the Scanning Electron Microscope and the Focused Ion Beam of the Nanotechlab of Catania (Italy).

Last but non least, I want to thank my family: my father Alfio, my mother Giuseppa and my brother Giuseppe for their love, their support and for always believing in me in all my life choices. Also my relatives and my friends deserve thanks: they were always on my side during these years. All that I am I owe to them and to those that are no more with us.

Thank you very much.

A

Activities during Ph.D. course

A.1 Publications on international journals

- B. Andò, S. Baglio, G. L'Episcopo, V. Marletta, N. Savalli and C. Trigona. *"A BE-SOI MEMS for inertial measurement in geophysical applications"*. IEEE Transactions on Instrumentation and Measurement, vol. 60, no. 5 , pp. 1991–1908, 2011.
- B. Andò, S. Baglio, G. L'Episcopo and C. Trigona. *"Investigation on Mechanically Bi-stable MEMS Devices for Energy Harvesting from Vibrations"*. IEEE Journal of Microelectromechanical Systems, vol. 21, I. 4, pp. 779–790, 2012.

- B. Andò, S. Baglio and G. L'Episcopo. *"A low cost, disposable and contactless resonant mass sensor"*. IEEE Transactions on Instrumentation and Measurement, vol. 62, I. 1, pp. 246–252, 2012.
- G. Vitellaro, G. L'Episcopo, C. Trigona, B. Andò and S. Baglio. *"A Compliant MEMS device for Out-of-Plane Displacements with Thermo-Electric Actuation"*. In press on IEEE Journal of Microelectromechanical System.

A.2 International conference proceedings

- B. Andò, S. Baglio and G. L'Episcopo. *"Lateral cantilever beam in BESOI technology"*. IEEE Instrumentation and Measurement Technology Conference (I2MTC), 2011, Binjang (China), pp. 1–6.
- B. Andò, S. Baglio, S. La Malfa and G. L'Episcopo. *"All inkjet printed system for strain measurement"*. IEEE Sensors 2011, Limerick (Ireland), pp. 215–217, 2011.
- S. Baglio, C. Trigona, B. Andò, F. Maiorca, G. L'Episcopo and A. Beninato. *"Energy Harvesting from weak random vibrations: Bistable strategies and architectures for MEMS*

devices". IEEE 55th International Midwest Symposium on Circuits and Systems (MWSCAS), pp. 154–157, 2012.

- B. Andò, S. Baglio, M. Baù A.R. Bulsara, V. Ferrari, M. Ferrari and G. L'Episcopo. *"Nonlinear Energy Harvester by Direct Printing Technology"*. Procedia Engineering, vol. 47, pp. 933–936 (2012). Eurosensors XXVI, Kraków (Poland), 2012
- B. Andò, S. Baglio, G. L'Episcopo, F. Maiorca and C. Trigona. *"Autonomous bistable microsensors for noninvasive AC electrical current measurements"*. IEEE Instrumentation and Measurement Technology Conference (I2MTC), 2013, Minneapolis (USA), pp. 93–97.

A.3 Book contributions

- B. Andò, S. Baglio, A. Beninato, G. L'Episcopo and G. Trigona. *"A Review on RTD-Fluxgate Magnetometers: From Single to Coupled Core and Toward Novel Systems with Innovative Materials"* in "Sensors", pp. 283-286, Springer, 2013.

- B. Andò, S. Baglio, G. L'Episcopo and G. Trigona. *"Microsensors for Harsh Environments: Review on Strategies for Contactless and Self-Powered Systems"* in "Sensors", pp. 219-222, Springer, 2013.
- B. Andò, S. Baglio and G. L'Episcopo. *"Low cost inkjet printed sensors"* in "Sensors", pp. 31-36, Springer, 2013.

A.4 Publications on Italian journals

- B. Andò, S. Baglio, G. L'Episcopo, C. Lombardo, V. Marletta, I. Medico and S. Medico. *"Prototipazione rapida di sensori: tecnologie, materiali e applicazioni"*. Tutto Misure, year. XIV, no. 3 , pp. 177–182, 2012.

A.5 Italian conference proceedings

- B. Andò, S. Baglio, S. Graziani, G. L'Episcopo and N. Pitrone. *"Sviluppo di dispositivi MEMS bistabili per vibration energy harvesting a elevata efficienza"*. GMEE 2010, Gaeta (Italy).

- B. Andò, S. Baglio, A. Beninato and G. L'Episcopo. *"Strategie di sviluppo e fabbricazione di nanosensori"*. GMEE 2011, Genova (Italy).
- B. Andò, S. Baglio, N. Dumas, L. Latorre, G. L'Episcopo, P. Nouet and C. Trigona. *"Study and experimental validation of periodically-forced non-resonant oscillators for energy harvesting from vibrations"*. Convegno Nazionale Sensori 2012, Roma (Italy).
- B. Andò, S. Baglio and G. L'Episcopo. *"Low cost Inkjet printed sensors"*. Convegno Nazionale Sensori 2012, Roma (Italy).
- B. Andò, S. Baglio, S. Graziani and G. L'Episcopo. *"Sviluppo di dispositivi MEMS meccanicamente bistabili per energy harvesting da vibrazioni meccaniche"*. GMEE 2012, Monopoli (Italy).
- B. Andò, S. Baglio, A. Beninato, S. Graziani and G. L'Episcopo. *"Strategie di sviluppo e prototipazione rapida di nanosensori"*. GMEE 2012, Monopoli (Italy).
- B. Andò, S. Baglio, S. Graziani, G. L'Episcopo, F. Maiorca and C. Trigona. *"Un sensore autonomo e bistable per la*

misura non invasiva di correnti elettriche alternate". GMEE 2013, Trento (Italy).

A.6 Attended conferences

- Convegno Nazionale Sensori. 15^{th}–17^{th} February 2012. Rome (Italy).
- Eurosensors XXVI. 9^{th}–12^{th} September 2012. Kraków (Poland).

A.7 Attended Ph.D. schools

- Scuola di dottorato in Ingegneria dei Sistemi 2011. 12^{th} September 2011 – 7^{th} October 2011. University of Catania (Italy).
- International Student Conference on Microtechnology. 8^{th}–14^{th} October 2012. Freiburg im Breisgau (Germany).

A.8 Attended contests

- "Science Presentation Competition" at the International Student Conference on Microtechnology. 8^{th}–14^{th} October 2012. Freiburg im Breisgau (Germany).

A.9 Attended courses at the University of Catania (Italy)

- Sistemi elettrici per energia.
- Fisica tecnica.
- Impianti Elettrici I.

A.10 Tutoring Activities at University of Catania (Italy)

- Misure elettriche ed elettroniche (2011).

References

General References

[22] S. Baglio, S. Castorina, and N. Savalli. *Scaling issues and design of MEMS*. Wiley Online Library, 2007 (cit. on p. 219).

[24] Minhang Bao and Heng Yang. "Squeeze film air damping in MEMS". In: *Sensors and Actuators A: Physical* 136.1 (2007), pp. 3–27 (cit. on p. 134).

[36] Ronald Newbold Bracewell and RN Bracewell. *The Fourier transform and its applications*. Vol. 31999. McGraw-Hill New York, 1986 (cit. on p. 149).

[38] Bernard Brogliato. "Absolute stability and the Lagrange–Dirichlet theorem with monotone multivalued map-

pings". In: *Systems & control letters* 51.5 (2004), pp. 343–353 (cit. on p. 14).

[44] John Charles Butcher. *The numerical analysis of ordinary differential equations: Runge-Kutta and general linear methods*. Wiley-Interscience, 1987 (cit. on p. 311).

[53] Y.H. Cho, A.P. Pisano, and R.T. Howe. "Viscous damping model for laterally oscillating microstructures". In: *Journal of Microelectromechanical Systems* 3.2 (1994), pp. 81–87 (cit. on p. 220).

[70] Ernest O Doebelin. *Measuring Systems - Application and Design*. McGraw-Hill, New York, 1990 (cit. on pp. 7, 364).

[73] Georg Duffing. *Erzwungene Schwingungen bei veränderlicher Eigenfrequenz und ihre technische Bedeutung*. R, Vieweg & Sohn, 1918 (cit. on pp. 23, 24, 145).

[84] Gene F Franklin, J David Powell, and Abbas Emami-Naeini. *Feedback control of dynamic systems*. Vol. 320. Addison-Wesley Reading, MA, 1991 (cit. on p. 7).

[93] Gustav Gautschi. *Piezoelectric sensorics: force, strain, pressure, acceleration and acoustic emission sensors, materials and amplifiers*. Springer, 2002 (cit. on pp. 158, 159).

[110] Xiao-Ting He, Shan-Lin Chen, and Jun-Yi Sun. "Applying the equivalent section method to solve beam subjected to lateral force and bending-compression column with different moduli". In: *International Journal of Mechanical Sciences* 49.7 (2007), pp. 919–924 (cit. on p. 296).

[115] MA Howaston, GP Lund, and DJ Todd. *Engineering tables and data*. Chapman and hall, 1991 (cit. on p. 246).

[116] Larry L Howell. *Compliant mechanisms*. Wiley-Interscience, 2001 (cit. on pp. 13, 15, 17, 23, 46, 190, 199).

[129] P.E. Kloeden and E. Platen. *Numerical solution of stochastic differential equations*. Springer, 1995 (cit. on pp. 200, 201).

[131] Jan Korvink and Oliver Paul. *MEMS: A practical guide to design, analysis and applications*. William Andrew, 2005 (cit. on pp. 43, 169, 283).

[139] R. Lensink, H. Bo, and E. Sterken. *Investment, capital market imperfections, and uncertainty: theory and empirical results*. Edward Elgar Pub, 2001 (cit. on p. 201).

[148] Aleksandr Mikhailovich Lyapunov. "The general problem of the stability of motion". In: *International Journal of Control* 55.3 (1992), pp. 531–534 (cit. on p. 12).

[163] Ned Mohan, Tore M Undeland, and William P Robbins. *Power electronics: Converters, applications, and design*. Wiley (New York), 1989 (cit. on pp. 157, 284).

[175] Henry W Ott. *Electromagnetic compatibility engineering*. Wiley. com, 2011 (cit. on p. 323).

[177] Ramon Pallas-Areny, John G Webster, and Ramo Areny. *Sensors and signal conditioning*. Wiley New York, 2001 (cit. on p. 8).

[194] Singiresu Rao. *Mechanical Vibrations*. Pearson Prentice Hall, 2004 (cit. on pp. 121, 123).

[199] Raymond Jefferson Roark and Warren Clarence Young. *Formulas for stress and strain*. McGraw-Hill, 1975 (cit. on pp. 251, 296).

[210] Otto H Schmitt. "A thermionic trigger". In: *Journal of Scientific Instruments* 15.1 (1938), p. 24 (cit. on p. 23).

[212] Raymond A Serway, Chris Vuille, and Jerry S Faughn. *College physics*. Vol. 10. Cengage Learning, 2008 (cit. on pp. 15, 16, 145, 168, 182, 260, 280, 295, 299, 300, 321, 329).

[213] James F Shackelford and William Alexander. *CRC materials science and engineering handbook*. CRC press, 2010 (cit. on pp. 193, 246, 307, 351, 352).

[219] Gabriel G Skitek, Stanley V Marshall, and Richard E DuBroff. *Electromagnetic concepts and applications*. Prentice-Hall, 1982 (cit. on p. 279).

[227] Steven Strogatz. *Nonlinear dynamics and chaos: with applications to physics, biology, chemistry and engineering*. Perseus Books Group, 2001 (cit. on p. 8).

[241] Timo Veijola and Marek Turowski. "Compact damping models for laterally moving microstructures with gas-

rarefaction effects". In: *Journal of Microelectromechanical Systems* 10.2 (2001), pp. 263–273 (cit. on p. 134).

[242] Benedetto Vigna. "Future of MEMS: an industry point of view". In: *EuroSime 2006. 7th International Conference on Thermal, Mechanical and Multiphysics Simulation and Experiments in Micro-Electronics and Micro-Systems, 2006.* IEEE. 2006, pp. 1–8 (cit. on pp. 44, 62, 63, 169).

[243] Daniel D Villani. "An analytic solution for the force between two magnetic dipoles". In: *Magnetic and Electrical Separation* 9 (1998), pp. 39–52 (cit. on p. 296).

[249] John-G Webster. *The Measurement, Instrumentation, and Sensors: Handbook*. Springer, 1999 (cit. on pp. 6, 277).

[250] Birron Mathew Weedy, Brian John Cory, N Jenkins, JB Ekanayake, and G Strbac. *Electric power systems*. John Wiley & Sons, 2012 (cit. on p. 276).

[266] QQ Zhang, SJ Gross, S Tadigadapa, TN Jackson, FT Djuth, and S Trolier-McKinstry. "Lead zirconate titanate films for d33 mode cantilever actuators". In: *Sen-*

sors and Actuators A: Physical 105.1 (2003), pp. 91–97 (cit. on p. 163).

Nonlinearity and Stochastic Resonance

[2] L Alfonsi, L Gammaitoni, S Santucci, and AR Bulsara. "Intrawell stochastic resonance versus interwell stochastic resonance in underdamped bistable systems". In: *Physical Review E* 62.1 (2000), p. 299 (cit. on p. 10).

[12] Bruno Andò, Salvatore Baglio, Adi Bulsara, Vincenzo Marletta, and Nicolo Savalli. "E-field ferroelectric sensors: Modeling and simulation [Instrumentation Notes]". In: *Instrumentation & Measurement Magazine, IEEE* 12.2 (2009), pp. 31–37 (cit. on pp. 11, 64, 65).

[13] Bruno Andò, Salvatore Baglio, Adi R Bulsara, and Vincenzo Marletta. "A Ferroelectric-Capacitor-Based Approach to Quasistatic Electric Field Sensing". In: *IEEE Transactions on Instrumentation and Measurement* 59.3 (2010), pp. 641–652 (cit. on pp. 11, 32, 65).

[14] Bruno Andò, Salvatore Baglio, Adi R Bulsara, and Vincenzo Sacco. "Residence times difference fluxgate". In:

Measurement 38.2 (2005), pp. 89–112 (cit. on pp. 11, 32).

[25] Roland Bartussek, Peter Hänggi, and Peter Jung. "Stochastic resonance in optical bistable systems". In: *Physical Review E* 49.5 (1994), p. 3930 (cit. on p. 29).

[29] Roberto Benzi, Giorgio Parisi, Alfonso Sutera, and Angelo Vulpiani. "A theory of stochastic resonance in climatic change". In: *SIAM Journal on applied mathematics* 43.3 (1983), pp. 565–578 (cit. on p. 10).

[34] Wolfgang Bornhöfft and Gerhard Trenkler. "Magnetic field sensors: Flux gate sensors". In: *Sensors Set: A Comprehensive Survey* (1989), pp. 153–203 (cit. on p. 29).

[40] Adi R Bulsara and Luca Gammaitoni. "Tuning in to noise". In: *Physics Today* 49 (1996), p. 39 (cit. on pp. 9, 21–23, 25, 26, 28, 30, 291).

[41] Adi R Bulsara, Visarath In, Andy Kho, Antonio Palacios, Patrick Longhini, Joe Neff, Gregory Anderson, Christopher Obra, Salvatore Baglio, and Bruno Andò. "Exploiting nonlinear dynamics in a coupled-core flux-

gate magnetometer". In: *Measurement Science and Technology* 19.7 (2008), p. 075203 (cit. on p. 11).

[42] Adi R Bulsara, C Seberino, L Gammaitoni, MF Karlsson, B Lundqvist, and JWC Robinson. "Signal detection via residence-time asymmetry in noisy bistable devices". In: *Physical Review E* 67.1 (2003), p. 016120 (cit. on p. 11).

[43] AR Bulsara, ME Inchiosa, and L Gammaitoni. "Noise-controlled resonance behavior in nonlinear dynamical systems with broken symmetry". In: *Physical review letters* 77.11 (1996), p. 2162 (cit. on p. 24).

[67] A Dari, L Bosi, and L Gammaitoni. "Nonlinear sensors: An approach to the residence time detection strategy". In: *Physical Review E* 81.1 (2010), p. 011115 (cit. on p. 10).

[76] FJ Elmer. "Bistability and strange nonlinear neutral curve in ferromagnetic resonance". In: *Physics Letters A* 118.1 (1986), pp. 25–28 (cit. on p. 146).

[77] FJ Elmer. "Nonlinear and nonlocal dynamics of spatially extended systems: stationary states, bifurcations

and stability". In: *Physica D: Nonlinear Phenomena* 30.3 (1988), pp. 321–342 (cit. on pp. 148, 149).

[88] L Gammaitoni and AR Bulsara. "Noise activated nonlinear dynamic sensors". In: *Physical review letters* 88.23 (2002), p. 230601 (cit. on pp. 10, 23, 30, 32, 37, 290, 319).

[89] L Gammaitoni, P Hänggi, P Jung, and F Marchesoni. "Stochastic Resonance: A remarkable idea that changed our perception of noise". In: *The European Physical Journal B* 69.1 (2009), pp. 1–3 (cit. on p. 10).

[90] L Gammaitoni, F Marchesoni, E Menichella-Saetta, S Santucci, et al. "Stochastic resonance in bistable systems". In: *Physical review letters* 62.4 (1989), pp. 349–352 (cit. on p. 12).

[91] Luca Gammaitoni, Peter Hänggi, Peter Jung, and Fabio Marchesoni. "Stochastic resonance". In: *Reviews of modern physics* 70.1 (1998), p. 223 (cit. on p. 9).

[92] Luca Gammaitoni, Igor Neri, and Helios Vocca. "The benefits of noise and nonlinearity: Extracting energy

from random vibrations". In: *Chemical Physics* 375.2 (2010), pp. 435–438 (cit. on pp. 8, 11, 290).

[101] John Guckenheimer and Philip Holmes. *Nonlinear oscillations, dynamical systems, and bifurcations of vector fields*. Springer-Verlag, 1983 (cit. on p. 146).

[104] Peter Hänggi, Mario E Inchiosa, Dave Fogliatti, and Adi R Bulsara. "Nonlinear stochastic resonance: The saga of anomalous output-input gain". In: *Physical Review E* 62.5 (2000), p. 6155 (cit. on p. 10).

[105] Peter Hänggi and Fabio Marchesoni. "Artificial Brownian motors: Controlling transport on the nanoscale". In: *Reviews of Modern Physics* 81.1 (2009), p. 387 (cit. on p. 9).

[106] Gregory Peter Harmer, Bruce R Davis, and Derek Abbott. "A review of stochastic resonance: Circuits and measurement". In: *Instrumentation and Measurement, IEEE Transactions on* 51.2 (2002), pp. 299–309 (cit. on p. 26).

[113] PJ Holmes and DA Rand. "The bifurcations of Duffing's equation: An application of catastrophe theory".

In: *Journal of Sound and Vibration* 44.2 (1976), pp. 237–253 (cit. on pp. 146, 147).

[114] John J Hopfield. "Neurons with graded response have collective computational properties like those of two-state neurons". In: *Proceedings of the national academy of sciences* 81.10 (1984), pp. 3088–3092 (cit. on p. 24).

[128] Seunghwan Kim, Seon Hee Park, and H-B Pyo. "Stochastic resonance in coupled oscillator systems with time delay". In: *Physical review letters* 82.8 (1999), p. 1620 (cit. on p. 28).

[164] Faisal Mohd-Yasin, N Zaiyadi, DJ Nagel, DS Ong, CE Korman, and AR Faidz. "Noise and reliability measurement of a three-axis micro-accelerometer". In: *Microelectronic Engineering* 86.4 (2009), pp. 991–995 (cit. on p. 169).

[167] Alexander Neiman and Lutz Schimansky-Geier. "Stochastic resonance in bistable systems driven by harmonic noise". In: *Physical review letters* 72.19 (1994), p. 2988 (cit. on p. 12).

[171] A Nikitin, NG Stocks, and AR Bulsara. "Asymmetric bistable systems subject to periodic and stochastic forcing in the strongly nonlinear regime: Switching time distributions". In: *Physical Review E* 68.1 (2003), p. 016103 (cit. on p. 14).

[226] NG Stocks, ND Stein, and Peter VE McClintock. "Stochastic resonance in monostable systems". In: *Journal of Physics A: Mathematical and General* 26.7 (1993), p. L385 (cit. on p. 28).

[228] Torsten Strunz and Franz-Josef Elmer. "Driven Frenkel-Kontorova model in uniform sliding states and dynamical domains of different particle densities". In: *Physical Review E* 58.2 (1998), p. 1601 (cit. on p. 150).

Bistable Systems

[35] P Boyle, DF Moore, R Breen, RRA Syms, H Zou, and J Stagg. "MEMS bistable clamp with electrical locking and release". In: *15th Micromechanics Workshop, MME'04*. 2004, pp. 45–48 (cit. on p. 186).

[39] M Brokate and AV Pokrovskiı. "Asymptotically stable oscillations in systems with hysteresis nonlinearities". In: *Journal of differential equations* 150.1 (1998), pp. 98–123 (cit. on p. 23).

[46] Jasmina Casals-Terre, Andreu Fargas-Marques, and Andrei M Shkel. "Snap-action bistable micromechanisms actuated by nonlinear resonance". In: *Journal of Microelectromechanical Systems* 17.5 (2008), pp. 1082–1093 (cit. on p. 18).

[50] Mu Chiao and Liwei Lin. "Self-buckling of micromachined beams under resistive heating". In: *Journal of Microelectromechanical Systems* 9.1 (2000), pp. 146–151 (cit. on p. 255).

[65] Luke J Currano, Miao Yu, and Balakumar Balachandran. "Latching in a MEMS shock sensor: Modeling and experiments". In: *Sensors and Actuators A: Physical* 159.1 (2010), pp. 41–50 (cit. on p. 33).

[98] Troy Gomm, Larry L Howell, and Richard H Selfridge. "In-plane linear displacement bistable microrelay". In:

Journal of Micromechanics and Microengineering 12.3 (2002), p. 257 (cit. on p. 19).

[103] Beat Hälg. "On a micro-electro-mechanical nonvolatile memory cell". In: *IEEE Transactions on Electron Devices* 37.10 (1990), pp. 2230–2236 (cit. on p. 255).

[117] Il-Han Hwang, Yu-Seok Shim, and Jong-Hyun Lee. "Modeling and experimental characterization of the chevron-type bi-stable microactuator". In: *Journal of Micromechanics and Microengineering* 13.6 (2003), p. 948 (cit. on p. 19).

[132] W Kreider and Ali H Nayfeh. "Experimental investigation of single-mode responses in a fixed-fixed buckled beam". In: *Nonlinear Dynamics* 15.2 (1998), pp. 155–177 (cit. on p. 18).

[147] Rajesh Luharuka and Peter J Hesketh. "Design of fully compliant, in-plane rotary, bistable micromechanisms for MEMS applications". In: *Sensors and Actuators A: Physical* 134.1 (2007), pp. 231–238 (cit. on p. 19).

[154] Tadao Matsunaga and Masayoshi Esashi. "Acceleration switch with extended holding time using squeeze film

effect for side airbag systems". In: *Sensors and Actuators A: physical* 100.1 (2002), pp. 10–17 (cit. on p. 33).

[165] P Mormile, L Petti, M Abbate, P Musto, G Ragosta, and P Villano. "Temperature switch and thermally induced optical bistability in a PDLC". In: *Optics communications* 147.4-6 (1998), pp. 269–273 (cit. on p. 34).

[169] NT Nguyen. "Micromachined flow sensors - a review". In: *Flow measurement and Instrumentation* 8.1 (1997), pp. 7–16 (cit. on p. 34).

[170] Son D Nguyen, Einar Halvorsen, and Igor Paprotny. "Bistable springs for wideband microelectromechanical energy harvesters". In: *Applied Physics Letters* 102.2 (2013), pp. 023904–023904 (cit. on pp. 39, 155).

[173] Patrick G Opdahl, Brian D Jensen, and Larry L Howell. "An investigation into compliant bistable mechanisms". In: *Proc. 1998 ASME Design Engineering Technical Conf.* 1998, pp. 13–16 (cit. on p. 15).

[179] M.B. Parkinson, B.D. Jensen, and G.M. Roach. "Optimization-based design of a fully-compliant bistable micromechanism". In: *Proceedings of the 2000 ASME Design En-*

gineering Technical Conferences, DETC2000/MECH-14119 (2000) (cit. on p. 186).

[191] Jin Qiu, Jeffrey H Lang, and Alexander H Slocum. "A centrally-clamped parallel-beam bistable MEMS mechanism". In: *Micro Electro Mechanical Systems, 2001. MEMS 2001. The 14th IEEE International Conference on*. IEEE. 2001, pp. 353–356 (cit. on p. 46).

[192] Jin Qiu, Jeffrey H Lang, and Alexander H Slocum. "A curved-beam bistable mechanism". In: *Journal of Microelectromechanical Systems* 13.2 (2004), pp. 137–146 (cit. on p. 255).

[195] Gabriel M Rebeiz and Jeremy B Muldavin. "RF MEMS switches and switch circuits". In: *Microwave Magazine, IEEE* 2.4 (2001), pp. 59–71 (cit. on p. 19).

[207] M Taher A Saif. "On a tunable bistable MEMS - theory and experiment". In: *Journal of Microelectromechanical Systems* 9.2 (2000), pp. 157–170 (cit. on p. 255).

[211] Arjun Selvakumar, Navid Yazdi, and Khalil Najafi. "A wide-range micromachined threshold accelerometer array and interface circuit". In: *Journal of Micromechan-*

ics and Microengineering 11.2 (2001), p. 118 (cit. on p. 33).

[220] U Sonmez. "Compliant MEMS crash sensor designs: the preliminary simulation results". In: *Intelligent Vehicles Symposium, 2007 IEEE*. IEEE. 2007, pp. 303–308 (cit. on p. 19).

[236] Jinni Tsay, Liang-Qing Su, and Cheng-Kuo Sung. "Design of a linear micro-feeding system featuring bistable mechanisms". In: *Journal of Micromechanics and Microengineering* 15.1 (2005), p. 63 (cit. on pp. 19, 186).

[239] Mattias Vangbo and Ylva Bäcklund. "A lateral symmetrically bistable buckled beam". In: *Journal of Micromechanics and Microengineering* 8.1 (1998), p. 29 (cit. on p. 255).

[240] M Vázquez, C Gómez-Polo, D-X Chen, and A Hernando. "Magnetic bistability of amorphous wires and sensor applications". In: *IEEE Transactions on Magnetics* 30.2 (1994), pp. 907–912 (cit. on p. 34).

[254] Thomas Wilhelm. "The smallest chemical reaction system with bistability". In: *BMC systems biology* 3.1 (2009), p. 90 (cit. on p. 23).

[267] Jian Zhao, Yintang Yang, Kefeng Fan, Ping Hu, and Hongxi Wang. "A bistable threshold accelerometer with fully compliant clamped-clamped mechanism". In: *Sensors Journal, IEEE* 10.5 (2010), pp. 1019–1024 (cit. on p. 33).

Technology References

[5] B Andò, S Baglio, M Baù, V Ferrari, E Sardini, N Savalli, M Serpelloni, and C Trigona. "Contactless electromagnetic interrogation of a MEMS-based microresonator used as passive sensing element". In: *Solid-State Sensors, Actuators and Microsystems Conference, 2009. TRANSDUCERS 2009. International*. IEEE. 2009, pp. 1429–1432 (cit. on p. 50).

[10] Bruno Andò, S Baglio, G L'Episcopo, and C Trigona. "Microsensors for Harsh Environments: Review on

Strategies for Contactless and Self-Powered Systems". In: *Sensors*. Springer, 2014, pp. 219–222 (cit. on p. 50).

[11] Brunò Ando and Salvatore Baglio. "Inkjet-printed sensors: A useful approach for low cost, rapid prototyping [Instrumentation Notes]". In: *Instrumentation & Measurement Magazine, IEEE* 14.5 (2011), pp. 36–40 (cit. on p. 100).

[15] Bruno Andò, Salvatore Baglio, Salvatore La Malfa, and Gaetano L'Episcopo. "All inkjet printed system for strain measurement". In: *IEEE Sensors, 2011.* IEEE. 2011, pp. 215–217 (cit. on pp. 105, 109).

[16] Bruno Andò, Salvatore Baglio, Gaetano L'Episcopo, Vincenzo Marletta, Nicolò Savalli, and Carlo Trigona. "A BE-SOI MEMS for inertial measurement in geophysical applications". In: *Instrumentation and Measurement, IEEE Transactions on* 60.5 (2011), pp. 1901–1908 (cit. on p. 50).

[18] Bruno Andò, Salvatore Baglio, Nicolo Savalli, and Carlo Trigona. "Cascaded "Triple-Bent-Beam" MEMS Sensor for Contactless Temperature Measurements in Nonac-

cessible Environments". In: *IEEE Transactions on Instrumentation and Measurement* 60.4 (2011), pp. 1348–1357 (cit. on pp. 52, 243).

[21] S Baglio, B Ando, and G L'Episcopo. "Lateral cantilever beam in BESOI technology". In: *Instrumentation and Measurement Technology Conference (I2MTC), 2011 IEEE*. IEEE. 2011, pp. 1–6 (cit. on p. 50).

[31] Mark T Bohr. "Nanotechnology goals and challenges for electronic applications". In: *IEEE Transactions on Nanotechnology* 1.1 (2002), pp. 56–62 (cit. on p. 69).

[37] Martin Brischwein, Sigrun Herrmann, Winfried Vonau, Frank Berthold, Helmut Grothe, Elena R Motrescu, and Bernhard Wolf. "The use of screen printed electrodes for the sensing of cell responses". In: *AFRICON 2007*. IEEE. 2007, pp. 1–5 (cit. on p. 101).

[45] Andrew Cao, Jongbaeg Kim, and Liwei Lin. "Bi-directional electrothermal electromagnetic actuators". In: *Journal of Micromechanics and Microengineering* 17.5 (2007), p. 975 (cit. on p. 52).

[49] J-S Chang, Phil A Lawless, and Toshiaki Yamamoto. "Corona discharge processes". In: *IEEE Transactions on Plasma Science* 19.6 (1991), pp. 1152–1166 (cit. on p. 180).

[51] Tsung-Shune Chin. "Permanent magnet films for applications in microelectromechanical systems". In: *Journal of Magnetism and Magnetic Materials* 209.1 (2000), pp. 75–79 (cit. on p. 83).

[55] Stephen Y Chou, Peter R Krauss, and Preston J Renstrom. "Nanoimprint lithography". In: *Journal of Vacuum Science & Technology B: Microelectronics and Nanometer Structures* 14.6 (1996), pp. 4129–4133 (cit. on p. 72).

[56] Claudio Contiero, Bnmo Murari, and Benedetto Vigna. "Progress in power ICs and MEMS". In: *Proceedings of The 16th International Symposium on Power Semiconductor Devices and ICs, 2004. ISPSD'04.* IEEE. 2004, pp. 3–12 (cit. on p. 60).

[62] Allen Cowen, Bruce Dudley, E Hill, M Walters, R Wood, S Johnson, H Wynands, and B Hardy. *Metal-*

MUMPs design handbook. Tech. rep. 4.0. `http://www.memscap.com/__data/assets/pdf_file/0015/1833/MetalMUMPs.DR.4.0.pdf`: MEMSCAP Inc., Durham, 2012 (cit. on pp. 52–54, 243, 246).

[63] Allen Cowen, G Hames, K Glukh, and B Hardy. *PiezoMUMPs design handbook*. Tech. rep. 1.2. `http://www.memscap.com/__data/assets/pdf_file/0020/5915/PiezoMUMPs.DR.1.2.pdf`: MEMSCAP Inc., Durham, 2012 (cit. on pp. 56–58, 303, 304).

[64] Karl et al. Crowley. "Fabrication of an ammonia gas sensor using inkjet-printed polyaniline nanoparticles". In: *Talanta* 77.2 (2008), pp. 710–717 (cit. on pp. 101, 103).

[79] Chang-Beom Eom and Susan Trolier-McKinstry. "Thin-film piezoelectric MEMS". In: *MRS Bulletin* 37.11 (2012), pp. 1007–1017 (cit. on p. 164).

[82] Leonard C Feldman and James W Mayer. *Fundamentals of surface and thin film analysis*. Vol. 119. North-Holland New York, 1986 (cit. on p. 95).

[86] Sawyer B Fuller, Eric J Wilhelm, and Joseph M Jacobson. "Ink-jet printed nanoparticle microelectromechanical systems". In: *Journal of Microelectromechanical Systems* 11.1 (2002), pp. 54–60 (cit. on p. 103).

[94] David Girbau, Lluis Pradell, Antonio Lazaro, and Alvar Nebot. "Electrothermally-actuated RF-MEMS suspended parallel switch". In: *Microwave and Optical Technology Letters* 49.12 (2007), pp. 2894–2896 (cit. on p. 52).

[97] Joseph Goldstein, Dale E Newbury, David C Joy, Charles E Lyman, Patrick Echlin, Eric Lifshin, Linda Sawyer, and Joseph R Michael. *Scanning electron microscopy and X-ray microanalysis*. Springer, 2003 (cit. on p. 95).

[100] F Grassia, G Izzo, N Piluso, A Di Stefano, and G Foti. "Spatial distribution of pulsed plasma emitted from a carbon target". In: *Radiation Effects & Defects in Solids: Incorporating Plasma Science & Plasma Technology* 165.6-10 (2010), pp. 713–720 (cit. on pp. 72, 86, 87, 91).

[109] Siyuan He, John S Chang, Lihua Li, and Hsu Ho. "Characterization of Young's modulus and residual stress gradient of MetalMUMPs electroplated nickel film". In: *Sensors and Actuators A: Physical* 154.1 (2009), pp. 149–156 (cit. on p. 246).

[133] Robert Krueger. "Dual-column (FIB–SEM) wafer applications". In: *Micron* 30.3 (1999), pp. 221–226 (cit. on p. 71).

[134] Riadh Lakhmi, Hélène Debéda, Isabelle Dufour, and Claude Lucat. "Force sensors based on screen-printed cantilevers". In: *IEEE Sensors Journal* 10.6 (2010), pp. 1133–1137 (cit. on p. 101).

[135] Giacomo Langfelder, Antonio Francesco Longoni, Alessandro Tocchio, and Ernesto Lasalandra. "MEMS motion sensors based on the variations of the fringe capacitances". In: *IEEE Sensors Journal* 11.4 (2011), pp. 1069–1077 (cit. on pp. 60, 62, 63).

[146] Yi Liu, Tianhong Cui, and Kody Varahramyan. "All-polymer capacitor fabricated with inkjet printing tech-

nique". In: *Solid-State Electronics* 47.9 (2003), pp. 1543–1548 (cit. on p. 103).

[151] M Mantysalo, Ville Pekkanen, Kimmo Kaija, Juha Niittynen, Santtu Koskinen, Eerik Halonen, P Mansikkamaki, and O Hameenoja. "Capability of inkjet technology in electronics manufacturing". In: *59th Electronic Components and Technology Conference, 2009. ECTC 2009.* IEEE. 2009, pp. 1330–1336 (cit. on p. 100).

[155] ME McHenry and DE Laughlin. "Nano-scale materials development for future magnetic applications". In: *Acta materialia* 48.1 (2000), pp. 223–238 (cit. on p. 83).

[172] *Novacentrix® Metalon Conductive Inks*. `http://www.novacentrix.com/products/metalon-inks`. Accessed: 2013-07-01 (cit. on pp. 106, 256).

[174] NP Ostbo. "MEMS-pie: The Integration of Piezo-electric Thin Films in a SOI-MEMS Process". In: *MST NEWS* 4 (2006), p. 40 (cit. on p. 164).

[180] RFW Pease. "Electron beam lithography". In: *Contemporary Physics* 22.3 (1981), pp. 265–290 (cit. on pp. 70, 72).

[182] FCM Van de Pol, FR Blom, and Th JA Popma. "RF planar magnetron sputtered ZnO films I: structural properties". In: *Thin Solid Films* 204.2 (1991), pp. 349–364 (cit. on p. 99).

[183] A Pomarico, A Morea, P Flora, G Roselli, and E Lasalandra. "Vertical MEMS resonators for real-time clock applications". In: *Journal of Sensors* 2010 (2010) (cit. on p. 60).

[184] Charles P Poole and Frank J Owens. *Introduction to nanotechnology*. Cambridge University Press, 2003 (cit. on pp. 68, 69).

[215] Rana I Shakoor, Shafaat A Bazaz, M Burnie, Y Lai, and MM Hasan. "Electrothermally actuated resonant rate gyroscope fabricated using the MetalMUMPs". In: *Microelectronics Journal* 42.4 (2011), pp. 585–593 (cit. on p. 52).

[217] SN Shtykov and T Yu Rusanova. "Nanomaterials and nanotechnologies in chemical and biochemical sensors: capabilities and applications". In: *Russian Journal of*

General Chemistry 78.12 (2008), pp. 2521–2531 (cit. on p. 83).

[222] Chavis Srichan, T Saikrajang, T Lomas, A Jomphoak, T Maturos, D Phokaratkul, T Kerdcharoen, and A Tuantranont. "Inkjet printing PEDOT:PSS using desktop inkjet printer". In: *6th International Conference on Electrical Engineering/Electronics, Computer, Telecommunications and Information Technology, 2009. ECTI-CON 2009.* Vol. 1. IEEE. 2009, pp. 465–468 (cit. on p. 103).

[224] FA Stevie, LA Giannuzzi, and BI Prenitzer. *Introduction to Focused Ion Beams: instrumentation, theory, techniques and practice*. New York: Springer, 2005 (cit. on pp. 72, 75).

[225] STMicroelectronics. *Design rules for ThELMA 22* (cit. on p. 231).

[229] Tuomo Suntola. "Atomic layer epitaxy". In: *Materials Science Reports* 4.5 (1989), pp. 261–312 (cit. on p. 72).

[234] A Tocchio, G Langfelder, A Longoni, and E Lasalandra. "In-plane and out-of-plane MEMS motion sensors

based on fringe capacitances". In: *Procedia Engineering* 5 (2010), pp. 1392–1395 (cit. on p. 62).

[238] Tomas Unander and H-E Nilsson. "Characterization of printed moisture sensors in packaging surveillance applications". In: *IEEE Sensors Journal* 9.8 (2009), pp. 922–928 (cit. on p. 101).

[248] Bertram E Warren. *X-ray Diffraction*. DoverPublications.com, 1969 (cit. on p. 96).

[252] George M Whitesides and Bartosz Grzybowski. "Self-assembly at all scales". In: *Science* 295.5564 (2002), pp. 2418–2421 (cit. on p. 72).

[253] Gary Wiederrecht. *Handbook of nanofabrication*. Access Online via Elsevier, 2010 (cit. on p. 70).

[255] Oliver Wilhelmi. "Rapid Prototyping with DualBeam Instruments". In: *Imaging & Microscopy* 9.3 (2007), pp. 54–56 (cit. on p. 73).

[257] Edward L Wolf. *Nanophysics and nanotechnology: an introduction to modern concepts in nanoscience*. John Wiley & Sons, 2008 (cit. on p. 71).

[265] NK Zayer, R Greef, K Rogers, AJC Grellier, and CN Pannell. “In situ monitoring of sputtered zinc oxide films for piezoelectric transducers”. In: *Thin Solid Films* 352.1 (1999), pp. 179–184 (cit. on p. 91).

Energy Harvesting

[1] SG Adams, FM Bertsch, KA Shaw, PG Hartwell, FC Moon, and NC MacDonald. “Capacitance based tunable resonators”. In: *Journal of Micromechanics and Microengineering* 8.1 (1998), p. 15 (cit. on pp. 139, 140).

[3] James J Allen. *Micro Electro Mechanical System Design (Mechanical Engineering)*. CRC, 2005 (cit. on pp. 42, 44, 45, 133, 134, 169).

[4] B Andò, S Baglio, M Baù, AR Bulsara, V Ferrari, M Ferrari, and G L’Episcopo. “A Nonlinear Energy Harvester by Direct Printing Technology”. In: *Procedia Engineering* 47 (2012), pp. 933–936 (cit. on pp. 105, 109, 251).

[6] B Andó, S Baglio, L Latorre, F Maiorca, P Nouet, and C Trigona. "Magnetically-Coupled Cantilevers with Antiphase Bistable Behavior for Kinetic Energy Harvesting". In: *Procedia Engineering* 47 (2012), pp. 1065–1068 (cit. on pp. 83, 154).

[8] B Andó, S Baglio, F Maiorca, and C Trigona. "Two Dimensional Bistable Vibration Energy Harvester". In: *Procedia Engineering* 47 (2012), pp. 1061–1064 (cit. on p. 154).

[9] B Andò, S Baglio, C Trigona, N Dumas, Laurent Latorre, and P Nouet. "Nonlinear mechanism in MEMS devices for energy harvesting applications". In: *Journal of Micromechanics and Microengineering* 20.12 (2010), p. 125020 (cit. on pp. 35, 38, 46, 83, 144, 287, 306).

[17] Bruno Andò, Salvatore Baglio, Gaetano L'Episcopo, and Carlo Trigona. "Investigation on Mechanically Bistable MEMS Devices for Energy Harvesting From Vibrations". In: *Journal of Microelectromechanical Systems* 21.4 (2012), pp. 779–790 (cit. on pp. 37, 39, 50, 122, 144, 155, 292).

[19] Steven R Anton and Henry A Sodano. "A review of power harvesting using piezoelectric materials (2003–2006)". In: *Smart Materials and Structures* 16.3 (2007), R1 (cit. on pp. 161, 167).

[27] SP Beeby, MJ Tudor, and NM White. "Energy harvesting vibration sources for microsystems applications". In: *Measurement Science and Technology* 17.12 (2006), R175–R195 (cit. on pp. 124, 169–172, 218, 234).

[28] Steve P Beeby, RN Torah, MJ Tudor, P Glynne-Jones, T O'Donnell, CR Saha, and S Roy. "A micro electromagnetic generator for vibration energy harvesting". In: *Journal of Micromechanics and Microengineering* 17.7 (2007), p. 1257 (cit. on p. 184).

[32] S Boisseau, G Despesse, T Ricart, E Defay, and A Sylvestre. "Cantilever-based electret energy harvesters". In: *Smart Materials and Structures* 20.10 (2011), p. 105013 (cit. on pp. 179–182).

[33] S Boisseau, G Despesse, and A Sylvestre. "Optimization of an electret-based energy harvester". In: *Smart*

Materials and Structures 19.7 (2010), p. 075015 (cit. on p. 182).

[47] Clemens Cepnik, Roland Lausecker, and Ulrike Wallrabe. "Review on Electrodynamic Energy Harvesters - A Classification Approach". In: *Micromachines* 4.2 (2013), pp. 168–196 (cit. on pp. 118, 129, 183).

[48] Vinod R Challa, MG Prasad, Yong Shi, and Frank T Fisher. "A vibration energy harvesting device with bidirectional resonance frequency tunability". In: *Smart Materials and Structures* 17.1 (2008), p. 015035 (cit. on pp. 139, 140).

[52] Yi Chiu and Victor FG Tseng. "A capacitive vibration-to-electricity energy converter with integrated mechanical switches". In: *Journal of micromechanics and microengineering* 18.10 (2008), p. 104004 (cit. on p. 179).

[54] WJ Choi, Yongbae Jeon, J-H Jeong, Rajendra Sood, and Sang-Gook Kim. "Energy harvesting MEMS device based on thin film piezoelectric cantilevers". In: *Journal of Electroceramics* 17.2-4 (2006), pp. 543–548 (cit. on p. 164).

[57] KA Cook-Chennault, N Thambi, and AM Sastry. "Powering MEMS portable devices - A review of non-regenerative and regenerative power supply systems with special emphasis on piezoelectric energy harvesting systems". In: *Smart Materials and Structures* 17.4 (2008), p. 043001 (cit. on p. 166).

[58] F. Cottone. "Nonlinear Piezoelectric Generators for Vibration Energy Harvesting". PhD thesis. Università, degli Studi di Perugia - Dottorato di Ricerca in Fisica - XX Ciclo, 2006/07 (cit. on pp. 134, 135).

[59] F Cottone, L Gammaitoni, H Vocca, M Ferrari, and V Ferrari. "Piezoelectric buckled beams for random vibration energy harvesting". In: *Smart materials and structures* 21.3 (2012), p. 035021 (cit. on pp. 144, 155).

[60] F Cottone, H Vocca, and L Gammaitoni. "Nonlinear energy harvesting". In: *Physical Review Letters* 102.8 (2009), p. 080601 (cit. on pp. 11, 142, 144, 145).

[74] C Eichhorn, F Goldschmidtboeing, and P Woias. "Bidirectional frequency tuning of a piezoelectric energy converter based on a cantilever beam". In: *Journal*

of Micromechanics and Microengineering 19.9 (2009), p. 094006 (cit. on p. 139).

[75] M El-Hami, P Glynne-Jones, NM White, M Hill, Stephen Beeby, E James, AD Brown, and JN Ross. "Design and fabrication of a new vibration-based electromechanical power generator". In: *Sensors and Actuators A: Physical* 92.1 (2001), pp. 335–342 (cit. on p. 184).

[80] A Erturk and DJ Inman. "An experimentally validated bimorph cantilever model for piezoelectric energy harvesting from base excitations". In: *Smart Materials and Structures* 18.2 (2009), p. 025009 (cit. on p. 164).

[81] Alper Erturk and Daniel J Inman. *Piezoelectric energy harvesting*. Wiley. com, 2011 (cit. on pp. 118, 129, 161, 164, 165, 294, 295).

[83] M Ferrari, V Ferrari, M Guizzetti, B Andò, S Baglio, and C Trigona. "Improved energy harvesting from wideband vibrations by nonlinear piezoelectric converters". In: *Sensors and Actuators A: Physical* 162.2 (2010), pp. 425–431 (cit. on pp. 11, 154).

[87] Tzeno Galchev, Hanseup Kim, and Khalil Najafi. "Micro power generator for harvesting low-frequency and nonperiodic vibrations". In: *Journal of Microelectromechanical Systems* 20.4 (2011), pp. 852–866 (cit. on pp. 38, 153).

[95] Fabio Giusa, Andrea Giuffrida, Carlo Trigona, Bruno Andò, Adi R Bulsara, and Salvatore Baglio. ""Random Mechanical Switching Harvesting on Inductor": A Novel Approach to Collect and Store Energy from Weak Random Vibrations with Zero Voltage Threshold". In: *Sensors and Actuators A: Physical* (2013) (cit. on p. 36).

[102] Arman Hajati and Sang-Gook Kim. "Ultra-wide bandwidth piezoelectric energy harvesting". In: *Applied Physics Letters* 99.8 (2011), pp. 083105–083105 (cit. on p. 166).

[107] RL Harne and KW Wang. "A review of the recent research on vibration energy harvesting via bistable systems". In: *Smart Materials and Structures* 22.2 (2013), p. 023001 (cit. on pp. 15, 16, 18–21, 37, 156, 166, 185).

[108] P Harrop and R Das. "Energy Harvesting and Storage for Electronic Devices 2009-2019". In: *IDTechEx, Cambridge, January* (2009) (cit. on p. 116).

[112] Daniel Hoffmann, Bernd Folkmer, and Yiannos Manoli. "Fabrication, characterization and modelling of electrostatic micro-generators". In: *Journal of Micromechanics and Microengineering* 19.9 (2009), p. 094001 (cit. on p. 178).

[118] Hamid Jabbar, Young S Song, and Taikyeong Ted Jeong. "RF energy harvesting system and circuits for charging of mobile devices". In: *IEEE Transactions on Consumer Electronics* 56.1 (2010), pp. 247–253 (cit. on p. 118).

[120] YB Jeon, R Sood, J-h Jeong, and S-G Kim. "MEMS power generator with transverse mode thin film PZT". In: *Sensors and Actuators A: Physical* 122.1 (2005), pp. 16–22 (cit. on p. 164).

[125] S Kerzenmacher, J Ducrée, R Zengerle, and F Von Stetten. "Energy harvesting by implantable abiotically cat-

alyzed glucose fuel cells". In: *Journal of Power Sources* 182.1 (2008), pp. 1–17 (cit. on p. 118).

[126] Gi-Woo Kim and Jaehwan Kim. "Compliant bistable mechanism for low frequency vibration energy harvester inspired by auditory hair bundle structures". In: *Smart Materials and Structures* 22.1 (2013), p. 014005 (cit. on p. 155).

[127] Hyeoung Woo Kim, Amit Batra, Shashank Priya, Kenji Uchino, Douglas Markley, Robert E Newnham, and Heath F Hofmann. "Energy Harvesting Using a Piezoelectric "Cymbal" Transducer in Dynamic Environment". In: *Japanese journal of applied physics* 43 (2004), p. 6178 (cit. on p. 166).

[136] Chengkuo Lee, Ye Mei Lim, Bin Yang, Rama Krishna Kotlanka, Chun-Huat Heng, Johnny Han He, Min Tang, Jin Xie, and Hanhua Feng. "Theoretical comparison of the energy harvesting capability among various electrostatic mechanisms from structure aspect". In: *Sensors and Actuators A: Physical* 156.1 (2009), pp. 208–216 (cit. on p. 178).

[138] Eli S Leland and Paul K Wright. "Resonance tuning of piezoelectric vibration energy scavenging generators using compressive axial preload". In: *Smart Materials and Structures* 15.5 (2006), p. 1413 (cit. on pp. 139, 140).

[144] Hélène Lhermet, Cyril Condemine, Marc Plissonnier, Raphaël Salot, Patrick Audebert, and Marion Rosset. "Efficient power management circuit: From thermal energy harvesting to above-IC microbattery energy storage". In: *IEEE Journal of Solid-State Circuits* 43.1 (2008), pp. 246–255 (cit. on p. 118).

[145] Huicong Liu, Chengkuo Lee, Takeshi Kobayashi, Cho Jui Tay, and Chenggen Quan. "Investigation of a MEMS piezoelectric energy harvester system with a frequency-widened-bandwidth mechanism introduced by mechanical stoppers". In: *Smart Materials and Structures* 21.3 (2012), p. 035005 (cit. on pp. 142, 143).

[150] Felice Maiorca, Fabio Giusa, Carlo Trigona, Bruno Andò, Adi R Bulsara, and Salvatore Baglio. "Diode-less Mechanical H-Bridge Rectifier for "Zero Threshold" Vi-

bration Energy Harvesters". In: *Sensors and Actuators A: Physical* (2013) (cit. on p. 36).

[152] Marcin Marzencki, Maxime Defosseux, and Skandar Basrour. "MEMS vibration energy harvesting devices with passive resonance frequency adaptation capability". In: *Microelectromechanical Systems, Journal of* 18.6 (2009), pp. 1444–1453 (cit. on p. 152).

[156] CR McInnes, DG Gorman, and MP Cartmell. "Enhanced vibrational energy harvesting using nonlinear stochastic resonance". In: *Journal of Sound and Vibration* 318.4 (2008), pp. 655–662 (cit. on p. 37).

[157] Scott Meninger, Jose Oscar Mur-Miranda, Rajeevan Amirtharajah, Anantha Chandrakasan, and Jeffrey H Lang. "Vibration-to-electric energy conversion". In: *IEEE Transactions on Very Large Scale Integration (VLSI) Systems* 9.1 (2001), pp. 64–76 (cit. on pp. 169, 218, 222, 234).

[158] Ulrich Mescheder, Antwi Nimo, Bernhard Müller, and Awad Saad Abou Elkeir. "Micro harvester using isotropic charging of electrets deposited on vertical sidewalls for

conversion of 3D vibrational energy". In: *Microsystem technologies* 18.7-8 (2012), pp. 931–943 (cit. on pp. 43, 182).

[160] Paul D Mitcheson, Tim C Green, Eric M Yeatman, and Andrew S Holmes. "Architectures for vibration-driven micropower generators". In: *Microelectromechanical Systems, Journal of* 13.3 (2004), pp. 429–440 (cit. on p. 179).

[161] Paul D Mitcheson, Elizabeth K Reilly, T Toh, Paul K Wright, and Eric M Yeatman. "Performance limits of the three MEMS inertial energy generator transduction types". In: *Journal of Micromechanics and Microengineering* 17.9 (2007), S211 (cit. on pp. 35, 136).

[162] Paul D Mitcheson, Tom Sterken, Cairan He, M Kiziroglou, EM Yeatman, and R Puers. "Electrostatic microgenerators". In: *Measurement and Control* 41.4 (2008), pp. 114–119 (cit. on pp. 118, 129, 173–176, 221).

[166] G Murillo, G Abadal, F Torres, JL Lopez, J Giner, A Uranga, and N Barniol. "Harvester-on-chip: Design

of a proof of concept prototype". In: *Microelectronic Engineering* 86.4 (2009), pp. 1183–1186 (cit. on p. 152).

[168] DS Nguyen, E Halvorsen, GU Jensen, and A Vogl. "Fabrication and characterization of a wideband MEMS energy harvester utilizing nonlinear springs". In: *Journal of Micromechanics and Microengineering* 20.12 (2010), p. 125009 (cit. on pp. 151, 152).

[176] Geffrey K Ottman, Heath F Hofmann, and George A Lesieutre. "Optimized piezoelectric energy harvesting circuit using step-down converter in discontinuous conduction mode". In: *IEEE Transactions on Power Electronics* 18.2 (2003), pp. 696–703 (cit. on p. 157).

[181] María Teresa Penella-López and Manuel Gasulla-Forner. "Optical Energy Harvesting". In: *Powering Autonomous Sensors*. Springer, 2011, pp. 81–123 (cit. on p. 118).

[188] Shashank Priya, Chih-Ta Chen, Darren Fye, and Jeff Zahnd. "Piezoelectric windmill: a novel solution to remote sensing". In: *Japanese Journal of Applied Physics* 44.3 (2005), pp. 104–107 (cit. on p. 166).

[189] Shashank Priya and Daniel J Inman. *Energy Harvesting Technologies*. Boston, MA: Springer US, 2009 (cit. on pp. 114, 122, 124, 183, 184).

[190] Yong Qin, Xudong Wang, and Zhong Lin Wang. "Microfibre–nanowire hybrid structure for energy scavenging". In: *Nature* 451.7180 (2008), pp. 809–813 (cit. on p. 166).

[193] R Ramlan, MJ Brennan, BR Mace, and I Kovacic. "Potential benefits of a non-linear stiffness in an energy harvesting device". In: *Nonlinear dynamics* 59.4 (2010), pp. 545–558 (cit. on p. 151).

[196] M Renaud, K Karakaya, Tom Sterken, P Fiorini, Christiaan Van Hoof, and Robert Puers. "Fabrication, modelling and characterization of MEMS piezoelectric vibration harvesters". In: *Sensors and Actuators A: Physical* 145 (2008), pp. 380–386 (cit. on p. 164).

[200] Shad Roundy. "On the effectiveness of vibration-based energy harvesting". In: *Journal of intelligent material systems and structures* 16.10 (2005), pp. 809–823 (cit. on pp. 34, 126).

[201] Shad Roundy, Eli S Leland, Jessy Baker, Eric Carleton, Elizabeth Reilly, Elaine Lai, Brian Otis, Jan M Rabaey, Paul K Wright, and V Sundararajan. "Improving power output for vibration-based energy scavengers". In: *Pervasive Computing, IEEE* 4.1 (2005), pp. 28–36 (cit. on pp. 142, 164).

[202] Shad Roundy, Paul K Wright, and Jan Rabaey. "A study of low level vibrations as a power source for wireless sensor nodes". In: *Computer communications* 26.11 (2003), pp. 1131–1144 (cit. on pp. 117–119, 126–128, 172, 173, 186, 205, 220, 221, 225, 230, 236).

[203] Shad Roundy, Paul Kenneth Wright, and Jan M Rabaey. *Energy scavenging for wireless sensor networks: with special focus on vibrations*. Springer, 2004 (cit. on p. 163).

[204] Shad Roundy and Yang Zhang. "Toward self-tuning adaptive vibration-based microgenerators". In: *Smart Materials, Nano-, and Micro-Smart Systems*. International Society for Optics and Photonics. 2005, pp. 373–384 (cit. on p. 138).

[205] Salem Saadon and Othman Sidek. "A review of vibration-based MEMS piezoelectric energy harvesters". In: *Energy Conversion and Management* 52.1 (2011), pp. 500–504 (cit. on p. 166).

[208] Ibrahim Sari, Tuna Balkan, and Haluk Kulah. "An electromagnetic micro energy harvester based on an array of parylene cantilevers". In: *Journal of Micromechanics and Microengineering* 19.10 (2009), p. 105023 (cit. on p. 184).

[214] SM Shahruz. "Design of mechanical band-pass filters for energy scavenging: multi-degree-of-freedom models". In: *Journal of Vibration and Control* 14.5 (2008), pp. 753–768 (cit. on pp. 141, 143).

[216] Dongna Shen, Jung-Hyun Park, Jyoti Ajitsaria, Song-Yul Choe, Howard C Wikle III, and Dong-Joo Kim. "The design, fabrication and evaluation of a MEMS PZT cantilever with an integrated Si proof mass for vibration energy harvesting". In: *Journal of Micromechanics and Microengineering* 18.5 (2008), p. 055017 (cit. on p. 164).

[223] Tom Sterken, Kris Baert, Christiaan Van Hoof, Robert Puers, Gustaaf Borghs, and Paolo Fiorini. "Comparative modelling for vibration scavengers [MEMS energy scavengers]". In: *Proceedings of IEEE Sensors, 2004.* IEEE. 2004, pp. 1249–1252 (cit. on pp. 132, 156).

[230] Yuji Suzuki, Daigo Miki, Masato Edamoto, and Makoto Honzumi. "A MEMS electret generator with electrostatic levitation for vibration-driven energy-harvesting applications". In: *Journal of Micromechanics and Microengineering* 20.10 (2010), p. 104002 (cit. on p. 182).

[231] Richard RA Syms. "Electrothermal frequency tuning of folded and coupled vibrating micromechanical resonators". In: *Journal of Microelectromechanical Systems* 7.2 (1998), pp. 164–171 (cit. on p. 139).

[232] Lihua Tang, Yaowen Yang, and Chee Kiong Soh. "Toward broadband vibration-based energy harvesting". In: *Journal of Intelligent Material Systems and Structures* 21.18 (2010), pp. 1867–1897 (cit. on p. 137).

[235] Carlo Trigona, Norbert Dumas, Laurent Latorre, Bruno Andò, S Baglio, and Pascal Nouet. "Exploiting Ben-

efits of a Periodically-Forced Nonlinear Oscillator for Energy Harvesting from Ambient Vibrations". In: *Procedia engineering* 25 (2011), pp. 819–822 (cit. on pp. 11, 37, 38, 291).

[237] Lars Geir Whist Tvedt, Duy Son Nguyen, and Einar Halvorsen. "Nonlinear behavior of an electrostatic energy harvester under wide-and narrowband excitation". In: *Microelectromechanical Systems, Journal of* 19.2 (2010), pp. 305–316 (cit. on pp. 151, 152).

[244] RJM Vullers, Rob van Schaijk, Inge Doms, Chris Van Hoof, and R Mertens. "Micropower energy harvesting". In: *Solid-State Electronics* 53.7 (2009), pp. 684–693 (cit. on pp. 115, 117, 118).

[245] Lei Wang and FG Yuan. "Vibration energy harvesting by magnetostrictive material". In: *Smart Material Structures* 17.4 (2008), p. 5009 (cit. on pp. 118, 129, 185).

[246] Zhong Lin Wang and Jinhui Song. "Piezoelectric nanogenerators based on zinc oxide nanowire arrays". In: *Science* 312.5771 (2006), pp. 242–246 (cit. on p. 166).

[256] P Woias, Y Manoli, T Nann, and FV Stetten. "Energy harvesting for autonomous microsystems". In: *MST news* 4 (2005), p. 42 (cit. on pp. 115, 118).

[258] Wen-Jong Wu, Yu-Yin Chen, Bor-Shun Lee, Jyun-Jhang He, and Yen-Tun Peng. "Tunable resonant frequency power harvesting devices". In: *Smart Structures and Materials*. International Society for Optics and Photonics. 2006, 61690A–61690A (cit. on p. 141).

[260] Sheng Xu, Yong Qin, Chen Xu, Yaguang Wei, Rusen Yang, and Zhong Lin Wang. "Self-powered nanowire devices". In: *Nature Nanotechnology* 5.5 (2010), pp. 366–373 (cit. on p. 166).

[261] Kiyotaka Yamashita, Makoto Honzumi, Kei Hagiwara, Yoshinori Iguchi, and Yuji Suzuki. "Vibration-driven MEMS energy harvester with vertical electrets". In: *Proc. PowerMEMS* (2010), pp. 165–168 (cit. on p. 180).

[262] Shi-Chune Yao, Xudong Tang, Cheng-Chieh Hsieh, Yousef Alyousef, Michael Vladimer, Gary K Fedder, and Cristina H Amon. "Micro-electro-mechanical systems (MEMS)-based micro-scale direct methanol fuel

cell development". In: *Energy* 31.5 (2006), pp. 636–649 (cit. on p. 120).

[263] Eric M Yeatman. "Energy harvesting from motion using rotating and gyroscopic proof masses". In: *Proceedings of the Institution of Mechanical Engineers, Part C: Journal of Mechanical Engineering Science* 222.1 (2008), pp. 27–36 (cit. on p. 124).

[264] Eric M Yeatman, Paul D Mitcheson, and Andrew S Holmes. "Micro-engineered devices for motion energy harvesting". In: *Electron Devices Meeting, 2007. IEDM 2007. IEEE International*. IEEE. 2007, pp. 375–378 (cit. on p. 128).

[268] Wenli Zhou, Wei-Hsin Liao, and Wen J Li. "Analysis and design of a self-powered piezoelectric microaccelerometer". In: *Society of Photo-Optical Instrumentation Engineers (SPIE) Conference Series*. Vol. 5763. 2005, pp. 233–240 (cit. on p. 164).

[269] D. Zhu, M.J. Tudor, and S.P. Beeby. "Strategies for increasing the operating frequency range of vibration

energy harvesters: a review". In: *Measurement Science and Technology* 21 (2010), p. 022001 (cit. on p. 137).

Electric Current Sensors

[7] B Ando, S Baglio, G L'Episcopo, F Maiorca, and C Trigona. "Autonomous bistable microsensors for noninvasive AC electrical current measurements". In: *IEEE International Instrumentation and Measurement Technology Conference (I2MTC) 2013*. IEEE. 2013, pp. 93–97 (cit. on pp. 287, 291).

[23] Salvatore Baglio, Laurent Latorre, and Pascal Nouet. "Development of novel magnetic field monolithic sensors with standard CMOS-compatible MEMS technology". In: *1999 Symposium on Smart Structures and Materials*. International Society for Optics and Photonics. 1999, pp. 417–424 (cit. on p. 284).

[30] Vincent Beroulle, Yves Bertrand, Laurent Latorre, and Pascal Nouet. "Monolithic piezoresistive CMOS magnetic field sensors". In: *Sensors and Actuators A: Physical* 103.1 (2003), pp. 23–32 (cit. on p. 286).

[61] RP Cowburn, AM Moulin, and ME Welland. "High sensitivity measurement of magnetic fields using microcantilevers". In: *Applied physics letters* 71.15 (1997), pp. 2202–2204 (cit. on p. 284).

[68] O Dezuari, E Belloy, SE Gilbert, and MAM Gijs. "Printed circuit board integrated fluxgate sensor". In: *Sensors and Actuators A: Physical* 81.1 (2000), pp. 200–203 (cit. on p. 281).

[69] Richard Dickinson and Shaun Milano. "Isolated open loop current sensing using Hall Effect technology in an optimized magnetic circuit". In: *Allegro MicroSystems, Inc.(Last visited: 7 th November 2007)* (2002) (cit. on p. 279).

[71] D Drung, C Assmann, J Beyer, A Kirste, M Peters, F Ruede, and Th Schurig. "Highly sensitive and easy-to-use SQUID sensors". In: *IEEE Transactions on Applied Superconductivity* 17.2 (2007), pp. 699–704 (cit. on p. 281).

[72] Dietmar Drung, Jörn Beyer, Margret Peters, J-H Storm, and Thomas Schurig. "Novel SQUID current sensors

with high linearity at high frequencies". In: *IEEE Transactions on Applied Superconductivity* 19.3 (2009), pp. 772–777 (cit. on p. 282).

[78] Harald Emmerich and Martin Schofthaler. "Magnetic field measurements with a novel surface micromachined magnetic-field sensor". In: *IEEE Transactions on Electron Devices* 47.5 (2000), pp. 972–977 (cit. on p. 286).

[96] SM Goedeke, SW Allison, and PG Datskos. "Non-contact current measurement with cobalt-coated microcantilevers". In: *Sensors and Actuators A: Physical* 112.1 (2004), pp. 32–35 (cit. on p. 284).

[99] D Gordon and RE Brown. "Recent advances in fluxgate magnetometry". In: *IEEE Transactions on Magnetics* 8.1 (1972), pp. 76–82 (cit. on p. 30).

[111] Agustín L Herrera-May, Luz A Aguilera-Cortés, Pedro J García-Ramírez, and Elías Manjarrez. "Resonant magnetic field sensors based on MEMS technology". In: *Sensors* 9.10 (2009), pp. 7785–7813 (cit. on p. 285).

[119] Albrecht Jander, Carl Smith, and Robert Schneider. "Magnetoresistive sensors for nondestructive evalua-

tion". In: *Nondestructive Evaulation for Health Monitoring and Diagnostics*. International Society for Optics and Photonics. 2005, pp. 1–13 (cit. on p. 283).

[121] Liao Jingsheng, Guo Xiaohua, Zhu Mingjun, Ye Miaoyuan, and Yang Zefu. "Rogowski coil current transducer for low amplitude current measurement I". In: *Automation of Electric Power Systems* 2 (2003), p. 013 (cit. on p. 280).

[122] Zsolt Kádár, Andre Bossche, and Jeff Mollinger. "Integrated resonant magnetic-field sensor". In: *Sensors and Actuators A: Physical* 41.1 (1994), pp. 66–69 (cit. on pp. 284, 286).

[123] J Kaienburg, M Lutz, B Maihofer, and R Schellin. "A precise and contactless angle detection sensor using surface micromachining technology". In: *Proceedings of The Eleventh Annual International Workshop on Micro Electro Mechanical Systems, 1998. MEMS 98.* IEEE. 1998, pp. 367–371 (cit. on p. 284).

[124] Franz Keplinger, Samuel Kvasnica, Artur Jachimowicz, Franz Kohl, Johannes Steurer, and Hans Hauser.

"Lorentz force based magnetic field sensor with optical readout". In: *Sensors and Actuators A: Physical* 110.1 (2004), pp. 112–118 (cit. on p. 286).

[130] William Koon. "Current sensing for energy metering". In: *Application Engineering. Analog Devices* (2002) (cit. on p. 277).

[137] Eli S Leland, Richard M White, and Paul K Wright. "Design and fabrication of a MEMS AC electric current sensor". In: *Advances in Science and Technology* 54 (2009), pp. 350–355 (cit. on pp. 284, 287, 301).

[140] James Lenz and S Edelstein. "Magnetic sensors and their applications". In: *IEEE Sensors Journal* 6.3 (2006), pp. 631–649 (cit. on p. 278).

[141] James E Lenz. "A review of magnetic sensors". In: *Proceedings of the IEEE* 78.6 (1990), pp. 973–989 (cit. on p. 278).

[149] Steven A Macintyre. "Magnetic field sensor design". In: *Sensor Review* 11.2 (1991), pp. 7–11 (cit. on p. 283).

[153] S Massoud Amin and Bruce F Wollenberg. "Toward a smart grid: power delivery for the 21st century". In:

IEEE Power and Energy Magazine 3.5 (2005), pp. 34–41 (cit. on p. 276).

[178] Igor Paprotny, Eli Leland, Christopher Sherman, Richard M White, and Paul K Wright. "Self-powered MEMS sensor module for measuring electrical quantities in residential, commercial, distribution and transmission power systems". In: *IEEE Energy Conversion Congress and Exposition (ECCE) 2010*. IEEE. 2010, pp. 4159–4164 (cit. on p. 286).

[185] RS Popovic, HP Baltes, and F Rudolf. "An integrated silicon magnetic field sensor using the magnetodiode principle". In: *IEEE Transactions on Electron Devices* 31.3 (1984), pp. 286–291 (cit. on p. 283).

[186] RS el Popovic, Z Randjelovic, and D Manic. "Integrated Hall-effect magnetic sensors". In: *Sensors and Actuators A: Physical* 91.1 (2001), pp. 46–50 (cit. on p. 279).

[197] Pavel Ripka. "Electric current sensors: a review". In: *Measurement Science and Technology* 21.11 (2010), p. 112001 (cit. on pp. 281, 284).

[198] Pavel Ripka. "Review of fluxgate sensors". In: *Sensors and Actuators A: Physical* 33.3 (1992), pp. 129–141 (cit. on p. 281).

[206] Daniel J Sadler and Chong H Ahn. "On-chip eddy current sensor for proximity sensing and crack detection". In: *Sensors and Actuators A: Physical* 91.3 (2001), pp. 340–345 (cit. on p. 284).

[209] Debashis Satpathi, Jeffrey A Moore, and Michael G Ennis. "Design of a Terfenol-D based fiber-optic current transducer". In: *IEEE Sensors Journal* 5.5 (2005), pp. 1057–1065 (cit. on p. 283).

[233] RD Tikhonov. "Sensors on bipolar magnetotransistors with the base in the well". In: *Solid-state electronics* 49.8 (2005), pp. 1302–1308 (cit. on p. 283).

[247] David A Ward and J La T Exon. "Using Rogowski coils for transient current measurements". In: *Engineering Science & Education Journal* 2.3 (1993), pp. 105–113 (cit. on p. 280).

[251] Harold Weinstock. *SQUID sensors: fundamentals, fabrication, and applications*. Vol. 329. Springer, 1996 (cit. on p. 282).

[259] Chucheng Xiao, Lingyin Zhao, Tadashi Asada, WG Odendaal, and JD Van Wyk. "An overview of integratable current sensor technologies". In: *Conference Record of the Industry Applications Conference, 2003. 38th IAS Annual Meeting.* Vol. 2. IEEE. 2003, pp. 1251–1258 (cit. on p. 278).

Internet Links

[20] *APC International, Ltd. Piezoelectric materials*. `http://www.americanpiezo.com/apc-materials/choosing.html`. Accessed: 2013-07-05 (cit. on p. 256).

[26] *Baumer Distance sensors*. `http://baumer.amirada.net/pfinder_sensor/downloads/Produkte/PDF/Datenblatt/Optoelektronische_Sensoren/OADM_12U6460_S35A_web_EN.pdf`. Accessed: 2013-09-05 (cit. on p. 267).

[66] *Daft Logic - List of the Power Consumption of Typical Household Appliances - Last Updated: 12th May 2008*. http://www.daftlogic.com/information-appliance-power-consumption.html. Accessed: 2013-07-05 (cit. on pp. 322, 351).

[85] *Fujifilm Industrial Inkjet Printheads*. http://www.fujifilmusa.com/products/industrial_inkjet_printheads/index.html. Accessed: 2013-07-01 (cit. on p. 103).

[142] Gaetano L'Episcopo. *FIB machined cantilever beam piezoelectrically actuated*. Youtube: http://www.youtube.com/watch?v=LllIZhyiEKY. Published: 2012-03-16 (cit. on p. 83).

[143] Gaetano L'Episcopo, Fabio Giusa, and Carlo Trigona. *Bistable MEMS Structure*. Youtube: http://www.youtube.com/watch?v=1No1QSEB4f4. Published: 2012-07-25 (cit. on p. 249).

[159] *Microdrop Technologies*. http://www.microdrop.de/. Accessed: 2013-07-01 (cit. on p. 103).

[187] *POWER Magnet Shop: Magnet 1 mm diameter x 1 mm height*. http://www.powermagnetshop.net/disc/266/magnet-1-mm-x-height-1-mm?c=2306. Accessed: 2013-05-05 (cit. on p. 307).

[218] Valentina Sinatra, Carlo Guzzetta, Adriano Leonardi, Carlo Trigona, and Gaetano L'Episcopo. *Bistable cantilever beam with permanent magnet actuated by AC current*. Youtube: http://www.youtube.com/watch?v=oBCXHP_qmRw. Published: 2013-09-14 (cit. on p. 356).

[221] *Sparkfun - Triple Axis Accelerometer Breakout - MMA7361*. https://www.sparkfun.com/products/9652. Accessed: 2013-09-05 (cit. on p. 267).

List of Figures

List of Tables